THE EFFECT OF ABRASIVE PROPERTIES ON THE SURFACE INTEGRITY OF GROUND FERROUS MATERIALS

S. C. E. BLACK

Ph.D. Thesis 1996

THE EFFECT OF ABRASIVE PROPERTIES ON THE SURFACE INTEGRITY OF GROUND FERROUS MATERIALS

SEAN C. E. BLACK

A thesis submitted in partial fulfilment of the requirements of Liverpool John Moores University for the degree of Doctor of Philosophy.

FEBRUARY 1996

Abstract

The effect of the thermal properties of alumina and CBN abrasives on workpiece temperatures in grinding was investigated. A review of the literature revealed a lack of knowledge of the thermal properties of CBN limiting the accuracy of theoretical predictions of the heat conduction in CBN grinding.

A grain contact analysis was developed to predict the energy partitioning between the workpiece and wheel. The analysis takes into account two dimensional transient heat transfer in the grain and maintains temperature compatibility at the grain wear flat-workpiece interface.

The proportion of the total grinding energy entering the workpiece, termed the partition ratio, was estimated by correlating measured temperature distributions with theoretical distributions. The partition ratios when grinding with CBN were substantially lower than grinding with alumina wheels for a range of ferrous materials. The lower partition ratios with CBN grinding were attributed to the higher thermal conductivity of the CBN abrasive. The effective thermal conductivity of alumina and CBN grains were quantified by correlating the theoretical partitioning model with the measured results. The effective thermal conductivity of CBN was found to be considerably lower than the reported theoretical value albeit much higher than the effective thermal conductivity of alumina.

A model to predict the background temperature in grinding was proposed based on the experimental findings. The thermal model takes into account a triangular heat flux distribution in the grinding zone, the real length of contact and experimentally validated grain thermal properties. The input parameters to the thermal model were specified. To avoid temper colours on the workpiece surface the maximum background temperature must not exceed 450 to 500deg.C. for commonly used ferrous materials.

Acknowledgements

I would like to thank all of those who assisted towards the completion of this thesis. In particular, Professor W. Brian Rowe for his invaluable guidance and continuing enthusiasm throughout.

I would also like to acknowledge the support and interest of Professor Ben Mills.

Many thanks also go to Dr. Hong-Sheng Qi, Dr. Michael Morgan and Dr. David Allanson for their practical assistance and invaluable discussions.

The invaluable assistance from the technician staff in the AMT Research Laboratory is gratefully acknowledged. In particular Paul Wright, Stephen Ebbrell and Peter Moran who assisted in the experimental work.

Further acknowledgements are due to EPSRC, DeBeers, Unicorn Abrasives and Liverpool John Moores University for financial support during the investigation.

Finally, I wish to thank my family and friends and in particular Miss Karen Martin for her continued encouragement and support over many years leading to the completion of this work.

Nomenclature : Upper case symbols

		units
A	constant defined in text	
A_r	ratio of real to apparent contact area	m^2
B	constant defined in text	
C	heat flux distribution constant	
D	Dimensionless thickness	
E	energy	J
E_s	Young's modulus: grinding wheel	N/m^2
E_w	Young's modulus: workpiece material	N/m^2
F_n	normal grinding force	N
F'_n	specific normal grinding force	N/m
F_t	tangential grinding force	N
H	ratio of heat transfer coefficients	
H_c	Dimensionless convection coefficient	
H'_c	Dimensionless convection coefficient	
I(x)	integral	
K_s	stiffness of the grinding wheel	N/m^2
K_w	stiffness of the workpiece	N/m^2
K_0	modified Bessel function of second kind of order zero	
L	Peclet number	
P	grinding power	W
Q	rate of heat liberated	W
R_w	fraction of the total energy partitioned to the workpiece	
R_{ws}	energy partitioning between the workpiece and wheel	
R_{ch}	fraction of the total energy partitioned to the chips	
R_f	fraction of the total energy partitioned to the fluid	
R_s	fraction of the total energy partitioned to the grining wheel	
R_r	roughness ratio	
V	volume	m^3
X,Y,Z	dimensionless cartesian coordinate referenced to the workpiece	m
X',Z'	dimensionless cartesian referenced to the workpiece	
Z	material removal rate	m^3/s

Nomenclature : Lower case symbols

		units
a	true depth of cut	m
b	width dimension	m
c	specific heat capacity	J/kgK
d	depth	m
d_e	equivalent wheel diameter	m
d_w	workpiece diameter	m
d_s	grinding wheel diameter	m
e_c	specific grinding energy	J/m^3
e_{cc}	grinding chips specific energy	J/m^3
e_c	grinding fluid specific energy	J/m^3
e_{msd}	measured specific grinding energy	J/m^3
e_c^*	critical specific grinding energy	J/m^3
h	heat transfer coefficient	W/m^2K
h_c	convection coefficient	J/m^2 sK
ln	natural logarithm	
l_f	contact length due to deformation	m
l_g	geometric grinding contact length	m
l_e	real grinding contact length	m
l_{est}	estimated contact length	m
l_m	length to the position of the maximum temperature	m
q	heat flux	W/m^2
q_o	normalised heat flux	W/m^2
r	theoretical ratio of l_e to l_g	
r_o	wear flat radius on plane	m
t,t'	time	s
u	integration variable	
v	heat source velocity	m/s
v_f	infeedrate	m/s
v_s	grinding wheel speed	m/s
v_w	workpiece speed	m/s
x,y,z	cartesian coordinates referenced to workpiece	m
x',y',z'	cartesian coordinates referenced to heat source	m

Nomenclature : Greek symbols

		units
α	thermal diffusivity, defined as $\kappa/(\rho c)$	m^2/s
ψ	constant for dimensionless temperature	
κ	thermal conductivity	W/mK
μ	coefficient of friction	Ns/m^2
θ	temperature	K
θ_{av}	average temperature	K
θ_{fb}	fluid boiling temperature	K
θ_m	maximum temperature	K
θ^*_m	critical maximum workpiece temperature	K
θ_{mt}	melting temperature	K
Θ	dimensionless temperature	
ϕ	transient function	
ρ	density	kg/m^3
τ, τ'	dimensionless time	
τc	convective dimensionless time	
υ	Poisson's ratio	
ζ	effective dimensionless time	

Suffices

c	specific
cc	specific (to chip)
cf	specific (to fluid)
est	estimated
fb	fluid boiling
g	grain
msd	measured
s	grinding wheel bulk
t	total
w	workpiece
wg	workpiece spike

CONTENTS *Page*

LIST OF FIGURES

LIST OF TABLES

LIST OF PLATES

Chapter 1 : Introduction

1.1 The grinding process

Grinding is a machining process suitable for materials of high hardness which cannot be accurately machined by conventional single point or multi-point tools. It is often the last process which takes place with components which have high added value. Grinding is therefore an important process and likely to remain so. The grains of a grinding wheel often have large negative rake angles which results in a high energy input per unit volume of material removed. This energy is dissipated as heat in the grinding zone. Although unrivalled in terms of dimensional accuracy, geometry and surface texture the high energy expended in the grinding process means that it can give rise to thermal damage to the workpiece. A substantial reduction in the energy in the grinding zone can be achieved by correct selection of the speed of the workpiece, the structure of the wheel and conditions for dressing the wheel and thereby the ability to produce a good quality surface free from thermal damage.

1.2 Workpiece thermal damage

Thermal damage in grinding is characterised by discoloration due to formation of oxides on the workpiece surface. This is termed workpiece burn and the burn marks are called 'temper colours'. Thermal damage is the main limitation to increasing removal rate while maintaining high quality surfaces. The high temperatures occurring at workpiece burn can cause various types of thermal damage and material transformations in the layers near the surface. For example in the grinding of hardened steels, transformations which may occur are tempering of the hard martensite with possible formation of brittle untempered martensite if the temperature generated is high enough to cause re-austenisation at the surface. Residual tensile stresses are found in burned workpieces which can drastically reduce the fatigue life of a component. This is particularly important for aerospace components where surface integrity must be

assured and the safety factors are very low (1.05 - 1.1) but it is also very important for a wide range of products in many industries.

1.3 Types of grinding wheels

The most common and inexpensive types of abrasive grit are aluminium oxide and silicon carbide. Cubic boron nitride (CBN) or diamond grits are harder but much more expensive. For grinding ferrous materials CBN wheels are more suitable than diamond. Diamond abrasive is found to be unsuitable for grinding ferrous materials due to graphitisation which results in relatively high wheel wear. CBN was first synthesised in 1957 at the General Electric Company as an alternative to diamond although it did not become commercially available as a superabrasive until 1969, marketed under the name of 'Borazon'. Like diamond, CBN is very expensive, CBN grinding wheels are two orders of magnitude more expensive than conventional grinding wheels.

A feature of CBN grinding is the reduced risk of thermal damage to the workpiece and CBN grinding should be considered where surface integrity of the part must be assured. CBN grinding is reported as giving beneficial compressive stresses instead of tensile stresses which can cause premature failure [1]. The reduced risk of thermal damage in CBN grinding has been attributed to lower specific energies [2, 3]. Recently theoretical analysis [4, 5, 6] has highlighted the potential for a large reduction in the proportion of the total heat that enters the workpiece when grinding with CBN due to the higher thermal conductivity of a CBN grain. The question of whether the type of abrasive grain in the grinding wheel affects the surface integrity of the workpiece has not been confirmed.

1.4 Need for the Research

The demand for superabrasive grinding wheels has been slow relative to the potential prospects for enhanced productivity. An estimated 25% of the conventional abrasive precision market could be converted to CBN giving potential to increase productivity and part quality. Today the market penetration is around 5% [3]. The application of CBN is mainly for grinding of hardened tool steel, bearing steels and aircraft alloys. CBN grinding wheels tend to be used when conventional wheels prove unsuitable rather than genuinely being considered as an alternative abrasive.

The slow take up of CBN grinding may be attributed to several factors. The high cost of the wheel and dressing equipment inhibits application although in some cases the additional cost could be justified by increased productivity and quality. The take up of CBN has also been slow in "progressive" firms. This may be partly explained by the fact that the grinding technology developed over many decades for conventional grinding wheels has been found to be not directly applicable to CBN grinding and a lengthy learning cycle may be required before the productivity benefits are realised. Resistance to change may also be a significant factor.

From the previous discussion it is apparent that industry may not be fully aware of the potential benefits of CBN grinding for quality. Workpiece surface integrity is often more important than productivity as applications become more critical and increased performance characteristics are required. It is a matter of much interest to manufacturers whether the benefits claimed for CBN are real. Manufacturers are also interested in the physical explanation of such benefits. The effects of the grinding wheel thermal properties on the surface integrity however need to be established and is the subject of investigation in this thesis.

1.5 Aims

The aim of the investigation was to determine experimentally the significance of the grinding wheel thermal properties on the surface integrity of the workpiece.

1.6 Objectives

(i) To determine the effect of the grinding wheel thermal properties on the energy partitioning to the workpiece.
(ii) To determine the workpiece critical temperature at the onset of thermal damage.
(iii) To propose a model of heat transfer in the grinding process and determine the value of the parameters used in the model.
(iv) To rationalise the proposed model for implementation into a process control environment.

1.7 Scope of the investigation

A thorough review of the literature revealed considerable research effort devoted to thermal aspects of grinding. The previous research effort was largely directed to conventional grinding. Recently theoretical publications have proposed methods for modelling the heat transfer in superabrasive grinding [4, 5, 6]. However no experimental evidence has been offered supporting these works.

An experimental investigation was undertaken to quantify the heat conduction into the grinding wheel for both conventional and superabrasive grinding wheels. A theoretical model for the prediction of the partition ratio was proposed. The experimental partition ratios were compared to the theoretical model and a method for controlling the workpiece surface integrity proposed.

2.1. Introduction to temperatures in grinding

Temperatures in grinding were first calculated by Outwater and Shaw in 1952 [7]. This analysis attempted to predict the temperature reached by the ground surface at the grain-workpiece interface, Figure 2.1. The grain was considered to act as a zero rake single point cutting tool with heat generation taking place entirely across the shear plane BC in Figure 2.1.

The assumption of the heat generation taking place at the shear plane was challenged by Hahn in 1956 [8]. Hahn modelled the grain as shown in Figure 2.2. The clearance face, plane AB in Figure 2.2, is called the grain wear flat. It was argued that in grinding, unlike conventional single point cutting, the rubbing forces on the grain at the clearance face were appreciable. This was justified on two accounts. Firstly the geometry of a grain indicated that there is no clearance angle in grinding. The second argument was based on the experimental evidence of the grinding forces. The ratio of tangential to normal forces in grinding is found to be typically of the order of 0.3 to 0.5 which is characteristic of a sliding process. This suggests that the principal location of heat generation is at the grain wear flats. In turning the ratio of tangential to normal forces is typically 2 to 3. Thus the grinding process was more realistically described by considering the frictional rubbing forces on the wear flat and neglecting the shear plane cutting forces. This was called the 'grain rubbing hypothesis'.

Hahn further developed the grain rubbing hypothesis to take account of the global effect of all the grains on the workpiece. It was reasoned that from the point of view of the workpiece a tremendous barrage of small intense heat sources move very rapidly over the contact length, l_e. The contact length of the contact zone is moving relatively slowly compared to the grinding wheel. At a particular instant in time only one or two grains may be in contact with the workpiece. These are moving at very high speed relative to

the workpiece. Therefore many grains pass over the contact length as a point on the workpiece passes under the wheel. The term 'wheel source' was used to describe the slower moving band of heat which passes over the workpiece. The wheel source consists of a large number of high speed grain sources which was regarded as a continuous band heat source of lower intensity moving over a stationary workpiece. The grain rubbing hypothesis and the wheel source model laid the foundation for further work in analysis of workpiece temperatures in grinding.

Two types of temperatures in the grinding zone were identified by Hahn [8] :

(i) localised temperatures at the abrasive grain wear flat and shear plane.
(ii) an average 'background' temperature due to the distributed action of all the grains in the grinding zone.

Malkin [9] assumed localised temperatures exist both at the wear flat on the grain and at the shear plane. Malkin assumed the maximum temperature at an abrasive grain is the summation of these two grain temperatures on the workpiece background temperature. At the time, Malkin was investigating the effect of temperatures on wheel wear and not in connection with surface integrity of the workpiece.

A clarification of the effect of the grinding temperatures at the shear plane was made by Des Ruisseaux in 1970 [10]. It was argued that high temperatures in the vicinity of the grain as calculated by Malkin are important with respect to abrasive wear, although these temperatures are not necessarily indicative of the temperatures which determine the workpiece quality. With respect to quality, it is the temperature reached by the material which remains on the workpiece which is of primary interest. This is shown as plane A in Figure 2.2. Des Ruisseaux related the temperature in the vicinity of the chip formation, plane BC in Figure 2.2, to the temperature experienced by the workpiece surface which remained after grinding, plane A. The theoretical analysis indicated that the temperatures predicted at the region of chip formation can be substantially greater

than those which result on the surface of the remaining workpiece material. This is because of a 'thermal barrier' formed by the layer of material which is being removed. This layer of workpiece material acts as thermal insulations between the chip and the workpiece material left behind. The temperature in the workpiece sub-surface was shown to be virtually unaffected by the chip shear plane temperature. Des Ruisseaux concluded that with respect to workpiece quality it is the maximum contact zone temperature that is the temperature of importance. Des Ruisseaux did not consider the effect of the localised temperature at the grain wear flat on workpiece quality. The localised temperature at the grain wear flat will be termed the workpiece 'spike' temperature.

The workpiece 'spike' temperature in grinding was considered in more detail by Shaw [11]. It was concluded that the short duration of such temperatures could not be directly responsible for the extensive depth of thermal damage found in ground workpieces. The thermal damage found in ground surfaces (such as burn, tempering, phase transformation) is diffusion driven and requires time to occur. The short duration of a single grain acting in isolation in the contact zone was found to be insufficient for such diffusion mechanisms to take place.

The workpiece surface integrity is determined by the distributed action of the grain wear flat heat sources. This gives rise to a heat flux which averaged over the contact area is of lower intensity and moves over the workpiece at the workpiece velocity. The modelling of workpiece temperatures to ensure workpiece surface integrity is therefore based on predicting the workpiece background temperature distribution in the contact area. Models used to determined these temperatures are reviewed below.

2.2 Moving heat source theory

The moving heat source theory of Jaeger [12] was used to model the workpiece

background temperature by various authors [13-18]. The heat flux at the workpiece surface was likened to a moving band heat source over the workpiece as proposed by Hahn [8].

Jaeger established a two dimensional quasi-steady state heat transfer theory for a moving heat source over an adiabatic semi-infinite body as shown in Figure 2.3.

The co-ordinate axis is fixed to the centre of the heat source and moves with the source as shown in Figure 2.3. The exact solution is developed from the instantaneous point source solution of the general heat conduction equation. The temperature for a moving band heat source of uniform intensity is normally expressed in dimensionless form

$$\frac{\theta \pi K v}{2 \alpha q_o} (X, Z) = \int_{X-L}^{X+L} e^{-u} K_o\left(Z^2 + u^2\right)^{1/2} du \qquad .. 2.1$$

where

$$X = \frac{v x}{2 \alpha} \qquad .. 2.2$$

$$Z = \frac{v z}{2 \alpha} \qquad .. 2.3$$

$$L = \frac{v l}{2 \alpha} \qquad .. 2.4$$

The magnitude of the dimensionless temperature at any dimensionless position (X, Z) in the semi-infinite body is governed by the Peclet number, L, which is a dimensionless heat source length. A consequence of the semi-infinite body solution is that after the heat source has travelled past a particular point on the workpiece, the temperature decays to zero.

At the surface, Z= 0, an exact solution of Equation 2.1 exists exclusively for the case of

a uniform heat flux

$$\frac{\theta\pi\kappa v}{2\alpha q_o}(X, 0) = (X+L)\,e^{X+L}\{K_o(X+L) + K_1(X+L)\}$$
$$- (X-L)\,e^{X-L}\{K_o(X-L) + K_1(X-L)\} \quad .. 2.5$$

Using tables to evaluate the Bessel functions Jaeger plotted the dimensionless temperature for a range of Peclet numbers. Jaeger's results are re-produced in Figure 2.4.

For low values of the Peclet number, L<0.1, the temperature distribution was found to be symmetrical with the maximum temperature occurring at X/L=0. As the Peclet number increases to L=5 the position of maximum temperature moves progressively towards the trailing edge of the heat source.

An approximate solution was obtained for the maximum dimensionless temperatures for L>5

$$\frac{\theta_m\pi\kappa v}{2\alpha q_o} = 3.543\,L^{1/2} \quad .. 2.6$$

where the approximate dimensionless average temperature is two thirds of the maximum value

$$\frac{\theta_{av}\pi\kappa v}{2\alpha q_o} = 2.362\,L^{1/2} \quad .. 2.7$$

When the above equations are used to predict the temperature for values of Peclet number down to L=1, which includes some practical grinding conditions, an error of 14% occurs in the calculation of the maximum temperature and a 5% error results in the calculation of the average temperature.

Jaeger's analysis assumes a semi-infinite body. The case of a moving band heat source over a body of finite depth was investigated by Rosenthal in 1946 [19]. Rosenthal's model is shown in Figure 2.5. It is assumed that the band source has been present for sufficient time to establish a quasi-steady state heat transfer. Lee [15] translated Rosenthal's solution into dimensionless form. In addition to the above dimensionless parameters, X, Z and L, the dimensionless thickness 'D' was defined as

$$D = \frac{v\,d}{2\,\alpha} \qquad .. 2.8$$

The solution given by Rosenthal for the temperature of a band heat source of uniform intensity moving over a body of finite thickness is

$$\frac{\theta \pi K v}{2 \alpha q_o} = \frac{\pi}{D}\left[L + \sum_{n=1}^{\infty} e^{(\mu_n - 1)X} \frac{1 - e^{-2L(\mu_n - 1)}}{\mu_n(\mu_n - 1)} \cos\left(\frac{\pi n Z}{D}\right)\right] \qquad .. 2.9$$

where

$$\mu_n = \sqrt{1 + \left(\frac{\pi n}{D}\right)^2} \qquad .. 2.10$$

A final bulk temperature, θ_{final}, is reached in the body after the heat source has moved away

$$\theta_{final} = \frac{q_o\,l}{\rho\,c\,d\,v} \qquad .. 2.11$$

From Equation 2.11 it is seen that as the thickness, d, increases to infinity and the body becomes semi-infinite the temperature after the heat source has passed approaches zero.

The form of the solution for a finite body is quite different to Jaeger's solution for a semi-infinite body. Rosenthal's solution requires the evaluation of a series to infinity whereas Jaeger's solution requires the evaluation of an integral.

Simplified formulae could not be presented by Rosenthal for the maximum and average temperatures as they depend not only on the Peclet number, L, but also on the dimensionless thickness, D.

Rosenthal's model be may more appropriate for certain grinding operations such as the grinding of thin wall cylinders where the length of the heat source is comparable to the workpiece thickness. This situation can be quantified by the ratio $L/D=(2d)^{-1}$. The contact length in grinding may be as large as 4mm and the wall thickness of a tubular component may be typically 1mm. A typical value of L/D to be encountered in the grinding of thin walled members is therefore two.

Jaeger's semi-infinite body theory was compared with Rosenthal's finite body solution for Peclet number L=10 at dimensionless depth, Z=10. Figure 2.6 shows dimensionless temperature distributions for various values of D at Z=10. The Mathematica programs used to solve Equations 2.1 and 2.9 are given in Appendix 1.

At large values of dimensionless thickness, D>30, the Jaeger theory predicts the same temperature distribution as Rosenthal's solution. The temperature distribution for D>30 will eventually decay to zero as the body is effectively semi-infinite.

It was found that if the dimensionless thickness, D, is much larger than the dimensionless depth, Z, at which the temperature is required then Jaegers solution can be used. For the case investigated, L=10 and Z=10, Jaeger's solution predicts the same temperature distribution as Rosenthals solution when D/Z>3.

As the dimensionless thickness is reduced, the finite body solution of Rosenthal predicts a higher sub-surface temperature than Jaegers semi-infinite body solution. A final temperature rise will remain in the body given by Equation 2.11. Large errors are noted in the sub-surface temperature when applying the Jaeger theory to bodies of finite

thickness when the dimensionless depth, D, is comparable to the dimensionless depth, Z. From Figure 2.6 the maximum temperature at Z=10 for a body of dimensionless depth D=10 is approximately twice the maximum temperature for a semi-infinite body.

Of practical interest in grinding is the control of the surface temperature, Z=0. The maximum dimensionless temperature is plotted against dimensionless depth, Z, for Peclet number, L=10, for various values of dimensionless thickness, D, in Figure 2.7. Rosenthal's solution predicts almost the same maximum surface temperature rise as the Jaeger solution for D>5. For D<5, the Rosenthal finite body solution predicts higher temperatures than Jaeger's semi-infinite body solution.

Although the surface temperature rises are almost the same for the Rosenthal and Jaeger solutions for D>5 the sub-surface temperatures differ markedly, Figure 2.8. For small values of dimensionless depth a bulk temperature given by Equation 2.11 exists in the body after the heat source has passed.

Lavine, 1988 [20] developed a temperature solution for a moving heat source. Ignoring heat conduction in the direction of motion, the energy equation for a semi-infinite body is

$$v\frac{\delta\theta}{\delta x} = \alpha \frac{\delta^2\theta}{\delta^2 z} \qquad .. 2.12$$

The assumption of ignoring heat conduction in the direction of motion is least accurate at low speeds.

The boundary conditions for the $\theta(X, Z)$ are

(i) The body has an initial ambient temperature

$$\theta(0, z) = 0 \qquad .. 2.13$$

(ii) Uniform heat flux across the semi-infinite surface

$$- k \frac{\delta\theta}{\delta z} = q_o \qquad .. 2.14$$

(iii) The temperature is finite at z = infinity

$$\theta(x, \infty) = 0 \qquad .. 2.15$$

The solution of Equation 2.12 with the given boundary conditions is

$$\theta = 2 \pi^{1/2} X^{1/2} \exp\left(- \frac{Z^2}{4 X}\right) - \pi Z \operatorname{erfc}\left(\frac{Z}{2 X^{1/2}}\right) \qquad .. 2.16$$

This equation can predict both surface and sub-surface temperatures. At the surface, Z = 0 and the local, maximum and average temperatures are given by

$$\theta = 2 \pi^{1/2} X^{1/2} \qquad .. 2.17$$

$$\theta_m = 2 \pi^{1/2} L^{1/2} = 3.545 L^{1/2} \qquad .. 2.18$$

and from Equation 2.17

$$\theta_{av} = \frac{2}{3} \theta_m \qquad .. 2.19$$

giving

$$\theta_{av} = \frac{4}{3} \pi^{1/2} L^{1/2} = 2.363 L^{1/2} \qquad .. 2.20$$

The coefficients for the maximum temperature given by Lavine is 3.544 which compares

with 3.543 from Jaeger's analysis. The coefficient for the average temperature given by Lavine is 2.363 which compares to 2.362 from Jaeger's analysis. The one dimensional Lavine model gives practically identical results to the Jaeger model for both the maximum and average surface temperatures. This indicates that the assumption of one dimensional heat flow is justified.

An important result from Lavine's analysis is that the distribution within the contact zone varies according to $x^{1/2}$. This was not reported by Jaeger.

Jaeger and Lavine models have been shown to be practically identical for L>5. Computational advantages are noted with the Lavine model for sub-surface temperatures. The Lavine model requires the evaluation of an exponential and an error function. Sub-surface temperature predictions from the Jaeger model requires numerical integration.

To simplify the prediction of sub-surface temperatures from Jaeger's solution, Takazawa, 1966 [13] and Maris, 1978 [21] curve fitted results for the maximum temperature for a uniform heat flux. The following exponential decay was given to fit Jaeger's solution to within 5%

$$\frac{\theta_m \pi \kappa v}{2\alpha q_o} = A\, L^a \exp\left[-B\, L^b\, Z\right] \qquad .. 2.23$$

The constants A, B, a & b were determined for the ranges $0<Z<20$ and $5>L<80$. The constants for the ranges that have been calculated by Takazawa [13] and Maris [21] are given in Table 2.1.

Range	A	B	a	b
$1 < L < 80$ $0 < Z < 4$	3.1	0.69	0.53	-0.39
$5 < L < 40$ $4 < Z < 10$	0.66	0.15	0.93	-0.06
$5 < L < 40$ $10 < Z < 20$	0.355	0.08	1.01	0.044
$40 < L < 80$ $4 < Z < 10$	1.64	0.288	0.67	0.244
$40 < L < 80$ $10 < Z < 20$	0.079	0.0187	1.43	0.44

Table 2.1 : Constants for sub-surface temperature approximations [13, 21]

The accuracy of these approximations can be checked using Figure 2.6 where the maximum dimensionless temperature for L=10 at Z=10 is 1.515. Using the Maris approximation for this range the maximum dimensionless temperature is 1.52. This is within the reported 5% error.

Shaw [11] developed a simplified analysis of the temperature distribution in the grinding zone. Based on Jaegers work for a uniform heat source it was proposed that for L>5 the temperature varied approximately linearly in the heating zone. The actual distribution is not linear and varies according to $x^{1/2}$ [20]. The linear simplification used by Shaw gives

$$\theta_{av} = \frac{1}{2}\theta_m \qquad .. 2.24$$

whereas the actual relationship is

$$\theta_{av} = \frac{2}{3}\theta_m \qquad .. 2.25$$

This simplification results in an over-estimate of the maximum temperature by 25%. The average temperature from Shaw's analysis differs from Jaeger's analysis by 6%.

The above models did not take account of convective cooling. This was investigated by Des Ruisseaux [22] who applied Jaegers analysis and extended it for uniform convective cooling, h_c, across the entire surface of the semi-infinite body, Figure 2.9.

A dimensionless convective cooling coefficient was introduced

$$H = \frac{h_c\, 2\,\alpha}{k\, v} \qquad .. 2.26$$

and the temperature distribution within the semi-infinite body was given by

$$\frac{\theta \pi k v}{2 \alpha q_o}(X, Z) = \int_{X-L}^{X+L} e^{-u}\, K_o\left(Z^2 + u^2\right)^{1/2} du \; -$$

$$H\, e^{H Z} \int_0^{\infty} \left\{ \tau_c \exp\left(H^2 \tau_c^2\right) \operatorname{erfc}\left(\frac{z}{2\tau_c} + H\tau_c\right) - \operatorname{erfc}\left(\frac{X+L}{2\tau_c} + \tau_c\right) - \operatorname{erfc}\left(\frac{X-L}{2\tau} + \tau_c\right) \right\} d\tau_c$$

.. 2.27

where

$$\tau_c = \frac{v \sqrt{\alpha\, t}}{2\,\alpha} \qquad .. 2.28$$

is the dimensionless time. Note that quasi-steady state conditions are obtained by integrating the dimensionless time, τ_c, to infinity.

The first part of Equation 2.27 is the same as Jaeger's solution. The second part is the reduction in dimensionless temperature due uniform convective cooling. Des Ruisseaux showed that significant reductions in workpiece surface temperatures could be obtained for a sufficiently large dimensionless convection coefficient, H>1. A large dimensionless convective coefficient is more likely to exist in creep feed grinding where the workpiece velocities are much lower than in conventional shallow cut grinding.

The application of the Des Ruisseaux model is limited by the complexity of the solution of Equation 2.27. To overcome this problem an alternative technique for treating the convective cooling for moving heat sources is given in Chapter 4.

2.3 Workpiece background temperature

The workpiece background temperature distribution is a result of the distributed action of all the grains which pass through the contact area. This temperature distribution can be calculated from moving heat source theory where one of the previously described solutions can be applied.

Sato [23] estimated the mean workpiece background temperature in 1961. The temperature was calculated based on the solution for an instantaneous point source. Sato superimposed a series of instantaneous point source solutions to approximate a number of cutting passes

$$\theta_w^n = \frac{1}{\sqrt{n}} \sum_{k=1}^{n\,(\text{inc.}2)} \frac{1}{\sqrt{k}} \frac{E}{A \kappa \rho} \frac{1}{\sqrt{\pi \alpha t}} \qquad .. 2.29$$

where

$$n = \frac{v_s}{v_w} \qquad .. 2.30$$

and 't' is half the time for the workpiece to pass through the contact zone of length, l_e.

The workpiece temperature distribution throughout the contact zone was not predicted from this analysis.

Takazawa [13] treated the effect of individual grain sources in the contact area as a moving band source as proposed by Hahn [8]. Jaeger's moving heat source solution was

applied to calculate the average and maximum workpiece background temperatures.

From Equation 2.6 the maximum surface temperature is

$$\theta_m = 1.13 \frac{q_w}{(\kappa\rho c)_w^{1/2}} \left(\frac{l_c}{v_w}\right)^{1/2} \quad .. 2.31$$

and from Equation 2.7 the average surface temperature in the contact zone is

$$\theta_{av} = 0.753 \frac{q_w}{(\kappa\rho c)_w^{1/2}} \left(\frac{l_c}{v_w}\right)^{1/2} \quad .. 2.32$$

Sato's solution can be further evaluated in order to compare it with the moving wheel source approach.

Numerical values of $\frac{1}{\sqrt{n}} \sum_{k=1}^{n\,(\text{inc.}2)} \frac{1}{\sqrt{k}}$ were evaluated for n=20 to 300 which are typical speed ratios in conventional shallow cut grinding.

Figure 2.10 shows a graph of $\frac{1}{\sqrt{n}} \sum_{k=1}^{n\,(\text{inc.}2)} \frac{1}{\sqrt{k}}$ against the speed ratio, n. It was found that the value is relatively insensitive to the speed ratio, n, and tends towards a constant value of 1.39. Therefore Equation 2.29 becomes

$$\theta_w = 1.39 \frac{E_w}{A \kappa \rho} \frac{1}{\sqrt{\pi \alpha t}} \quad .. 2.34$$

Substituting the following into Equation 2.34

$$E_w = \frac{Q_w}{t} \quad .. 2.35$$

$$q_w = \frac{Q_w}{A} \quad .. 2.36$$

$$t = \frac{l_e}{2\,v_w} \qquad \text{..2.37}$$

gives

$$\theta_w = 1.1\,\frac{q_w}{(\kappa\rho c)_w^{1/2}}\left(\frac{l_e}{v_w}\right)^{1/2} \qquad \text{..2.38}$$

This equation has the same form as Jaeger's solution for the maximum temperature. A 15% difference in the coefficient is found.

Neither the temperature distribution within the grinding zone, the magnitude of the maximum surface temperature nor the sub-surface temperatures can be determined from Sato. Thus for further investigation the Jaeger theory has considerable advantage. Sato was however the first researcher to develop heat transfer theory for application to the grinding process.

The moving heat source theory of Jaeger has been applied by various researchers to determine the background workpiece temperature [13-18]. Rowe and Pettit [18] and Malkin [14] used the background temperature solution as the basis of a strategy for prevention of thermal damage in grinding.

It is seen that prediction methods for workpiece background temperature rely heavily on Jaegers theory. This theory provides versatility in its application to determine the temperature distribution on the workpiece surface and sub-surface. Jaeger's theory has also been extended for convective cooling [22].

Five assumptions are made when applying Jaeger's theory to the grinding process.

(i) The workpiece is a semi-infinite body. The validity of this assumption for a

particular situation was checked by comparison with Rosenthal's theory [19] which takes into account a body of finite thickness. This assumption should be re-considered in the grinding of thin walled members. In many grinding operations the dimensions of the contact length relative to the workpiece thickness is usually small. In surface grinding the workpiece is normally held by a magnetic chuck which can be considered as an extension of the workpiece below the surface.

(ii) A quasi-steady state condition is attained with respect to the frame of reference of the moving heat source. Jaeger showed that quasi-steady state conditions are reached when the heat source has travelled for several heat source widths. The number of heat source widths required to attain quasi-steady state conditions decreases with higher Peclet numbers. For surface grinding transient effects will exist at the very beginning of the wheel-workpiece contact.

(iii) The rectangular heat source in grinding can be approximated by a band heat source i.e. infinite in the direction perpendicular to motion. This agrees well with the contact length being small relative to the grinding width. Jaeger showed that for $L>2$, elongation of the heat source perpendicular to the direction of motion makes little difference to the maximum and average temperatures.

(iv) No heat conduction takes place perpendicular to the direction of motion. This assumption improves with higher Peclet numbers and is valid for $L>5$ [12].

(v) The heat source can be considered to be acting on the plane of the workpiece surface. In reality the heat source is inclined. This angle is very small, typically less than one degree [17].

The energy partitioned to the workpiece, q_w, and the grinding wheel-workpiece contact length, l_e, must be known in order to determine the grinding temperature from the moving heat transfer solutions.

2.4 Partition models

For evaluation of the workpiece background temperature the magnitude is required of the heat flux, q_w, entering the workpiece. The concept of a partition ratio has been universally adopted to represent the proportion of the total energy entering the workpiece

$$R_w = \frac{q_w}{q_t} \qquad .. 2.40$$

Outwater [7] partitioned the grinding energy at the shear plane energy. However it is essentially a model for single point machining as it ignores the heat generation at the wear flat. Further as discussed in Section 2.1 the heat partitioned towards the workpiece at the shear plane is likely to be removed in the progressive movement of the wheel and therefore has small influence on workpiece surface integrity.

An analysis which took into account the heat generation at the grain wear flat was proposed by Hahn [24]. The physical model is illustrated in Figure 2.11. The grain was modelled as a stationary body subject to a heat flux. The grain was idealised as a protrusion of infinitesimal depth on a semi-infinite body. The grain wear flat was taken to be a square of half side r_o. Hahn determined the energy partitioned between the workpiece and wheel, R_{ws}, which is given by the ratio

$$R_{ws} = \frac{R_w}{R_w + R_s} \qquad .. 2.40a$$

A steady state solution for a square heat flux of half side r_o on stationary semi-infinite body was taken from Jaeger [12]

$$\theta_g = \frac{0.946\, q_g\, r_o}{k_g} \qquad .. 2.41$$

The increase in workpiece temperature, θ_{wg}, due to the grain passing over its surface was modelled by Hahn as a quasi-steady state temperature condition. It was appreciated that this solution would not be valid in the initial stages of the grain-workpiece contact. The grain was considered to be a square heat source travelling at the wheel speed across the workpiece. From Jaeger, 1942 [12]

$$\theta_{wg} = 1.064\, q_{wg} \left(\frac{r_o}{v_s\, (\kappa\rho c)_w}\right)^{1/2} \qquad .. 2.42$$

The energy partitioning between the workpiece and wheel was determined by equating the interface temperatures

$$R_{ws} = \left[1 + \frac{1.125\, k_g}{(r_o\, v_s)^{1/2}\, (\kappa\rho c)_w{}^{1/2}}\right]^{-1} \qquad .. 2.43$$

In order to evaluate the partitioning from Equation 2.43 the thermal properties of both the grain and workpiece are required. The wear flat dimension, r_o, and wheel speed must also be known. This model assumes a steady state condition for the grain. This assumption would be expected to be more accurate for high conductivity grains, such as CBN than for alumina grains. The quasi-steady state assumption for the workpiece temperature solution was justified after the grain travelled approximately four wear flat dimensions.

The assumption of a circular contact of radius r_o rather than a square contact makes a small difference to the partition ratio. Repeating Hahn's analysis with a circular contact of radius, r_o, the partition between the workpiece and wheel is

$$R_{ws} = \left[1 + \frac{0.974\, k_g}{(r_o\, v_s)^{1/2}\, (\kappa\rho c)_w{}^{1/2}}\right]^{-1} \qquad .. 2.44$$

Malkin [9] argued that three distinct processes take place when a grain traverses through the grinding zone, rubbing (or sliding), ploughing and cutting. In the rubbing region no material removal takes place, elastic and/or plastic deformation in the work material does occur. This leads into the ploughing region where the grain disturbs work material in its path resulting in predominantly plastic flow ahead of the grain. Finally, the cutting action takes place and rapid material removal occurs. During the sliding and ploughing stages all of the heat generated was assumed to enter the workpiece. In the cutting stage it was estimated 45% of the cutting energy enters the workpiece. The value of 45% was determined from Outwater's shear plane partitioning criterion [7] and from calorimetry. The partition ratio, R_w, was said to be

$$R_w = \frac{e_c - 0.45\, e_{ch}}{e_c} \qquad .. 2.45$$

From a series of grinding trial data the chip formation energy was estimated to be e_{ch}=13.8 J/mm^3. Therefore

$$R_w = \frac{e_c - 6.21}{e_c} \qquad .. 2.46$$

It is noted that a value for the specific energy is required in order to evaluate the partition ratio. Malkin's model assumes that all the sliding and ploughing energy is partitioned to the workpiece

$$R_{ws} = 1 \qquad .. 2.47$$

It is further noted from Hahn's analysis that if a fraction of the sliding or ploughing energy is conducted into the grain then this model could not be evaluated. The heat conducted to the grain may be significant for superabrasives due to their high conductivity. Also the model does not take into account that the shear energy may be

removed by the grain and therefore it may be more realistic to subtract all the chip formation energy. For these reasons, Malkin's model would be expected to overestimate the energy to the workpiece and therefore be conservative in use. The effect of grinding fluid in Malkin's model would be reflected in the lower specific energies in the process.

Rowe and Pettit [18] proposed a partitioning model by applying Jaegers band source theory to both the wheel and workpiece as shown in Figure 2.12. This can be termed a wheel contact analysis.

For the grinding wheel a moving heat source passes across its surface at the wheel velocity. Applying Jaeger's moving heat source equation

$$\theta_{av} = 0.754 \frac{R_s q_s}{(\kappa\rho c)_w^{1/2}} \left(\frac{l_e}{v_w}\right)^{1/2} \quad .. 2.48$$

The application of Jaeger's equation to the wheel requires the specification of the bulk thermal properties of the wheel. Rowe and Pettit determined the bulk wheel thermal properties by steady state experiments of a wheel sample.

Applying moving heat transfer theory to the workpiece background the mean temperature is

$$\theta_w = 0.754 \frac{R_w q_w}{(\kappa\rho c)_w^{1/2}} \left(\frac{l_e}{v_w}\right)^{1/2} \quad .. 2.49$$

The solutions for the average workpiece background temperature and the average wheel contact temperature were equated. The result is

$$R_{ws} = \left[1 + \sqrt{\frac{v_s}{v_w} \frac{(\kappa\rho c)_s}{(\kappa\rho c)_w}}\right]^{-1} \quad .. 2.50$$

Introducing the partitioning ratio into Jaegers equation, the critical specific energy was

established in terms of the grinding variables for a given critical maximum value of the workpiece background temperature

$$e_c^* = 0.89\,\theta_m^* \left(\frac{l_e}{v_w}\right)^{1/2} \frac{(\kappa\rho c)^{1/2}}{a}\, R_{ws} \qquad .. 2.51$$

This was termed a lower bound solution. An upper bound solution was proposed to take into account the energy removed by the grinding chips and the coolant. Energy taken away by the chips and the coolant was added to the lower bound specific energy given by Equation 2.51, so that the upper bound value is

$$e_c^* = 0.89\,\theta_m^* \left(\frac{l_e}{v_w}\right)^{1/2} \frac{(\kappa\rho c)^{1/2}}{a}\, R_{ws} + e_{cc} + e_{cf} \qquad .. 2.52$$

where the energy convected by the fluid in the grinding zone is

$$e_{cf} = h_c \frac{l_e\,\theta_{fb}}{a\,v_w} \qquad .. 2.53$$

θ_{fb} is the fluid boiling temperature.

The energy convected to the chips is given by

$$e_{cc} = \rho c \theta_{mt} \qquad .. 2.54$$

and θ_{mt} is the melting temperature of the workpiece material.

In this manner the upper bound solution includes the maximum energy taken away by the fluid and chips. Experimental results from previous studies were shown to lie between the lower and upper bounds of the Rowe and Pettit model.

Shaw in 1990 [6] developed a macroscopic partitioning model based on the linearised Jaeger model. The linearisation was shown to over estimate the maximum grinding

zone temperature by 25% compared to Jaegers solution. A 6% difference was found for the average temperatures.

Shaw's partitioning model adopted the approach of Rowe and Pettit applying the linearised band source model to both the wheel and workpiece. An area ratio factor, Ar, was introduced to take into account the fact that the actual contact area at the wheel interface is a fraction of the apparent contact area, A. The partition ratio was given as

$$R_{ws} = \left[1 + \sqrt{\frac{v_s}{v_w}\frac{A_r(\kappa\rho c)_g}{(\kappa\rho c)_w}}\right]^{-1} \quad .. 2.55$$

It is noted that Equation 2.55 takes the same form as the Rowe and Pettit model if

$$A_r(\kappa\rho c)_g = (\kappa\rho c)_s \quad .. 2.56$$

The model was extended to include fluid. It was assumed that the entire wheel surface has a fluid film attached to it. Ignoring energy convected away by the chips the partition ratio is

$$R_{ws} = \left[1 + \sqrt{\frac{v_s}{v_w}\frac{A_r(\kappa\rho c)_g}{(\kappa\rho c)_w}} + \sqrt{\frac{v_s}{v_w}\frac{(\kappa\rho c)_f}{(\kappa\rho c)_w}}\right]^{-1} \quad .. 2.57$$

For water it was noted that the last term was close to one giving

$$\frac{R_w}{R_w + R_s} = \left[2 + \sqrt{\frac{v_s}{v_w}\frac{A_r(\kappa\rho c)_g}{(\kappa\rho c)_w}}\right]^{-1} \quad .. 2.58$$

Rowe and Morgan [5] achieved a partitioning solution incorporating a transient solution for the temperature rise of the grain. The grain was modelled as a stationary truncated cone subject to a constant heat flux for the duration of its passage through the contact zone, Figure 2.13. A transient solution was employed given by Lavine [4]. A feature of the conical grain solution is the attempt to include the shape of the grain in the

temperature prediction. The grain geometry is defined by a circular wear flat area of radius r_o and a semi-included angle, θ.

Lavine's transient solution for the surface temperature of a conical grain subject to heat flux for the entire contact length is

$$\theta_g = \frac{2}{\pi^{1/2}} \frac{q_g \, l_e^{1/2}}{[(\kappa\rho c)_g \, v_s]^{1/2} f(\zeta)} \qquad .. 2.59$$

where

$$f(\zeta) = \frac{2}{\pi^{1/2}} \frac{\zeta}{1 - \exp(\zeta^2)\,\mathrm{erfc}(\zeta)} \qquad .. 2.60$$

and

$$\zeta = \left[\frac{\gamma^2 \alpha_g \, l_e}{r_o^2 \, v_s}\right]^{1/2} \qquad .. 2.61$$

Rowe and Morgan noted that the Lavine solution with θ=0 degrees was equivalent to a one dimensional transient solution for a semi-infinite body subject to a heat flux across its surface. For this case [25]

$$\theta_g = \frac{2}{\pi^{1/2}} \frac{R_s \, q_t \, l_e^{1/2}}{[(\kappa\rho c)_g \, v_s]^{1/2}} \qquad .. 2.62$$

Assuming insulated sides a cylindrical grain was modelled using Equation 2.62. However it is noted that when Equation 2.62 is used the grain temperature is not a function of the contact dimension, r_o.

The workpiece temperature rise, θ_{wg}, was modelled using a solution for a quasi-steady state circular moving heat source over a semi-infinite body given by Archard [26]

$$\theta_{wg} = \frac{0.974\ q_{wg}\ r_o^{1/2}}{[(\kappa\rho c)v_s]^{1/2}} \qquad .. 2.63$$

The incorporation of the transient solution allowed the partition ratio to be evaluated at each point in the contact zone. Two formulae were given for the average partition ratio through the contact zone. A general formula was given and an approximate solution for $\zeta>3$

(i) The general solution is

$$R_{ws} = \left[1 + \left(\frac{r_o}{l_e}\right)^{1/2} \left[\frac{(\kappa\rho c)_g}{(\kappa\rho c)_w}\right]^{1/2} \frac{f(\zeta)}{\psi} \right]^{-1} \qquad .. 2.64$$

where

$$\psi = \frac{1.16}{1.5 - \tan\beta} \qquad .. 2.65$$

The value of ψ was evaluated from graphical data where β is the gradient of the curve $f(\zeta)$ versus log l_e. For conventional wheels ψ was reported to vary between 0.85 and 1.

(ii) Particular solution for $\zeta>3$,

$$R_{ws} = \left[1 + \left(\frac{r_o}{l_e}\right)^{1/2} \left[\frac{(\kappa\rho c)_g}{(\kappa\rho c)_w}\right]^{1/2} 2\zeta \right]^{-1} \qquad .. 2.66$$

Although the model featured a transient solution for the grain, it is noted that the partitioning solution proposed for $\zeta>3$ is steady state. This is shown in Figure 2.14 which plots partition ratio against the contact length for various values of thermal conductivity. The solutions for $\zeta>3$ give horizontal lines and are therefore not a function of the contact length which represents the time base in the solution.

A closed form solution of the Rowe and Morgan model was derived in this investigation and is given in Appendix A2. The closed form solution takes the form

$$\frac{R_w}{R_w + R_s} = \left[1 + 0.862\left(\frac{r_o}{l_e}\right)^{1/2} g(\zeta) \left[\frac{(\kappa\rho c)_g}{(\kappa\rho c)_w}\right]^{1/2}\right]^{-1} \quad .. 2.67$$

where

$$g(\zeta) = \frac{2}{\pi^{1/2}} \frac{\zeta^3}{\left(1 + \zeta^2 - \frac{2}{\pi^{1/2}}\zeta - \exp(\zeta^2)\mathrm{erfc}(\zeta)\right)} \quad .. 2.68$$

The closed form solution is compared with the solutions proposed by Rowe and Morgan in Figure 2.14. The Rowe and Morgan general solution correlates well with the exact solution. The Rowe and Morgan $\zeta>3$ solution was found to under-estimate the energy partitioning in the $\zeta>3$ range. The closed form of the Rowe and Morgan solution is used in the parametric evaluations of the models.

The effect of the energy convected by the grinding fluid and the chips was accounted for using the upper and lower bound technique of Rowe and Pettit

$$R_w = \frac{R_w}{R_w + R_s} \frac{e_c^* \text{ (lower bound)}}{e_c^* \text{ (upper bound)}} \quad .. 2.70$$

The energy convected to the fluid, e_{cf}, was estimated by using a 'fluid wheel' model. The fluid was assumed to fill all the space in the contact zone and move across the workpiece at the wheel speed. This condition was analysed using the Jaeger moving heat source equation

$$e_{cf} = \frac{0.89}{a\, v_w} \theta_{fb}^* \, (\kappa\rho c)_f^{1/2} \, (l_e\, v_s)^{1/2} \quad .. 2.71$$

The accuracy of the Rowe and Morgan model depends in turn on the accuracy of Lavine's conical grain solution. An important limitation of Lavine's conical grain solution was found by comparing the solution with a steady state solution for a circular heat source on a semi-infinite body. Figure 2.15 compares the temperature against time for the semi-infinite body solution and the conical body solution with θ=45degrees. It was found that the conical grain solution approaches the steady state value of the semi-infinite body solution. Clearly the flux into a cone must be less than the flux into a plane surface. This indicates that the maximum value for realistic application of the conical model is approximately 45 degrees since the conical grain temperature already gives a value approaching the semi-infinite body contact. This is an important limitation of the conical grain solution which previously has not been reported.

2.5 Evaluation of the Partition Ratio Models

Table 2.2 lists the parameters that are required to evaluate the partition ratio expressions given above

Model	Grinding Variables	Thermal Properties	Misc.
Hahn	v_s	κ_g	r_o
Malkin	-	-	e_c, e_{ch}
Rowe/Pettit	v_s, v_w	$(\kappa\rho c)_s^{1/2}$	-
Shaw	v_s, v_w	$(\kappa\rho c)_g^{1/2}$	A_r
Rowe / Morgan	v_s	$(\kappa\rho c)_g^{1/2}$	r_o, γ, le

Table 2.2 : Parameters used in the partition ratio models

It is noted that the grain thermal properties are required with the exception of the case of the Rowe and Pettit model which uses the bulk thermal properties of the grinding wheel. The Rowe and Pettit model uses the bulk wheel thermal properties and therefore includes the effect of wheel porosity and bond in the values of $(\kappa\rho c)_s^{1/2}$. The quantity $(\kappa\rho c)^{1/2}$ is seen to feature in three of the described models. This is known as the thermal contact coefficient [27]. Each of the above models with the exception of Malkin is equally applicable to both alumina and CBN by taking into account the different thermal properties of the abrasive type. The abrasive thermal properties used in each of the models are given in Table 2.3.

Model	alumina			CBN		
	k_g W/mK	ρ_g kg/m^3	c_g J/kgK	k_g W/mK	ρ_g kg/m^3	c_g J/kgK
Shaw	16.8	3800	712	88	3450	754
Rowe / Morgan	35	3910	765	1300	3480	506
Lavine	46	4000	770	1300	3450	506

Table 2.3 : Thermal properties used in the partition ratio models.

It is noted that significant differences in the values of thermal conductivity are used by different researchers. The thermal conductivity for alumina range from 16W/mK to 45W/mK. The highest reported thermal conductivity value of alumina in literature is 55W/mK. The sensitivity of the partitioning between the workpiece and wheel to the thermal conductivity assumed for alumina grains is shown in Figure 2.16. The energy partitioning is relatively constant across the range of reported values.

For CBN large differences in the values of thermal conductivity are used, Shaw [6] used 87W/mK whilst others used a theoretical value of 1300W/mK [4, 5]. The former value is a measured value on a PCBN and the latter a theoretical value. All values of thermal

conductivity for CBN have been traced back to a single reference [28]. The differences in the reported specific heat and density are far lower than for the thermal conductivity. The partition ratio for each of the models with these values of thermal conductivity for CBN are shown in Figure 2.17. A large range of partition ratio are predicted depending on the assumed values of thermal conductivity of the thermal conductivity. The lack of information on the thermal conductivity of CBN limits the accuracy of the theoretical predictions.

The bulk thermal contact coefficient $(\kappa\rho c)_s^{1/2}$ is used in the Rowe and Pettit model [18]. This value was obtained from steady state measurements of a wheel sample using Lee's thermal conductivity test and calorimetry. The thermal contact coefficient was measured to be $514 J/(s^{1/2}m^2K)$ for an alumina wheel. Morgan [29] investigated the effect of wheel structure for both alumina and CBN wheels. Morgan found that the steady state measurements of the bulk wheel thermal contact coefficient $(\kappa\rho c)_s^{1/2}$ could not clearly differentiate the thermal conductivity of abrasives.

Each of the grain contact analyses requires specification of the grain dimension, r_o, [4, 5, 8] or an estimate of the actual grain contact area, A_r, in the grinding zone [6]. The wear flat dimension and the fractional contact area are representative of the grinding wheel wear. Reported values of wear flat radius and contact area are given in Table 2.4. Lavine [4] commented that values of the contact dimensions for CBN wheels are not well known.

The sensitivity of the partition ratio models with these values is shown in Figure 2.18. The partitioning solution from the Rowe and Morgan model and the Hahn model are relatively insensitive to the value of the wear flat dimension, r_c, for values greater than $15\mu m$. The sensitivity increases slightly at higher values of grain thermal conductivity. The grain contact models of Rowe and Morgan and Hahn predict increasing energy partitioning with wheel wear.

The Shaw model predicts the opposite tendency with the energy partitioning to the workpiece decreasing with wheel wear, Figure 2.19. The sensitivity increases for higher values of grain thermal conductivity.

	Alumina		CBN	
	r_o (μm)	Ar (%)	r_o (μm)	Ar (%)
Rowe/Morgan	25	-	25	-
Malkin	-	1-5	-	-
Lavine	64.5	-	11.5	-
Shaw	-	1	-	1

Table 2.4 : Assumed values of wear flat radius and contact area

Rowe and Pettit [18] and Shaw [6] feature the speed ratio in the expression for the partition ratio. In the grain models of Rowe and Morgan [5] and Hahn [8] the wheel speed v_s is used. Strictly this should be v_s +/- v_w , however since $v_w << v_s$ then $v_s+/v_w \approx v_s$.

The sensitivity of the Rowe and Pettit and Shaw models depends on the thermal properties employed for the grinding wheel, Figure 2.20. The energy partitioned to the workpiece increases with increasing workspeed. Increasing the thermal contact coefficient of the wheel increases the sensitivity of the solutions with workspeed.

The models of Rowe and Pettit and Shaw are valid for Peclet numbers L>5, though errors in the heat transfer calculations are relatively small down to L=1 [12]. Taking L=1 and assuming a contact length of l_e=5mm, the models are valid down to a workspeed of 0.006m/s. This is well outwith the workspeed range 0.1-1m/s which is a typical range for conventional shallow cut grinding

Malkin's model requires the specification of the specific energy in the process. Values from the Malkin model are given in Figure 2.21 for specific energies ranging from 20-100J/mm^3 which are typical values for conventional wheels. At higher specific energies the partition ratio approaches one.

2.6 Measurements of the partition ratio.

The previous studies all concerned methods of predicting partition ratio from theory. With the aid of some basic theoretical assumptions it is possible to measure partition ratio.

Experimental studies have mainly involved aluminium oxide grinding wheels. To date there has been only one limited experimental study of partitioning for CBN wheels undertaken by Ramanath [30].

Sato [23] measured the partition ratio for a medium carbon steel ground by an aluminium oxide wheel in the cylindrical grinding process. The precise details of the experimental method was not given. The energy entering the workpiece was estimated from measurements of the workpiece bulk temperature. The experimental set up is shown in Figure 2.22. The workpiece surface temperature was measured by trailing a thermocouple across the surface of the workpiece as it rotates. The bulk temperature of the workpiece was thus measured in the absence of grinding fluid. The energy to the workpiece was then estimated from

$$E_w = m\, c\, \theta_w \qquad .. 2.72$$

The total energy consumed in the process was estimated by recording the motor power and hence the partition ratio was determined. The partition ratio was measured as 84%. The remaining energy, 16%, was assumed to be distributed between the grinding chips

and the grinding wheel. The energy taken away by the chips was estimated from the grinding sparks and was reported to be 4%. This leaves 12% of the total grinding energy conducted to the grinding wheel.

A calorimetric study was also undertaken by Malkin [9] who measured the partition of energy in dry surface grinding. The average temperature of a thin insulated workpiece was measured by attaching a thermocouple to the centre of the workpiece as shown in Figure 2.23. After a single pass of the grinding wheel the average temperature was recorded and the heat conducted to the workpiece estimated from Equation 2.72. The total power was measured by recording the tangential force and the wheel speed. Before each pass, the wear flat area of the grinding wheel was estimated by mounting an optical microscope on the grinding wheel. In this manner the partition ratio was determined for blunt and sharp wheels. The partition ratio was found to increase with increasing wear flat area according to the following relationship [16]

$$R_w = (0.6 + 500\ A_r) \qquad .. 2.73$$

It is noted that Malkin's experimental results give the opposite tendency to the Shaw theoretical model which predicted a reduction in partition ratio with the A_r. Partition ratio measurements by Malkin are of the same order as that reported by Sato.

Ramanath [30] used calorimetry in surface grinding to estimate the partition ratio for both alumina and CBN wheels in dry surface grinding. The results indicated lower partition ratios for the CBN grinding wheels. The average value of partition ratio for a CBN wheel was 56% compared to 79% for an aluminium oxide wheel. A reduction of 35% of the energy entering the workpiece was therefore found with the CBN wheel.

Calorimetric techniques are restricted to dry grinding. For measurement of partition ratio in wet grinding operations semi-empirical techniques have been used.

Lee [31] used a semi-empirical technique to determine the partition ratio in both dry and wet grinding. The partition ratio was determined from a thermal model of the bulk workpiece temperature solutions given by Des Ruisseaux [32]. The bulk temperature solutions are a function of the heat input, Q_w, and the convection coefficient, hc. The energy input to the workpiece was determined from bulk temperature solutions by measuring the workpiece bulk temperature and measuring the convection coefficient.

A two stage experiment was carried out in cylindrical grinding to estimate the partition ratio. In the first experiment the energy input to grinding was simulated with heaters in order to estimate the convection coefficient. The second experiment involved a grinding experiment where the workpiece bulk temperature was measured. Both stages must be carried out in order to evaluate the partition ratio.

Stage 1 of experiment - Measurement of the convective heat transfer coefficient

The convection coefficient was estimated by using an electrically heated testpiece with embedded thermocouples. The test apparatus was mounted as if it was about to be ground with the rotating grinding wheel position close but not touching the test workpiece. The electrical heater in the workpiece was switched on and the fluid was engaged. After steady state conditions were reached the temperatures from the subsurface thermocouples were recorded. Through measurement of the heat supplied from the heaters, the embedded thermocouple readings and the fluid temperature the convection coefficient for various fluids and delivery systems was measured. The convective coefficients measured by Lee are given in Table 2.5.

Fluid	h_c $W/(m^2K)$
Air	98
Synthetic Fluid (Standard Delivery)	6,814
Synthetic Fluid (Improved Delivery System)	17,604

Table 2.5 : Measurements of the convection coefficients

Stage 2 of experiment - Measure workpiece bulk temperature during a grinding trial

In the second experiment on a modified workpiece the bulk temperature of the workpiece was measured using embedded thermocouples at a known radius. The grinding power and grinding conditions are monitored and the partition ratio evaluated from the bulk temperature solutions [32].

Lee's results for the measured partition ratio are summarised in Table 2.6.

	R_w
Dry grinding	0.8
Wet grinding	0.3

Table 2.6 : Lee's measurements of the partition ratio in cylindrical grinding [26]

Sauer [33] developed a semi-empirical method for determining the partition ratio in surface grinding. Subsurface temperature measurements were correlated with a thermal model. Measurements were taken at positions remote from the heat source to improve accuracy since the temperature gradients in these regions are small. A feature of the temperature model was the inclusion of sub-surface heat generation due to the plastic deformation in the workpiece material. The calculated temperature depended on two unknown parameters, the partition ratio and the convection coefficient. Since there are

two unknowns the parameters could not be evaluated directly. An optimisation strategy was used to determine the partition ratio and the convection coefficient based on successive approximations. This was repeated until the calculated values correlated with the measured temperature. Sauer noted that the temperature model was relatively insensitive to the convection coefficient and therefore the value could only be estimated approximately.

Sauer's results for the convection coefficient are given in Table 2.7. Water based fluids were found to have substantially higher convection coefficients than grinding with oil but resulted in higher energy levels. It is noted that the convective heat transfer coefficients are broadly in agreement with Lee's measurements.

Fluid	h_c $W/(m^2K)$
Air	0
Synthetic Fluid 4%	9400
Synthetic Fluid 10%	1400
Synthetic Fluid 20%	2000
Oil	294

Table 2.7 : Measurements of the convection coefficients from Sauer [33]

The partition ratio was found to decrease strongly with the material removal rate. Partition ratios were measured from 0.73 at low removal rate to 0.23 at high removal rates. Sauer suggested that the reduction in partition ratio at high removal rates was due a larger proportion of the grinding energy convected to the chips.

2.7 Prevention of thermal damage in grinding

Models used for the prevention of thermal damage in grinding [9, 18] are based on Jaegers moving heat transfer theory with an appropriate partitioning model.

$$\theta_m = 1.13 \frac{R_w q_w}{(\kappa \rho c)_w^{1/2}} \left(\frac{l_e}{v_w}\right)^{1/2} \quad .. 2.74$$

The grinding specific energy can be monitored in-process by recording the grinding power and grinding variables.

To use Equation 2.74 in the monitoring and prediction of thermal damage the following parameters must be established

(i) partition ratio 'R_w'

(ii) contact length 'le'

(iii) the critical workpiece temperature, θ_m^* ,for the onset of damage

Partition ratio models have already been reviewed. The model of Rowe and Morgan is the most advanced model and will be used as a basis for further study. However the validity of the conical grain model requires further investigation.

The real contact length in grinding has been measured up to three times the geometric value [34, 35, 36]. Rowe and Pettit incorporated an empirical equation [21] for the contact length in their thermal model based on Verkerk's experimental results [34]. Other researchers, eg. Peters and Maris [37] used a constant value of 2 l_g. Malkin used the geometric contact length in his thermal model [38]. Malkin argues that a large proportion of the heat generated is dissipated in the geometric contact length.

The reason for the real contact length being greater than the geometric value is the elastic deformation of the grinding wheel and the roughness of the grinding wheel [39].

From Equation 2.74 it is seen that the workpiece temperature varies inversely proportional to the root of the heat source length. The choice of the heat source length parameter used in the thermal model has therefore large sensitivity on the result obtained. The correct choice of contact length for thermal modelling has yet to be verified.

An industrial criterion for the occurrence of thermal damage is workpiece burn. This is characterised by the occurrence of 'temper' colours on the workpiece surface. Temper colours range from light straw to dark blue. The temper colours are caused by oxidation of the workpiece surface due to the high temperatures in the grinding zone.

Metallurgical investigations of the ground surface [40, 41] have reported several types of thermal damage to the workpiece.

(i) Untempered martensite is often reported in the immediate sub-surface in hardened steels. This indicates that the workpiece in the region has been raised above the eutectic temperature.

(ii) Overtempered Martensite is also found in hardened steels. Overtempered martensite is a result of further tempering of the original martensite during the grinding process.

Malkin [38] undertook a series of experiments to determine the conditions at which workpiece burn occurs. The results are shown in Figure 2.24. The experimental conditions at workpiece burn were then compared to a proposed thermal model based on the geometric contact length

$$e_c^* = 0.45\, e_{cc} + \beta\, d_e^{1/4} a^{-3/4} v_w^{-1/2} \qquad .. 2.75$$

where

$$\beta = \frac{k\,\theta_m^*}{1.13\,\alpha^{1/2}} \qquad ..2.76$$

Equation 2.75 takes a linear form with respect to $d_e^{1/4}a^{-3/4}\,v_w^{-1/2}$.

The value of the chip formation energy, e_{cc}, was obtained directly from the intercept on Figure 2.24 and β from the gradient. The workpiece thermal properties are known and the critical maximum temperature, θ_m^*, was evaluated to be 670deg.C. from Equation 2.76. Malkin concluded that due to possible bulk temperatures in the workpiece and inaccuracies in the modelling that the critical temperature for ferrous materials, θ_m^*, should be the eutectic temperature of 723 deg.C.

Malkin's analysis was repeated using l=2lg then θ_m^* equal to 460deg.C. This further demonstrates the importance of determining the effective contact length in grinding.

A different approach was adopted by Rowe and Pettit [18]. It was argued that straw temper colours appear in heat treatment as low as 220deg.C for mild steels. Relating this to the average temperature from Jaegers analysis the maximum critical temperature was estimated to be around 330deg.C.

2.8 Conclusions

The workpiece surface integrity in grinding is determined by the distributed action of the localised grain heat sources in the contact area. This gives rise to a workpiece background temperature over the entire contact length.

The workpiece background temperature may be modelled as a heat source moving across the workpiece surface at the workpiece speed. This situation can be analysed using the theory of moving heat sources developed by Jaeger.

The energy partitioned to the workpiece and the length of the heat source are required to evaluate the workpiece background temperature.

The partition ratio can be analysed at the wheel contact or at the grain contact. The accuracy of the partition ratio prediction for CBN grinding is limited due to the lack of knowledge of the thermal conductivity of the CBN abrasive.

The predicted background temperature is sensitive to the length of the heat source. Researchers have used different assumptions for the length of the heat source.

A number of studies have been undertaken to measure the partition ratio for alumina wheels. Few measurements of the partition ratio have been undertaken for CBN grinding wheels.

The critical workpiece temperature for the occurrence of workpiece burn has been reported between 330deg.C and 723deg.C for ferrous materials. Direct measurements of the workpiece temperature at the onset of visible thermal damage has not been undertaken.

Chapter 3 : Theoretical Model for the Prediction of the Partition Ratio

In this chapter the principles of energy partitioning are introduced. This provides the basis for the development of a grain contact partitioning model. The heat conduction into the grain was characterised by an effective contact radius and effective thermal properties for a plane contact model. This approach overcomes the problems of needing to characterise a large number of abrasive properties. Two closed form solutions are presented for the energy partitioning between the workpiece and wheel. The first solution takes account of transient heat conduction into the grain. The second solution assumes steady state heat transfer into the grain and a simpler expression is obtained for the partition ratio. The two solutions are compared and the error in assuming steady state heat transfer conditions is determined.

3.1 Energy partitioning in the grinding zone

The total heat flux, q_t, generated in the grinding zone is mainly comprised of the heat fluxes into the workpiece, q_w, into the grinding wheel, q_s, into the grinding chips, q_{ch}, and into the grinding fluid, q_f. The partitioning of energy in the grinding zone is shown schematically in Figure 3.1.

$$q_t = q_w + q_s + q_{ch} + q_f \qquad .. 3.1$$

The partition ratio, R_w, is the proportion of the total heat conducted into the workpiece

$$R_w = \frac{q_w}{q_t} \qquad .. 3.2$$

and R_{ch}, R_f, and R_s are the proportions of the total heat entering the chips, fluid and wheel

$$R_{ch} = \frac{q_{ch}}{q_t} \qquad .. 3.3$$

$$R_f = \frac{q_f}{q_t} \qquad .. 3.4$$

$$R_s = \frac{q_s}{q_t} \qquad .. 3.5$$

From Equations 3.2 to 3.5, the energy partitioned between workpiece and wheel is

$$\frac{R_w}{R_w + R_s} = \left[1 + \frac{q_s}{q_w}\right]^{-1} \qquad .. 3.6$$

The heat flux into the workpiece may be expressed as the product of the average workpiece background temperature, $\bar{\theta}_w$, and a heat transfer coefficient, h_w

$$q_w = R_w\, q_t = h_w\, \bar{\theta}_w \qquad .. 3.7$$

The heat flux into the grinding wheel may be expressed in a similar manner, as the product of the average grinding wheel contact zone temperature, $\bar{\theta}_s$, and a heat transfer coefficient, h_s

$$q_s = R_s\, q_t = h_s\, \bar{\theta}_s \qquad .. 3.8$$

Compatibility of the average interface temperatures expressed in equations 3.7 and 3.8 requires that

$$\overline{\theta_s} = \overline{\theta_w} \qquad .. 3.9$$

Substituting Equations 3.7, 3.8 and 3.9 into Equation 3.6 gives the energy partitioned between the workpiece and wheel in terms of heat transfer coefficients

$$\frac{R_w}{R_w + R_s} = \left[1 + \frac{h_s}{h_w}\right]^{-1} \quad .. 3.10$$

3.2 Energy convected by the chips and fluid

The total specific energy, e_c, dissipated in the grinding zone is not all partitioned between the wheel and workpiece. The partition ratio predicted by Equation 3.10 must be reduced by the factor, $(1 - R_{ch} - R_f)$, to make an allowance for the specific energy, e_{cc}, convected away by the chips and the specific energy, e_{cf}, convected away by the coolant.

Making the allowance for the effect of the chips and coolant leads to the expression for the partition ratio

$$R_w = \left[1 + \frac{h_s}{h_w}\right]^{-1} \left(1 - R_{ch} - R_f\right) \quad .. 3.11$$

From Equations 3.3 and 3.4

$$R_{ch} + R_f = \frac{e_{cc} + e_{cf}}{e_c} \quad .. 3.12$$

A typical value of, e_{cc}, is 6 J/mm^3 for ferrous materials [18] and, e_{cf}, tends to be small where fluid boiling occurs [42]. Under the conditions at fluid boiling e_{cf} is negligible and

$$R_{ch} \approx \frac{6}{e_c} \quad .. 3.13$$

It can therefore be seen that the effect on the partition ratio of the energy removed by the chips is increasingly significant at lower specific energies as shown in Figure 3.2. This signifies that the potential for the energy convected by the chips and the fluid to significantly reduce grinding temperatures is greater in high efficiency grinding.

3.3 Grain contact analysis

The grain contact analysis considers the energy partitioning at the grain wear flat-workpiece interface, Figure 3.3. The total heat flux is divided between the workpiece, grinding wheel, grinding chips and fluid so that equations 3.1 to 3.10 apply.

In the grain contact analysis it is assumed that the energy partitioning takes place at the grain-workpiece interface. The partitioning is therefore defined in terms of the average heat flux, q_g, into a grain as it traverses through the grinding contact zone. Similarly the average heat flux into the workpiece, q_{wg}, for the grain contact interface must be determined during the passage of the grain through the contact zone.

Equation 3.6 can therefore be expressed as

$$\frac{R_w}{R_w + R_s} = \left[1 + \frac{q_g}{q_{wg}}\right]^{-1} \qquad .. 3.14$$

The heat flux into the workpiece, q_{wg}, at a grain contact is expressed as

$$q_{wg} = h_{wg}\,\theta_{wg} \qquad .. 3.15$$

where, θ_{wg}, is the instantaneous increase in temperature in the workpiece under the grain averaged over the grain contact. For graphic simplicity, θ_{wg}, is termed the spike temperature.

The workpiece experiences a background temperature. The spike temperature due to the heat generation at the grain wear flat-workpiece interface is superimposed upon the background temperature. These temperatures are shown schematically in Figure 3.4.

The surface temperature of the workpiece at a point under a grain is therefore the sum of (i) the base temperature for the workpiece which is the background temperature, θ_w and (ii) the temperature increase, θ_{wg}, which arises due to the heat generation at the grain wear flat-workpiece interface.

The total temperature of the workpiece under a grain, θ_{wt}, at any position in the contact zone is therefore the superposition of the spike temperature, θ_{wg}, on the background temperature, θ_w

$$\theta_{wt} = \theta_w + \theta_{wg} \qquad .. 3.16$$

The heat flux into the grain, q_g, is

$$q_g = h_g \theta_g \qquad .. 3.17$$

The surface temperature of the grain as it passes through the grinding zone is the sum of (i) an increase in temperature of the grain due to the background temperature of the workpiece, θ_w

$$\theta_{g1} = \theta_w \qquad .. 3.18$$

and

(ii) An increase in temperature, θ_g, due to heat generation at the grain wear flat-workpiece interface

$$\theta_{g2} = \theta_g \qquad .. 3.19$$

The total temperature of the grain, θ_{gt} is obtained from the principle of superposition

$$\theta_{gt} = \theta_{g1} + \theta_{g2} = \theta_w + \theta_g \qquad .. 3.20$$

For compatibility of temperatures at the grain-workpiece interface

$$\theta_{wt} = \theta_{gt} \qquad .. 3.21$$

and from Equations 3.16 and 3.20

$$\theta_{wg} + \theta_w = \theta_g + \theta_w \qquad .. 3.22$$

or

$$\theta_{wg} = \theta_g \qquad .. 3.23$$

From Equations 3.14, 3.15, 3.17 and 3.23, the partitioning between the workpiece and grinding wheel for the grain contact analysis is

$$\frac{R_w}{R_w + R_s} = \left[1 + \frac{h_g}{h_{wg}}\right]^{-1} \qquad .. 3.24$$

3.4 Heat transfer coefficients

The heat transfer coefficient, h_{wg}, for the workpiece at the grain contact is assumed to be given by the steady state solution for a circular heat source moving over a semi-infinite body as shown in Figure 3.5.

Archard [26] analysed sliding contacts in friction pairs and gave a solution for the heat transfer coefficient for a circular sliding source for quasi steady state conditions. From the work of Jaeger [12] quasi state conditions are attained after the heat source has travelled approximately four times its own length.

Assuming that the abrasive grain can be modelled as a circular sliding source, the heat transfer coefficient into the workpiece, h_{wg}, is

$$h_{wg} = \frac{(\kappa \rho c)_w^{1/2} \, v_s^{1/2}}{0.974 \, r_0^{1/2}} \qquad .. 3.25$$

This solution is valid for

$$L = \frac{v_s \, r_0}{2 \, \alpha_g} > 5 \qquad .. 3.26$$

The grain is modelled as a stationary body subject to a constant circular heat flux for its duration in the grinding zone. The grain was taken as a protrusion of infinitesimal depth on a semi-infinite body. The grain temperature is determined from a classical solution for a stationary semi-infinite body subject to a circular heat flux. This will be termed the plane body solution. This model is shown in Figure 3.6. For transient two dimensional heat conduction the heat transfer coefficient is [43]

$$h_g = \frac{\kappa_g}{2r_o\tau}\left[\frac{1}{\pi^{1/2}} - \text{ierfc}\left(\frac{1}{2\tau'}\right)\right]^{-1} \quad .. 3.27$$

where

$$\tau' = \left(\frac{\alpha_g}{r_o^2}t\right)^{1/2} \quad .. 3.28$$

and ierfc is the imaginary complementary error function

$$\text{ierfc}(x) = \frac{\exp[-x^2]}{\sqrt{\pi}} - x\,\text{erfc}[x] \quad .. 3.29$$

Lavine [4] modelled the grain as a truncated cone. Lavine's solution was found by comparison with the accurate plane body solution to be invalid. It is clear that the thermal resistance of a conical body must be greater than a plane body. This is illustrated in Figure 3.7. For a given heat flux the temperature at the surface of the conical body will be greater than that of the plane body. This statement is true regardless of the cone angle. The temperatures from the 40 degree conical solution and the plane body solution are compared in Figure 3.8. It was found that the conical solution gives lower temperatures than the plane body solution at an angle of 40 degrees. Considering the geometry of the two models this is an impossible result. As the cone angle is increased beyond 40 degrees the temperature evaluated becomes lower than the plane body solution. Taking into account the geometry of the two models it is clear that the validity of the conical model is restricted to angles much less than 40 degrees. This is a serious limitation of the conical model which previously has not been documented. The conical model might be considered to be more accurate representation of the average shape of the grains in a wheel. However it will be shown later that by selecting appropriate values of effective thermal conductivity of the grain it is possible to avoid the need to characterise the effective cone angle and the corresponding heat transfer coefficient, h_g. To overcome this problem a closed form

partitioning solution was derived modelling the grain as a plane body in the transient mode. This reduces the number of parameters by one and greatly reduces the complexity of the solution without loss of accuracy.

3.5 Transient partitioning analysis at the grain contact

3.5.1 Exact solution

The grain may be assumed to enter the grinding zone at time t=0 and exit the grinding zone at $t=t_1$. The average partitioning ratio between the workpiece and wheel for the duration of the grain in the grinding zone may be determined as follows.

Equation 3.24 can be re-written as

$$R_{ws} = \frac{H}{1 + H} \qquad .. 3.30$$

where H is the ratio of the heat transfer coefficients

$$H = \frac{h_{wg}}{h_g} \qquad .. 3.31$$

The average partitioning between the workpiece and grinding wheel over the entire contact zone is

$$R_{ws} = \frac{\overline{H}}{1 + \overline{H}} \qquad .. 3.32$$

where

$$\overline{H} = \frac{1}{t_1}\int_0^{t_1} \frac{h_{wg}}{h_g}\,dt \qquad .. 3.33$$

The indefinite integral $\int \frac{h_{wg}}{h_g}\,dt$ was solved by a series of integration by parts and is detailed in Appendix A.3. The exact solution is

$$\frac{2}{3\sqrt{\pi}} B\, t^{3/2} - \frac{2\,B\,\sqrt{t}\,(A^2 + t)}{3\sqrt{\pi}\,\exp\left[\frac{A^2}{t}\right]} - \frac{2}{3} A^3\, B\, \mathrm{erf}\left[\frac{A}{\sqrt{t}}\right] + A\, B\, t\, \mathrm{erfc}\left[\frac{A}{\sqrt{t}}\right] \qquad .. 3.34$$

where

$$A = \frac{r_o}{2\sqrt{\alpha}} \qquad .. 3.35$$

and

$$B = h_{wg}\,\frac{2\sqrt{\alpha}}{\kappa} \qquad .. 3.36$$

The definite integral $\overline{H} = \frac{1}{t_1}\int_0^{t_1} \frac{h_{wg}}{h_g}\,dt$ is required to determine the average energy partitioning in the grinding zone.

From Equation 3.33 and 3.34

$$\overline{H} = \frac{1}{t_1}\left[\frac{2}{3\sqrt{\pi}} B\, t^{3/2} - \frac{2\,B\,\sqrt{t}\,(A^2 + t)}{3\sqrt{\pi}\,\exp\left[\frac{A^2}{t}\right]} - \frac{2}{3} A^3\, B\, \mathrm{erf}\left[\frac{A}{\sqrt{t}}\right] + A\, B\, t\, \mathrm{erfc}\left[\frac{A}{\sqrt{t}}\right]\right]_0^{t_1}$$

.. 3.37

(i) The lower limit of integration is determined by letting t=0

For the first part of Equation 3.37, as time t approaches zero

$$\frac{2}{3\sqrt{\pi}} B\, t^{3/2} = 0 \qquad \text{.. 3.38}$$

For the second part of Equation 3.37, as time t approaches zero

$$\frac{2\,B\,\sqrt{t}\left(A^2 + t\right)}{3\sqrt{\pi}\,\exp\left[\frac{A^2}{t}\right]} = 0 \qquad \text{.. 3.39}$$

since $\exp[\infty] = \infty$.

For the third part of Equation 3.37, as time t approaches zero

$$\frac{2}{3} A^3 B\, \mathrm{erf}\left[\frac{A}{\sqrt{t}}\right] = \frac{2}{3} A^3 B \qquad \text{.. 3.40}$$

since $\mathrm{erf}[\infty] = 1$.

For the fourth part of Equation 3.37, as time t approaches zero

$$A\,B\,t\,\mathrm{erfc}\left[\frac{A}{\sqrt{t}}\right] = 0 \qquad \text{.. 3.41}$$

since $\mathrm{erfc}[\infty] = 0$.

From Equations 3.38 to 3.41 as time t approaches zero

$$\frac{2}{3\sqrt{\pi}} B\, t^{3/2} - \frac{2\,B\,\sqrt{t}\,(A^2 + t)}{3\sqrt{\pi}\,\exp\left[\frac{A^2}{t}\right]} - \frac{2}{3} A^3\, B\, \mathrm{erf}\left[\frac{A}{\sqrt{t}}\right] + A\, B\, t\, \mathrm{erfc}\left[\frac{A}{\sqrt{t}}\right] = -\frac{2}{3} A^3\, B$$

.. 3.42

(ii) For the upper limit of integration, $t=t_1$, the bracketed term in Equation 3.37 becomes

$$\frac{2}{3\sqrt{\pi}} B\, t_1^{3/2} - \frac{2\,B\,\sqrt{t_1}\,(A^2 + t_1)}{3\sqrt{\pi}\,\exp\left[\frac{A^2}{t_1}\right]} - \frac{2}{3} A^3\, B\, \mathrm{erf}\left[\frac{A}{\sqrt{t}}\right] + A\, B\, t_1\, \mathrm{erfc}\left[\frac{A}{\sqrt{t_1}}\right] \quad .. 3.43$$

and from Equations 3.37, 3.42 and 3.43

$$\overline{H} = \frac{2}{3} A^3 \frac{B}{t_1} + \frac{2}{3\sqrt{\pi}} B t_1^{1/2} - \frac{2\,B\,(A^2 + t_1)}{3\sqrt{\pi}\,\sqrt{t_1}\,\exp\left[\frac{A^2}{t_1}\right]} - \frac{2}{3} \frac{A^3\, B}{t_1}\, \mathrm{erf}\left[\frac{A}{\sqrt{t_1}}\right] + AB\, \mathrm{erfc}\left[\frac{A}{\sqrt{t_1}}\right]$$

.. 3.44

This expression may be transformed into the dimensionless time variable

$$\tau = \left(\frac{\alpha}{r_o^2} t_1\right)^{1/2} = \frac{1}{2A} t_1^{1/2} \quad .. 3.45$$

Substituting Equation 3.45 into 3.44 gives

$$\overline{H} = h_{wg} \frac{r_o}{\kappa_g} \frac{1}{\Phi(\tau)} \quad .. 3.46$$

where the transient function $\Phi(\tau)$ is

$$\Phi(\tau) = 1 + \frac{1}{6\tau^2} + \frac{4\tau}{3\sqrt{\pi}} \left\{1 - \exp\left[\left(\frac{1}{4\tau^2}\right)^{-1}\right]\left(1 + \frac{1}{4\tau^2}\right)\right\} - \mathrm{erf}\left[\frac{1}{2\tau}\right]\left(1 + \frac{1}{6\tau^2}\right) \quad ..3.47$$

The grain is in the grinding zone for the duration,

$$t_1 = \frac{l_e}{v_s} \qquad .. 3.48$$

therefore Equation 3.45 becomes

$$\tau = \left(\frac{\alpha_g}{r_o^2}\,\frac{l_e}{v_s}\right)^{1/2} \qquad .. 3.49$$

Substituting Equation 3.46 into 3.32 gives the expression for the average partitioning between the workpiece and wheel over the contact length

$$R_{ws} = \left[1 + \frac{\kappa_g}{h_{wg}\, r_o}\,\frac{1}{\Phi(\tau)}\right]^{-1} \qquad .. 3.50$$

and substituting h_{wg} from Equation 3.26

$$R_{ws} = \left[1 + \frac{0.974\,\kappa_g}{(\kappa\rho c)_w^{1/2}\, r_o^{1/2}\, v_s^{1/2}}\,\frac{1}{\Phi(\tau)}\right]^{-1} \qquad .. 3.51$$

The following parameters must be determined in order to evaluate the partition ratio from Equation 3.51

r_0 - wear flat radius

l_e - contact length

v_s - wheel speed

$(\kappa\rho c)_w^{1/2}$ - workpiece thermal contact coefficient

$(\kappa\rho c)_g^{1/2}$ - grain thermal contact coefficient

The real contact length in grinding can be predicted by the model of Rowe and Qi [39]. The explanation for the real contact length being greater than the geometric value was attributed to roughness of the grinding wheel and elastic deformation. The main parameters influencing the contact length in the model of Rowe and Qi are the real depth of cut, the elastic deformation of the grinding wheel and the surface topography of the grinding wheel.

The real length of contact, l_e, is given by the orthogonal relationship between the contact length due to deflection, l_f, and the geometric contact length, l_g

$$l_e^2 = l_f^2 + l_g^2 \qquad .. 3.52$$

The geometric contact length, l_g, is given by

$$l_g = \sqrt{a d_e} \qquad .. 3.53$$

where 'a' is the depth of cut and 'd_e' is the equivalent diameter given by

$$\frac{1}{d_e} = \frac{1}{d_S} + \frac{1}{d_W}$$

The contact length due to deflection, l_f, is given by

$$l_f = \left(8 R_r^2 \frac{F_n}{b} (K_s + K_w) d_e\right)^{1/2} \qquad .. 3.54$$

where

$$K = \frac{1 - \upsilon^2}{\pi E} \qquad .. 3.55$$

and

R_r is a roughness factor which characterises the grinding wheel topography

E is the modulus of elasticity

ν is Poissons ratio

F_n is the normal grinding force

b is the grinding width.

3.5.2 Simplification of the transient function

The error function in Equation 3.47 presents computational complexity for implementation of the partitioning model into process control. The transient function $\Phi(\tau)$ was fitted to a first order response

$$\Phi(\tau) = 1 - \exp\left[-\frac{\tau}{\tau_o}\right] \qquad .. 3.56$$

The transient function $\Phi(\tau)$ reaches 63.2% of its steady state value at τ=1.2, Figure 3.9. Therefore the time constant, τ_o, of the function is 1.2 and the simplified transient function becomes

$$\Phi(\tau) = 1 - \exp\left[-\frac{\tau}{1.2}\right] \qquad .. 3.57$$

A comparison of the transient function and the first order approximation is given in Figure 3.9. The first order approximation reaches steady state before the transient function.

The maximum errors in the first order approximation are +10% and -5%. The maximum error of +10% of the first order approximation occurs at τ=4. A positive error in the

estimation of the transient function will result in a higher predicted partition ratio and will therefore be conservative in use.

3.6 Steady state partitioning

A simplified expression for the partition ratio may obtained by considering steady state heat transfer in the grain. Steady state conditions exist when time, t, tends towards infinity.

The transient part of the partitioning solution is incorporated in the function

$$\Phi(\tau) = 1 + \frac{1}{6\tau^2} + \frac{4\tau}{3\sqrt{\pi}}\left\{1 - \exp\left[\left(\frac{1}{4\tau^2}\right)^{-1}\right]\left(1 + \frac{1}{4\tau^2}\right)\right\} - \operatorname{erf}\left[\frac{1}{2\tau}\right]\left(1 + \frac{1}{6\tau^2}\right) \quad .. 3.58$$

As t->∞, then

$$\Phi(\tau) = 1 \quad .. 3.59$$

Therefore at steady state, Equation 3.51 becomes

$$\frac{R_w}{R_w + R_s} = \left[1 + \frac{0.974\,\kappa_g}{(\kappa\rho c)_w^{1/2}\, r_0^{1/2}\, v_s^{1/2}}\right]^{-1} \quad .. 3.60$$

The steady state solution is much simpler to evaluate than the transient analysis.

3.7 Comparison of the transient and steady state solution

The transient function $\Phi(\tau)$ is plotted against dimensionless time, τ, in Figure 3.10. The function $\Phi(\tau)$ was found to reach 90% of its steady state value at a value of τ=5. At τ=10 the function is within 95% of the steady state value.

The dimensionless time is given by

$$\tau = \left(\frac{\alpha_g}{r_o^2}\frac{l_e}{v_s}\right)^{1/2} \qquad .. 3.61$$

From Equation 3.61 it is seen that the steady state solution is least accurate for the following conditions

(i) abrasives of low thermal diffusivity
(ii) large wear flat radius
(iii) small contact lengths
(iv) high wheel speeds

Values of the dimensionless time for an alumina grinding wheel operating at 30m/s are shown in Figure 3.11 for various values of wear flat radius, ro. It is seen that the value of τ only reaches 5 at large contact lengths and small wear flat radii. At small contact lengths and large contact radii the value τ is less than 1. From Figure 3.9, the assumption of steady state heat transfer in the grain at τ=1 gives a 43% error in the transient function $\Phi(\tau)$.

Values of the dimensionless time for a CBN grinding wheel operating at 30m/s are shown in Figure 3.12 for various values of wear flat radius, ro. At large contact lengths and small values of contact radius the value τ reaches 20, this gives a 3% error in the transient

function $\Phi(\tau)$. At small contact lengths and large contact radii the value τ is less than 2. The assumption of steady state heat transfer in the grain at τ=2 gives a 15% error in the transient function $\Phi(\tau)$.

The error in the predicted partition ratio is smaller than the error in the transient function $\Phi(\tau)$ as may be seen from Equation 3.51. In Figure 3.13, the transient and steady state solutions are compared for a wear flat radius ro=10μm. The steady state solution over-estimates the partition ratio. The error in using the steady state solution for ro=10μm is given in Figure 3.14. For contact length values greater than 5mm the steady state solution over-estimates the partition ratio by less than 5% for both alumina and CBN.

The transient and steady state solutions are compared for wear flat radius ro=50μm in Figure 3.15. For contact length values greater than 5mm the steady state solution over-estimates the partition ratio by less than 10% for both alumina and CBN, Figure 3.16.

For small values of contact length the steady state solution can grossly over estimate the partitioning between the workpiece and the grinding wheel. The largest error occurs at large values of wear flat radius and small values of contact length, Figures 3.14 and 3.16. Small contact lengths and large values of wear flat radius correspond to small values of the dimensionless time τ.

The advantage of the steady state solution is that it is simpler than the transient analysis. The steady state solution should only be used when $\tau > 5$. For values of $\tau > 5$ the transient function reaches within 90% of the steady state value. For $\tau < 5$ the assumption of steady state becomes increasingly inaccurate and the transient solution should be used.

The partition ratio model assumes quasi steady state heat transfer for the workpiece spike temperature. There are two criteria for this assumption to be applicable (i) the Peclet

number $L = v_s r_o/(2 \alpha_g)$ should be greater than five and (ii) the heat source must have travelled four times its own length [24].

The first condition will be violated when the wear flat radius becomes very small. A plot of the Peclet number against wear flat radius is shown in Figure 3.17. The Peclet number falls below five at for wear flat radii less than 2.5μm. This condition is therefore generally valid.

The second condition is likely to be violated at large values of the wear flat radius. For r_o=50μm the quasi steady state assumption will not be valid until the grain has travelled 400μm through the grinding zone. In fine grinding the contact length may be of comparable dimensions and the accuracy of the partitioning solution will be reduced.

From Figures 3.13 and 3.15 the partition ratio is seen to drop sharply to zero as the contact length approaches zero. The result of the zero partition ratio at zero contact length is expected since there has been no time for heat transfer to take place in the grain and the transient function $\Phi(\tau)$ is zero. However, the partition drops to zero too quickly at small values of contact length. This is a consequence of assuming quasi steady state conditions for the workpiece spike temperature. From equation 3.25 the quasi steady state temperature solution for the workpiece is

$$\theta_{wg} = \frac{0.974\, q_{wg}\, r_o^{1/2}}{(\kappa \rho c)^{1/2}\, v_s^{1/2}} \qquad .. \ 3.62$$

The temperature under the heat source increases from zero to the value given by Equation 3.62 as the grain travels to four times its length. When the heat source has travelled less than four times its own length the temperature under the heat source will be less than predicted from Equation 3.62. For simplicity the coefficient in Equation 3.62 will be assumed to be less than 0.974 when the heat source has travelled less than four times its

own length. With reference to the partitioning Equation 3.51 the effect of this will be to have a higher partition ratio than predicted by the model. The actual gradient of the partition ratio in the region where the heat source has travelled less than four times its own length will therefore be less than shown in Figures 3.13 and 3.15.

3.8 Conclusions

An analysis has been presented to determine the partition ratio in grinding.

A closed form solution for the partition ratio has been derived which takes into account transient heat transfer throughout the contact zone. A closed form transient solution for the average partition ratio throughout the contact zone has not previously been proposed. The closed form solution was presented in the form of a steady state solution multiplied by a transient function to take account of transient heat conduction in the grain.

A simpler analysis for energy partitioning was found by assuming steady state heat transfer in the grain. The steady state solution can be used when the value of the dimensionless time parameter, τ, is greater than five. The steady state solution over estimates the partition ratio and is therefore conservative when used to estimate the level of grinding power which can be safely employed without damaging the workpiece.

An advance has been made by characterising the grain properties by an effective contact radius and effective heat transfer properties for a plane contact model of the grain. This approach takes into account two dimensional heat conduction in the grain and overcomes the problem of needing to characterise the cone angle of the abrasive grain and the corresponding heat transfer coefficient.

The reduction in partition ratio due to energy removed by the grinding chips and fluid is increasingly significant at lower specific energies.

Chapter 4 : Theory for Experimental Partitioning

4.1 Semi-empirical measurement of the partition ratio.

The measurement of the partition ratio is based on the correlation of measured and theoretical temperature distributions. A theory to relate the workpiece background temperature in grinding to the energy input into the surface is developed in this chapter. This theory will be used with the temperature measurement technique described in Chapter 5 to measure the partition ratio.

In general terms a heat flux, q, can be expressed as the product of a heat transfer coefficient, h, and a temperature difference, θ

$$q = h\,\theta \qquad ..4.1$$

It is proposed to determine the heat flux to the workpiece, q_w, by measuring the grinding zone temperature, θ_w, and a theoretical heat transfer coefficient, h_w. The application of a theoretical heat transfer coefficient will be justified by matching the theoretical temperature distribution and the measured temperature distributions.

The total heat, Q_t, consumed in the process can be determined by measuring the grinding power. The proportion of the energy partitioned to the workpiece can therefore be evaluated and expressed as the partition ratio 'R_w'

$$R_w = \frac{Q_w}{Q_t} \qquad ..4.2$$

The next section is concerned with the development of the grinding zone heat transfer coefficient, h_w.

4.2 Grinding zone heat transfer coefficient, h_w

4.2.1 Heat flux distribution in the grinding zone

The background temperature in grinding is normally predicted by the theory of moving heat sources developed by Jaeger, 1942 [12]. Jaeger presented a solution for the particular case of a uniform heat flux in the grinding zone, Figure 2.3. It can be strongly argued that the heat flux is not uniform in the case of grinding. The generation of heat in the grinding zone would be expected to be proportional to the local forces on the grains. Each grain sees a variation in depth of cut as it traverses through the grinding zone from zero to some maximum value in upcut grinding or the reverse in downcut grinding. It would be expected that the heat flux distribution in the grinding zone would take a similar form. The forces at the grain can be assumed to be proportional to the local chip thickness. Ignoring elastic deformation of the grinding wheel the local chip thickness can be shown to vary approximately linearly over the geometric contact length [38]. Therefore for the cutting process of the grain the heat flux distribution could be approximated as linear over the geometric contact length. However the cutting energy in grinding only accounts for a proportion of the total grinding energy [9]. A significant proportion of energy is dissipated in the form of ploughing and sliding. The maximum cutting energy can be considered to be the energy required to melt the chip volume [18] which is typically $6J/mm^3$. A typical grinding specific energy is $50J/mm^3$ and therefore in this case over $40J/mm^3$ is expended in sliding. The sliding energy is dissipated over the whole sliding contact length, l_e, whereas the cutting energy is mainly dissipated over the geometric contact length, l_g. The distribution of the sliding energy over the contact zone is not known.

The heat flux distribution in grinding has previously been proposed as linear [45], Figure 4.1. This however fails to take into account sliding energy which is dissipated over the entire contact length. In this thesis a square law heat flux distribution was also investigated, Figure 4.2. A square law heat flux approximates the long tail of the flux distribution due to elastic deflection, surface roughness effects and variable grain protrusions.

In order to analyse the grinding process more realistically it was necessary to develop the theory of moving heat sources with a variable flux distribution.

4.2.2 Theory of moving heat sources with variable heat flux distributions

Jaeger's theory was extended to take into account a variable heat flux by normalising the heat liberated in the band source to the heat liberated in the uniform heat flux solution. For a uniform heat flux the total heat liberated in the contact zone is

$$Q = q_o \, l_e \, b \qquad .. 4.3$$

where q_o is the magnitude of the heat flux, l_e is the length of the contact zone and b is the width of the contact zone.

Assuming a power law heat flux

$$q = q_n \left(x'\right)^n \qquad .. 4.4$$

where n is an exponent representing the heat flux shape.

When n=0, the heat flux is uniform and the original solution presented by Jaeger is obtained.

The case n=1, corresponds to a triangular distribution.

The case n=2, represents a square law heat flux distribution.

A comparison of the triangular and square law heat fluxes normalised to liberate the same quantity of heat as the uniform heat flux is shown in Figure 4.3.

The power law heat flux distribution must be normalised to liberate the same amount of heat as the uniform heat flux solution. The heat liberated for a power law heat flux is

$$Q = q_n\, b \int_0^{l_e} (x')^n \, dx' \qquad .. 4.5$$

Equations 4.1 and 4.3 give the value of q_n

$$q_n = (n+1)\frac{q_o}{l_e^{\,n}} \qquad .. 4.6$$

For consistency with Jaeger's solution, the power law heat flux distribution is referenced to the centre of the heat source

$$q_n = (n+1)\frac{q_o}{l_e^{\,n}}\left(x' + \frac{l_e}{2}\right)^n \qquad .. 4.7$$

The coordinate x' referenced to the moving heat source may be transformed to the workpiece variable x by the transformation [12]

$$x' = x - \frac{2\alpha u}{v} \qquad .. 4.8$$

Substituting Equation 4.8 into 4.7 gives

$$q(x) = (n+1)\, q_o \left(\frac{x}{l_e} - \frac{2\alpha u}{v l_e} + \frac{1}{2}\right)^n \qquad .. 4.9$$

or expressed in terms of the dimensionless parameters X and L

$$q(x) = (n+1)\, q_o \left(\frac{X}{2L} - \frac{u}{2L} + \frac{1}{2}\right)^n \qquad ..4.10$$

For a variable heat flux the temperature under a sliding heat source is given by

$$\frac{\theta \pi K v}{2 q_o \alpha} = \int_{X-L}^{X+L} e^{-u} K_o \left(Z^2 + u^2\right)^{1/2} q(x)\, du \qquad .. 4.11$$

Substituting Equation 4.10 into 4.11, the dimensionless temperature for a moving power law heat source is

$$\frac{\theta \pi K v}{2 q_o \alpha} = \int_{X-L}^{X+L} e^{-u} K_o \left(Z^2 + u^2\right)^{1/2} (n+1) \left(\frac{X}{2L} - \frac{u}{2L} + \frac{1}{2}\right)^n du \qquad .. 4.12$$

4.2. 3 Comparison of uniform, triangular and square law flux distribution

Surface temperature with a uniform heat flux, investigated by Jaeger is the only case which can be solved analytically. All other cases must be solved numerically. A program was written in 'Mathematica' to solve Equations 4.12. The program is given in Appendix A2.. The equation was solved at twenty locations in the contact zone. Using the standard numerical integral command on a Macintosh LCII computer the computational time was three minutes for each X/L location evaluated.

The dimensionless surface temperatures are compared for the uniform, triangular and square law heat flux for Peclet number L=10 in Figure 4.4. The most notable difference in the solutions is the shape of the temperature distribution. Both the triangular and square law solutions have the maximum temperature position lying towards the leading edge of the heat source.

The relationship between the Peclet 'L' number and the magnitude and position of the maximum temperatures was investigated. The solutions for the triangular and square law were evaluated for Peclet numbers 1 to 100, in increments of 1.

It was found that the shape of the temperature distribution for L>5 was independent of the Peclet number for both the triangular and square law heat flux distributions. The position of maximum temperature was located at the centre of the heat source, X/L=0, for the triangular distribution. For the square law heat flux the position of the maximum temperature lies closer to the leading edge of the heat source at X/L= -0.375.

The maximum temperature for the triangular distribution is lower than the uniform heat flux solution. For the square law heat flux the maximum temperature is greater than the uniform heat flux. A graph of the maximum dimensionless temperature against Peclet number for the uniform, triangular and square law heat flux distributions is given in Figure 4.5.

The data obtained for the maximum temperature was fitted to the following relationship

$$\frac{\theta \pi K v}{2 \alpha q_o} = C\, L^{0.5} \qquad .. 4.13$$

For a uniform heat flux and L>5, Jaeger evaluated the constant 'C' to be 3.336.

To find the coefficient 'C' for the triangular and square law heat flux cases the standard procedure of taking the logarithm of Equation 4.13 was used

$$\ln\left(\frac{\theta\pi K v}{2q_o\alpha}\right) = \ln(C) + 0.5\ln(L) \qquad \text{.. 4.14}$$

The data for the triangular and square law flux distributions were found to fit Equation 4.15 as shown in Figures 4.6 and 4.7 The constant 'C' was evaluated from the intercept of the y-axis. The value of the constant 'C' was evaluated to be 3.336 for the triangular heat flux and 3.775 for the square law heat flux.

It was found that varying the heat flux in the grinding zone substantially changes the shape of the temperature distribution. The magnitude of the maximum temperature was also found to change with the heat flux distribution. For uniform, triangular and square law heat fluxes the dimensionless temperature was related to the Peclet number by Equation 4.13. The magnitude of the constant 'C' and the position of the maximum temperature for each distribution are summarised in Table 4.1.

	Uniform	Triangular	Square Law
Coefficient 'C'	3.543	3.336	3.775
Position X/L of maximum temperature	1	0	-0.375

Table 4.1 : Magnitude and position data of maximum temperature

4.3 Influence of convective cooling on the grinding zone temperature

Most grinding operations take place with grinding fluid. The influence of convective cooling on the workpiece surface temperature distribution was investigated by Des Ruisseaux [22]. Uniform convective cooling was assumed to act across the entire surface of a semi-infinite body, Figure 2.9. It was considered possible that convective cooling within the contact zone might modify the shape of the temperature distribution. It was therefore decided to investigate this question as part of the validation of the heat flux assumption.

4.3.1 Iterative solution for convective cooling

To overcome the long calculation times involved in the Des Ruisseaux solution an iterative method was used to evaluate the effect of fluid on the grinding zone temperature distribution.

The technique involved computing the effect of moving heat sources without cooling to determine a value of θ and successively reducing the heat flux by an incremental amount, $h_c\theta$, for convective cooling until convergence was achieved.

The starting point was the calculation of the temperature for a moving heat source without cooling

$$\Theta = \frac{\theta \pi K v}{2 q_o \alpha} = \frac{\theta A}{q_o} = \int_{X-L}^{X+L} e^{-u} K_o [\,|u|\,]\, q(x)\, du \qquad .. 4.15$$

$$\text{where } A = \frac{\pi K v}{2\alpha} \qquad .. 4.16$$

and Θ is the dimensionless temperature at a position X.

The value of the integral $\int_{X-L}^{X+L} e^{-u} K_o [\,|u|\,] q(x)\, du$ remains constant for the particular X location investigated and is denoted by ψ. Therefore

$$\psi = \frac{\theta A}{q_0} \qquad .. 4.17$$

For the first iteration, the heat flux is reduced by the amount $h_c\, \theta$

$$\frac{\theta_1 A}{(q_o - h_c\, \theta)} = \psi \qquad .. 4.18$$

This can be expressed in dimensionless form

$$\Theta_1 = \frac{\theta_1 A}{q_o} = \frac{\psi}{q_o}(q_o - h_c\theta) \qquad .. 4.19$$

The starting value of θ is taken as the temperature predicted without cooling. Substituting $\theta = \frac{q_o}{A}\psi$ from Equation 4.17 into Equation 4.19 gives the dimensionless temperature for the first iteration

$$\Theta_1 = \frac{\theta_1 A}{q_o} = \psi\left(1 - \frac{h_c}{A}\psi\right) \qquad .. 4.20$$

or

$$\Theta_1 = \frac{\theta_1 A}{q_o} = \psi(1 - H'_c\, \psi) \qquad .. 4.21$$

where the dimensionless convective coefficient is

$$H'_c = \frac{h_c}{A} = \frac{h_c 2\alpha}{\pi k v} \qquad .. 4.22$$

This is related to the Des Ruisseaux dimensionless convective coefficient 'H_c' by

$$H'_c = \frac{H_c}{\pi} \qquad .. 4.23$$

For iteration two, the heat flux is reduced by the amount $h_c \theta_1$

$$\Theta_2 = \frac{\theta_2 A}{q_o - h_c \theta_1} \qquad .. 4.24$$

where θ_1 is given from Equation 4.21

$$\theta_1 = \frac{q_o \psi}{A} (1 - H'_c \psi) \qquad .. 4.25$$

Substituting Equation 4.25 into 4.24 the following expression is found for the dimensionless temperature after the second iteration

$$\Theta_2 = \frac{\theta_2 A}{q_o} = \psi [1 - H'_c \psi (1 - H'_c \psi)] \qquad .. 4.26$$

Reducing the heat flux by the amount $h_c \theta_2$, the dimensionless temperature for iteration three is

$$\Theta_3 = \frac{\theta_3 A}{q_o} = \psi \{1 - H'_c \psi [1 - H'_c \psi (1 - H'_c \psi)]\} \qquad .. 4.27$$

It is seen that a pattern emerges which takes the form after 'n' iterations

$$\Theta_n = \frac{\theta_n A}{q_o} = \psi\left[\sum_{j=1}^{j=n-1}(-1)^{j-1}(H'_c\psi)^{j-1} + (-1)^{n-1}(H'_c\psi)^{n-1}(1 - H'_c\psi)\right] \quad .. 4.28$$

The above analysis reduces the cooling problem to a series of summations which may be readily implemented on a simple microcomputer program. Des Ruisseaux requires numerical integration to infinity and evaluation of error functions which results in long computational times. Identical results were found with the Des Ruisseaux analysis after 20 iterations for $H_c<0.2$. The above procedure is repeated for each location in the grinding zone.

It is noted that this method could also be extended to investigate non-uniform cooling in the grinding zone by specifying a variable convective coefficient. This may be more representative of the actual grinding process and cannot be investigated by the method of Des Ruisseaux.

4.3.2 Theoretical results for the effect of convective cooling

The reduction in maximum temperature due to uniform convection across the grinding zone was investigated using the iteration method for a square law heat flux. The square law heat flux was chosen because it takes account of the gradual transition between the cutting, sliding and ploughing energies in grinding. The solution was therefore evaluated at X/L= -0.375 which is the position of the maximum temperature for a square law heat flux.

Convective cooling was investigated for the range of Peclet numbers from L=5 to 80. This range covers most grinding operations. Cooling up to the maximum possible dimensionless convective cooling was investigated. From Equation 4.22 the maximum dimensionless cooling occurs at the lowest workspeed and largest convection coefficient.

The lowest workspeed in shallow cut grinding is typically 0.1m/s and the highest reported convective heat transfer coefficient is 20,000W/(m^2K) [31, 33]. Using these values with typical workpiece thermal properties the maximum value of dimensionless convection coefficient, H_c, is 0.1.

The reduction in dimensionless temperature was evaluated for the range of Peclet numbers from L=5 to 80 in increments of 2. Convective cooling was investigated up to the maximum value of H_c=0.1 in increments of 0.01. The results for the reduction in dimensionless temperature due to convective cooling employing the iterative cooling solution are shown in Figure 4.8.

The data in Figure 4.8 was curve fitted and was found to follow within a maximum error of +4.7%/-4.76 %

$$\frac{\Delta\theta\pi K v}{2q_o\alpha} = L\left[1.69\,H_c + 0.725\,H_c^2\ln(H_c)\ln(L)\right] \qquad ..\ 4.29$$

This equation covers a wide range of grinding conditions from L=5 to 80 and if required could easily be implemented into a process control system.

For prediction of the maximum temperature for a square law heat flux with uniform convective cooling up to H_c=0.1 the following relationship is obtained by combining Equation 4.29 with the solution for a square law heat flux, Equation 4.13

$$\frac{\theta\pi K v}{2q_o\alpha} = 3.775\,L^{0.5} - L\left[1.69\,H_c + 0.725\,H_c^2\ln(H_c)\ln(L)\right] \qquad ..\ 4.30$$

The percentage reduction in the maximum temperature for a square law heat flux distribution due to uniform convective cooling is given in Figure 4.9. The maximum percentage reduction of approximately 20% occurs at high dimensionless convective

coefficients and high Peclet numbers. At lower Peclet numbers with the maximum convective coefficient H_c=0.1 the percentage reduction in cooling is around 13 %. A more realistic value of H_c for the grinding fluid would be 0.05 based on a convective coefficient h_c=10,000 W/(m^2K) [31, 33] which is an average value quoted in literature. For the grinding experiments carried out in this investigation the Peclet number ranges from 5 to 30. In this region the percentage reduction in maximum temperature due to cooling is approximately 7%, Figure 4.9.

The above analysis assumed convective cooling on the workpiece surface. In practice it has been found that fluid boiling takes place at 120 deg.C [42] for water based grinding fluids. At fluid boiling conditions the convection coefficient drastically reduces and essentially dry grinding conditions prevail. For dry grinding conditions h_c=500W/(m^2K) [31]. This magnitude of convective cooling was found to make negligible difference to the temperature distribution. It was therefore decided to ignore the effect of convection from the fluid in the experimental determination of partition ratio.

4.4 Equation for the measurement of the partition ratio

The results of the cooling analysis and consideration of fluid boiling indicate that moving heat source theory without cooling can be used to determine the workpiece background temperature in both dry and wet grinding operations.

The equation for the partition ratio was derived from the background temperature solution. Noting that Equation 4.13 applies to half the heat source length, the maximum dimensionless workpiece temperature is

$$\frac{\theta_m \pi \kappa_w v_w}{2\alpha_w q_w} = C\left(\frac{v_w l_e}{4\alpha_w}\right)^{0.5} \qquad .. 4.31$$

where C is a factor representing the heat flux distribution and is given by Table 4.1.

The heat flux to the workpiece, q_w, is

$$q_w = R_w q_t = \frac{R_w Q_t}{b\, l_e} \qquad .. 4.32$$

Substituting Equation 4.32 into 4.31 and rearranging gives an expression for the partition ratio

$$R_w = \frac{\pi}{C} b \left(\kappa \rho c\right)_w^{1/2} v_w^{1/2} \frac{\theta_m\, l_e^{1/2}}{Q_t} \qquad .. 4.33$$

The following parameters must therefore be established in order to determine the partition ratio

(i) Maximum grinding zone background temperature, θ_m.

(ii) Heat source length, le.

(iii) Total heat liberated, Q_t.

(iv) Heat flux distribution in order to determine the coefficient 'C'.

(v) Workpiece thermal properties, κ, ρ and c.

Measurement of the grinding zone temperature and heat source length is outlined in Chapter 5.

The solution assumes constant workpiece thermal properties. Thermal conductivity and specific heat capacity vary considerably for metals. Figure 4.10 shows the variation of thermal conductivity and specific heat capacity with temperature for mild steel AISI-1020.

Density variation is relatively small in comparison. The analytical solution of the general heat conduction equation with temperature dependent thermal properties is non-linear.

The effect of the temperature dependent thermal properties on the sliding band source problem can be investigated using an iterative technique [17, 46]. The data for thermal conductivity and specific heat capacity were fitted to a polynomial. The temperature calculation was then iterated with thermal properties calculated from the temperature from the previous iteration. Vansevant [17] reported a 10% reduction in the maximum background temperature employing using temperature dependent thermal properties compared to the constant thermal properties solution. Isenberg [46] reported a diminishing effect of temperature dependent thermal properties with increasing Peclet number.

The relative insensitivity of the temperature calculation to temperature dependent thermal properties is explained by consideration of the workpiece thermal contact coefficient, $(\kappa\rho c)_w^{1/2}$. The decrease in thermal conductivity with temperature is seen to be partially offset by the increase in specific heat capacity, Figure 4.11. It was therefore decided to employ an average value of the workpiece thermal contact coefficient.

4.5 Conclusions

A theoretical basis has been presented to measure the partition ratio in grinding. The method is based on the correlation of a theoretical and measured temperature distributions. The maximum background temperature, the length of the heat source and the total heat generated in the grinding zone must be measured.

The theory of moving heat sources has been developed for a power law heat flux distribution. This solution is expected to be more representative of the actual grinding process than the uniform heat flux solution.

A solution for convective cooling has been presented which overcomes the long computation times required in the previously published method of Des Ruisseaux. The results indicate that the theory of moving heat sources without cooling can be used to model the background temperature distribution in wet grinding.

5.1 General description of the measuring system

The workpiece surface temperature was measured in surface grinding using 'grindable' thermocouples exposed at the workpiece surface. The temperature measurement technique was implemented on an Abwood 5025 surface grinding machine. A schematic representation of the measuring system is shown in Figure 5.1. The workpiece was located on a jig containing an amplifier circuit. The jig was rigidly attached to a calibrated load sensor. The grinding wheel dimensions and rotational speed were measured using a tachometer. The surface temperature and grinding forces were recorded as the workpiece passed under the grinding wheel. The grinding power was computed from the product of the tangential force and the grinding wheel speed. The workpiece speed was obtained by timing the normal force signal which was data logged to a PC. The contact length was computed from the product of the workpiece speed and a contact time taken from the measured temperature distribution. The real depth of cut was measured by comparing measurements on a reference surface and the test surface before and after grinding using a mechanical gauge mounted on the wheel head.

Photographs of the measuring apparatus and instrumentation are given in Plates 1 to 3.

5.2 Workpiece surface temperature measurement

Direct measurement of surface temperature was made using thermocouples exposed at the workpiece surface. In this manner a grindable transducer was created which recorded the temperature signal at the workpiece surface. Two types of grindable thermocouple were used to measure the workpiece surface temperature, a standard thermocouple and a single pole thermocouple. The standard thermocouple and the single pole thermocouple sensor were incorporated in the same workpiece.

5.2.1 The standard thermocouple

The standard thermocouple is a smaller version of the technique described by Nee [47] where two insulated electrodes were housed in a split workpiece. A flattened wire thermocouple was used in Nee's investigation of temperatures in dry grinding. The measuring junction size, 0.46mm, was relatively large compared to the grinding wheel-workpiece contact length. The contact length in fine grinding is of comparable dimensions. The advantage of the standard thermocouple method is that standard calibration data can be applied to the voltage output of the thermocouple [47].

In this investigation a commercially available standard type K foil thermocouple (RS 256-130) was used. The use of a foil thermocouple allowed the thickness of the measuring junction to be minimised. The foil thermocouple technique was previously used to determine the wheel-workpiece contact length in grinding by Qi [48]. A type K thermocouple consists of chromel and alumel measuring poles and has a measuring range between 0deg.C to 1400deg.C. The dimensions of the foil thermocouple are given in Figure 5.2. The foil was measured and found to have a thickness of between 5-10 μm. The foil thermocouple was split into two halves at the junction. The poles of the thermocouple were then sandwiched between layers of mica insulation as shown in Figure 5.3. Each member of the measuring junction was smeared with a thin layer of polyurethane strain gauge adhesive before assembly. The junction was then clamped between the two parts of the split workpiece. A slot was pre-machined in the workpiece to facilitate the assembly of the thermocouple-mica sandwich and allow the workpiece faces to be accurately butted together. Figure 5.4 shows a plan view of the measuring junction after assembly and the thickness of the junction after assembly was 90 μm. A signal from the standard thermocouple was obtained by a single pass of the grinding wheel over the workpiece. As the grinding wheel passes the measuring junction the insulated thermocouple poles are connected by plastic deformation of the workpiece material in the grinding zone.

5.2.2 The single pole-workpiece thermocouple

To reduce the measuring junction size further and potentially improve the signal quality a non-standard single pole configuration was adopted. The junction is formed between the single pole and the workpiece. The configuration of the single pole thermocouple sensor is shown in Figure 5.5. The chromel (positive) thermocouple pole was used. Compared with the standard thermocouple the measuring junction was reduced by one thermocouple pole, two layers of insulation and two layers of adhesive. After assembly the insulation between the thermocouple pole and the workpiece was checked by a multi-meter to ensure there was no short circuit between the chromel foil and the workpiece. The chromel-workpiece thermocouple was assembled to a thickness of approximately 25μm. A photograph of the measuring junction after assembly is shown in Figure 5.6.

Both the standard thermocouple and the single pole transducer were housed at the same joint in a specially designed workpiece, Figure 5.7. Engineering drawings for the temperature measurement workpiece and amplifier jig are given in Appendix 4.

The life of the temperature measuring system was determined by the usable length of the thermocouple. The foil thermocouple used had approximately 6mm of measuring length with an average depth of cut of 30 μm. Approximately 200 trials were obtained.

5.2.3 Assembly of temperature measurement workpiece

The thickness of the pre-machined slot in the workpiece is critical to the success of the assembly operation. This is of particular importance in the case of the standard thermocouple configuration. Once assembled the thermocouple should just fit inside the slot. If the standard thermocouple assembly is larger than the machined slot size the clamping operation slides the two thermocouple poles between the mica. The thermocouples poles then no longer directly face each

other. In the case of the single pole thermocouple sensor there was no precise positioning to preserve and assembly was therefore achieved more easily. It was found that the minimum thickness of mica that could be cut from a 200μm sheet using a scalpel was 10μm. Further decreases in insulation size resulted in fracture of the mica during the clamping operation. For these reasons the measuring junctions assembled are considered to be close to their optimum size.

5.2.4 Signal conditioning and data logging

The nominal output of a type K thermocouple is 4mV per 100deg.C rise above 0deg.C [49]. Vibration and noise from the grinding machine added a high noise level to the thermocouple signal. To minimise noise on the signal the output of the thermocouple was interfaced to an amplifier located in a jig underneath the workpiece as shown in Plate 1.

The output from the thermocouple was amplified using a commercial thermocouple amplifier AD595 manufactured by Analog Devices (RS 301-779). The AD595 is a 14 pin monolithic chip which when used with a type K thermocouple produces an output of 10mV/deg.C. The measuring range of the chip is 0deg.C up to 1100deg.C. The AD595 chip also performs ice point compensation. The chip adds a level to the thermocouple voltage which is in direct proportion to the potential difference which exists between the 0deg.C and the chip temperature. The chip has negligible self-heating characteristics. The circuit diagram of the AD595 is given in Figure 5.8. The amplifier was housed in a rectangular slot machined in the jig. The slot was sealed with epoxy resin (RS 561-628) to protect the amplifier circuit from coolant. The entry and exit points of the thermocouple cables in the workpiece and amplifier were sealed with non-corrosive silicone rubber (RS 494-118) to keep out the coolant.

The output of the chromel-workpiece thermocouple was interfaced to an AD595 amplifier as used with the standard thermocouple. The output signal of the amplifier used with the single pole thermocouple required calibration.

No filter was applied to the output of the amplifiers. The data was captured using a 2 channel Tektronix 2211 digital storage oscilloscope. The accuracy in the range used was better than 3%. The oscilloscope stores 400 samples on each channel. The data logging frequency was typically 80kHz. The data stored on the oscilloscope was downloaded to an OPUS 238 personal computer using the IBM serial communication protocol 'COM1'.

Due to the short duration of the signal (typically 10-20ms) a trigger was used from the thermocouple signal to initiate data logging. Electrical noise from the table feed switch was found to give a large 'spike' of up to 1V on the thermocouple signal. This resulted in false triggering. A resistance (100Ω) - capacitance (9μF) series circuit connected across the switch terminal solved this problem. The single pole thermocouple sensor provided a reliable trigger mechanism. The trigger level was set between 0.4-0.7V.

5.2.5 Examples of measured temperature distributions

A signal from each thermocouple was recorded simultaneously during a single pass of the workpiece under the grinding wheel.

An example of the signal output from the standard thermocouple in dry grinding is given in Figure 5.9. The signal is seen to rise to a maximum temperature and gradually decay. The spikes on the signal were not attributed to noise. The signal was interpreted by comparing it to the idealised temperature distribution shown in Figure 3.4. The measured signal is also seen to exhibit spike temperatures on the base background temperature. The spike temperatures on the signal do not reach their maximum value due to the response time of the transducer.

The repeatability of the measurement was testing by repeating nominally the same grinding conditions on successive signals. Figure 5.10 shows a signal recorded for

nominally the same grinding conditions as the signal shown in Figure 5.9. The difference between the maximum temperatures is less than 5%.

Several characteristics were noted using the standard thermocouple technique. There was a tendency for the signal level to fall to zero after the maximum temperature as indicated in Figure 5.11. This corresponds to a non-contact condition between the two thermocouple poles. The thermocouple poles are more likely to disconnect as the forces in the grinding zone decrease. The signal was also found to rise to the supply voltage of the amplifier in regions after the maximum temperature as indicated in Figure 5.11. The amplifier was tested with a rheostat to simulate variable contact conditions across the thermocouple pole. It was found that when the resistance between the thermocouple was greater than 1kΩ the output of the amplifier jumped to the supply voltage of 12 V. The tendency for the output signal of the standard thermocouple to rise to high level at the tail end of the signal was therefore attributed to a poor contact condition between the thermocouples. In general, the quality of the signals from the standard thermocouple improved at higher depths of cut. This coincided with higher grinding forces giving increased plastic deformation at the measuring junction.

The presence of grinding fluid had a detrimental effect on the quality of the thermocouple signals [50]. Relatively high quality signals can be obtained in wet grinding using the standard thermocouple as shown in Figure 5.12. However, in general the reliability of the standard thermocouple in wet grinding was poor, particularly for the hardened workpieces M2 and AISI 52100.

The reliability of the single pole thermocouple sensor was found to be of significantly greater quality than the standard grindable thermocouple in both dry and wet grinding. An example of the signal output from the single pole sensor in dry grinding is given in Figure 5.13. The standard thermocouple signal recorded simultaneously is shown in Figure 5.14. An important characteristic of the single pole thermocouple was that the

junction contact between the chromel foil and the workpiece was always maintained. The output of the transducer was therefore only a function of temperature.

In direct surface temperature measurements the presence of grinding fluid is detrimental to the signal quality. Signal quality is improved by decreasing the size of the measuring junction [50]. The presence of grinding fluid has a tendency to degrade the quality of any contact between the workpiece and the thermocouple poles. In the wet grinding tests the signal quality of the standard thermocouple was generally poor. The output from the single pole thermocouple sensor was however found to be of relatively high quality. A typical example of the signal obtained from a wet grinding test for the chromel single pole thermocouple sensor with the hardened AISI 52100 workpiece is given in Figure 5.15. The equivalent standard thermocouple signal recorded simultaneously is shown in Figure 5.16.

5.2.6 Interpretation of the measured temperature distributions

The objective of the temperature measuring system was to measure the workpiece background temperature. A consistent method of interpreting the thermocouple output signal is required to compare the effect of grinding variables on the workpiece surface properties.

The thermocouple signals were interpreted as indicating spikes temperatures above a workpiece background temperature, Figure 5.14. An objective criterion is desirable in order to minimise human error introduced into the measurement. Low pass filters are often used to distinguish a low frequency from a high frequency signal. However, the nature of the signals was un-suitable for processing with a low pass filter. A low pass filter will bias towards the mean of the difference between the maximum value of the spike temperatures and the lower level of the background temperature. A low pass filter will therefore select an artificially high background temperature.

With reference to Figure 5.17 a frequency of approximately 1.5kHz is seen to run through the background temperature distribution. The lower envelope of this frequency corresponded approximately with a lower estimate of the workpiece background temperature. This was a characteristic found in all the measured results. The background temperature distribution was selected by taking the mean through the 1.5kHz waveform. The maximum background temperature was determined by taking the maximum value of the mean line. There is inevitably some degree of subjective error in processing the data in this way. The maximum possible error in the selection of the maximum possible temperature was estimated to be within range of ±10%. This tolerance band is indicated on Figure 5.17.

5.2.7 Calibration of the thermocouples

Calibration of the thermocouples was undertaken by pouring hot water over the measuring junction and recording the thermocouple output voltage. The temperature of the hot water was measured to an accuracy of ±1 deg.C using a RS digital thermometer (RS 610-067). The output from each of the thermocouples was recorded in a Tektronix 2211 digital storage oscilloscope. Calibration was carried out from 20 to 100deg.C in 10deg.C intervals.

The results of the calibration procedure for the standard thermocouple are shown in Figure 5.18. The standard thermocouple was found to correlate well with the measured temperature with a maximum error of ±5%. It was concluded that type K calibration charts could be applied directly to the output of the standard thermocouple configuration as claimed by Nee [47].

The output from the single pole thermocouple was linear over the range 20 to 100deg.C, Figure 5.18. The output from the single pole thermocouple was half the output from the standard thermocouple. The calibrated output of the single pole transducer was

5mV/deg.C. The single pole thermocouple technique was used for the AISI 5100 and M2 workpieces. A further calibration procedure was carried to check the linearity of the single pole thermocouple above 100deg.C. A series of dry grinding tests were conducted which yielded high quality signals from each thermocouple. Calibration of the non-standard thermocouple was obtained in-process by comparing the magnitude of the single pole thermocouple sensor with the calibrated output of the standard thermocouple. By varying the grinding conditions calibration of the single pole thermocouple sensor was achieved over a wide range of temperatures. The calibration data for the chromel-AISI 52100 single pole thermocouple sensor are shown in Figure 5.19.

The calibration taken from the hot water calibration tests was found to fit the results to within ±14% error. Taking into account the subjective error in selecting the maximum temperature values from the recorded signals the result indicates a linear response of the single pole thermocouple at 5mV/deg.C up to 600 deg.C.

5.2.8 Selection of the heat source length

On some of the measured signals the length of the heat source could be estimated directly. For example in Figure 5.14 the heat source could be taken as the end of the workpiece spike temperatures. The length of the heat source was determined as the product of the measured time from the signal and the measured workspeed.

However, in many of the signals the tail part of the distribution was poor due to loss of contact at the measuring junction. Poor contact conditions are more likely to occur at this region of the signal as the local forces in the grinding zone are decreasing.

A feature of the measured signals that could be consistently estimated was the time of the start of the signal to the position of the maximum. This is indicated as 'l_m' in Figure 5.20. In Chapter 4 the theoretical ratio 'r' of the distance of 'lm' of the maximum

temperature to the overall distance 'l_e' was determined for uniform, triangular and square law heat fluxes. The position of the maximum temperature was estimated from the measured temperature distributions and the heat source length evaluated using the theoretical distribution. In this manner the theoretical distributions were correlated with the measured distributions.

The maximum error in selection the position of maximum temperature and hence the contact length was to estimated to be ±15%. This tolerance band is indicated on Figure 5.20.

5.3.9 Thermocouple time constant

The response time of a thermocouple depends on the area of the measuring junction [49]. Lee [15] measured the time constant for a 150μm wire thermocouple to be 2ms. The area of the measuring junction used in this investigation was substantially smaller than the area of the junction in Lee's investigation and therefore the response time of the thermocouples used in this investigation would be expected to be considerably lower than 2ms.

The response time of the transducer was estimated from the measured spike temperatures. A maximum value of the workpiece spike temperature was expected to be of the same order as the melting temperature of the work material. For ferrous materials the melting temperature is around 1500deg.C. The maximum value of temperature reached by the workpiece underneath a grain would occur at the maximum value of the background temperature.

The workpiece spike temperature at the position of the maximum background temperature was estimated from a measured temperature as shown in Figure 5.14. The spike temperature was estimated from Figure 5.14 as approximately 195deg.C. Taking the melting temperature as the maximum workpiece temperature the estimated actual spike

temperature is 1500-495 = 1005deg.C. The thermocouple signal was logged at 80KHz and therefore the thermocouple responded in 12.5μs. The thermocouple was assumed to follow a first order response

$$\theta = \theta_m\left[1 - \exp\left(-\frac{t}{\tau_o}\right)\right] \qquad .. 5.1$$

Taking θ=195deg.C., θ_m=1005deg.C. and t =12.5μs the time constant τ_o of the thermocouple is 58μs. Taking into account the approximate nature of this analysis and at the worst case an order of magnitude error the maximum time constant is approximately 0.58ms. To accurately measure a transient signal the time constant of the transducer should be one fifth of the duration of the signal. A time constant of 0.58ms compares favourably with the time of the measured temperature distributions which is typically 10 to 20ms. No correction factor was therefore applied to the thermocouple signal to take account of the transducer time constant.

5.3 Power measurement

The grinding power was computed from measuring the tangential grinding force and a wheel speed. The workpiece was located on a jig which was rigidly attached to a Kistler AGCH-8408 piezo electric load cell. The charge output of the load cell was converted to voltage using a FLYDE 128CA charge amplifier. The voltage output from the charge amplifiers was datalogged at 200Hz to an OPUS 386 personal computer using a 12bit MetraByte DAS-20 analogue to digital converter card. The calibration of the load sensor is detailed in reference [48]. The raw force data and filtered force data was recorded. A 5Hz resistance-capacitor low pass filter was applied to the force data. An example of a force file is shown in Figure 5.21.

5.4 Estimated error in the measurement of the partition ratio

The partition ratio was evaluated from Equation 4.33

$$R_w = \frac{\pi}{C} b (\kappa\rho c)_w^{1/2} v_w^{1/2} \frac{\theta_m l_e^{1/2}}{Q_t} \quad .. 5.2$$

The absolute error in the measurement of the maximum temperature comes from the accuracy of the temperature calibration, the accuracy of the digital storage oscilloscope used to capture the data and the selection of the position of the maximum temperature from the recorded signal. The combined error in the measurement of the maximum workpiece background temperature was estimated to be ±10%. The error in selection the position of maximum temperature and hence the contact length was estimated to be ±15%. The estimated error in the measured grinding power was ±3%.

Equation 5.2 is in the form

$$\frac{a\, b^n}{c} \quad .. 5.3$$

where $a=\theta_m$, $b=l_e$ and $c=Q_t$.

Let the percentage error in a, b, and c be x, y and z.

Differentiating Equation 5.3 using the product rule

$$d\left(\frac{a\, b^n}{c}\right) = \frac{a}{c}\, db^n + b^n d\left(\frac{a}{c}\right) \quad .. 5.4$$

$$d\left(\frac{a\, b^n}{c}\right) = \frac{a}{c}\, nb^{n-1}\, db + b^n\, d\left(\frac{a}{c}\right) \quad .. 5.5$$

and differentiating $d\left(\frac{a}{c}\right)$

$$d\left(\frac{a}{c}\right) = a\, dc^{-1} + c^{-1}\, da \quad .. 5.6$$

$$d\left(\frac{a}{c}\right) = - ac^{-2}\, dc + c^{-1}\, da \qquad ..5.7$$

Substituting Equation 5.7 into Equation 5.5

$$d\left(\frac{a\, b^n}{c}\right) = \frac{a}{c}\, nb^{n-1}\, db - \left(ac^{-2}\, dc + da\, c^{-1}\right) b^n \qquad .. 5.8$$

If

$$da = x\, a \qquad .. 5.9$$

$$db = x\, b \qquad .. 5.10$$

$$dc = x\, c \qquad .. 5.11$$

Substituting Equation 5.9, 5.10 and 5.11 into Equation 5.8 and dividing by $\frac{a\, b^n}{c}$ gives the percentage error in $\frac{a\, b^n}{c}$ as

$$\Delta = n\, y + x - z \qquad .. 5.12$$

Referring to Equation 5.2, n =0.5, y=15%, x=10% and z=3%. Therefore the estimated maximum error in the measurement of the partition ratio is $10 + 0.5x15 + 3 = 20.5\%$. Assuming the errors to follow a normal distribution the mean error after 'n' experiments is

$$\bar{\varepsilon} = \frac{\sigma}{\sqrt{n}} \qquad .. 5.13$$

Five experiments were conducted for each grinding condition. The mean error in the averaged result is therefore

$$\bar{\varepsilon} = \frac{\pm 20.5\%}{\sqrt{5}} = \pm 9.2\% \qquad .. 5.14$$

5.5 Measurement of the true depth of cut

The true depth of cut in surface grinding can be considerably less than the set value due to deflections in the grinding spindle. The actual depth of cut was measured to an accuracy of ±5% using a comparator [15]. A Mitutoyo 1μm resolution mechanical gauge was used to measure the relative difference in level between the thermocouple junction on the ground workpiece and the level of a reference surface before and after grinding. The actual depth of cut was computed from the difference between the two readings. The measuring scheme is shown in Plate 1.

5.6 Measurement of the workspeed

The normal grinding force was recorded in order to accurately measure the workspeed. An example of the recorded force signal is shown in Figure 5.21. The length of the workpiece was 100mm and for the case shown the measured contact time was 0.2s. The workpiece speed was therefore 0.2m/s.

5.7 Inspection of the workpiece thermal damage

The onset of temper colours on the workpiece surface was investigated by correlating the measured maximum background temperature with visible burn on the workpiece surface. A seven point scale given in Table 5.1 was used to characterise the visible burn.

Scale	Description	Temper colour
0	no burn	none
1	margin	slight straw discoloration
2	light	straw
3	light/medium	straw/bronze
4	medium	bronze
5	medium/heavy	bronze/blue
6	heavy	blue

Table 5.1 : Scale used to characterise visible burn on the workpiece surface

The nature of the thermal damage to the workpiece was investigated using the standard metallographic etching technique on polished specimens. The specimens were polished in the plane perpendicular to the grinding direction. The specimens were prepared using abrasive papers : 200, 400, 600 and 1000 grit and successive polishing using 6μm and 1μm diamond pastes. A 2% nital etchant for 30 seconds revealed the grain structure of the workpieces. The nital etch gave valuable information regarding the phase changes and tempering of the workpiece. However quantitative data was not obtained for the sub-surface hardness distribution.

The hardness distribution immediately below the surface was measured on taper sections. The taper section technique is illustrated in Figure 5.22. The mechanical magnification is given by the cosecant of the taper angle. The recommended taper angle using this technique is 6 degrees which gives a tenfold mechanical magnification [51]. A nominal 6

degree angle was ground on the reverse face of the sample. The actual angle was measured using a Rank Taylor Hobson Form Talysurf-120 and varied between 5.6 to 6.4 degrees. The specimen was mounted in a mixture of bakelite and edge retention compound. A ratio of 5:1 bakelite to edge retention compound gave satisfactory edge retention on the specimen. The taper section specimens were prepared down to a 6μm diamond paste polish.

Hardness indentations were made on the taper sections using a Leitz miniload micro-hardness tester. The Leitz miniload micro-hardness tester is shown in Plate 4. The miniload hardness tester is a micro version of the standard Vickers hardness testing machine. On a miniload hardness tester the sample can be moved throughout the measuring stage at 25μm intervals which compares to millimetres on a standard Vickers hardness tester. An example of the indentations on a taper specimen is shown in Figure 5.23

Indentations were made with a selected load, P, and the diagonals of the indented pyramid were measured using an optical micrometer. The diagonals were measured to an accuracy of ±0.1μm.

A 500g load was used for the hardened materials M2 and AISI 52100. A 100g load was used for the medium carbon steel AISI 1055. The typical size of a diagonal of the intended pyramid was 20μm. The micro-hardness testing technique was found to be unsuitable for cast iron as the size of the indentations were of comparable size to the cementite particles in microstructure.

The microhardness in units of kg/mm^2 was calculated by the formula [52]

$$H_v = \frac{1854\ P}{d^2} \qquad .. 5.15$$

where P is the load in grammes and d is the mean of the measured diagonals in microns.

The hardness tester was supplied with a calibration specimen. The measured hardness of the calibration block was within 8% of the calibrated hardness. The apparatus was re-calibrated before each specimen was tested.

The use of the taper section technique together with the micro-hardness tester allowed the hardness to be measured at 5μm intervals below the sub-surface.

The sub-surface hardness distributions were measured with no visible burn, light straw and blue temper colours.

5.8 Measurement of the effective grain contact radius

An Olympus BHM optical microscope was mounted over the grinding wheel to estimate the grain contact area. The machine guard was modified to accommodate the mounting of the microscope. The microscope mounted over the grinding wheel is shown in Plate 5. Photographs of the wheel surface were taken at random locations around the wheel periphery. The large depth of field of the grinding wheel surface gave focus problems and the maximum magnification was restricted to 200. The photographs were calibrated using a 10μm stage micrometer. The wear flat area of individual grains was estimated from the photographs and the effective contact radius evaluated. The effective contact radius was measured for both the alumina grinding wheels and the CBN grinding wheel. Measurements of the grain contact area were taken after the grinding wheels were stabilised as described in Section 5.9.4.

The shape of the alumina and CBN grain were found to differ considerably in appearance. A low magnification photograph of the surface of the alumina wheel 19A60K7V is shown in Figure 5.24. This photograph was taken after a long period of grinding and hence high wheel wear in order to make the wear flats more easily

distinguishable. The grain wear flats are clearly visible appear as light areas running across ridges on the surface of the grains. Higher magnification photographs of wear flat on the A200 alumina wheel are shown Figures 5.25 and 5.26. The average value of wear flat was 25μm for the 19A60K7V alumina wheel and 15μm for A200 alumina wheel. These are approximate average values since a range of wear flat radii were found. These average wear flat dimensions compare to a nominal grit diameter of 250μm for the 19A60K7V alumina wheel and a nominal grit diameter of 90μm for the A200 alumina wheel. The shape of the CBN grains were found to be more geometrical in appearance, Figures 5.27 to 5.30. A range of wear radii from 5 to 30μm were measured for the CBN wheel. The average value of wear flat was 15μm for the CBN wheel which compares to a nominal grain diameter of 90μm.

5.9 Experimental conditions

5.9.1 Machine details

The experimentation was undertaken on an Abwood 5025 surface grinding machine. The grinding spindle was powered by a 3kW ac motor with a fixed spindle speed of 3400rpm. The minimum table speed was 0.025m/s and the maximum table speed was 0.37m/s. The coolant used was TRIM VHPE200 synthetic coolant at 2% dilution in water.

5.9.2 Workpiece materials

Four materials cast iron, 0.55% medium carbon steel (AISI 1055/En9), M2 tool steel and a bearing steel (AISI 52100/En31) were used in the investigation. Both cast iron and medium carbon steel have wide general engineering application. M2 is a widely used tool material. The hardened bearing steel AISI 52100 is widely used in the lightly tempered condition for parts requiring high surface hardness and wear resistance. The range of

materials selected was expected to give a range of specific energies which allow the partition ratio to be measured under widely different energy conditions.

The grinding length was 100mm and the grinding width was 15mm.

Details of the work materials are given below in Tables 5.2 and 5.5. AISI 1055 was used in the normalised condition. The heat treatment details of M2 and AISI 52100 are given in Table 5.5.

Material	Composition		
Cast iron (260)	3% C	2.2% Si	
AISI 1055	0.55% C	0.55% Mn	
M2	5% Mo,	6% W	2% V
AISI 52100	1% C	1% Cr	

Table 5.2 : Composition of materials

Material	BS970 En Series	BS970 Revised	DIN
Cast iron (260)	-	-	-
AISI 1055	En 9	070M55	1.7222
M2	-	-	1.3343
AISI 52100	En 31	534A99	1.3505

Table 5.3 : Related specifications

Material	Hv kg/mm^2	E GPa	κ W/mK	ρ Kg/m^3	c J/kgK	ref
Cast iron (260)	210	128	53.7	7300	511	53
AISI 1055	216	208	42.6.	7840	477	54
M2	810	270	23.5	7860	515	55
AISI 52100	650	221	34.3	7815	506	54

Table 5.4 : Mechanical and thermal properties

	Harden	Quench	Temper
M2	850 deg.C. for 30 mins 1220 deg.C. for 10 mins	oil	Double temper 550deg.C for 2hrs
AISI 52100	840 deg.C. for 80 mins	oil	150deg.C for 2hrs

Table 5.5 : Heat treatment details for M2 and AISI 52100

5.9.3 Grinding wheels

Two alumina grinding wheels and a CBN wheel were used in the investigation. The details of the grinding wheels are given in Table 5.6. The alumina wheel A200 was specially manufactured by an industrial collaborator to have nominally the same bond and porosity and grain size as the CBN wheel.

Grade	Outside Dia	Inside Dia.	Width
19A60L7V	170mm	30mm	20mm
A200	174mm	30mm	17mm
B91ABN200	174mm	30mm	17mm

Table 5.6 : Specification of the grinding wheels

5.9.4 Grinding wheel dressing conditions

The alumina wheels were dressed with a single point diamond dresser. 10 passes were taken across the wheel at an increment of 20μm with a 200μm/rev lead. The grinding power after the dressing operation was found to decrease with the number of passes as shown in Figure 5.30. Results were taken after the power level had reached a relatively stable level.

The CBN wheel was dressed with Norton Model 2 manual brake dresser. The dressing tool was an 80mm diameter by 13 mm wide diamond wheel. Five passes were taken across the wheel at an increment of 2μm at traverse rate of 5mm/s. The brake dressing of the CBN wheel is shown in Plate 6. Results were taken after the wheel was stabilised.

5.9.5 Range of grinding conditions investigated

The nominal grinding wheel speed was 30m/s.
The workspeed range investigated was 0.1, 0.17, 0.2, 0.25 and 0.3 m/s.
Dry and wet grinding trials were undertaken.

The workpiece-wheel combinations together with the range of grinding conditions investigated is given in Table 5.7.

Material	Wheel	Condition	Workspeed	Depth of cut
Cast Iron	19A60K7V	wet	0.1m/s	0-40μm
Cast Iron	19A60K7V	wet	0.3m/s	0-40μm
AISI 1055	19A60K7V	dry	0.1m/s	0-35μm
AISI 1055	CBN	dry	0.1m/s	0-30μm
AISI 1055	19A60K7V	wet	0.1m/s	0-50μm [1]
AISI 52100	A200	wet	0.3m/s	0-12μm
AISI 52100	A200	dry	0.3m/s	0-8μm
AISI 52100	A200	dry	0.2m/s	0-12μm [1]
AISI 52100	CBN	wet	0.3m/s	0-14μm
AISI 52100	CBN	dry	0.3m/s	0-8μm
AISI 52100	CBN	wet	0.2m/s	0-20μm [1]
AISI 52100	CBN	dry	0.2m/s	0-16μm
M2 tool steel				
M2	A200	wet	0.25m/s	0-7μm
M2	A200	dry	0.25m/s	0-8μm
M2	CBN	wet	0.25m/s	0-13μm
M2	CBN	dry	0.25m/s	0-25μm

Table 5.7 : Workpiece-wheel combinations and range of grinding conditions

[1] Results are not presented for these set of trials due to poor quality thermocouple signals.

5.9.6 Experimental Procedure

Three to seven trials were carried out for each test point depending on the repeatability and reliability of the trials for a set workspeed. The average number of trials undertaken for a given set depth of cut was five. The mean value for the real depth of cut, the

grinding forces, maximum background temperature and position of the maximum temperature were computed. To minimise the effect of systematic error in the results the values of depth of cut were selected in randomised order for a given workspeed.

The experimental procedure was as follows

(i) The workpiece speed was set using the normal force signal.

(ii) The grinding wheel was dressed and stabilised.

(iii) The difference in level between the test surface and the reference surface was measured on the workpiece using the mechanical comparator.

(iv) The set depth of cut was programmed on the machine tool.

(v) The trigger level for capturing the temperature signals was set to between 0.4-0.7V using the single pole thermocouple.

(vi) The grinding operation was initiated. The force signals were data logged to a PC and the temperature data were captured on the digital storage oscilloscope.

(vii) The temperature data were downloaded to the personal computer using the serial communications port.

(viii) The difference in level between the test surface and the reference surface was measured on the workpiece using the mechanical comparator.

6.1 Comparison of partition ratios for alumina and CBN grinding

6.1.1 Wet grinding of AISI 52100 at 0.3m/s

Comparisons were made grinding AISI 52100 steel with the A200 alumina wheel and the CBN wheel. The alumina wheel used in these tests was specially manufactured to have nominally the same grit size and bond structure as the CBN wheel.

The tangential forces in wet grinding with alumina and with CBN are compared in Figure 6.1. The tangential force increases almost linearly with the depth of cut. Extrapolating the experimental results in Figure 6.1 a value of tangential force was found at zero depth of cut. At zero depth of cut there is no material removed. The intercept value of tangential force at zero depth of cut indicates the presence of sliding energy in the grinding process. The forces with the alumina wheel are lower than the forces with the CBN wheel. The lower forces with the alumina wheel indicates that the alumina wheel was grinding more efficiently than the CBN wheel.

Specific energy is a fundamental parameter for characterising the grinding process. The specific energy is related to the grinding power and the removal rate by

$$e_c = \frac{P}{av_w b} \qquad .. 6.1$$

The specific energies reflect the greater suitability of the alumina wheel for the AISI 52100 steel, Figure 6.2. The specific energy for the alumina wheel is almost half the specific energy for the CBN wheel. Despite the higher specific energy levels for the CBN wheel, the temperatures for the CBN and alumina wheels were similar, Figure 6.3. These results strongly indicate that an increased proportion of the total grinding energy is conducted into the wheel with CBN grinding compared to grinding with alumina.

To evaluate the partition ratio a heat flux distribution must be assumed. It will be shown that the assumption of the heat flux distribution determines the contact length. Uniform, triangular and square law heat flux distributions were investigated. The theoretical temperature distributions for these cases were solved in Chapter 4.

A measured temperature distribution for the AISI 52100 steel is given in Figure 6.4. The geometric contact length, lg, is plotted on the time axis. It is clear that there is significant cutting activity well beyond the geometric contact length. The real contact length was estimated from the measured temperature distribution as shown in Figure 6.5. For the example shown the real contact length, l_{est}, was estimated to be 2.1 times the geometric contact length. The value of l_{est} is based on the length over which there is clear evidence of frequent grain contacts.

Theoretical temperature distributions were correlated to the measured temperature distribution by matching the magnitude of the maximum temperature and matching the estimated contact length. The temperature distribution for the uniform heat flux is matched to the measured temperature distribution in Figure 6.6. It is seen that the position of the maximum temperature distribution is too far to the right of the measured position and gives a very poor representation of the measured distribution. The triangular heat flux distribution is matched to the measured temperature distribution in Figure 6.7. The position of the maximum temperature falls slightly to the right of the measured position of the maximum temperature. However, the triangular heat flux gives a much improved fit than the uniform heat flux case. The cooling of the theoretical distribution is slower than the measured distribution which would be expected since the theoretical curve was calculated with adiabatic heat transfer at the surface and therefore indicates the slowest possible cooling. The square law heat flux distribution is matched to the measured temperature distribution in Figure 6.8. The position of the maximum temperature falls to the left of the measured position of the maximum temperature. Furthermore, the cooling on the theoretical distribution is faster than the measured cooling

rate. The theoretical curve assumes no convection at the surface whereas in the measurement there will be some convection at the surface. It is implausible for the theoretical distribution to cool faster than the measured distribution. It was concluded that the triangular distribution gives the best comparison between theory and experiment.

In many of the signals the tail part of the measured temperature distribution was poor, Figure 5.20, due to loss of contact of the thermocouple poles and the length of the heat source could not be estimated directly. The contact length was determined by estimating the distance to the position of maximum temperature, l_m, and using the theoretical ratio 'r' of l_m/l_e evaluated in Chapter 4. The distance to the position of the maximum temperature, l_m, is shown in Figure 6.9. From Chapter 4 the theoretical ratio 'r' is 1 for the uniform heat flux, 1.9 for the triangular heat flux and 2.8 for the square law heat flux. The length of heat transfer using this technique is shown in Figure 6.9. The assumption of a uniform heat flux gives approximately $l_e = l_g$. The triangular distribution slightly under estimates the contact length. The square law heat flux over estimates the contact length. From Section 4.4 the partition ratio is directly proportional to the square of the contact length. Therefore the assumption of a uniform heat flux gives the lowest value of partition ratio and the assumption of the square law heat flux gives the highest value of partition ratio for a given measured temperature and specific energy.

In Chapter 3 it was proposed to use the contact length model of Rowe and Qi [39] to determined the length of the heat source

$$l_e = \sqrt{8\, R_r^2 \frac{F_n}{b} (K_s + K_w)\, d_s + a d_s} \qquad .. 6.2$$

where

$$K_s = \frac{1 - \upsilon_s^2}{\pi\, E_s} \qquad .. 6.3$$

and

$$K_w = \frac{1 - \upsilon_w^2}{\pi E_w} \qquad .. 6.4$$

The contact length model requires a roughness parameter, Rr, which characterises the topography of the grinding wheel. The roughness parameter was estimated by correlating Equation 6.2 with the measured contact lengths and the grinding conditions. The parameters given in Table 6.1 were used to determine the roughness parameter from Equation 6.2. for the temperature distribution shown in Figure 6.4.

a = 7.75μm	ds = 174mm	Fn = 184N
vs = 30m/s	b = 0.015m	
Ew = 221GPa	Es = 51GPa	
νw = 0.3	νs = 0.3	

Table 6.1 : Parameters used to determine the roughness factor

The roughness parameters evaluated are given in Table 6.2

Assumption	Rr
Estimated contact length	6.05
Uniform heat flux	0
Triangular heat flux	5.16
Square law heat flux	8.5

Table 6.2 : Roughness parameters

The partition ratios for the alumina and the CBN wheel are compared in Figure 6.10 for the uniform heat flux assumption. The partition ratio was found to marginally increase with depth of cut. The average value of the partition ratio was 0.24 for CBN and 0.53 for alumina. However, given the finding that l_e is greater than l_g it is considered that these values are lower than the real values.

The partition ratios for the alumina and CBN wheel are compared in Figure 6.11 for the triangular and square law heat flux assumption. In these cases the partition ratio reduces with the depth of cut. The partition ratios with the CBN wheel were substantially lower than the partition ratios for the alumina wheel. The partition ratios evaluated with the triangular and square law heat flux were higher than the partition ratios evaluated with the uniform heat flux. It is considered that more reliance can be given to the average values obtained for the triangular heat flux distribution of Rw ≈ 0.4 for CBN and 0.78 for alumina.

Values of the energy partitioning between the workpiece and grinding wheel can be determined from Equation 3.11

$$R_{ws} = \frac{R_w}{\left(1 - \frac{6}{e_c}\right)} \qquad .. 6.5$$

Values of the energy partitioning between the workpiece and wheel are compared in Figures 6.12 and 6.13. When a uniform heat flux is assumed the energy partitioning between the workpiece and wheel, Figure 6.12, increases more with the depth of cut than the overall partition ratio, Figure 6.10. This is the opposite to the trend for the triangular and square law, Figure 6.13. The energy partitioning between the workpiece and wheel for the alumina wheel are substantially higher than the overall partition ratio evaluated for the alumina wheel due to the lower specific energy in the alumina grinding of AISI 52100. The values for the square law heat flux distribution when grinding with alumina are above 100% at small depth of cut. These implausible values raise questions of the validity of the square law assumption. The high values of R_{ws} could also mean that the

assumed values of chip energy were too large. However, it was considered that the triangular distribution gives the best match for reasons previously explained.

The prediction of the partition requires accurate measurements of the grain thermal conductivity which has caused problems for CBN. Measurement of the thermal conductivity of CBN is inhibited by the small size of specimens that can be synthesised. It will be shown that previous researchers have grossly overestimated the capacity of the CBN grinding wheel as a heat sink.

An estimate of the appropriate value of thermal conductivity of the CBN grain was made by correlating the grain contact analysis with the experimental values. The experimental values based on the triangular heat flux were used since this gave the best agreement between theory and experiment. A wear flat radius of 15μm was used which was an average measured value. The effective grain thermal conductivity was obtained by extrapolating the partition ratio results for the triangular distribution to zero depth of cut. At zero depth of cut the energy transmitted to the chips is zero. The partition ratio was taken as 42% for CBN and 84% for alumina. The thermal conductivity evaluated was 290W/mK for CBN and 36W/mK for alumina. The effective thermal conductivity of alumina lies within the reported range in literature of 15-55W/mK giving confidence in this technique. The effective thermal conductivity of CBN is considerably lower than the reported theoretical value. It will be shown that the evaluation of the effective thermal conductivity of the abrasive gives improved prediction of the partition ratio and grinding temperatures.

The maximum background temperature can be predicted by the theory of moving heat sources together with the measured specific energy and grinding parameters. For a triangular heat flux distribution

$$\theta_m = 1.06 \frac{R_w e_c a}{(\kappa \rho c)_w^{1/2}} \left(\frac{v_w}{l_e}\right)^{1/2} \qquad .. 6.6$$

The length of the heat source can be predicted from Equation 6.2. The energy partitioning between the workpiece and wheel is calculated from the grain contact analysis

$$R_{ws} = \left[1 + \frac{0.974\ \kappa_g}{(\kappa\rho c)_w^{1/2}\ r_0^{1/2}\ v_s^{1/2}}\ \frac{1}{\Phi(\tau)}\right]^{-1} \qquad .. 6.7$$

where $\Phi(\tau) = 1$ for steady state heat transfer.

Taking into account energy transference to the chips, the partition ratio is

$$R_w = R_{ws}\ \frac{6}{e_c} \qquad .. 6.8$$

The predicted partition ratios are compared with the measured partition ratios in Figure 6.14. The predicted partition ratios for alumina are slightly lower than the measured values. The predicted values are also relatively insensitive to the depth of cut whereas the measured values reduce with depth of cut. For CBN it was found that using the theoretical thermal conductivity of 1300W/mK under estimates the partition ratio by more than half the actual values. Good agreement between theory and experiment was obtained using the effective value of thermal conductivity of CBN. There is a smaller difference between the transient and steady state solutions for CBN. This is because the value of the dimensionless time is much greater than in the case of alumina due to the higher effective thermal conductivity of CBN. Most researchers have used the theoretical value of the thermal conductivity of 1300W/mK given by GE [28]. These results show that using the theoretical thermal conductivity of CBN for the prediction of partition ratios and grinding temperatures was to grossly over estimate the heat conduction into the grinding wheel.

The predicted temperature is compared to the measured temperature in Figure 6.15 for the alumina wheel. Good agreement was observed between the theoretical and measured temperatures. At high depth of cut the predicted temperature is lower than the measured temperature. From the temperature equation, Equation 6.6, this may be due to under

estimating the partition ratio or over estimating the contact length. However, since the predicted partition ratios were higher than the measured partition ratios at high depth of cut this was attributed to over estimating the contact length. The predicted temperature is compared to the measured temperature for CBN in Figure 6.16 using the effective and theoretical values of thermal conductivity. Using the theoretical grain conductivity in the calculation grossly under estimates the measured temperature. Improved prediction is obtained using the effective thermal conductivity value of CBN. The temperature prediction is within the estimated scatter of the measurements.

6.1.2 Dry grinding AISI 1055 with the alumina and CBN wheel at 0.1m/s

Values of the partition ratio were measured when grinding medium carbon steel AISI 1055 with alumina and CBN wheels. Experiments were carried out in dry grinding of AISI 1055 with the alumina wheel 19A60L7V and the CBN wheel B91ABN200 at a workspeed of 0.1m/s .

The tangential forces using the alumina wheel and the CBN wheel are compared in Figure 6.17. The tangential forces were higher in dry grinding of AISI 1055 with the CBN wheel than dry grinding of AISI 1055 with the alumina wheel. The specific energies for the alumina and the CBN wheels are compared in Figure 6.18. The improved performance of the alumina grinding is characterised by a lower specific energy. These results show that CBN wheels do not always grind with a lower specific energy than alumina wheels. The specific energy depends on the suitability of the grade of the grinding wheel to the workpiece material and also the dressing conditions.

The maximum background temperatures for the alumina wheel and the CBN wheel are compared in Figure 6.19. Despite the significantly higher specific energy when grinding with the CBN wheel compared to grinding with the alumina wheel, the temperatures were similar for both wheels indicating that an increased proportion of the total grinding energy is conducted into the wheel with CBN grinding compared to grinding with alumina.

The partition ratios assuming a uniform heat flux for the alumina wheel and the CBN wheel are compared in Figure 6.20. When a uniform heat flux is assumed the partition ratio is relatively constant with the depth of cut. The partition ratios evaluated with a triangular and square law heat flux are shown in Figure 6.21. The partition ratios reduce with the depth off cut. This suggests that the variation with depth of cut may be a contact length effect. The partition ratio with the CBN wheel is substantially lower than the partition ratio evaluated with the alumina wheel. The partition ratio depends on the assumed heat flux distribution. Assuming a triangular heat flux, the average partition ratio is approximately 0.42 for the CBN wheel and approximately 0.68 for the alumina wheel. Values of energy partitioning between the workpiece and wheel are given in Figures 6.22 and 6.23. For the uniform heat flux the values of the energy partitioning between the workpiece and wheel increase more with the depth of cut than the overall partition ratio. For the triangular and square law heat flux the energy partitioning between the workpiece and wheel is less sensitive to the depth of cut than the overall partition ratio. The energy partition ratios between the workpiece and wheel were substantially lower when grinding CBN than grinding with the alumina wheel. A greater increase in the partitioning between the workpiece and wheel compared to the overall partition ratio is apparent for grinding with the alumina wheel due to the lower specific energies.

The effective thermal conductivity of the abrasives are determined by correlating the grain contact analysis with the measured values of partition ratio. The measured values taken at zero depth of cut were 74% for the alumina wheel and 43% for the CBN wheel. The average measured wear flat radii were approximately 25μm for the alumina wheel and 15μm for the CBN wheel. The effective thermal conductivity was evaluated to be

54W/mK for the alumina wheel and 325W/mK for the CBN wheel. The predicted partition ratios are compared to the measured partition ratios assuming a triangular heat flux in Figure 6.24. The predicted partition ratios for the alumina wheel are slightly larger than the measured values at high depth of cut. For the CBN wheel the predicted values of partition ratio give good agreement with the measurements. The partition ratios predicted with the theoretical thermal conductivity of CBN are clearly in error.

The predicted and measured temperatures for the alumina wheel are compared in Figure 6.25. The predicted temperatures are greater than the measured temperatures at high depth of cut. This would be expected since the predicted partition ratios at high depth of cut were larger than the measured values. The steady state solution over estimates the partition ratio by more than the transient solution.

The predicted and measured temperatures for the CBN wheel are compared in Figure 6.26. Good agreement was obtained between the theoretical and measured values through the entire depth of cut range. The steady state solution gave the best agreement with the measurements. Using the theoretical thermal conductivity of CBN grossly under predicts the measured temperatures. The results for AISI 1055 give reasonable agreement with the predicted values. However, when comparing the effective thermal conductivity values of the alumina wheel for the two workpiece materials, there is a large difference. This gives some cause for concern. It might be expected that the thermal conductivity should remain approximately constant. This may be partly due to the extrapolation technique used to estimate the partition ratio at zero depth of cut. A small difference in the extrapolation of the data may change the intercept values by typically ±0.02 on the partition ratio at zero depth of cut. The grain contact partitioning solution is very sensitive to the grain thermal conductivity in the range of thermal conductivity values expected for alumina, Figure 2.17, and a ±0.02 difference gives a ±6W/mK tolerance on the value of the effective thermal conductivity.

6.1.3 Wet grinding of M2 tool steel with alumina and CBN wheels at 0.25m/s

The tangential forces, specific energies and temperatures when grinding with the alumina wheel and grinding with the CBN wheel with coolant are compared in Figures 6.27 to 6.29. The forces, specific energy and temperature are much higher when grinding tool steel with alumina compared to grinding with CBN.

The partition ratios for the alumina and CBN wheel are compared in Figure 6.30 for the uniform heat flux assumption. The partition ratios for the alumina and CBN wheel based on the uniform heat flux are relatively insensitive with the depth of cut. The partition ratios increase for the triangular and square law heat flux assumptions compared with the uniform heat flux assumption, Figure 6.31. This is because the measured values of contact length were larger than the value of lg used for the uniform heat flux. Partition ratios with the alumina wheel were found to reduce with the depth of cut. The partition ratios for CBN were lower than the partition ratio for alumina. As with the other workpiece materials tested these results confirm that a higher proportion of the energy is convected by the CBN wheel than the alumina wheel.

Values of the energy partitioning between the workpiece and wheel are compared in Figures 6.32 and 6.33. The results using a uniform heat flux are analysed based on the geometric contact length. It can be seen that the values of the energy partitioning between the workpiece and wheel with alumina are very little larger than the values with CBN. However, this is misleading. It was quite apparent that the real contact length was much greater than the geometric contact length and that as with other materials R_{ws} is much larger with alumina than with CBN as shown in Figure 6.33. These results provide further evidence that the uniform heat flux assumption is unjustified. The values of energy partitioning between the workpiece and wheel show similar variations with depth of cut as the overall partition ratio. The energy partitioning between the workpiece and wheel is substantially lower for the CBN wheel than the alumina wheel.

The effective thermal conductivity was evaluated taking the partition ratio to be 75% for alumina and 45% for CBN at zero depth of cut, Figure 6.31. The average measured wear flat radius was 15μm. The effective thermal conductivity for the alumina grain was 51W/mK and 230W/mk for CBN grain. The value of 51W/mK is somewhat higher than previously evaluated for the same abrasive in the testing of the AISI 52100 workpiece.

The predicted partition and measured partition ratios for the alumina wheel are compared in Figure 6.34. Reasonable agreement was obtained using either the transient solution or the steady state solution. This is also demonstrated by the predicted grinding temperature, Figure 6.35. The predicted and measured partition ratios for the CBN wheel are compared in Figure 6.36. The predicted temperatures give good agreement with the measured values using a roughness factor of 3.5 as shown in Figure 6.37.

6.2 Comparison of partition ratios in dry and wet grinding

6.2.1 Dry and wet grinding M2 tool steel at 0.25m/s with the CBN wheel

The tangential forces in dry and wet grinding M2 with the CBN at a workspeed of 0.25m/s are compared in Figure 6.38. The forces with coolant were significantly lower than in dry grinding. This indicates that the coolant is lubricating the grinding zone and therefore reduces the grinding forces. Values of specific energy in dry and wet grinding with the CBN wheel are compared in Figure 6.39. The specific energy reduces with increasing depth of cut. The specific energy in dry grinding is almost twice the specific energy in wet grinding. Grinding with coolant can therefore substantially improve the efficiency of the grinding process. The maximum background temperatures are compared in Figure 6.40. The temperatures in dry grinding were much higher than the temperatures in wet grinding due to the increased forces in dry grinding.

The partition ratios for the uniform heat flux assumption are insensitive with the depth of cut, Figure 6.41. Similar values of partition ratios were found in both dry and wet grinding. The partition ratios for the triangular heat flux are greater than the partition ratios for the uniform heat flux, Figure 6.42. There is very little difference between the partition ratios in dry and wet grinding with approximately 42% of the total energy entering the workpiece. Values of the energy partitioning between the workpiece and wheel remain approximately constant and indicate that there is negligible difference in the partitioning between the workpiece and wheel in wet and dry grinding, Figure 6.43.

The predicted partition ratios are compared to the measured partition ratios for wet grinding in Figure 6.44. The implications of different assumptions over the heat sinks are shown. Three different sets of assumptions are shown (i) no convection to the chips and fluid (ii) convection to the chips only and (iii) convection to the chips and fluid. Convection to the fluid wheel was estimated using the fluid wheel model [5]

$$e_{cf} = \frac{0.89\ \theta^{*}_{fb}}{a\ v_w} (\kappa \rho c)_f^{1/2} (v_s\ l_e)^{1/2} \qquad .. 6.9$$

Ignoring convection to the chips and coolant over estimates the partition ratio and hence the grinding temperatures, Figure 6.45. Taking into account convection to both the chips and fluid underestimates the partition ratio and hence the grinding temperature. Best correlation was obtained between theory and experiment when only convection to the chips was taken into account.

The predicted partition ratios are compared to the measured partition ratios for dry grinding in Figure 6.46. The partition ratio ignoring the convection to the chips is also shown. For the case of the dry grinding tests the difference in the assumptions is not so significant. This is because the specific energy in dry grinding was approximately twice the specific energy in wet grinding and the proportion of the chip energy to total energy much smaller. Good correlation was found between the predicted and measured temperatures in dry grinding, Figure 6.47.

6.2.2 Dry and wet grinding M2 at 0.25m/s with the alumina wheel

Comparison were also made of dry and wet grinding of M2 with the alumina A200 wheel. The tangential forces in wet grinding were lower than the forces in dry grinding due to the lubrication by the coolant, Figure 6.48. The lubricating action of the coolant is also evident from the specific energies, Figure 6.49, The specific energies in dry grinding are substantially higher than the specific energy in wet grinding. The higher energy in dry grinding gives rise to higher temperatures than in wet grinding, Figure 6.50.

The measured partition ratios based on the triangular heat flux for dry and wet grinding are shown in Figure 6.51. Similar values of partition ratio were found in both dry and wet grinding. Approximately 70% of the total energy enters the workpiece. The effective thermal conductivity was evaluated to be 53W/mK in dry grinding and 51W/mK in wet grinding. Values of the energy partitioning between the workpiece and wheel for dry and wet grinding are shown in Figure 6.52. There is a larger increase in the values of energy partitioning between the workpiece and wheel from the overall partition ratio in wet grinding since the specific energy in wet grinding was lower than the specific energy in dry grinding. Similar values were obtained in both dry and wet grinding and these results further support ignoring fluid in the partitioning model.

The theoretical and measured partition ratios for wet grinding of M2 with alumina are shown in Figure 6.53. Good agreement was obtained using the effective thermal conductivity and convection to the chips. Ignoring convection to the chips slightly over estimates the partition ratios. However, since the specific energies are relatively large compared to the chip energy the difference in the predicted partition ratios ignoring energy to the chips and taking energy to the chips into account is small. Taking into account convection to the fluid leads to serious errors in the prediction of partition ratios. The

partition ratios predicted taking into account convection to the fluid grossly under estimates the measured values. This is particularly significant at low depths of cut. At small depths of cut the energy is lower than at high depths of cut. Also the specific energy convected to the fluid is inversely proportional to the depth of cut. Therefore at small values of depth of cut the specific energy convected to the fluid is large and the grinding energy is at its least. At small values of depth of cut the predicted energy convected to the fluid was of comparable size to the measured values of grinding energy. This is clearly not true. The temperature prediction for the various assumptions over the heat sinks in the grinding zone are compared in Figure 6.54. Good agreement was obtained between theory and experiment taking into account convection to the chips. Ignoring convection to the chips slightly over estimates the grinding temperatures. The prediction taking into account convection to the fluid and chips is in large error. This is particularly apparent at low depths of cut where the predicted temperature is an order of magnitude lower than the measured values.

The predicted partition ratios are compared to the measured partition ratios for the dry grinding of M2 tool steel with an alumina wheel in Figure 6.55. Best agreement between theory and experiment is obtained when convection to the chips is included in the analysis. Ignoring convection to the chips slightly over estimates the partition ratios and hence the grinding temperatures. However there is small difference in the two solutions because the values of the specific energies were high compared to the chip energy, Figure 6.56.

6.2.3 Dry and wet grinding of AISI 52100 at 0.3m/s with the CBN wheel

The tangential forces in dry and wet grinding AISI 52100 with the CBN wheel at 0.3m/s are compared in Figure 6.57. Whereas for the other tests the forces were substantially lower in wet grinding than in dry grinding, the forces in this test for dry and wet grinding were similar. This demonstrates a characteristic of CBN wheels which is that the

condition of the wheel changes over a period of time [2]. Due to the expensive and thin layer of abrasive on the CBN wheel it was not possible to re-dress. Values of specific energy in dry and wet grinding with the CBN wheel are compared in Figure 6.58. The specific energy reduces with the depth of cut. The specific energies in dry grinding are slightly higher than the specific energies in wet grinding. The maximum background temperatures are compared in Figure 6.59. The temperatures in dry grinding were slightly higher than the temperatures in wet grinding.

There is very little difference between the partition ratios based on a triangular heat flux in dry and wet grinding. Approximately 40% of total energy enters the workpiece, Figure 6.60. Values of the energy partitioning between the workpiece and wheel indicates that there is negligible difference in the partitioning in dry and wet grinding, Figure 6.61.

The various assumptions over the heat sinks were investigated. Predicted partition ratios are compared against the measured values for wet grinding in Figure 6.62. As in the previous tests it was found that including convection to the fluid under estimates the partition ratios. Taking into account of convection to the chips gives good agreement with the measured values. Ignoring the chip energy slightly over estimates the partition ratios. As expected the predicted temperatures are lower than the measured temperature when convection to fluid is included in the analysis, Figure 6.63. This is because the partition ratios are too low when convection to the fluid is taken into account. These results confirm that convection to the fluid in the grinding zone is negligible.

For dry grinding tests, the best agreement between theory and experiment was obtained by taking account convection to the chips. Ignoring convection to the chips slightly over estimates the partition ratios, Figure 6.64. There is only a small difference in the solutions because the grinding energy is relatively high compared to the chip energy. The predicted temperatures give good agreement with the measured values throughout the range of depth of cut, Figure 6.65.

6.3 Comparison of partition ratios at different workspeeds

6.3.1 Cast iron workpiece

Grey cast iron workpieces were ground at workspeeds of 0.1 and 0.3m/s with an alumina wheel using coolant.

The relationship between the tangential force and the depth of cut is shown in Figure 6.66. The tangential force increases almost linearly with the depth of cut. This was true for both workspeeds. The tangential forces at the high workspeed was found to be higher than at low the workspeed. The range of depths of cut investigated for the 0.3m/s workspeed was smaller than the range for the 0.1m/s workspeed due to the limitation of the available power from the machine motor. The specific energies for the two workspeeds are compared in Figure 6.67. The specific energy was found to reduce with increasing depth of cut. The specific energy at the 0.1m/s workspeed was lower than the specific energy at the 0.1m/s workspeed due to the higher material removal rate at the higher workspeed. The maximum background temperatures are compared in Figure 6.68. The background temperature increases with depth of cut as expected due to the increased forces. The temperatures at 0.3m/s were only slightly higher than the temperatures at 0.1m/s despite the higher forces at 0.3m/s.

The partition ratios evaluated assuming a triangular heat flux distribution are given in Figure 6.69. The partition ratios evaluated with the triangular heat flux distribution reduce with increasing depth of cut. Similar values of partition ratio were evaluated for both workspeeds. For the triangular heat flux distributions the partition ratios varied between 0.85 at small depth of cut to 0.7 at larger depths of cut. Values of the energy partitioning between the workpiece and wheel were slightly higher at 0.3m/s than 0.1m/s. This is because the specific energies were lower at the 0.3m/s workspeed.

The effective thermal conductivity of the alumina wheel was determined by correlating the grain contact analysis with the measured values of partition ratio. The measured values taken at zero depth of cut were 84% for 0.1m/s workspeed and 86% for the 0.3m/s workspeed. The average measured wear flat radius was approximately 25μm. The effective thermal conductivity was evaluated to be 45W/mK at 0.1m/s workspeed and 41W/mK at 0.3m/s workspeed.

The overall partition ratio and the energy partitioning between the workpiece and wheel were found to be virtually independent of workspeed. For the grain contact analysis the partitioning is independent of workspeed other than the effect of workspeed on the contact length. From the contact length model of Rowe and Qi, Equation 6.2, the higher forces at the higher workspeed give larger values of contact length for a given wheel roughness and depth of cut. This increases the dimensionless time but does not significantly increase the partitioning between the workpiece and wheel. The effect of the workspeed on the partitioning between the workpiece and wheel for CBN would be even less since the values of dimensionless time for CBN are large and the transient function approaches the steady state value of one. The steady state solution is independent of the contact length. The predicted partition ratios from the grain contact analysis and the measured values at 0.1m/s are compared in Figure 6.71. A stronger variation with depth of cut was apparent in the measured data. The predicted and measured temperatures at 0.1m/s workspeed are compared in Figure 6.72. Good agreement was obtained between theory and experiment throughout the range of depths of cut from 2 to 40μm. This is a large range of depth of cut and covers a wide range of grinding conditions. The predicted partition ratios and the measured values at 0.3m/s are compared in Figure 6.73. The predicted partition ratios closely follow the trend of the measured partition ratios. The predicted and measured temperatures at 0.3m/s workspeed are compared in Figure 6.74. The predicted temperatures from the transient and steady state solutions straddle the measured temperatures.

The partition can also be analysed at the wheel contact level [18, 6, 46]

$$R_{ws} = \left[1 + \sqrt{\frac{v_s}{v_w}\frac{(\kappa\rho c)_s}{(\kappa\rho c)_w}}\right]^{-1} \quad .. 6.10$$

For the wheel contact analysis the partition ratio is more sensitive to the workspeed. The difficulty with the wheel contact analysis is the choice of the bulk wheel thermal contact coefficient $(\kappa\rho c)_s^{1/2}$. Rowe and Pettit [18] measured the bulk wheel thermal contact coefficient using steady state measurements on wheel samples. Other researchers estimated the bulk wheel thermal contact coefficient by correlating the grain properties with an area ratio [6] or using a wheel porosity factor [45]. However, the accuracy to which such factors can be theoretically predicted is open to question. The appropriate values for the bulk wheel thermal contact coefficient were determined by correlating the Equation 6.10 to the measured values. The measured values taken at zero depth of cut were 84% for 0.1m/s workspeed and 86% for the 0.3m/s workspeed. The effective thermal contact coefficients $(\kappa\rho c)_s^{1/2}$ were evaluated as $155 J/(s^{1/2}m^2K)$ at 0.1m/s and $230 J/(s^{1/2}m^2K)$ at 0.3m/s. The average value of the effective bulk wheel thermal contact coefficient is $192 J/(s^{1/2}m^2K)$. There is a larger difference in the effective thermal properties evaluated from the wheel contact analysis compared to the effective thermal conductivity values determined from the grain contact analysis. The effective bulk wheel thermal contact coefficients range of 155 to $230 J/(s^{1/2}m^2K)$ are considerably lower than the steady state measured value of $514 J/(s^{1/2}m^2K)$. The predicted partition ratios from the wheel contact analysis and the measured values at 0.1m/s are and 0.3m/s are compared in Figure 6.75 and 6.76. Predictions of partition ratios are shown based on the actual effective thermal contact coefficient, the average thermal contact coefficient and the steady state measured value. Good agreement is obtained using the actual values of bulk wheel thermal contact coefficient and using the average effective value of the bulk wheel thermal contact coefficient. Using the steady state value of $(\kappa\rho c)_s^{1/2} = 514 J/(s^{1/2}m^2K)$ underestimates the partition ratio. The results indicate that the wheel contact analysis can be used to predict the partition when the appropriate wheel thermal properties are employed. However, it is conceptually difficult that the wheel thermal properties should change with the workspeed.

Shaw [6] adopted a wheel contact model and proposed to determine the wheel thermal properties by correlating the grain thermal properties with an area ratio factor, Ar. The models of Rowe and Pettit [18] and Shaw [6] are equivalent when

$$A_r(\kappa\rho c)_g = (\kappa\rho c)_s \qquad .. 6.11$$

The validity of this approach was examined by estimating the area ratio factor from Equation 6.11 by correlating the effective grain properties with effective measured wheel thermal properties. Taking κ_g = 43W/mK, ρ_g = 3910kg/m^3 and c_g = 765J/kgK for the effective grain thermal properties and $(\kappa\rho c)_s^{1/2}$ = 192J/(s$^{1/2}$m^{2}K), the area ratio factor from Equation 6.11 expressed as a percentage is 0.03%. This is two orders of magnitude smaller than measured values of the area ratio of 1 to 5% [9]. The large differences in the area ratio factor questions the validity of Shaw's assumption.

6.3.2 Comparison of dry grinding of AISI 52100 with the CBN wheel at 0.2m/s and 0.3m/s

The tangential forces in wet grinding of AISI 52100 steel with CBN at 0.2m/s and 0.3m/s are compared in Figure 6.77. The forces are higher at the higher workspeed. The specific energies reduced with increasing depth of cut and were similar for both workspeeds, Figure 6.78. The maximum background temperatures are compared in Figure 6.79. The temperatures are slightly higher at the 0.3m/s workspeed. The partition ratios were evaluated assuming a triangular heat flux distribution, Figure 6.80. The partition ratio varied between 0.45 at low depths of cut to 0.4 at larger depths of cut. The partition ratios were only marginally higher at the 0.2m/s workspeed than the partition ratios at the 0.3m/s workspeed. Similar values of the energy partitioning between the workpiece and wheel were obtained, Figure 6.81. It was concluded therefore that the partitioning between the workpiece and wheel is independent of the workspeed.

The effective thermal conductivity of the CBN wheel was determined by correlating the grain contact analysis with the measured values of partition ratio. The measured values taken at zero depth of cut were 46% for 0.2m/s workspeed and 42% for the 0.3m/s workspeed. The average measured wear flat radius was approximately 15μm. The effective thermal conductivity was evaluated to be 274W/mK at 0.1m/s workspeed and 290W/mK at 0.3m/s workspeed. The effective bulk wheel thermal contact coefficient $(\kappa\rho c)_s^{1/2}$ is required for the wheel contact analysis. The effective thermal contact coefficients $(\kappa\rho c)_s^{1/2}$ were evaluated as 1140J/($s^{1/2}m^2K$) at 0.2m/s and 1581J/($s^{1/2}m^2K$) at 0.3m/s. The average value of the effective thermal contact coefficient is 1360J/($s^{1/2}m^2K$). The average bulk wheel thermal contact coefficient for the CBN wheel is 7 times greater than the bulk wheel thermal contact coefficient for the alumina wheel.

The partition ratios and grinding temperatures were predicted using the grain contact analysis and the wheel contact analysis. A comparison of the predicted and measured partition ratios at 0.2m/s workspeed are given in Figure 6.82. The scale of the partition ratio axis ranges from 0 to 0.5. The predicted partition ratios with the grain contact analysis and the wheel contact analysis employing the effective thermal properties are virtually identical. This is also the case for predicted temperatures, Figure 6.83. The partition ratios predicted from the wheel contact analysis employing the average effective thermal contact coefficient under estimates the measured values of partition ratios and temperatures.

The predicted partition ratios and temperatures are compared against the measured values at the 0.3m/s workspeed in Figures 6.84 and 6.85. Using the wheel contact analysis with the average value of wheel thermal contact coefficient gives slightly higher estimates of the partition ratios. This is because the average value of the wheel thermal contact coefficient is lower than the actual value of the wheel thermal contact coefficient . The predicted temperatures give reasonable correlation with the measured values for each of the analyses, Figure 6.85.

These results indicate as was the case for the alumina wheel that accurate predictions of partition ratios can be obtained when the thermal properties of the grinding wheel are taken as a function of workspeed. For both the CBN and alumina wheel the effective thermal contact coefficient of the wheel increases with workspeed. The use of an average value of the bulk wheel thermal contact coefficient gives reasonable accuracy. For the grain contact analysis the effective thermal conductivity of the abrasives and hence the predicted partition ratios were not found to be significantly effected by the workspeed.

The area ratio factor for the CBN wheel was evaluated from Equation 6.11 by correlating the effective grain properties with effective measured wheel thermal properties. Taking κ_g = 282W/mK, ρ_g = 3480kg/m^3 and c_g = 506J/kgK for the effective grain thermal properties and $(\kappa\rho c)_s^{1/2}$ = 1360J/(s$^{1/2}$m^{2}K), the area ratio factor from Equation 6.11 expressed as a percentage is 0.003%. This is an order of magnitude lower than the value evaluated for the alumina wheel and indicates that the CBN wheel was sharper than the alumina wheel. However, as was the case with the alumina wheel these values seem very low.

6.4 Discussion

The measurement of the workpiece temperature during grinding gave the basis for validating the wheel source model proposed by Hahn [8]. The two types of grinding temperatures were experimentally verified. The spike temperatures were shown to superimpose upon a background temperature. The thermocouples did not accurately measure the spike temperatures which last for the order of less than 10μs. The background temperature which lasted for typically 10 to 20ms was measured successfully using grindable thermocouples with an estimated time constant of 0.58ms. The moving wheel source was modelled by the theory of moving heat sources [12]. The theory of moving heat sources was found to give good correlation with the measured background

temperature when consideration was made to the variable heat flux in the grinding zone. The theory of moving heat sources has therefore been experimentally validated for the analysis of background temperatures. Accurate predictions of the background temperatures were obtained by taking into account the energy partitioning in the grinding zone. The heat flux to the workpiece, q_w, was determined from the measured temperature distribution. The total power expressed as a heat flux, q_t, was measured from the product of the measured tangential force and wheel speed divided by the area of contact. In this way the experimental value of the partition ratio, R_w, was evaluated as the ratio of q_w to q_t.

The measured partition ratios were found to be sensitive to the assumed heat flux distribution. The assumed heat flux determines the contact length. The uniform heat flux gave the lowest values of partition ratios and the square law heat flux gave the highest values of partition ratios. The uniform heat flux gave a very poor representation of the measured background temperatures. The square law heat flux gave improved agreement and the triangular heat flux gave the best agreement with the measured signals. The linear increase in heat flux throughout the grinding zone is explained by the increasing forces with the increasing grain depth of cut. The actual length of the heat transfer, le, in grinding was found to be greater than the geometric value, lg. Typically the real contact length was 50% to 250% greater than the geometric value. The greatest increase was found at small depths of cut. The implication of the real contact length being greater than the geometric values was significant for the measurement of the partition ratios and the prediction of grinding temperatures. Assuming the length of the heat source to be equal to the geometric contact length as proposed by Malkin [38] gives lower than the actual values of the measured partition ratio. The real values of partition ratios were typically over 25% greater than the values evaluated using the geometric contact length. Rowe and Qi [39] attributed the increase in contact length due to elastic deformation and the roughness of the grinding wheel. The roughness parameter, Rr, used in the contact length model of Rowe and Qi was evaluated by correlating the model to the measured contact lengths.

The error in assuming the geometric contact length in predicting the partition ratio is not nearly as significant as assuming the geometric contact length in the measured partition ratios. For the theoretical prediction of the partition ratio from the grain contact analysis the use of the geometric contact length gives lower values of dimensionless time, τ

$$\tau = \left(\frac{\alpha_g \, l_e}{r_0^2 \, v_s} \right)^{1/2} \qquad .. \; 6.12$$

and therefore gives lower than the actual values of partition ratio. The partition ratios predicted with the geometric contact length are compared to the predicted value using the real contact length in Figure 6.86. Only a small difference results in using the geometric values. There are computational advantages using the geometric contact length in the analysis as it avoids the use of the contact length model which requires the normal grinding force. The normal force in grinding is difficult to measure directly in production work. For CBN the difference is even smaller as the higher thermal diffusivity makes the dimensionless time large, Figure 6.87. The theoretical values of the energy partitioning between the workpiece and wheel are almost constant with the contact length ratio.

The partition ratios, R_w, and values of the energy partitioning between workpiece and the wheel, R_{ws}, when grinding with CBN were found to be substantially lower than the partition ratios when grinding with alumina. The partition ratios for CBN grinding were typically 0.45 which compares to typically 0.8 for the grinding with alumina. The reduction in partition ratio when grinding with CBN compared to grinding with alumina was attributed to an increased energy being taken away by the wheel in CBN grinding. The results indicate that a major advantage of CBN grinding is the lower partition ratio which can greatly reduce the temperatures experienced by the workpiece. Malkin [2] suggested that the reduced risk of thermal damage with CBN grinding is due to the lower specific energies when grinding with CBN compared to grinding with alumina. However, it was found that CBN wheels do not always grind with lower specific energies than alumina wheels. The specific energy when grinding with CBN was found

to be greater or smaller than when grinding with alumina. The specific energy depends on the wheel-workpiece combination, the dressing conditions and the wear of the grinding wheel. The lower partition ratios in CBN grinding were attributed to the higher thermal conductivity of the CBN abrasive. CBN wheels have been widely reported to have very high thermal conductivity but the conductivity of the wheel has not previously been quantified. The effective thermal conductivity of alumina and CBN were determined by correlating the grain contact analysis to the measured partition ratios. The evaluation of the effective thermal conductivity of the abrasives was a key point for the improved prediction of partition ratios and grinding temperatures.

The grain contact analysis characterises the grain as a plane body subjected to a circular heat source. The actual contact geometry of the grain wear flats was not circular but formed ridges across the grains in case of alumina wheels and were more geometrical in nature for CBN, Figures 5.24 to 5.29. The contact area was found to differ from grain to grain. Due to the widely varying size and shape of contact of the wear flats it was considered reasonable to model the grains by a simple geometrical shape with an effective contact radius. A plane body was chosen to characterise the grain shape. The grains however were not plane bodies but have increasing cross section with depth into the wheel. Lavine [4] modelled the grain as a truncated cone. However it was shown that the conical model of Lavine was inaccurate and could lead to nonsensical results due to a one dimensional heat transfer assumption in the analysis. It was therefore considered important to model two dimensional heat transfer. Ideally a two dimensional conical grain modelled would be used to model the heat transfer in the grain but this case could not be solved analytically. The grain was therefore modelled as a plane body and a classical solution for two dimensional heat transfer in a plane body subjected to a circular heat source was adopted. A two dimensional heat transfer plane body solution will predict lower temperatures than a two dimensional heat transfer conical body solution. The partitioning analysis incorporating a conical grain solution would give higher partition ratios than an analysis based on the plane body grain solution. Therefore the effective thermal conductivity evaluated from the grain contact analysis incorporating the

plane body solution for the grain will evaluate higher thermal values of thermal conductivity than the real values.

For alumina the effective thermal conductivity were evaluated to be 34 to 54W/mK which is in the range of the reported measured values in literature of 15 to 55W/mK. For CBN the effective thermal conductivity was evaluated to be between 230 to 325 W/mK. This range is approximately one fifth of the reported theoretical value of 1300W/mK [28]. The theoretical thermal conductivity of CBN has been used in previous analyses of partition ratio with the exception of Shaw [6] who used a value of 87W/mK which is a measured value on PCBN. Using the theoretical thermal conductivity in the analysis gave errors of over 100% in the prediction of partition ratios. Consequently the predicted grinding temperatures were much lower than the measured values. It is not surprising the actual thermal conductivity of CBN is lower than the theoretical value since in practice the CBN grains contain impurities. An advantage of obtaining the effective thermal properties from the grinding experiments is that the measurements are taken at grinding temperatures. Furthermore, the theoretical value used by previous researchers was estimated at ambient temperature. Thermal conductivity decreases with temperature and therefore the value established at ambient temperature will not necessarily be applicable at grinding temperatures which are very much higher. Measurements of the thermal conductivity of single crystals of CBN are found to be difficult due to the small size of specimens that can be manufactured and the high thermal conductivity which requires precise measurement of small temperature differences. Another reason for the effective thermal conductivity being lower than the theoretical value may be due to the interface conditions at the grain wear flat-workpiece. Extreme plastic deformation in the workpiece material takes place under the grain wear flat interface [64]. In the absence of plastic deformation at this location the relative velocity between the grain and the workpiece is $v_s \pm v_w$. However, with plastic flow in the workpiece a boundary layer effect can take place at the most outer layers of the workpiece. This is similar to the boundary layer found in fluid mechanics. Therefore the relative velocity at the grain-workpiece interface is zero and the actual conditions with respect to heat conduction to the grain is a thin layer of workpiece

material smeared over the grain. This would have the effect of lowering the effective thermal conductivity of CBN grains since the thermal conductivity of steel is much lower than the reported thermal conductivity of CBN. In the case of alumina the presence of such a layer would not be as significant since the thermal conductivity of alumina and steel are comparable. The effect of a layer on the grain wear flat was not quantified analytically. However, the evaluation of the effective grinding wheel thermal conductivity from grinding experiments will take such phenomena into account. The effective thermal conductivity of the abrasives were evaluated from the measured partition ratios assuming a triangular heat flux. The triangular heat flux was chosen because it gave the best agreement between the theoretical and the measured temperature distributions.

Prediction of grinding temperatures using the contact length model of Rowe and Qi is difficult in many applications as it requires the normal force. Considerable computational advantage would be obtained using the geometric length in the analysis. The direct application of the geometric contact length in the prediction of the background temperature can lead to significant errors. The predicted temperatures assuming the geometric contact length are compared against the measured temperatures in Figure 6.88. When the heat source is taken equal to the geometric value the predicted temperatures are much higher than the measured values. Assuming the heat is liberated over the geometric contact length gives artificially high values of heat flux in the grinding zone and therefore the predicted temperatures are too high.

The third critical parameter for the accurate prediction of the partition ratio and temperature were the assumptions concerning the energy convected to the fluid and chips. The partition ratio and values of the energy partitioning between the workpiece and wheel were evaluated to be similar in both dry and wet grinding. The results indicate that the fluid does not reduce the heat conduction into the workpiece. The effective thermal properties were evaluated to be similar in both dry and wet grinding. The inclusion of a fluid model in the analysis was found to under estimate the partition ratios and

temperatures. The energy convected to the fluid was estimated using the fluid wheel model. For the fluid wheel model the energy to the fluid is inversely proportional to the depth of cut. At low depths of cut the predicted energy convected to fluid was found to be comparable in size and in some cases larger than the total energy. The energy partitioned to the workpiece is given by

$$R_w = R_{ws}\left(1 - \frac{e_{cc}}{e_c} - \frac{e_{cf}}{e_c}\right) \qquad .. 6.13$$

Therefore very low partition ratios were predicted and in some cases negative partition ratios were evaluated which are meaningless. These results support the fluid boiling principle widely reported in literature [12, 20]. In Chapter 4 a theoretical analysis was presented which showed that a substantial reduction in the maximum background temperatures was unlikely with convection in shallow cut grinding. The primary role of the fluid in reducing the background temperatures is lubrication of the contact zone and not through convection within the contact zone. The conclusion that the fluid is ineffective with regard to cooling within the contact zone does not detract from the importance of the cooling in minimising bulk temperatures in the workpiece. Bulk heating was avoided in the experiments as only single pass tests were undertaken. In practice the grinding wheel is repeatedly passed over the workpiece. In the absence of effective cooling outside the grinding zone bulk heating occur in the workpiece. This is particularly important in cylindrical grinding where the workpiece continually passes through the grinding zone. The error in ignoring the energy convected to the chips depends on the relative proportion of the chip energy to the total grinding energy. Ignoring the chip energy over estimates the temperatures and would therefore be conservative when employed to predict the critical level of grinding energy to prevent thermal damage. The best correlation between theory and experiment was obtained when convection to the grinding chips was taken into account. The value of the chip energy was assumed constant at $6J/mm^3$ which is the maximum value for melting energy for the chip [18]. It was not possible to conclude whether this value is too high though it was found to give reasonable agreement with the measured partition ratios.

The grain contact analysis and temperature solution were compared to the measured values for a range of workpiece materials, grinding wheels, workspeeds and depths of cut. This allowed the model to be tested under widely different energy levels. The measured partition ratios were found to have a greater dependence on the depth of cut than the theoretical values. The measured values reduced with depth of cut whereas the theoretical partition ratio was relatively insensitive to the depth of cut. However, the maximum error between the predicted partition ratios and the measured partition ratios was typically 8%. There was a tendency to over estimate the partition ratio at larger depths of cut. This was a result of the measured values decreasing with depth of cut. At larger values of depth of cut the grinding chips are larger and it may be possible that more grinding energy is removed by the chip than at low depths of cut. The analysis assumed a constant value of e_{cc}=6J/mm^3. Taking into account the chip energy to be a function of depth of cut would give improved agreement between theory and measurement. The difference between the transient partitioning solution and the steady solution was larger for grinding with alumina than grinding with CBN. This is because the values of dimensionless time, τ, in alumina grinding are smaller than for CBN grinding due to the lower thermal diffusivity of the alumina abrasive. in many cases the steady state solution gave reasonable accuracy especially for CBN. The difference between the transient solution and steady state solution was not as significant with CBN since the values of the dimensionless time were typically greater than four. It was shown in Chapter 3 that for $\tau > 5$ the transient function is within 90% of its steady state value. The values of energy partitioning between the workpiece and wheel were less sensitive to the depth of cut than the overall partition ratios. The partitioning between the workpiece and wheel was found to be substantially lower when grinding with CBN compared to grinding with alumina. A greater increase in the values of the energy partitioning between the workpiece and wheel compared to the overall partition ratio were obtained at lower specific energies. The energy partitioned between the workpiece and wheel varied between 0.7 and 0.9 for alumina and 0.45 to 0.6 for CBN. Estimating the energy partitioning between the workpiece and wheel requires assumptions on the energy convected away by the chips

and therefore greater reliance should be placed on the absolute values of the measured partition ratios.

A range of workpiece materials was investigated with various thermal conductivities. Cast iron has a thermal conductivity of 53.7W/mK whereas M2 tool steel has a thermal conductivity of 23.5W/mK. Under nominally the same conditions of abrasive thermal conductivity, wear flat radius and contact length the energy partitioned between the workpiece and wheel would be lower for the higher conductivity abrasive, Figure 6.89 and 6.90. Therefore the lowest values of the energy partitioning between the workpiece and wheel partition ratio would be expected for M2 tool steel and the highest values for cast iron. However, a direct comparison of the results could not be made due to the varying contact lengths and wear radii in the grinding experiments.

The range of materials investigated provide a range of energies from 30 to 170J/mm^3. The specific energy was found to reduce with the depth of cut. The thermal model was found to give good agreement with the measured partition ratios and temperatures over the range of energy levels. The assumptions concerning the convection to the chips and fluids were more significant at the lower energies. Lower forces and specific energies were encountered in wet grinding indicating that the grinding fluid is successful in lubricating the contact zone. Lower specific energies has two advantages with regard to reducing the workpiece temperatures. Firstly, a lower grinding energy means there is less heat liberated in the contact zone. The second advantage is a greater proportion of the grinding energy is convected away with the chips. The effect of the wheel wear was taken into account through the specific energy which characterises the stage of wheel wear. Wheel wear can also manifest itself in the form of increasing wear flat radii. The sensitivity of the partitioning analysis with the assumed wear flat radius is shown in Figure 6.91. The energy partitioning between the workpiece and wheel is more sensitive for CBN than for alumina. The partitioning between the workpiece and wheel is relatively insensitive to the assumed wear flat radius for values greater than 10μm.

The effect of workspeed on the partition ratio was investigated. It was found that the measured values of energy partitioned between the workpiece and wheel were insensitive to the workspeed. This corresponds to the prediction from the grain contact analysis where only small increases in the partitioning between the workpiece and wheel are expected with workspeed. The grain contact analysis takes into account changes in workspeed through the contact length model. For alumina the forces at the higher workspeeds were found to be higher than the forces at the low workspeeds. Therefore for the same depth of cut and wheel surface roughness the contact length would be higher at the higher workspeed. The energy partitioning between the workpiece and wheel was shown to be relatively insensitive to the contact length and therefore relatively insensitive to the workspeed. The effective thermal conductivities evaluated at different workspeeds were similar for alumina and CBN. This was expected since the energy partitioning between the workpiece and wheel is insensitive to workspeed. However, for the wheel contact analysis the bulk wheel thermal contact coefficient $(\kappa\rho c)_s^{1/2}$ was found to vary with workspeed. Therefore for prediction of partition ratios with the wheel contact analysis the bulk wheel thermal contact coefficient must be taken as a function of workspeed. It is conceptually difficult that the thermal properties of the wheel should differ with the workspeed. The bulk wheel thermal contact coefficient was found to increase with workspeed. However, good agreement between theory and experiment can be obtained by taking account of the dependence of the wheel thermal properties on workspeed in the partitioning analysis. The workspeed range investigated in the experiments was 0.1 to 0.3m/s which was the range of the machine and typical of surface grinding machines. In cylindrical grinding operations considerably larger values of workspeed are used, typically 0.5m/s and higher. The results indicate that for the wheel contact analysis the thermal properties would need continually adjusted throughout the workspeed range. Further experimentation at higher values of workspeed would be required to investigate the sensitivity of the bulk wheel thermal contact coefficient to the workspeed.

The temperature prediction was based on the theory of moving heat sources modified to take into account the actual heat flux entering the workpiece. Good agreement was obtained over the range of workpiece-grinding wheel and grinding conditions investigated. The model gave the same parametric trends as the measured results. The typical accuracy was 7% employing the effective thermal conductivity and roughness factors from the individual experiments. The range of thermal conductivity values were evaluated from 34W/mK to 54W/mK for alumina and 230W/mK to 325W/mK for CBN. The differences in the evaluated effective thermal conductivity may be due to sensitivity of assumed wear flat radius, varying degrees of plastic layers at the grain-workpiece interface and the extrapolation of the experimental partition ratios to zero depth of cut. For application of the results to general grinding the average values of 43W/mK for alumina and 260W/mK for CBN are proposed. The finding that the real contact length was greater than the geometric contact length was critical to the prediction of the background temperatures. The roughness factor was evaluated in the range 3.5 to 6 to give correlation with the measured temperatures. An average value of four is proposed in the analysis of grinding temperatures. Averaging the effective thermal properties and roughness factor has the effect of reducing the accuracy of the predictions. Typical results are shown in Figures 6.92 and 6.93. The typical maximum error in using the average values of effective thermal conductivity and roughness factor was 12%. It is concluded that the proposed model of the grain contact analysis taking into account convection of chips together with the temperature solution developed from the theory of moving heat sources gives good agreement with measurements over widely different grinding conditions. The theoretical model makes provision to take account of a wide number of conditions which can be important. These include the thermal properties of the workpiece and the wheel, the sharpness of the wheel, the speeds of the wheel and workpiece, the depth of cut, convection to the chips and the real contact length.

The ratio of real to geometric contact length for any result can be calculated from

$$\frac{l_e}{l_g} = \sqrt{\frac{R_w \text{ based on the triangular heat flux distribution}}{R_w \text{ based on the uniform heat flux distribution}}} \qquad .. 6.14$$

6.5 Conclusions

6.5.1 Measured partition ratios

(i) The evaluation of the partition ratio depends strongly on the assumed heat flux distribution. The differences arise due to the implications for the measured contact length.

(ii) Under some conditions the assumption of a uniform heat flux and a contact length, lg, can clearly lead to misleading results.

(iii) The square law heat flux distribution can lead to values of partition ratio close to 100%. It is therefore concluded that the triangular flux gives the best overall results.

(iv) The partition ratios when grinding with CBN were substantially lower than grinding with alumina wheels. The partition ratio was found to reduce with the depth of cut.

(v) The energy partition ratios between the workpiece and wheel were substantially lower when grinding with CBN than grinding with alumina.

(vi) The energy partitioning between the workpiece and wheel was less sensitive to the depth of cut than the overall partition ratio.

(vii) The partition ratio and the energy partitioning between the workpiece and wheel was found to be relatively insensitive to workspeed.

(viii) The specific energy when grinding with CBN may be greater or smaller than when grinding with alumina. The specific energy depends on the wheel and workpiece combination, the dressing conditions and the wear of the wheel.

(ix) The overall partition ratios and the energy partitioning between the workpiece and wheel were similar for wet and dry grinding. It is therefore concluded that the fluid has little effect on the partition ratio. The main effect of the grinding fluid was to reduce the grinding forces and grinding energy by lubrication in the grinding zone.

(x) The energy partitioned between the workpiece and wheel when grinding with CBN was higher than the reported theoretical estimates in the literature.

6.5.2 Theoretical analysis

(i) The theory of moving heat sources provides a good basis for predicting the workpiece background temperatures.

(ii) The partitioning to the workpiece can be quantified using the grain contact analysis and the effective thermal conductivity of the grains.

(iii) The average effective conductivity of CBN grains is larger than the effective thermal conductivity of alumina grains. The average effective thermal conductivity of alumina grains was 43W/mK. The average effective thermal conductivity of CBN grains was 260W/mK.

(iv) The effective thermal conductivity of CBN is substantially lower than the reported theoretical thermal conductivity of 1300W/mK

(v) The geometric contact length can be used in the partitioning analysis with small error.

(vi) An average wear flat radius can be used in the partitioning analysis with small error.

(vii) The grinding wheel thermal properties for the wheel contact analysis appear to increase with workspeed.

(viii) The energy convected away by the fluid in the grinding zone is negligible.

(ix) The energy convected to the chips can be estimated by the energy required to melt the chip volume.

(x) The real contact length is important for the calculation of grinding temperatures.

(xi) The real contact length can be calculated from the model of Rowe and Qi [39] with an average roughness factor of four.

(xii) The workpiece background temperature can be estimated within 12% using the average values of effective thermal conductivity of the grain, the average roughness factor, Rr and the average wear flat radius.

Chapter 7 : Investigation of Workpiece Thermal Damage

7.1 Types of thermal damage found in ground surfaces

The nature of thermal damage in ground workpieces was investigated using the standard metallurgical technique of etching polished specimens and microhardness tests on taper sections.

7.1.1 AISI 52100, 1%C, 1%Cr bearing steel

The heat treated structure of AISI 52100 consists of tempered martensite with a dispersion of carbide particles not dissolved during the austenitising, Figure 7.1. AISI 52100 is used widely in bearing applications and is lightly tempered at 150deg.C to give a hardness of 62 Rc.

The microstructure of an abusively ground AISI 52100 workpiece is shown in Figure 7.2. This workpiece exhibited dark blue temper colours on the surface. Three distinct zones were found in the microstructure (i) a non-etching white layer of thickness of approximately 15μm formed immediately below the ground surface (ii) a dark banded region of thickness approximately 100μm and (iii) a light coloured region which is the original heat treated bulk material. There is a gradual transition between each stage. The microhardness against depth below the surface for the dark blue temper colour workpiece is shown in Figure 7.3. Three distinct regions are noted which correspond to the three regions observed in microstructure in Figure 7.2. The microhardness graph shows that the non-etching white layer has a greater hardness than the hardness of the bulk material. This confirms the non-etching white layer to be martensite. The formation of martensite indicated that the material at the workpiece surface was raised above the eutectoid temperature of the steel which is approximately 730deg.C. The austenite formed above the eutectoid temperature has been transformed to the hard non-etching martensitic layer by the quenching of the cooler bulk material. This type of thermal damage is called

rehardening [40]. Untempered martensite is extremely hard but is too brittle for use in engineering applications [56]. With reference to the microhardness graph in Figure 7.3, the dark banded region in the microstructure has a hardness lower than the hardness of the bulk material. This indicates that the dark region has been over tempered during the grinding process. This type of thermal damage is called 'tempering' [40]. The tempering indicates that the surface was heated substantially above the tempering temperature of the material which was 150deg.C. It is evident that tempering will always accompany rehardening in a workpiece. The degree of tempering was quantified as the ratio of the minimum hardness to the heat treated hardness. A tempering value of one indicates no tempering. A low value of tempering indicates significant tempering of the workpiece. The maximum value of tempering was 0.61. The microhardness graph shows the hardness of the specimen recovering to the original heat treated hardness. The total depth of the heat affected zone is approximately 300μm.

Micro-cracks were also found in the dark blue temper colour specimen as shown in Figure 7.4. The microcrack has propagated from the ground surface to a depth of approximately 20μm. The existence of microcracks in a component can lead to a catastrophic failure in service [57].

For a workpiece ground with straw temper colours on the surface there was only a dark banded region in the microstructure, Figure 7.5. Rehardening was not found with workpieces ground with straw temper colours on the surface. This indicates that the surface temperature of the workpiece remained below the eutectoid temperature of 730deg.C during grinding. The microhardness graph, Figure 7.6, for the straw temper colour specimen confirms that this region is tempering for a depth of 100μm. The maximum value of tempering occurs at the workpiece surface and has a value of 0.82. This may be an unacceptable level of tempering as this steel is mainly used for its high hardness and wear resistance properties.

For workpieces ground with no temper colours on the surface there was no detectable change in the microstructure. The micro hardness graph, Figure 7.7, shows evidence of tempering to a depth of 40μm. The maximum value of tempering occurs at the workpiece surface and has a value of 0.95.

7.1.2 AISI 1055, 0.55% medium carbon steel

Rehardening and tempering was found in the 0.55% medium carbon steel (AISI 1055) when ground to exhibit dark blue temper colours. This material was ground in the normalised condition. Rehardening burn and tempering are noted from the microhardness graph, Figure 7.8. The tempering in the normalised steel was found to be not as significant as in the case of the hardened ball bearing steel. A lower value of tempering would be expected in a normalised material than a hardened material as martensite is more sensitive to temperature than material in the normalised condition.

For the 0.55% C steel ground with straw temper colours on the surface there was no detectable change in the microstructure or microhardness graph. The microstructure for a 0.55%C steel consists of ferrite (white) in a matrix of pearlite (dark regions), Figure 7.9. The ferrite is present in the form of grains and in the form of envelopes at the grain boundaries. At straw temper colours no significant change in the microstructure was found in the specimen apart from some evidence of an increased proportion of ferrite in the form of envelopes around the pearlite. This is consistent with recrystallisation of the ferrite at grain boundaries. This effect was exaggerated with repeated heating of the workpiece. Recrystallisation around the grain boundaries can be clearly seen in Figure 7.10 which shows a workpiece ground in internal grinding. In internal grinding the workpiece is repeatedly passed under the grinding wheel, the cumulative effect of the heating over the duration of the grinding cycle has caused recrystallisation at the grain boundaries.

No detectable change was found in the specimen ground with no temper colours.

7.1.3 M2 Tool steel, 5% Mo, 6% W, 2% V

The microhardness graph for the M2 tool steel ground with dark blue temper colours on the surface is shown in Figure 7.11. Rehardening and tempering were found. The lower eutectoid temperature for tool steel is 850deg.C and therefore the surface has exceeded 850deg.C. The maximum tempering is 0.78 and the total depth of the heat affected zone is 140μm.

At straw temper colours the immediate surface layer was found to exhibit tempering to a maximum value of 0.92, Figure 7.12. The absence of rehardening for this specimen indicates that the temperature at straw temper colours did not reach the eutectoid temperature. M2 tool steel obtains high hardness from the secondary hardening of carbides particles in the martensitic matrix [58]. The heat treatment of M2 consists of austenitising and a double tempering at 550deg.C for 2hrs. The decrease in hardness with further heating due to the grinding operations indicates that the tool steel had reached the optimum hardness during the heat treatment process.

With no visible temper colours the M2 tool steel was found to exhibit a maximum value of tempering of 0.96.

7.1.4 Grey cast iron

The microstructure of the cast iron consists of ferrite dendrites in a matrix of ferrite and fine graphite. On mechanical magnification of the subsurface using the taper section method the structure becomes very coarse relative to the size of the diamond indentor. The microhardness technique was therefore unsuitable for the cast iron workpieces.

The microstructure for the cast iron workpiece ground with blue temper colours was investigated. The ferrite dendrites were found to have a random orientation at the near surface layers indicating that re-austenisation had taken place during grinding.

There was no detectable change in the microstructure of the cast iron at straw temper colours or grinding with no visible burn.

7.1.4 Depth of the heat affected zone

The depth of the heat affected zone was found to vary between 100 to 300μm for abusively ground workpieces. The grinding conditions most likely to affect the depth of the heat affected zone can be deduced from an alternative interpretation of the Peclet number. Archard [26] showed that the Peclet number is inversely proportional to the depth of heat penetration into the bulk medium. The depth of penetration of a heat source is a function of the Peclet number

$$L = \frac{v_w l_e}{4 \alpha}$$

For a given contact length and thermal properties of the workpiece the depth of heat penetration into the workpiece is therefore largest at lower workspeeds. From the theory of moving heat sources, Equation 4.13, the maximum temperature of the workpiece surface is inversely proportional to the root of the workspeed. Grinding operations at low workspeeds will therefore give both the undesirable conditions of higher surface temperatures and a larger depth of heat penetration.

7.2 Ground surface morphology

The morphology of a ground surface with no visible thermal damage is shown in Figure 7.13. The surface shows a series of overlapping scratches each generated by individual grains. The cutting direction is evident from the grinding striations.

Examples of surface damage on the a workpiece with straw temper colours are shown in Figure 7.14 to 7.17. The overall appearance of the workpiece surface is more coarse and there is increased plastic flow due to ploughing. In addition to the grinding scratches the coarsely ground surface exhibits chips and cuttings which may be partially bonded to the parent material [59]. These chips and cuttings can become detached during service and form debris. There is also evidence of material re-deposited on the workpiece from the grain. Another feature which was found were small craters on the surface. Craters on the workpiece surface result in localised stress concentrations on the workpiece surface which would adversely affect the fatigue life in service.

The formation of oxides on the workpiece surface can be resolved on an electron microscope. The oxide layer does not conduct electicity and appears as bright blisters which are readily distinguishable from the undamaged material. An example of a blistered oxide layer viewed under an SEM taken from reference 59 is shown in Figure 7.18.

7.3 Critical workpiece temperature

The formation of oxide layers on the workpiece surface was found to coincide with significant thermal damage to workpieces. The onset of temper colours is also an established industrial criterion for thermal damage in grinding.

The measured maximum background temperature was correlated with visible thermal damage for each of the four materials. The results are shown in Figure 7.19 -7.22. It was found that the onset of straw temper colours occurred between 450 and 500deg.C for each of the materials. The temperature range 450-500deg.C is considerably higher than figures commonly published for the onset of light straw temper colours [60]. The temper colours and temperatures for steady state heat treatment are shown in Figure 7.23. For steady state heat treatment temper colours are found to occur at an average temperature of 220deg.C. Figure 7.24 shows a non damaged workpiece, a workpiece with light straw temper colours and a workpiece with dark blue temper colours. The higher temperatures are required in grinding because the duration of the thermal pulses is very short, typically less than 20 ms. The rate of oxide formation is known to follow an Arhenius relationship with temperature [57].

The results shown in Figure 7.19 to 7.22 were obtained from the grinding tests outlined in Table 5.7 and reported in Sections 6.1 to 6.3.

7.5 Conclusions

Thermal damage in grinding can manifest itself in the form of rehardening, tempering and microcracks in the immediate surface layers.

The degree of tempering on the workpiece depends on the initial heat treated condition of the workpiece. Hardened materials are more prone to tempering than materials ground in the normalised condition.

The depth of the heat affected zone was typically 100 to 300μm in depth. The depth of the heat affected zone is governed by the Peclet number. Low workspeeds will give larger heat affected zones and higher surface temperatures than higher workpieces.

A significant change in the morphology of the ground surface was observed at the onset of temper colours. The changes in morphology at the onset of temper colours are detrimental to the service life of the workpiece.

Temper colours were found to appear on the workpiece surface when the maximum background temperature exceeds 450-500deg.C for a range of commonly used ferrous materials.

Chapter 8 : Procedure for the Prevention of Thermal Damage in Grinding

This thesis has described a series of heat transfer algorithms to model the energy partitioning in the grinding zone and the grinding background temperature. In this chapter the models are collated to provide the basis for a strategy for the prevention of thermal damage in grinding. The thermal model is presented and the recommended input parameters to the model are specified. The thermal model used together with in-process power measurement can be used as a quality monitoring tool or can be incorporated into an adaptive control system for the prevention of thermal damage in grinding.

8.1 Overview of the thermal model

The thermal model predicts the critical value of specific energy above which thermal damage to the workpiece will take place. There are four main stages to the proposed procedure. The first step is the measurement of the grinding power and the determination of the specific energy using the programmed values of the grinding parameters. The second stage is the determination of the real contact length. The contact length is an input parameter to both the partitioning analysis and the workpiece background temperature model. The third stage is the calculation of the partition ratio. The product of the partition ratio and the grinding energy gives the energy entering the workpiece. The final stage is the application of the workpiece background temperature solution to determine the critical value of specific energy for a specific critical value of workpiece temperature.

8.2 Workpiece background temperature

A close correlation was found between the measured temperatures distributions and modelling the workpiece with a moving band heat source of variable strength over its

surface. The theory of moving heat sources with variable heat flux was developed in Section 4.2.2. The temperature distribution within the workpiece can therefore be predicted by

$$\frac{\theta \pi \kappa v}{2 q_o \alpha} = \int_{X-L}^{X+L} e^{-u} K_o \left(Z^2 + u^2\right)^{1/2} q(x)\, du \qquad .. 8.1$$

To maintain the workpiece quality the maximum temperature in the grinding zone must be controlled. From Section 4.2.3, the maximum dimensionless temperature at the surface is related to the Peclet number by

$$\frac{\theta_m \pi \kappa v}{2 \alpha q_o} = C\, L^{0.5} \qquad .. 8.2$$

The constant 'C' depends on the heat flux distribution in the grinding zone. A triangular heat flux was found to give best correlation with the measured distributions. The value of C from Table 4.1 is 3.336.

It was found in Section 4.3 that the convective cooling made small difference to the maximum dimensionless temperature. Equation 8.2 can therefore be applied in both dry and wet grinding operations.

From Equation 4.8 the maximum workpiece temperature is

$$\theta_m = \frac{C\, q_w}{(\kappa \rho c)_w^{1/2}} \left(\frac{v_w}{l_e}\right)^{1/2} \qquad .. 8.3$$

and

$$q_w = R_w\, q_t = R_w \frac{Q_t}{l_e\, b} \qquad .. 8.4$$

The heat dissipated, Q_t, in the grinding zone can estimated from the grinding power, P. The grinding power is given by the product of the specific energy, e_c, and the material removal rate, Z

$$Q_t = P = e_c\, Z \qquad .. 8.5$$

The material removal rate is given by

$$Z = a\, v_w\, b \qquad .. 8.6$$

Substituting Equations 8.5 and 8.6 into Equation 8.4

$$q_w = R_w \frac{e_c\, a\, v_w}{l_e} \qquad .. 8.7$$

and substituting Equation 8.7 into 8.3

$$\theta_m = \frac{C\, R_w\, e_c\, a}{(\kappa \rho c)_w{}^{1/2}} \left(\frac{v_w}{l_e}\right)^{1/2} \qquad .. 8.8$$

If the critical temperature of the workpiece is $\theta_m{}^*$ then re-arranging Equation 8.8 gives the critical value of specific energy, $e_c{}^*$

$$e_c{}^* = \frac{\pi}{C} (\kappa \rho c)_w{}^{1/2} \left(\frac{l_e}{v_w}\right)^{1/2} \frac{\theta_m{}^*}{R_w\, a} \qquad .. 8.9$$

If the measured value of the specific energy, e_c, in the process exceeds the critical value, e_c^*, given by Equation 8.9 then thermal damage to the workpiece will occur.

8.3 Contact length

The measured temperatures indicated that the actual length of the contact length was greater than the geometric value.

From Rowe and Qi [39] the contact length is

$$l_e = \sqrt{8 R_r^2 \frac{F_n}{b} (K_s + K_w) d_e + a d_e} \qquad .. 8.10$$

where K_S is the compliance of the grinding wheel

$$K_s = \frac{1 - \upsilon_s^2}{\pi E_s} \qquad .. 8.11$$

and K_W is the compliance of the workpiece

$$K_w = \frac{1 - \upsilon_w^2}{\pi E_w} \qquad .. 8.12$$

and

R_r is a roughness factor which characterises the grinding wheel topography

E is the modulus of elasticity

υ is the Poisson ratio

F_n is the normal grinding force

b is the grinding width.

The application of Equation 8.10 is limited as the value of the normal force must be known. The normal force cannot be readily obtained in most grinding processes.

The normal force can be estimated from the tangential force and assuming a value of the coefficient of friction [48]. The tangential grinding force may be determined by measuring the grinding power and the wheel speed. Using the power signal to estimated the normal force Equation 8.10 becomes

$$l_e = \sqrt{8 R_r^2 \frac{P d_e}{\mu v_s b} (K_s + K_w) + a d_e} \qquad .. 8.13$$

The model of Rowe and Qi was correlated to the measured heat source length and the value of the roughness parameter estimated to be $R_r = 4$. The grinding power signal, P, was used to estimate the normal force using a value of friction coefficient of 0.4. The roughness factor, R_r, was taken as 4 and Poissons ratio was taken as 0.3. The modulus of elasticity of the grinding wheel was 50GN/m^2 and the modulus of elasticity of the workpiece was 210GN/m^2.

The contact length is then given by

$$l_e = \sqrt{2.32 \times 10^{-9} \frac{P d_e}{b v_s} + a d_e} \qquad .. 8.14$$

8.4 Partition ratio

The energy partitioned between the wheel and workpiece is

$$R_{ws} = \left[1 + \frac{0.974\ \kappa_g}{(\kappa\rho c)_w^{1/2}\ r_0^{1/2}\ v_s^{1/2}}\ \frac{1}{\Phi(\tau)}\right]^{-1} \qquad .. 8.15$$

where

$$\Phi(\tau) = 1 - \exp\left[-\frac{\tau}{1.2}\right] \qquad .. 8.16$$

and

$$\tau = \left(\frac{\alpha_g}{r_0^2}\ \frac{l_e}{v_s}\right)^{1/2} \qquad .. 8.17$$

Making an allowance for the energy convected to the grinding chips the partition ratio is

$$R_w = R_{ws}\ \frac{6}{e_c} \qquad .. 8.18$$

where e_c is the measured specific energy in J/mm^3.

8.5 Summary of the thermal model

The critical value of specific energy is given by

$$e_c^* = \frac{1}{C}\ (\kappa\rho c)_w^{1/2} \left(\frac{l_e}{v_w}\right)^{1/2}\ \frac{\theta_m^*}{R_w\ a} \qquad .. 8.19$$

where the contact length can be determined from

$$l_e = \sqrt{2.32 \times 10^{-9} \frac{P\, d_e}{b\, v_s} + a d_e} \qquad .. 8.20$$

and the partition ratio from

$$R_w = \left[1 + \frac{0.974\, \kappa_g}{(\kappa \rho c)_w^{1/2}\, r_o^{1/2}\, v_s^{1/2}} \frac{1}{\Phi(\tau)}\right]^{-1} \frac{6}{e_c} \qquad .. 8.21$$

where e_c is the measured specific energy in J/mm^3 and the transient function is given by

$$\Phi(\tau) = 1 - \exp\left[-\frac{\tau}{1.2}\right] \qquad .. 8.22$$

where

$$\tau = \left(\frac{\alpha_g}{r_o^2} \frac{l_e}{v_s}\right)^{1/2} \qquad .. 8.23$$

8.6 The input parameters to the thermal model

8.6.1 Workpiece thermal properties

The thermal conductivity varies considerably for different ferrous materials. Alloy steels have lower values of thermal conductivity than low carbon steels and cast irons. A typical range of thermal conductivity values is 15-55W/mK at 20deg.C.

Specific heat capacity and density do not vary as much as thermal conductivity for different types of steels. Typical values of specific heat capacity range from 450 to 550J/KgK for

ferrous materials. The density variation is relatively small for different steels, density varies between 7000 and 8000 Kg/m^3.

A comprehensive list of data for thermal conductivity, specific heat capacity and density for ferrous materials can be found in references 54, 54 and 55.

8.6.2 Grain thermal properties

The effective grain thermal properties have been determined for alumina and CBN abrasives. A small range of values of specific heat capacity and density have been reported in the literature and these data will be used. The recommended average values of thermal properties for the grain are given in Table 8.1

Abrasive type	κ_g W/mK	ρ_g Kg/m^3	c_g J/KgK
Alumina	43	3910	765
CBN	260	3480	506

Table 8.1 : Recommended thermal properties for the grain

8.6.3 Grain wear flat radius

The grain wear flat radius was measured between 5 and 30μm for CBN and between 10 and 50μm for alumina abrasives. The partition ratio model was found to be relatively insensitive to the value of wear flat radii greater than 10μm. A value of 15μm can be used for modelling purposes.

8.6.4 Critical workpiece temperature

The temperature for the onset of tempers on the workpiece surface was investigated for a range of commonly used ferrous materials. It was found that the onset of straw temper colours occurred between 450 and 500 deg.C. Based on this study a mean value of 475deg.C is proposed for ferrous materials. Taking into account an ambient temperature of the workpiece material of typically 15deg.C then the critical workpiece temperature rise, θ_m^*, for use in the thermal model is 460deg.C. This temperature range may not be acceptable for the service requirements of all applications and can be selected as deemed appropriate.

In critical applications the absence of temper colours on the workpiece surface may not satisfy the quality requirements. Residual tensile stresses which are primarily thermal in origin may be unacceptable. Data for critical workpiece temperature is extremely limited.

8.7 Application of the thermal model

The total energy in the grinding process can be estimated from the motor power after subtracting the light running power before grinding commences. Power monitoring using a low cost Hall Effect transducer provides a cheap and reliable method of measuring the grinding power [61].

The grinding specific energy, e_c, is determined through the power measurement and the grinding parameters

$$e_c = \frac{P}{a\, v_w\, b} \qquad .. 8.24$$

In cylindrical grinding between centres the depth of cut is given by

$$a = \frac{v_f}{v_w} \pi d_w \qquad .. 8.25$$

Therefore in cylindrical grinding the specific energy is calculated from

$$e_c = \frac{P}{\pi d_w v_f b} \qquad .. 8.26$$

The measured specific energy, e_{msd} is compared with the calculated critical value, e_c^*, predicted from the thermal model, Equation 8.19. If the measured specific energy is below the critical specific energy the infeedrate may be increased, thereby maximising removal rates and reducing cycle time. If the measured specific energy is greater than critical specific energy corrective action should be taken. This may include reducing the infeedrate, increasing the workspeed or re-dressing the wheel. In practice changes in infeedrate and workspeed must also satisfy the surface roughness criterion, the power capacity of the machine tool and avoid workpiece chatter [62].

The application of the thermal model and power measurement provides the basis of an adaptive strategy for the prevention of thermal damage in grinding. A PC can be used for power monitoring, temperature calculations and updating the grinding parameters through the standard communication ports. Alternatively, the procedure can take place within an intelligent CNC [63]. Real time monitoring of the grinding power takes into account the changing topography of the grinding wheel due to wheel wear. The strategy, summarised in Figure 8.1, can be used to maximise removal rate at the thermal damage threshold.

A simpler arrangement is obtained by using the thermal model together with in-process power measurement as a monitoring tool. In this application there is no communication between the PC and the controller and no updating of the grinding parameters takes place.

The calculated workpiece temperature can be displayed on the screen of the computer and a warning message is given if the critical temperature is exceeded.

8.8 Conclusions

A thermal model has been presented which when used with in-process power measurement provides a potential monitoring tool for the control of workpiece temperatures in grinding.

The model is applicable to both alumina and CBN grinding. Accurate partition ratio values are obtained using the experimentally determined effective grain thermal conductivity. Differences in the specific energy levels with alumina and CBN abrasives and wheel wear is taken into account through the power measurement.

The input parameters for the thermal model have been specified.

Chapter 9 : Conclusions

A grain contact analysis has been presented which considers energy partitioning at the grain wear flat-workpiece interface. The key features of the analysis are grain-workpiece temperature compatibility and two dimensional transient heat transfer. A closed form solution was found for the average partitioning between the workpiece and wheel. The solution clearly differentiates between transient and steady state heat transfer.

A close correlation was found between the measured background temperatures and the theoretical distributions based on the theory of moving heat sources with a variable heat flux distribution. A triangular heat flux distribution gave the best agreement between theory and measurements.

The real length of contact was experimentally verified to be greater than the geometric contact length. Evaluating the partition ratio with the geometric contact length gave artificially low values of the partition ratio. Using the geometric contact length for the prediction of grinding background temperatures can lead to large errors.

The partition ratios when grinding with CBN were substantially lower than grinding with alumina wheels. However, the energy partitioning between the workpiece and wheel when grinding with CBN was higher than the reported theoretical estimates in the literature.

Correlating the grain contact analysis with the measured partition ratios allowed the evaluation of the effective thermal conductivity of the abrasives. The effective thermal conductivity of CBN was evaluated to be 260W/mK which is substantially lower than the reported theoretical value of 1300W/mK.

Thermal damage to the workpiece was found to manifest itself in the form of rehardening, tempering, microcracks and oxidation on the workpiece surface. Temper colours were

found to appear on the workpiece surface when the maximum background temperature exceeded 450 to 500 deg.C. for commonly used ferrous materials. The degree of tempering on the workpiece near surface layers at the onset of temper colours depends on the initial heat treatment of the workpiece.

Chapter 10 : Recommendations for Further Work

The thermal model proposed in this thesis was based on the results of experimentation undertaken in straight surface grinding with vitrified alumina and CBN wheels. The applicability of the findings to external and internal grinding requires investigation. The effect of resin and metal wheel bonding systems on the heat conduction to the grinding wheel requires further experimentation.

The theory of moving heat sources with a triangular heat flux distribution was found to give best agreement with the measured temperature distributions. However, an exact match was not obtained. Further theoretical work is required to investigate alternative heat flux distributions to obtain improved correlation with the measurements.

The thermal model can be used to prevent the critical workpiece temperature being exceeded during grinding. The critical temperature for the onset of temper colours was established. However, in critical applications the absence of temper colours on the workpiece surface may not satisfy the quality requirements. Residual stresses which are primarily thermal in origin may be unacceptable. The critical temperature for the onset of tensile residual stresses requires research.

REFERENCES

[1] Tarasov, L.P., Hyler, W.S., Letner, H.R, 1957, Effect of grinding conditions and resultant residual stresses on the fatigue strength of hardened steel, 16th Annual Meeting of the American Society for Testing and Materials, pp. 601-623.

[2] Malkin, S., 1985, Current trends in CBN grinding technology, Annals of the CIRP, 34/2, pp. 557-563.

[3] King, R.I and Hahn, R. S., 1986, Handbook of modern grinding technology, Published by Chapman and Hall, ISBN 0-412-01081-X.

[4] Lavine, A.S., Malkin, S., Jen, T.C., 1989, Thermal aspects of grinding with CBN wheels, Annals of the CIRP, 38/1, pp. 557-560.

[5] Rowe W.B., Morgan M.N., Allanson D.R., 1991, An advance in the modelling of thermal effects in the grinding process, CIRP Annals, 40,1, pp. 339-345.

[6] Shaw, M.C., 1990, A simplified approach to workpiece temperatures in fine grinding, Annals of the CIRP, volume 39/1, pp. 345-347.

[7] Outwater, J.O., Shaw, M.C., 1952, Surface temperatures in grinding, Transactions of ASME, 74, pp. 73-85.

[8] Hahn R. S. , 1956, The relation between grinding conditions and thermal damage in the workpiece, Trans. ASME, 78, pp. 807-812.

[9] Malkin, S., The attritious and fracture wear of grinding wheels, Ph.D. Thesis, M.I.T.

[10] Des Ruisseaux, N.R., and Zerkle, R.D., 1970, Thermal analysis of the grinding process, Trans. ASME, Jnl. of Eng. for Ind., 92, pp. 428-524.

[11] Shaw, M.C., 1984, Surface melting in grinding operations, Annals of the CIRP, 33, 1, pp. 221-223.

[12] Jaeger J.C., 1942, Moving sources of heat and the temperature at sliding contacts, Proceedings of the Royal Society of New South Wales, 76, pp. 203-224.

[13] Takazawa, K., 1966, Effects of grinding variables on surface structure of hardened steel, Bulletin of the Japan Society of Precision Engineering, volume 2, 1, pp. 14-21.

[14] Malkin, S., 1974, Thermal aspects of grinding. Part 1-Energy partition, Part 2-Surface temperatures and workpiece burn, Journal of Engineering for Industry, 96, pp. 1184-1191.

[15] Lee, D.G, 1971, An experimental study of the thermal aspects of grinding, Ph.D. Thesis, Univ. of Cincinnati.

[16] Snoeys, R., Maris, M., Peters, J., 1978, Thermally induced damage in grinding, Annals of the CIRP, volume 27/2, pp. 571-581.

[17] Vansevenant, Ir.E., 1987, A subsurface integrity model in grinding, Ph.D. Thesis, Katholieke Universiteit Leuven, Belgium.

[18] Rowe, W.B., Pettit, J.A., Boyle, A., Moruzzi, J.L., 1988, Avoidance of thermal damage in grinding and prediction of the damage threshold, Annals of the CIRP, 37/1, pp. 327-330.

[19] Rosenthal, D., 1946, The theory of moving heat sources of heat and its application to metal treatment, Trans. ASME, 1946, pp. 849-866.

[20] Lavine, A.,S., 1988, A simple model for convective cooling during the grinding process, Jnl. of Eng. for Ind., Vol. 110/1, pp. 1-6.

[21] Maris, M., 1978, Thermal aspects of grinding, Ph.D. Thesis, Katholieke Universiteit Leuven, Belgium.

[22] Des Ruisseaux, N., 1970, Temperature in semi-infinite and cylindrical bodies to moving heat sources and surface cooling, Jnl. of Heat Transfer, Vol. 92, pp. 456-464.

[23] Sato, K., 1961, Grinding temperatures, Bull. of Jap. Soc. of Grinding Eng., 1, pp. 31-33.

[24] Hahn R.S., 1962, On the nature of the grinding process, 3rd MATADOR Conf, pp. 129-155.

[25] Holman, 1986, Heat transfer, 6th Edition, 6th Edition, Published by McGraw-Hill.

[26] Archard, J.F., 1958, The temperature of rubbing surfaces, Wear, volume 2, pp. 438-455.

[27] Blok H., 1954, The dissipation of frictional heat, Appl. Sci, Section A, 5, pp. 151-181.

[28] DeVries, R.C., 1972, Cubic Boron Nitride: Handbook of properties, General Electric Technical Information Series, General Electric Company Corporate Research and Development, No 72CRD178.

[29] Morgan, M.N, 1995, Modelling for the prediction of thermal damage in grinding, Ph.D. Thesis, Liverpool John Moores Univ.

[30] Ramanath, S., 1986, Residual stress in grinding hardened steel, Ph.D. Thesis, Arizona State University.

[31] Lee, D.G., Zerkle, R.D. and Des Ruisseaux, N.R., 1971, An experimental study of thermal aspects of cylindrical plunge grinding, ASME paper WA-71/Prod. -4.

[32] Des Ruisseaux, N.R., 1968, Thermal aspects of the grinding process, Ph.D. Thesis, University of Cincinnati.

[33] Sauer, W.J., 1972, Thermal aspects of surface grinding, Proc. Int. Grinding Conf., pp. 391-411.

[34] Verkerk, J.,1975, The real contact length in cylindrical and plunge grinding, Annals of the CIRP volume 24 /1, pp. 259-263.

[35] Gu, D.Y. and Wagner J.G., 1990, further evidence on the contact zone in surface grinding, Annals of the CIRP, 39, 1, pp. 349-353.

[36] Brown, R.H., Wager, J.G and Watson, J.D., 1977, An examination of the wheel-work interface using an explosive device to suddenly interrupt the surface grinding process, Annals of the CIRP, 25, 1, pp.183-187.

[37] Peters, J., Vansevenant, E., Leuven, K.U., 1983, A thermal model covering pendulum grinding and creep feed grinding, Annals of the CIRP, volume 32/1, pp. 491-494.

[38] Malkin, S., 1978, Burning limit for surface and cylindrical grinding of steels, Annals of the CIRP, volume 27/1, pp. 233-235.

[39] Rowe, W.B., Qi, H.S., Morgan, M.N., Zheng, H.W., 1993, The effect of deformation on the contact area in grinding, Annals of the CIRP, volume 42/1, pp. 409-412.

[40] Tarasov, L.P., Some metallurgical aspects of grinding, Machining-theory and practice, ASME, 1950, pp. 409-425.

[41] Torrance, A.A., 1978, Metallurgical effects associated with grinding, Proceedings of 19th International Machine Tool Design and Research Conference, Manchester, pp 637-644.

[42] Howes, T.D., Neailey, K. and Harrison A.J., 1987, Fluid film boiling in shallow cut grinding, Annals of the CIRP, 25, 1, pp. 223-226.

[43] Carlslaw, H.S. and Jaeger, J.C., 1946, Conduction of heat in solids, Published by Oxford Science Publications Ltd, ISBN 0-19-853368-3.

[44] Malkin, S.,1989, Grinding technology - theory and applications of machining with abrasives, Publisher by Ellis Horwood Ltd, ISBN 0-85312-756-5.

[45] Guo, C. and Malkin, S., 1992, Heat transfer in grinding, Jnl. Matl. Proc. & Mfr. Sci., 1, pp. 16-27.

[46] Isenberg, J and Malkin, S., 1975, Effects of variable thermal properties on moving band source temperatures, Trans. ASME, pp. 1074-1076.

[47] Nee, A.Y.C. and Tay, O.A., 1981, On the Temperature Measurement of Surface Grinding Temperature, Int.J.Mach.Tool.Des.Res. 21/3, p279.

[48] QI, H.S., 1995, A Model of the Grinding Wheel - Workpiece Contact, PhD Thesis, Liverpool John Moores University.

[49] Labfacility Ltd., 1994, Temperature sensing with thermocouples and resistance thermometers, 2nd Edition, Peter Spiegl & Co.

[50] V.G. Lebedev, 1973, Assessing Ground-Surface Contact Temperature Using Grindable Thermocouples, Machs Tool 44/9, p.45.

[51] Greaves, R. H., 1967, Practical microscopical metallography, Published by Science paperbacks.

[52] Leitz Miniload Hardness tester Instructions, Published by Leitz Wetzlar, Germany.

[53] Smithells Metal reference Book, 1992, Published by Butterworth Heinemann Ltd., 7th Edition.

[54] Woolman J., Mottram R.A., 1966, "The mechanical and physical properties of the British standard En steels", Published by The British Iron and Steel Research Association, Pergamon Press, Oxford, 1966.

[55] Rothman, M.F., 1978, High temperature property data - ferrous alloys, Published by SAM Int.

[56] Higgins, R.A., 1983, Engineering metallurgy - Part 1, 5th Edition, Published by Hodder and Stoughton Ltd.

[57] Ashby, M.F. and Jones, D.R.H., 1986, Engineering Materials 2 : An introduction to microstructures, processing and design, Published by Pergamon Ltd.

[58] Davies, D.J. and Oelman, L.A., 1983, The structure, properties and heat treatment of metals, Published by Pitman Ltd.

[59] Engel, L., 1981, An atlas of metal damage, 18 An atlas of metals damage, Published by Wolfe Ltd.

[60] Palmer, F.R., 1971, Tool steel simplified, 4th Edition, Published by Chilton Co.

[61] Kelly S., Rowe W.B. and Moruzzi J.L., 1989, Adaptive grinding control, Adv. Mfr. Eng., 1, pp. 287-295.

[62] Rowe W.B., Bell. W.F., Brough D., 1986, Limit charts for high removal rate centreless grinding, Proceedings of 25th International Machine Tool Design and Research Conference, Manchester.

[63] Rowe W.B., Allanson D.R., Pettit J.A., Moruzzi J.L. and Kelly S., 1991, Intelligent CNC for grinding, Proc. Instn. Mech. Engrs., Vol 205, pp. 233-345.

[64] Ramanath S., Shaw M.C, 1988, Abrasive grain temperature at the beginning of a cut in fine grinding, Jnl. of Eng. for Ind., 110, pp.15-18.

APPENDICES

Appendix A1 : Program to solve the general theory of moving heat sources (Equation 4.12)

■ Input the power law exponent

```
n = Input["Enter the power law exponent 'n'"];
L = Input["Enter the Peclet number 'L'"];
```

■ Program

```
qdistribution :=(n+1) (X/L - u/(2 L) +1/2)^n
qdistribution
```

$$(1 + n)\ \left(\frac{1}{2} - \frac{u}{2\ L} + \frac{X}{L}\right)^{n}$$

```
(*  c  & d are the limits
for Jaegers definite integral *)

c := X - L
d := X + L

(* Evaluate Equation 4.12 from X/L =-2.1 to 2.1
in intervals of 1/8                              *)

Do[

  Print [

        NIntegrate[Exp[-u] * BesselK[0,Abs[u]]* qdistribution
        ,{u,c,d}]

        ]


,{X,-2.1*L,2.1*L , L/8 } ]
```

Appendix A2 : Derivation of the closed form solution of the Rowe and Morgan partitioning model

From Rowe and Morgan [5], the average value of the partitioning between the workpiece and wheel is

$$\frac{R_w}{R_w + R_s} = \frac{F_{av}}{1 + F_{av}} \qquad \text{.. A2.1}$$

where

$$F_{av} = \frac{1}{l_e} \int_0^{l_e} \frac{1.16}{r_0^{1/2}} \left[\frac{(\kappa\rho c)_w}{(\kappa\rho c)_g}\right]^{1/2} \frac{x^{1/2}}{f(x)} \qquad \text{.. A2.2}$$

and

$$f(x) = \frac{2}{\pi^{1/2}} \frac{\zeta_x}{1 - \exp[\zeta_x^2]\,\mathrm{erfc}[\zeta_x]} \qquad \text{.. A2.3}$$

and

$$\zeta_x = \left(\frac{\gamma^2 \alpha_g x}{r_0^2 v_s}\right)^{1/2} \qquad \text{.. A2.4}$$

A closed form solution was not found by Rowe and Morgan for the integral in Equation A2.2. A closed form for the integral A2.2 has been found during this investigation and is derived below.

Equation A2.2 is re-written as

$$F_{av} = \frac{1}{l_e} \int_0^{l_e} A \frac{x^{1/2}}{h(x)} dx \qquad .. A2.5$$

where

$$A = \pi^{1/2} \frac{1.16}{2 r_o^{1/2}} \left[\frac{(\kappa\rho c)_w}{(\kappa\rho c)_g}\right]^{1/2} \qquad .. A2.6$$

and

$$h(x) = \frac{\zeta_x}{1 - \exp[\zeta_x^2] \operatorname{erfc}[\zeta_x]} \qquad .. A2.7$$

Let

$$\zeta_x = B\, x^{1/2} \qquad .. A2.8$$

where

$$B = \left(\frac{\gamma^2 \alpha_g}{r_o^2 v_s}\right)^{1/2} \qquad .. A2.9$$

Substituting Equation A2.8 into A2.7

$$h(x) = \frac{B\, x^{1/2}}{1 - \exp[B^2 x] \operatorname{erfc}[B x^{1/2}]} \qquad .. A2.10$$

and substituting Equation A2.10 into A2.5

$$F_{av} = \frac{A}{B}\frac{1}{l_e}\int_0^{l_e} \left(1 - \exp\left[B^2 x^2\right] \operatorname{erfc}\left[B x^{1/2}\right]\right) dx \qquad \text{.. A2.11}$$

or

$$F_{av} = \frac{A1}{Bl_e}\left\{x - \int_0^{l_e} \exp\left[B^2 x^2\right] \operatorname{erfc}\left[B x^{1/2}\right] dx\right\} \qquad \text{.. A2.12}$$

The integral in Equation A2.12 is

$$\int \exp\left[B^2 x^2\right] \operatorname{erfc}\left[B x^{1/2}\right] dx \qquad \text{.. A2.13}$$

Equation A2.13 can be solved by integration by parts

$$\int u\, v' = u\, v - \int u'\, v \qquad \text{.. A2.14}$$

where

$$u = \operatorname{erfc}\left[B x^{1/2}\right] \qquad \text{.. A2.15}$$

and

$$v' = \exp\left[B^2 x\right] \qquad \text{.. A2.16}$$

Differentiating Equation A2.15

$$u' = -\frac{1}{\sqrt{\pi}} \frac{B x^{-1/2}}{\exp\left[B^2 x\right]} \qquad \text{.. A2.17}$$

Integrating Equation A2.16

$$v = \frac{\exp[B^2 x]}{B^2} \qquad \text{.. A2.18}$$

Substituting Equations A2.15, A2.17 and A2.18 into Equation A2.14

$$\frac{\text{erfc}[B x^{1/2}] \exp[B^2 x]}{B^2} + \int \frac{x^{-1/2}}{\sqrt{\pi} B} dx \qquad \text{.. A2.19}$$

giving

$$\frac{\text{erfc}[B x^{1/2}] \exp[B^2 x]}{B^2} + \frac{2 x^{1/2}}{\sqrt{\pi} B} \qquad \text{.. A2.20}$$

Substituting Equation A2.20 into A2.12

$$F_{av} = \frac{A1}{B l_e} \left[x - \frac{\text{erfc}[B x^{1/2}] \exp[B^2 x]}{B^2} + \frac{2 x^{1/2}}{\sqrt{\pi} B} \right]_0^{l_e} \qquad \text{.. A2.21}$$

and after taking the limits of integration

$$F_{av} = \frac{A1}{B^3 l_e} \left(1 + B^2 l_e - \frac{2}{\sqrt{\pi}} B l_e^{1/2} - B l_e^{1/2} \exp[B^2 l_e] \right) \qquad \text{.. A2.22}$$

Substituting Equations A2.6 and A2.9 into Equation A2.22

$$F_{av} = \frac{1.16}{r_o^{1/2}} \frac{l_e^{1/2}}{g(\zeta)} \left[\frac{(\kappa\rho c)_w}{(\kappa\rho c)_g} \right]^{1/2} \qquad \text{.. A2.23}$$

where

$$g(\zeta) = \frac{2}{\pi^{1/2}} \frac{\zeta^3}{1 + \zeta^2 - \frac{2}{\pi^{1/2}} \zeta - \exp[\zeta^2] \operatorname{erfc}[\zeta]} \quad \text{.. A2.24}$$

and

$$\zeta = \left(\frac{\gamma^2 \alpha_g l_e}{r_o^2 v_s} \right)^{1/2} \quad \text{.. A2.25}$$

Substituting Equation A2.23 into Equation A2.1 gives the partitioning between the workpiece and wheel

$$\frac{R_w}{R_w + R_s} = \left[1 + 0.862 \left(\frac{r_o}{l_e} \right)^{1/2} g(\zeta) \left[\frac{(\kappa \rho c)_g}{(\kappa \rho c)_w} \right]^{1/2} \right]^{-1} \quad \text{.. A2.26}$$

APPENDIX A3 : Derivation of integral for the grain contact analysis

Equation 3.32 is

$$\int B\sqrt{t}\left(\frac{1}{\sqrt{\pi}} - \frac{1}{\sqrt{\pi}\exp\left[\left(\frac{A}{\sqrt{t}}\right)^2\right]} + \frac{A}{\sqrt{t}}\operatorname{erfc}\left[\left(\frac{A}{\sqrt{t}}\right)\right]\right)dt \qquad \text{.. A3.1}$$

Equation A3.1 can be solved using the method of integration by parts

$$\int u\,v' = u\,v - \int u'\,v \qquad \text{.. A3.2}$$

Let

$$u = B\sqrt{t} \qquad \text{.. A3.3}$$

therefore

$$u' = \frac{B}{2}\frac{1}{\sqrt{t}} \qquad \text{.. A3.4}$$

Let

$$v' = \frac{1}{\sqrt{\pi}} - \frac{1}{\sqrt{\pi}\exp\left[\left(\frac{A}{\sqrt{t}}\right)^2\right]} + \frac{A}{\sqrt{t}}\operatorname{erfc}\left[\left(\frac{A}{\sqrt{t}}\right)\right] \qquad \text{.. A3.5}$$

and

$$v = \int\left(\frac{1}{\sqrt{\pi}} - \frac{1}{\sqrt{\pi}\exp\left[\frac{A^2}{t}\right]} + \frac{A}{\sqrt{t}}\operatorname{erfc}\left[\frac{A}{\sqrt{t}}\right]\right)dt \qquad \text{.. A3.6}$$

A3.1 The solution of Equation A3.6

Equation A3.6 is re-written as

$$v = \int \frac{1}{\sqrt{\pi}}\,dt - \int \frac{1}{\sqrt{\pi}\,\exp\left[\frac{A^2}{t}\right]}\,dt + \int \frac{A}{\sqrt{t}}\,\mathrm{erfc}\left[\frac{A}{\sqrt{t}}\right]dt \qquad \text{.. A3.7}$$

The first two terms in Equation A3.7 can be readily solved

$$\int \frac{1}{\sqrt{\pi}}\,dt = \frac{t}{\sqrt{\pi}} \qquad \text{.. A3.8}$$

and

$$\int -\frac{1}{\sqrt{\pi}\,\exp\left[\left(\frac{A}{\sqrt{t}}\right)^2\right]}\,dt \qquad \text{.. A3.9}$$

has the form of a standard integral

$$\int \frac{1}{\exp\left[\frac{a}{x}\right]}\,dt = \frac{x}{\exp\left[\frac{a}{x}\right]} - \mathrm{Ei}\left[-\left(\frac{a}{x}\right)\right] \qquad \text{.. A3.10}$$

where Ei[z] is the exponential integral function defined as

$$\mathrm{Ei}\,[z] = -\int_{-z}^{\text{infinity}} \frac{\exp[-x]}{x}\,dx \qquad \text{.. A3.11}$$

Using the standard integral given in Equation A3.10, Equation A3.9 becomes

$$\int \frac{1}{\sqrt{\pi}\exp\left[\frac{A^2}{t}\right]}\,dt = -\frac{1}{\sqrt{\pi}}\frac{t}{\exp\left[\frac{A^2}{t}\right]} - \frac{A^2}{\sqrt{\pi}}\,Ei\left[-\left(\frac{A^2}{t}\right)\right] \quad \text{.. A3.12}$$

The third term in Equation A3.6 is

$$\int \frac{A}{\sqrt{t}}\,erfc\left[\frac{A}{\sqrt{t}}\right]dt \quad \text{.. A3.13}$$

Equation A3.13 takes the form of a product and must be solved by integration by parts.

A3.1.2 Solution of Equation A3.13

Let

$$\int \frac{A}{\sqrt{t}}\,erfc\left[\frac{A}{\sqrt{t}}\right]dt \quad \text{.. A3.14}$$

take the form

$$\int m\,n' = mn - \int n\,m' \quad \text{.. A3.15}$$

where

$$m = erfc\left[\frac{A}{\sqrt{t}}\right] \quad \text{.. A3.16}$$

and

$$n' = \frac{A}{\sqrt{t}} \qquad \text{.. A3.17}$$

Differentiating Equation A3.16 gives

$$m' = \frac{A}{\exp\left[\frac{A^2}{t}\right]\sqrt{\pi}\, t^{3/2}} \qquad \text{.. A3.18}$$

Integrating Equation A3.17 gives

$$n = 2A\sqrt{t} \qquad \text{.. A3.19}$$

The integral $\int n\, m'$ in Equation A3.15 is therefore

$$\int n\, m' = \int \left(2A\sqrt{t}\ \frac{A}{\exp\left[\frac{A^2}{t}\right]\sqrt{\pi}\, t^{3/2}}\right) dt = \int \left(\frac{2A^2}{\exp\left[\frac{A^2}{t}\right]\sqrt{\pi}\, t^{1/2}}\right) dt \qquad \text{.. A3.20}$$

From the definition of the exponential integral given in Equation A3.10, Equation A3.20 becomes

$$\left(\frac{2A^2}{\sqrt{\pi}}\, Ei\left[-\left(\frac{A^2}{t}\right)\right]\right) \qquad \text{.. A3.21}$$

Substituting Equations A3.16, A3.19 and A3.21 into A3.15 gives

$$\int \frac{A}{\sqrt{t}} \operatorname{erfc}\left[\frac{A}{\sqrt{t}}\right] dt = 2A\sqrt{t}\, \operatorname{erfc}\left[\frac{A}{\sqrt{t}}\right] + \frac{2}{\sqrt{\pi}} A^2\, Ei\left[-\left(\frac{A^2}{t}\right)\right] \qquad \text{.. A3.22}$$

Substituting Equations A3.8, A3.12 and A3.22 into Equation A3.7 gives the required quantity v

$$v = \frac{t}{\sqrt{\pi}} - \frac{t}{\sqrt{\pi}\exp\left[\frac{A^2}{t}\right]} + 2A\sqrt{t}\,\mathrm{erfc}\left[\frac{A}{\sqrt{t}}\right] + \frac{A^2}{\sqrt{\pi}}\mathrm{Ei}\left[-\left(\frac{A^2}{t}\right)\right] \quad \text{.. A3.23}$$

A3.2 Solution of $\int u\,v' = u\,v - \int u'\,v$

Substituting the Equations for u and v from Equations A3.3 and A3.23

$$uv = \frac{B\,t^{3/2}}{\sqrt{\pi}} - \frac{B\,t^{3/2}}{\sqrt{\pi}\exp\left[\frac{A^2}{t}\right]} + 2ABt\,\mathrm{erfc}\left[\frac{A}{\sqrt{t}}\right] + \frac{A^2B\sqrt{t}}{\sqrt{\pi}}\mathrm{Ei}\left[-\left(\frac{A^2}{t}\right)\right] \text{.. A3.24}$$

Substituting the equations for u' and v' from Equations A3.4 and A3.5 the second part of Equation A3.2 becomes

$$\int u'\,v = \int\left(\frac{B\sqrt{t}}{2\sqrt{\pi}} - \frac{B\sqrt{t}}{2\sqrt{\pi}\exp\left[\frac{A^2}{t}\right]} + AB\,\mathrm{erfc}\left[\frac{A}{\sqrt{t}}\right] + \frac{A^2B}{\sqrt{\pi}}\frac{1}{2}\frac{1}{\sqrt{t}}\mathrm{Ei}\left[-\left(\frac{A^2}{t}\right)\right]\right)dt$$

.. A3.25

Each term in Equation A3.25 may be integrated separately.

For the first term in Equation A3.25

$$\int \frac{B\sqrt{t}}{2\sqrt{\pi}}\,dt = \frac{B\,t^{3/2}}{3\sqrt{\pi}} \quad \text{.. A3.26}$$

For the second term in Equation A3.25 the following standard integral was used

$$\int -\frac{B\sqrt{t}}{2\sqrt{\pi}\exp\left[\frac{A^2}{t}\right]}\,dt = \frac{B(2A^2 - t)\sqrt{t}}{3\sqrt{\pi}\exp\left[\frac{A^2}{t}\right]} + \frac{2}{3}A^3B\,\mathrm{erf}\left[\frac{A}{\sqrt{t}}\right] \quad \text{.. A3.28}$$

For the third term in Equation A3.25 the following standard integral was used

$$\mathrm{ierfc}\left[\frac{a}{\sqrt{x}}\right]dx = -\frac{2a\sqrt{x}}{\sqrt{\pi}\exp\left[\frac{a^2}{x}\right]} - 2a^2\,\mathrm{erf}\left[\frac{a}{\sqrt{x}}\right] + x\,\mathrm{erfc}\left[\frac{a}{\sqrt{x}}\right] \quad \text{.. A3.29}$$

therefore

$$\int A\,B\,\mathrm{erfc}\left[\frac{A}{\sqrt{x}}\right]dT = -\frac{2A^2B\sqrt{t}}{\sqrt{\pi}\exp\left[\frac{A^2}{t}\right]} - 2A^3B\,\mathrm{erf}\left[\frac{a}{\sqrt{t}}\right] + A\,B\,t\,\mathrm{erfc}\left[\frac{A}{\sqrt{t}}\right]$$

.. A3.30

For the fourth term in Equation A3.25 the following standard integral was used

$$\int \frac{\mathrm{Ei}\left[-\left(\frac{a}{x}\right)\right]}{\sqrt{x}}\,dx = \frac{4\sqrt{\pi}}{\exp\left[\frac{a}{x}\right]} + 4\sqrt{a}\sqrt{\pi}\,\mathrm{erf}\left[\left(\frac{a}{x}\right)^{1/2}\right] + 2\sqrt{x}\,\mathrm{Ei}\left[-\left(\frac{a}{x}\right)\right] \quad \text{.. A3.31}$$

therefore

$$\int \frac{A^2B}{2\sqrt{\pi}}\frac{\mathrm{Ei}\left[-\left(\frac{A^2}{t}\right)\right]}{\sqrt{t}}\,dt = \frac{2A^2B}{\exp\left[\frac{A^2}{t}\right]} + 2A^3B\,\mathrm{erf}\left[\frac{A}{\sqrt{t}}\right] + \frac{A^2B\sqrt{t}}{\sqrt{\pi}}\,\mathrm{Ei}\left[-\left(\frac{A^2}{t}\right)\right]$$

.. A3.32

Substituting Equations A3.26, A3.28, A3.30 and A3.32 into Equation A3.25

$$\frac{B\,t^{3/2}}{3\sqrt{\pi}} + \frac{B\,(2\,A^2 - t)\,\sqrt{t}}{3\sqrt{\pi}\,\exp\left[\frac{A^2}{t}\right]} + \frac{2}{3}A^3\,B\,\mathrm{erf}\left[\frac{A}{\sqrt{t}}\right] + A\,B\,t\,\mathrm{erfc}\left[\frac{A}{\sqrt{t}}\right] + \frac{A^2}{\sqrt{\pi}}B\,\sqrt{t}\,\mathrm{Ei}\left[-\left(\frac{A^2}{t}\right)\right]$$

.. A3.33

Substituting Equation A3.24 for uv and Equation A3.33 for $\int u'\,v$ into Equation A3.2 gives the solution of Equation A3.1

$$\frac{2}{3\sqrt{\pi}}B\,t^{3/2} - \frac{2\,B\,\sqrt{t}\,(A^2 + t)}{3\sqrt{\pi}\,\exp\left[\frac{A^2}{t}\right]} - \frac{2}{3}A^3\,B\,\mathrm{erf}\left[\frac{A}{\sqrt{t}}\right] + A\,B\,t\,\mathrm{erfc}\left[\frac{A}{\sqrt{t}}\right]$$

.. A3.34

APPENDIX A4 : Engineering drawings of the temperature measurement workpiece and amplifier jig

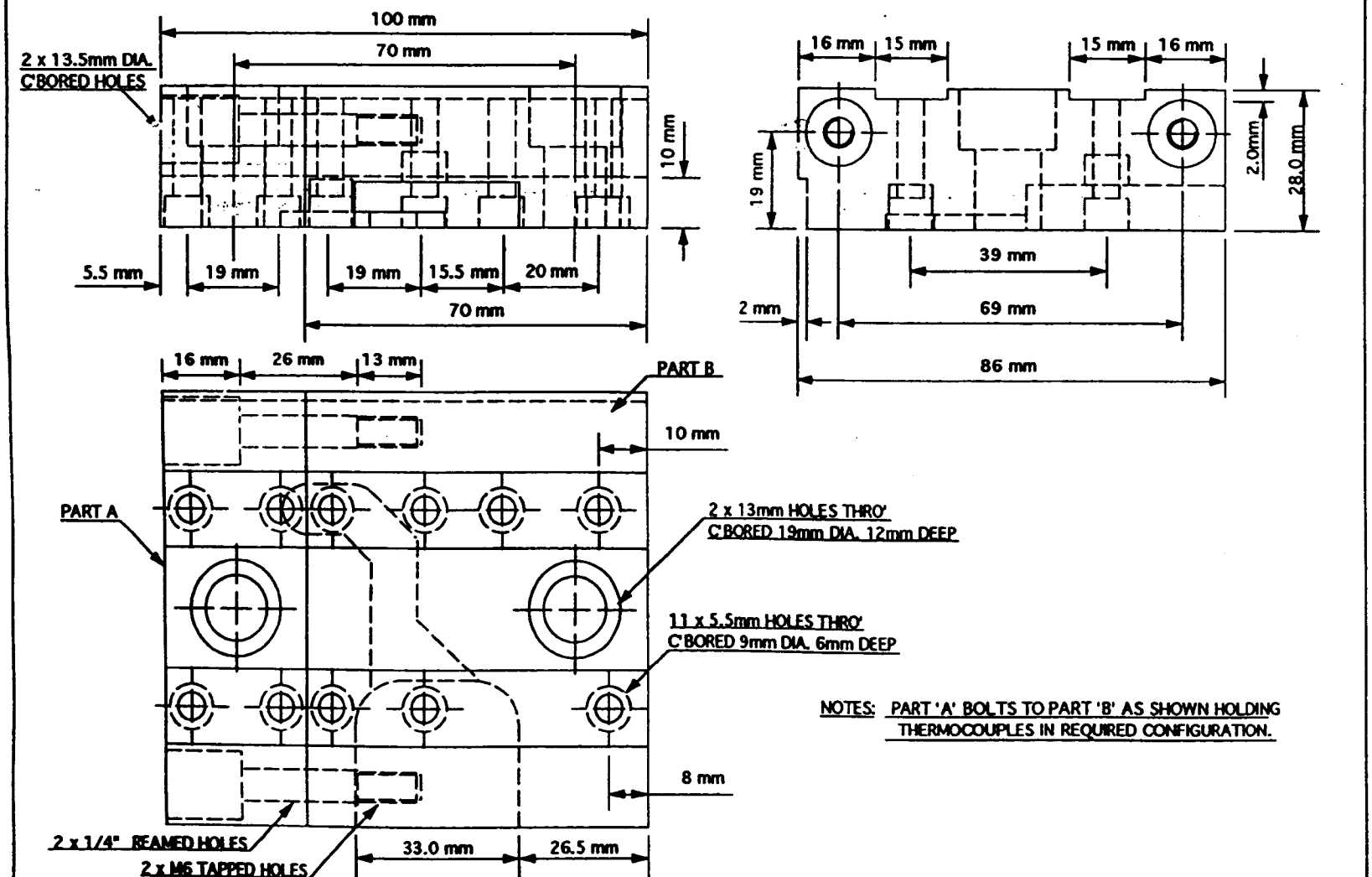

NOTES: PART 'A' BOLTS TO PART 'B' AS SHOWN HOLDING THERMOCOUPLES IN REQUIRED CONFIGURATION.

REMARKS: 3 OFF EN9	TOL: +/- 0.1mm SCALE 1:1	DRAWING TITLE: THERMOCOUPLE WORKPIECE	DRAWING No. SB/A002 DRAWN BY S.C.E.BLACK DATE 03/05/94

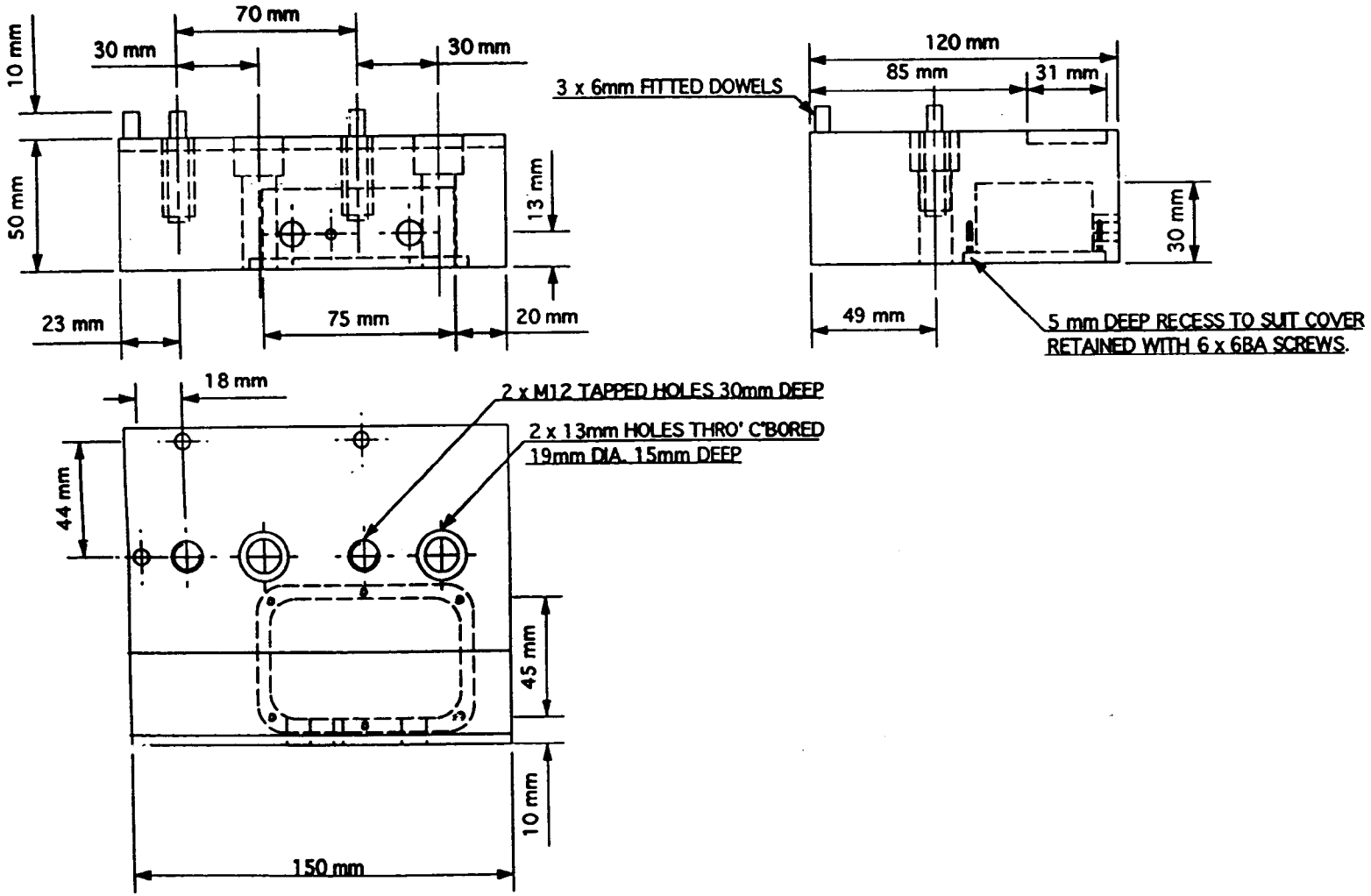

REMARKS 1 OFF MILD STEEL TOL: +/- 0.1mm SCALE 1:2	DRAWING TITLE: JIG FOR THERMOCOUPLE WORKPIECE	DRAWING No.	SB/A001
		DRAWN BY	S.C.E.BLACK
		DATE	12/08/93

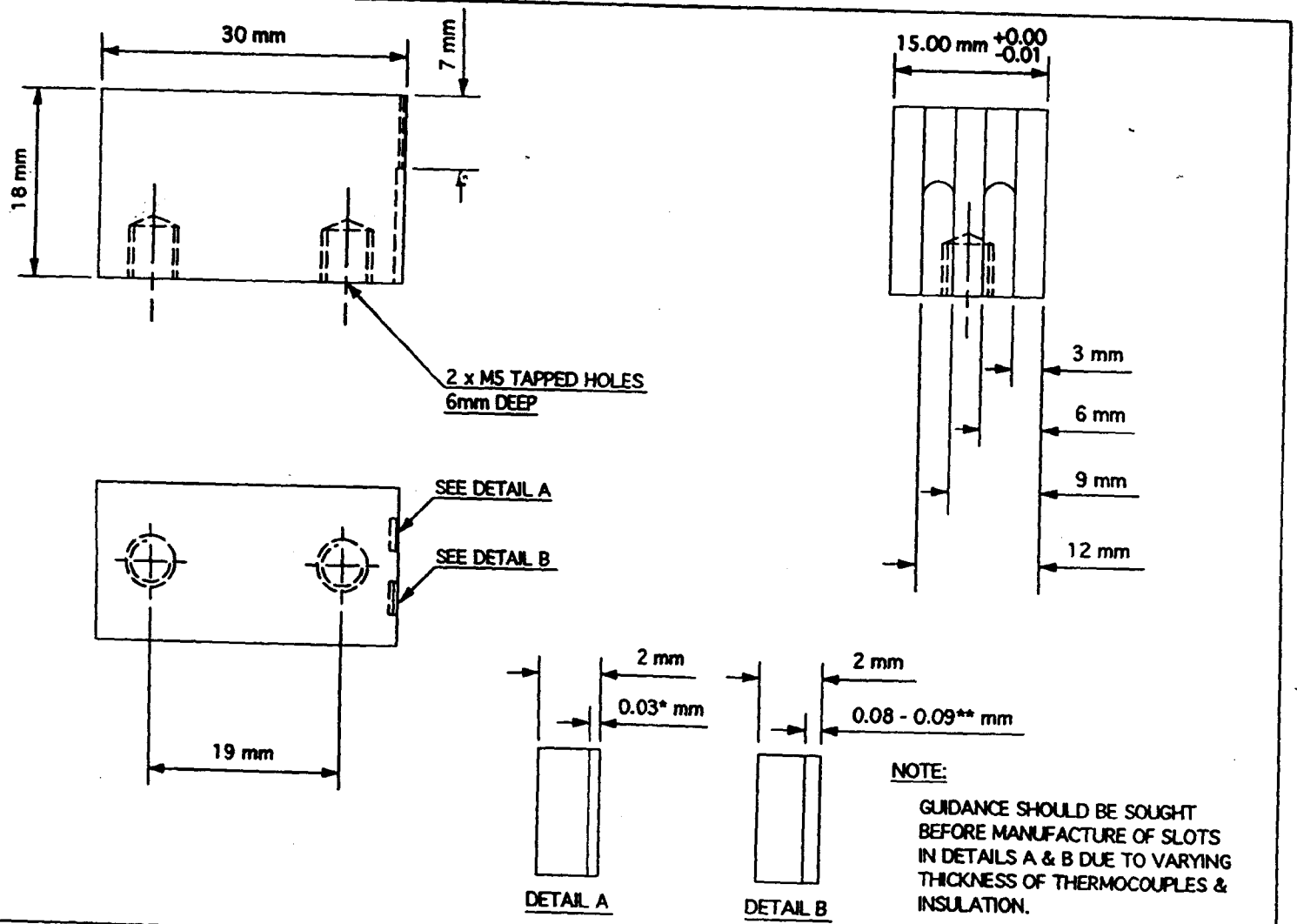

REMARKS

SCALE 2:1 TOL: +/- 0.05 UNLESS OTHERWISE STATED
TOL FOR: SLOT * + 0.005/-0.001 SLOT ** AS INDICATED

DRAWING TITLE

THERMOCOUPLE SEGMENT

DRAWING No.	SB/A006
DRAWN BY	S.C.E.BLACK
DATE	05/05/94

APPENDIX A5 : List of the Author's Relevant Publications

Papers published :

Rowe W.B., Black S.C.E. and Mills B., 1995, "Temperatures in CBN grinding", Industrial Diamond Review, Issue 4/95.

Rowe W.B., Black S.C.E. and Mills B., 1995, "Temperature control in grinding", Accepted for publication in the Journal of Advanced Manufacturing Technology, August 1995.

Rowe W.B, Black S.C.E., Mills B., Qi H.S. and Morgan M.N., 1994, "Experimental investigation of heat transfer in grinding." Annals of the CIRP, 44, 1, 329-332.

Black S.C.E, Rowe W.B., Mills B and Qi H.S, 1994, "Experimental energy partitioning in grinding.", Proc . of EuroMetalWorking Conf, Udine.

Black S.C.E., Rowe W.B., Qi H.S and Mills B., 1995, "Temperature measurement in grinding", MATADOR Conf., Manchester 20-21st April 1995, 409-414.

Black S.C.E, Rowe W.B., Mills B and Qi H.S, 1994, "Energy partitioning in grinding.", IMechE Seminar on Mission of Tribology, 6th Dec. 1994, Westminser.

Papers under review :

Rowe W.B., Black S.C.E., Mills B. and Qi H.S., 1995, "Analysis of grinding temperatures by energy partitioning", Submitted to the IMechE journal of Engineering Manufacture, September 1995.

Rowe W.B., Black S.C.E., Mills B., Morgan M.N. and Qi H.S., 1995, "Prediction of grinding temperatures ", Submitted to the Royal Society, October 1995.

Rowe W.B., Morgan M.N, Black S.C.E. and Mills B., 1996, "A simplified approach to control of thermal damage in grinding", Submitted to the Annals of the CIRP, January 1996.

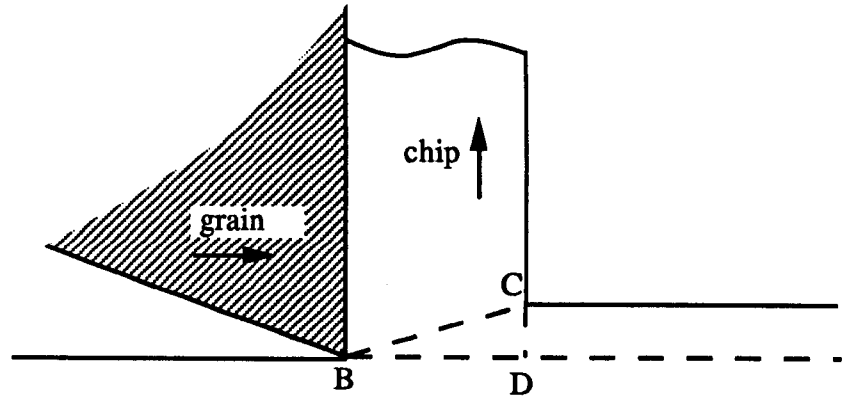

Figure 2.1 : Partitioning over the shear plane after Shaw [1]

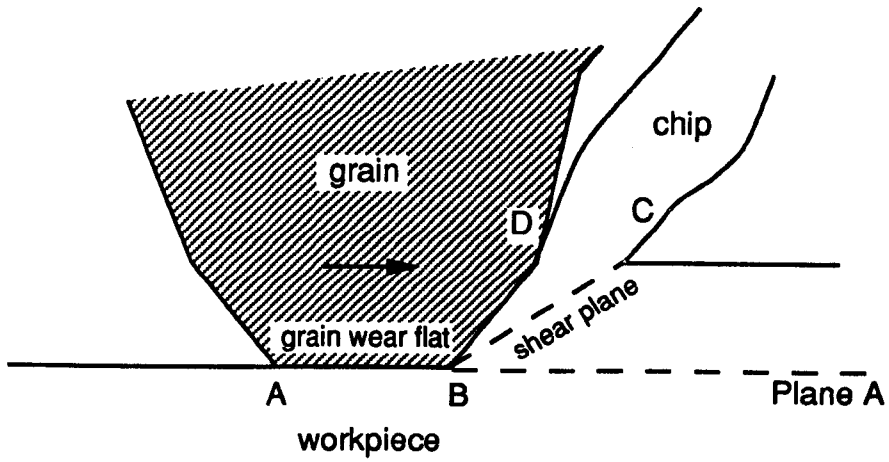

Figure 2.2 : Modelling of the heat sources at an abrasive grain after Hahn [8]

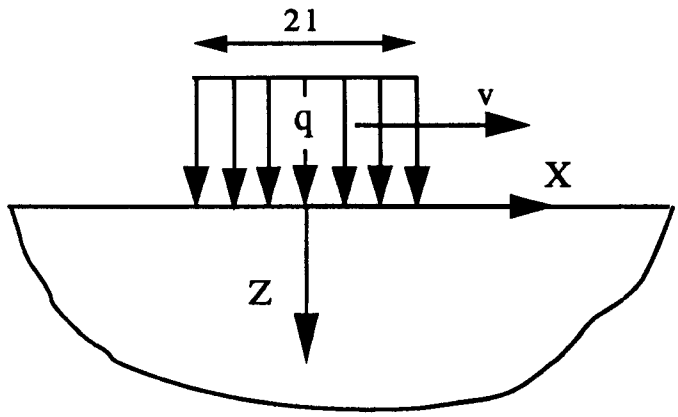

Figure 2.3 : Jaeger's model of a moving heat source on a semi-infinite body [12]

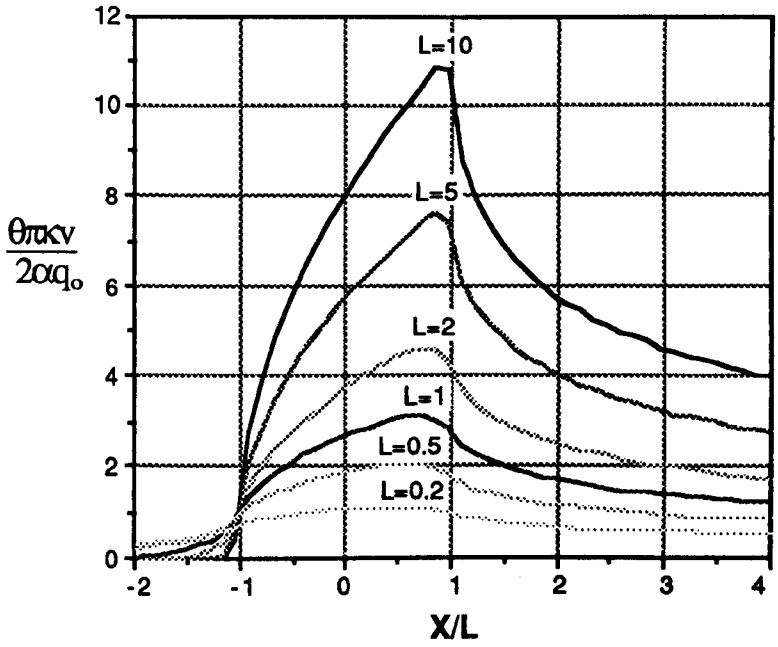

Figure 2.4 : Dimensionless temperature against dimensionless distance for various Peclet numbers

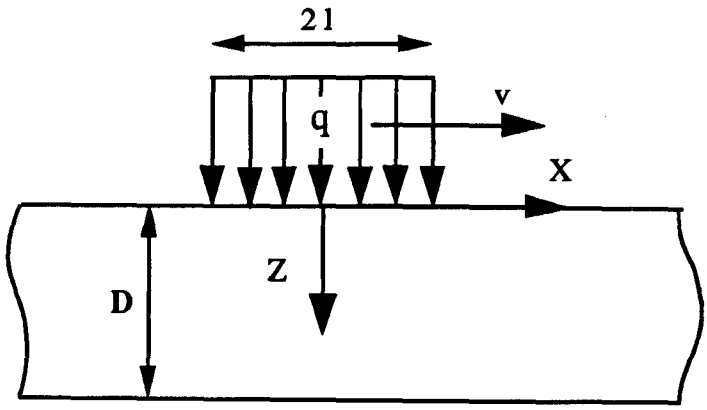

Figure 2.5 : Rosenthal's model of a moving heat source on a body of finite thickness [15]

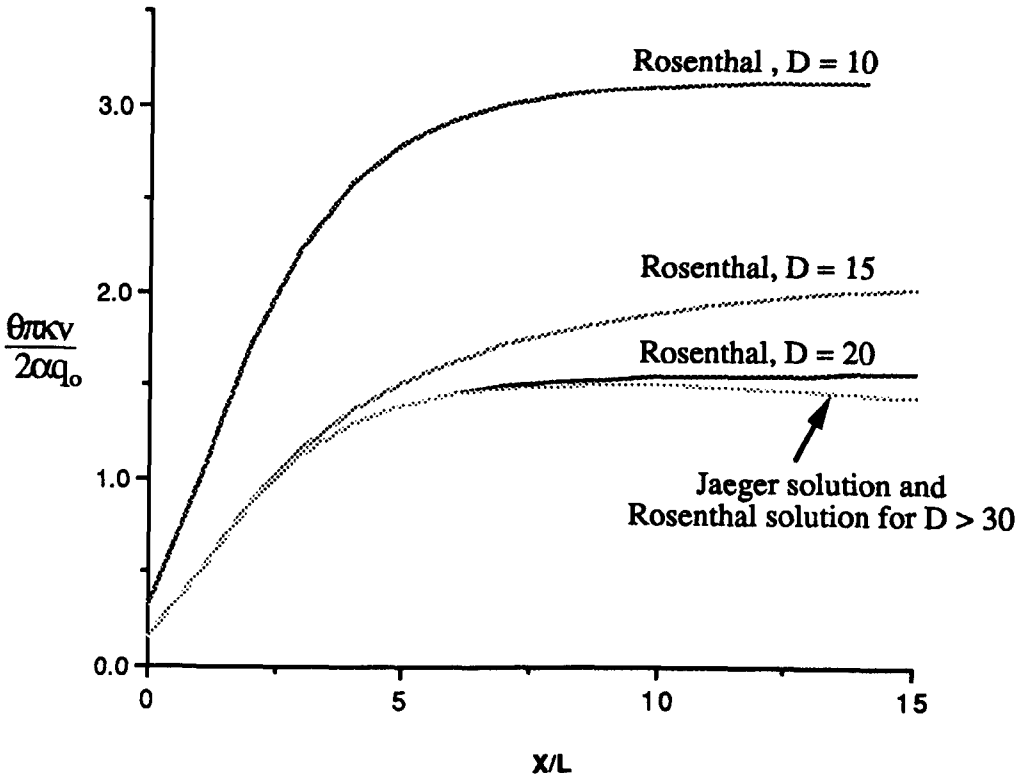

Figure 2.6 : Dimensionless temperature for a body of finite thickness at Z= 10

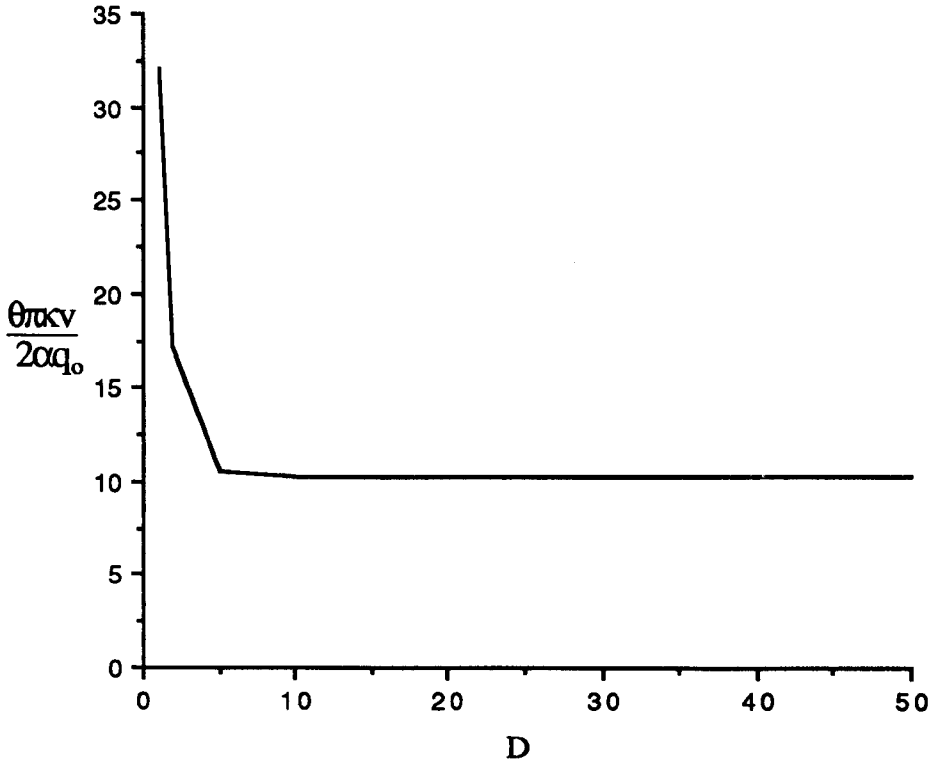

Figure 2.7 : Dimensionless surface temperature for a body of varying finite thickness for Peclet number L = 10

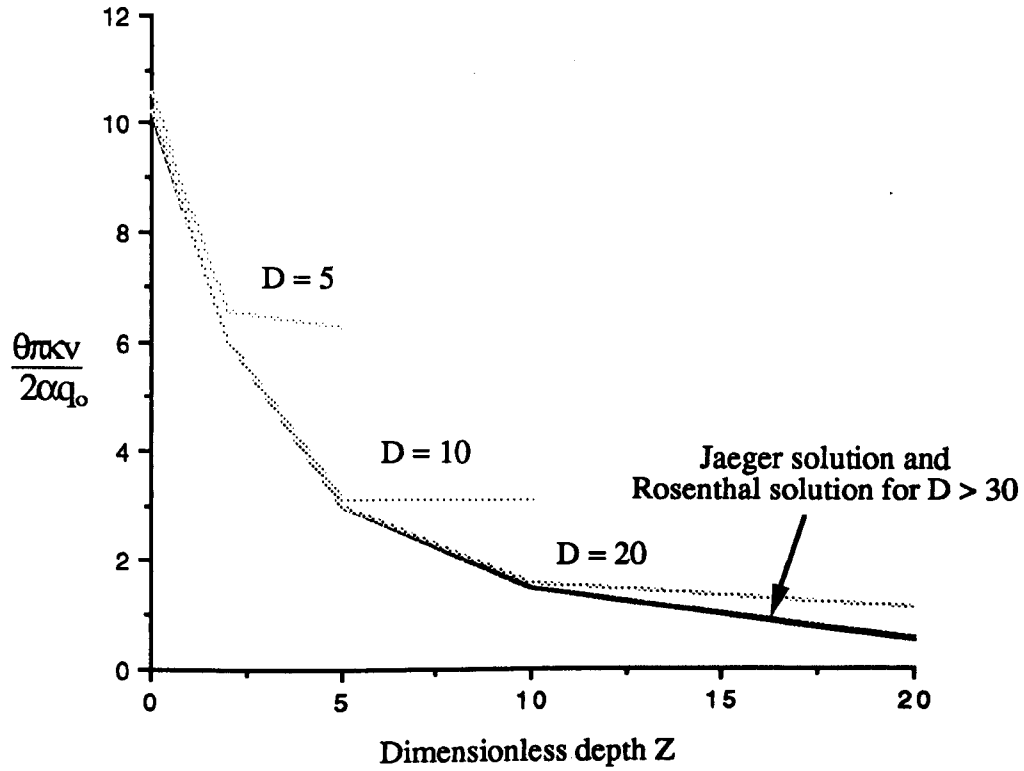

Figure 2.8 : Sub-surface dimensionless temperature for a body of finite thickness

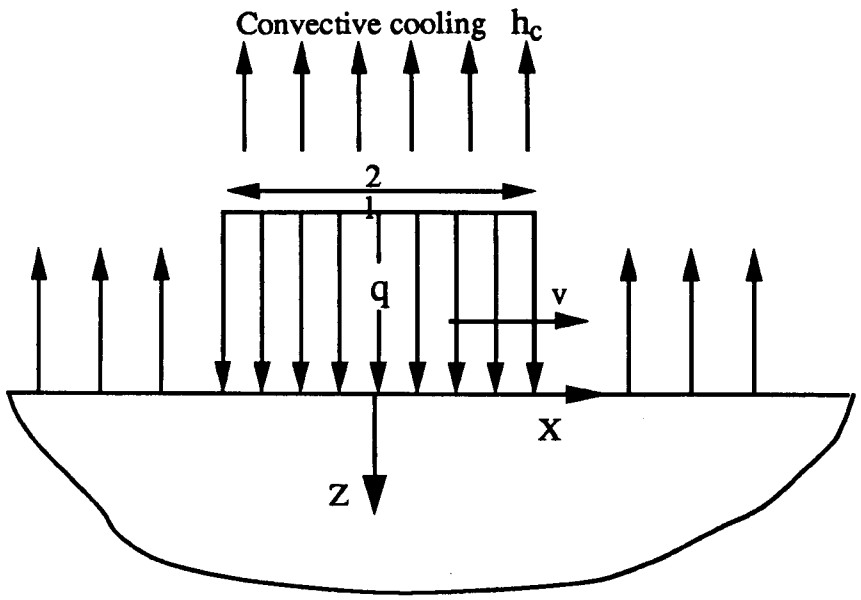

Figure 2.9 : Des Ruisseaux's model of a moving heat source on a semi-infinite body with convective cooling [22]

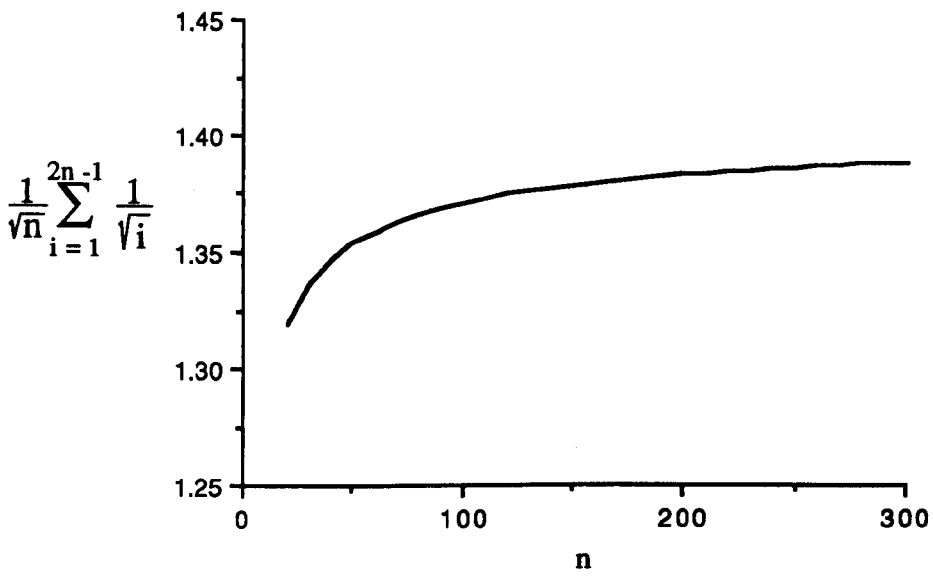

Figure 2.10 : Evaluation of Sato's modelling approach [23]

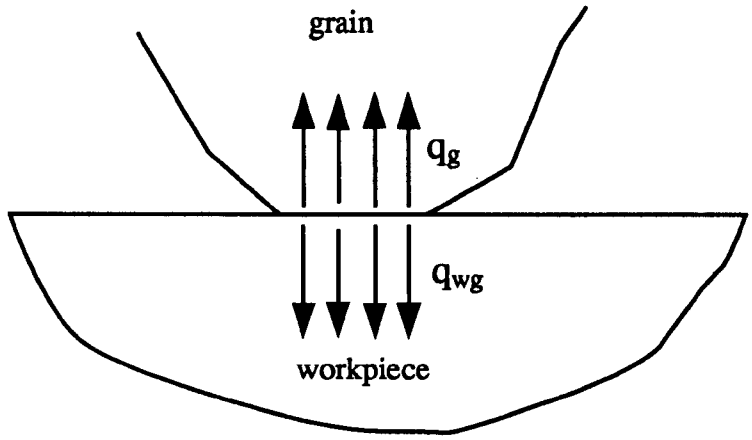

Figure 2.11 : Hahn's grain partitioning model [24]

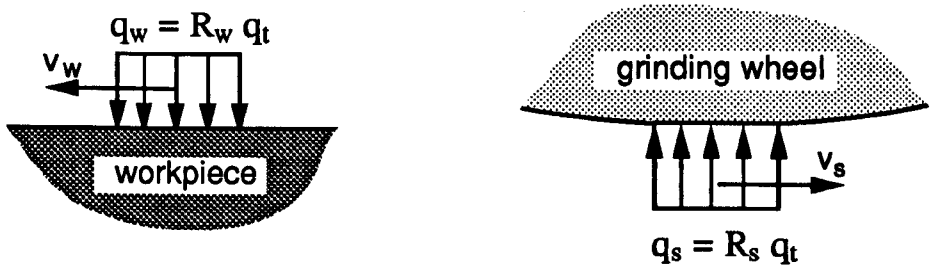

Figure 2.12 : Rowe and Pettit's wheel contact partitioning model [12]

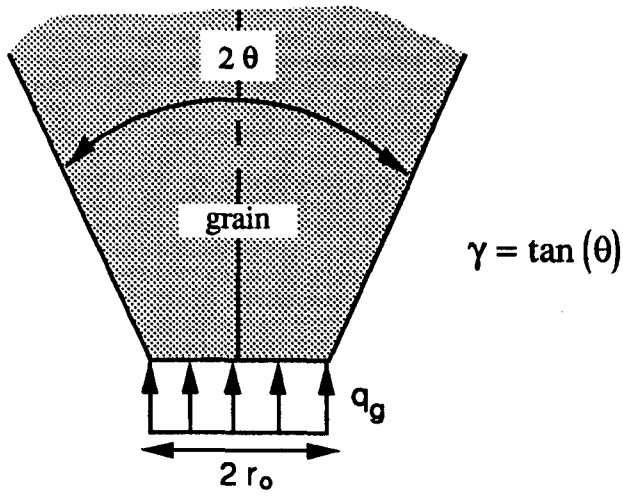

Figure : 2.13 Lavine's conical grain model [24]

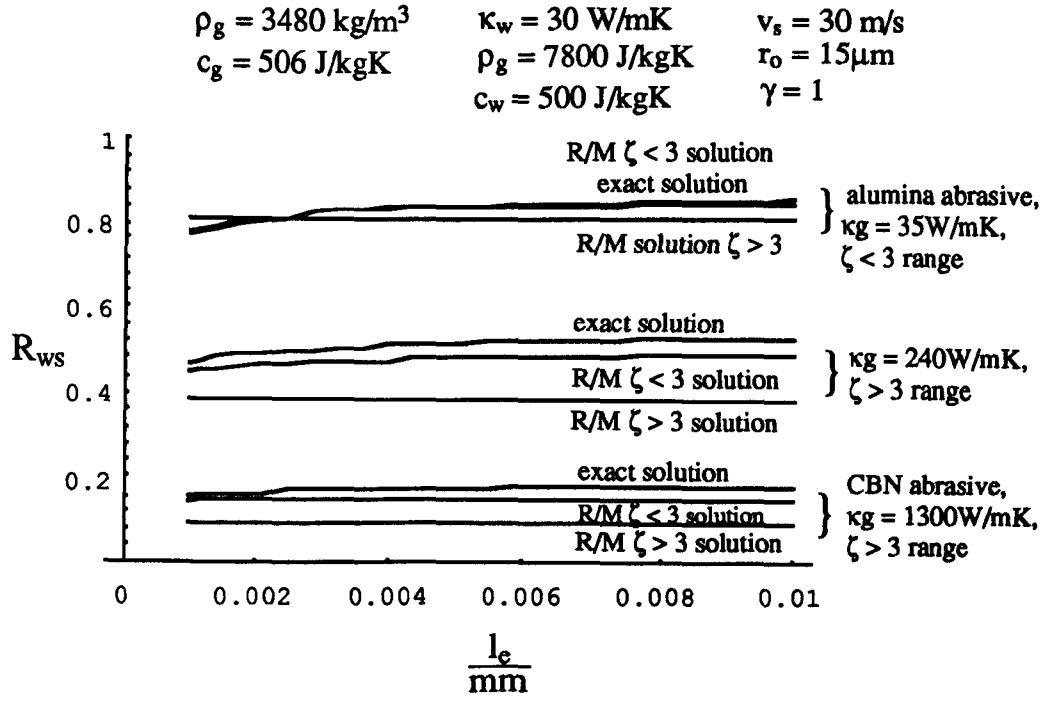

Figure : 2.14 Comparison of Rowe and Morgan solution with exact solution

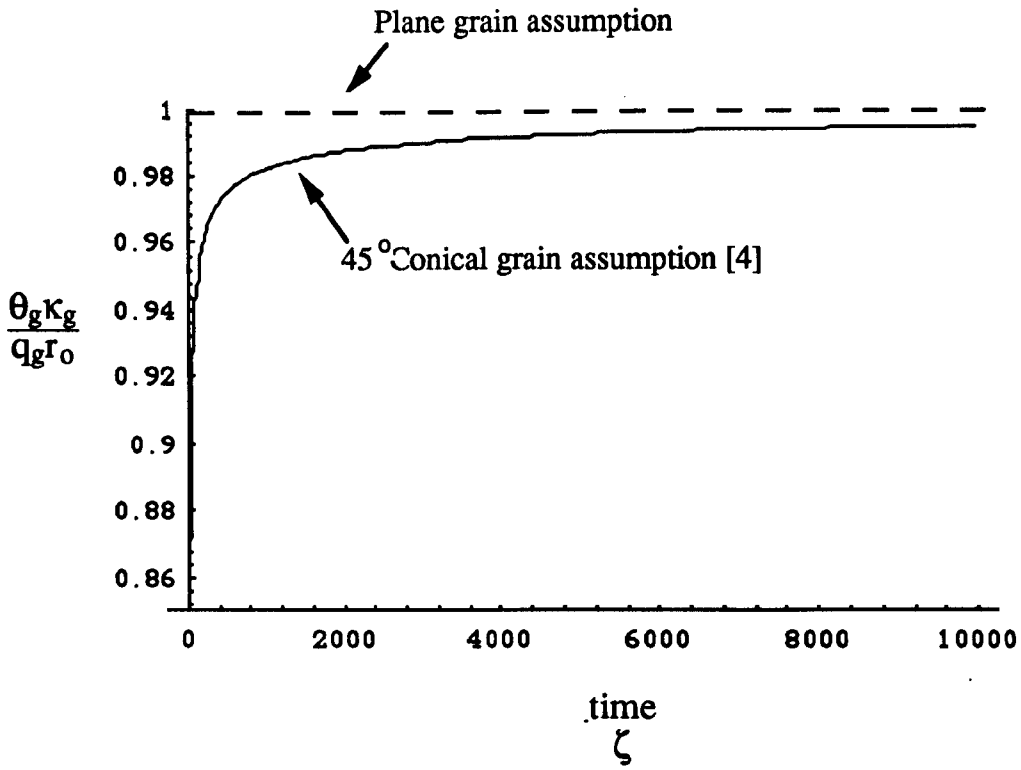

Figure 2.15 : Models of conduction into a grain : Steady state plane model and transient 45 deg. cone model by Lavine [4]

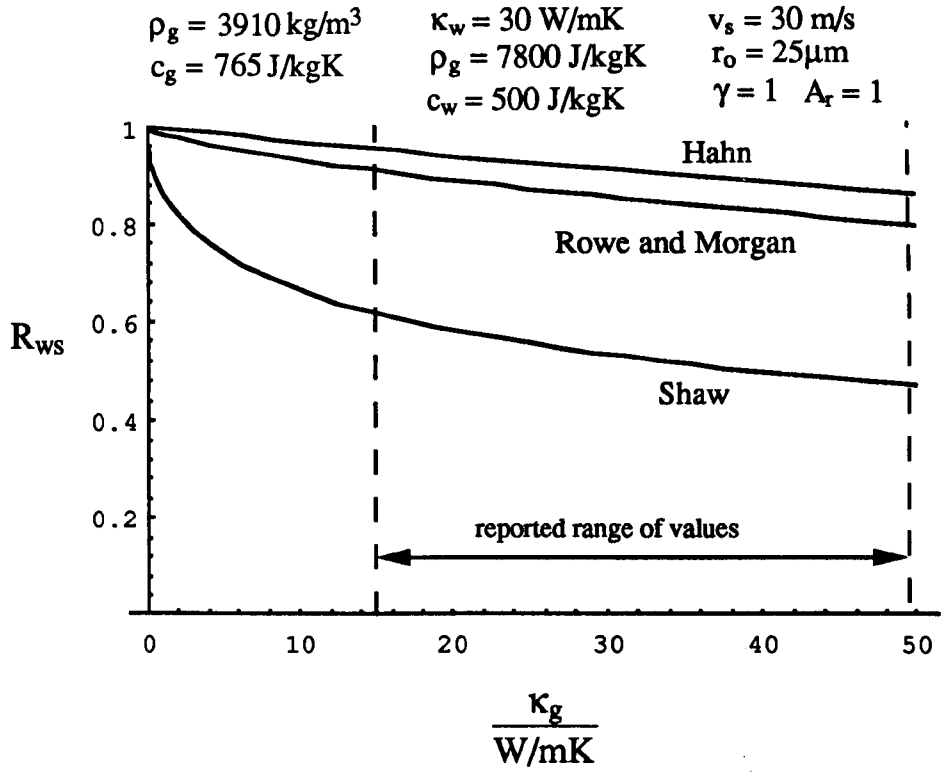

Figure 2.16 : Energy partitioning between workpiece and wheel against reported values of thermal conductivity for alumina abrasive

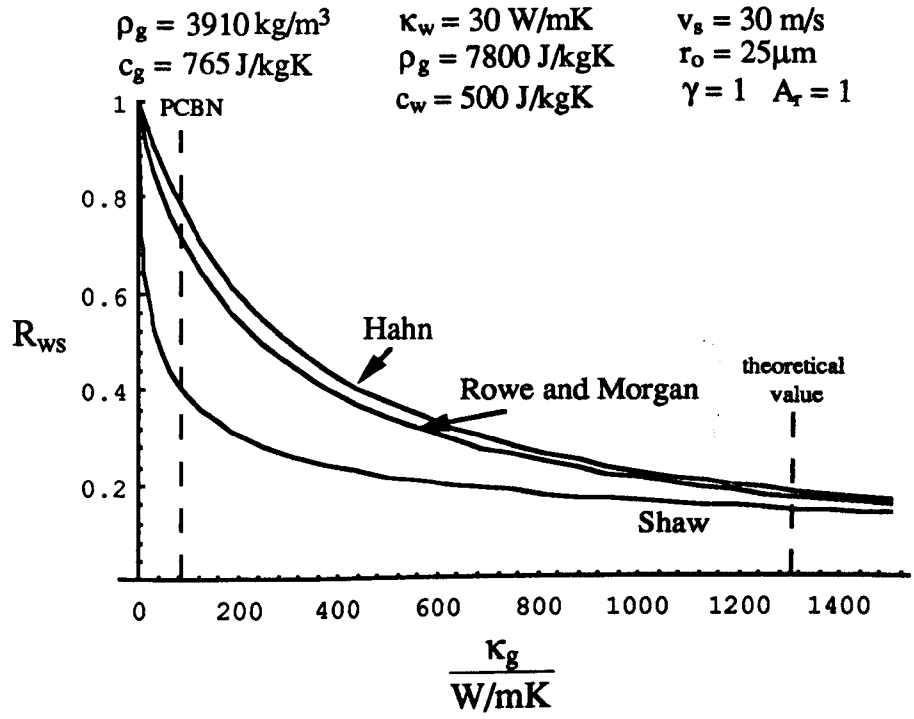

Figure 2.17 : Energy partitioning between workpiece and wheel against reported values of thermal conductivity for CBN abrasive

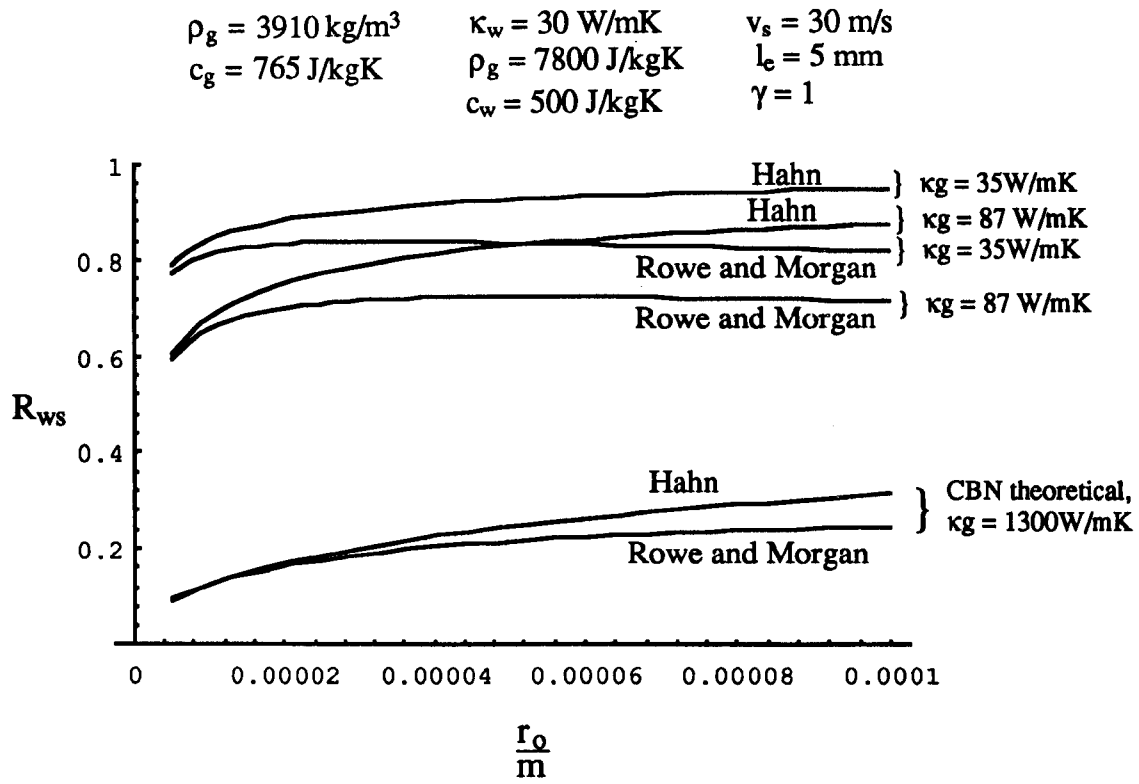

Figure 2.18 : Energy partitioning between workpiece and wheel against grain wear flat radius

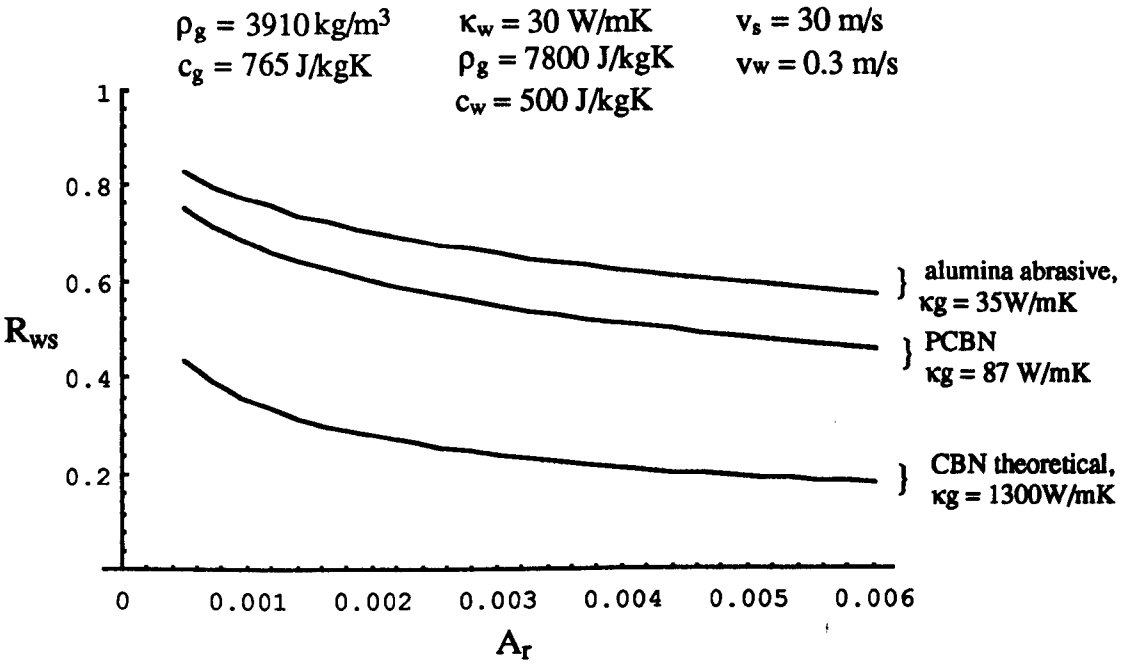

Figure 2.19 : Energy partitioning between workpiece and wheel against fractional contact area according to Shaw [6]

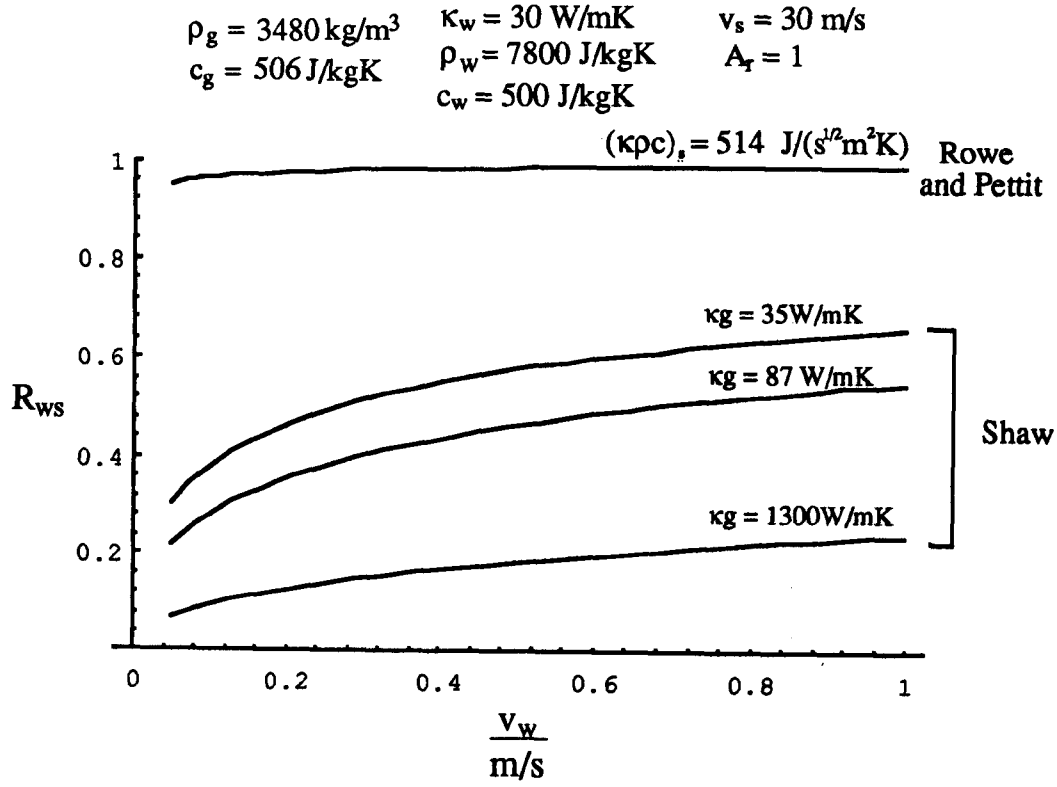

Figure 2.20 : Energy partitioning between workpiece and wheel against workpiece speed

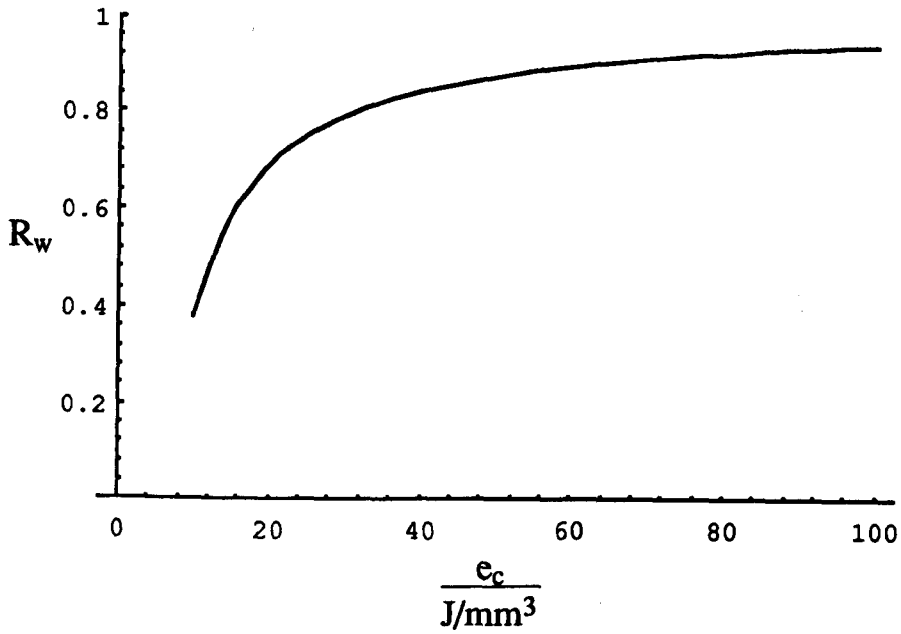

Figure 2.21 : Partition ratio against specific energy according to Malkin [9]

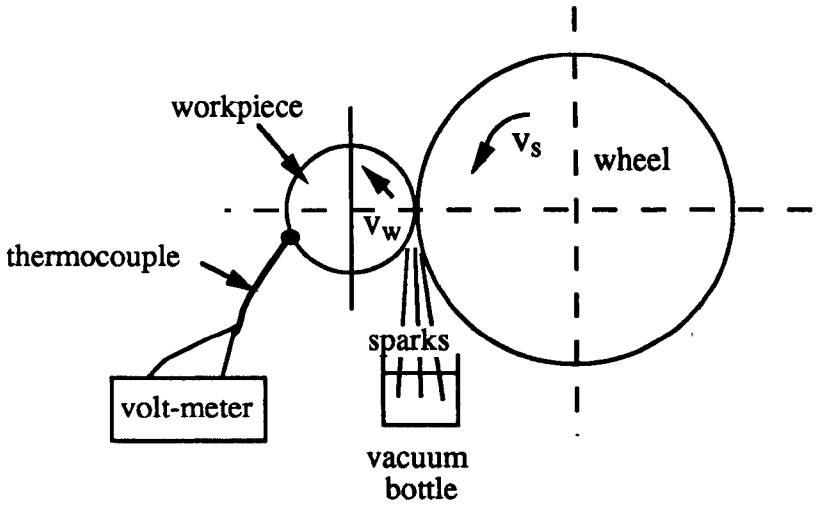

Figure 2.22 : Apparatus for Sato's measurements of the partition ratio in cylindrical grinding [23]

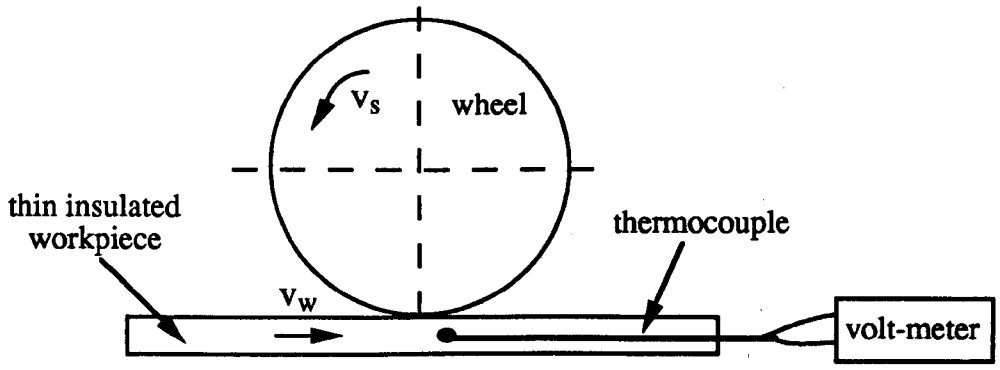

Figure 2.23 : Apparatus for Malkin's measurements of the partition ratio in surface grinding [9]

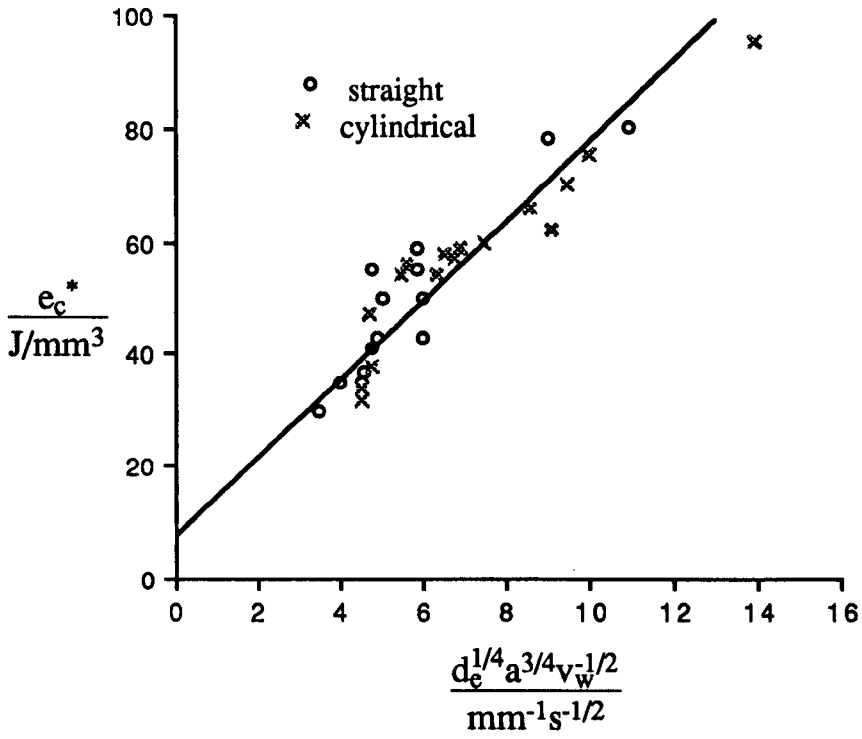

Figure 2.24 : Malkin's burn results [38]

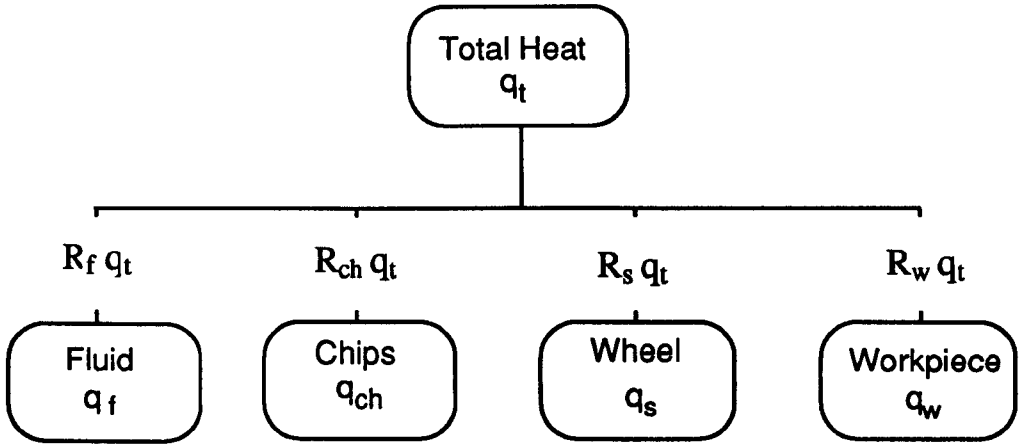

Figure 3.1 : Energy partitioning in the grinding zone

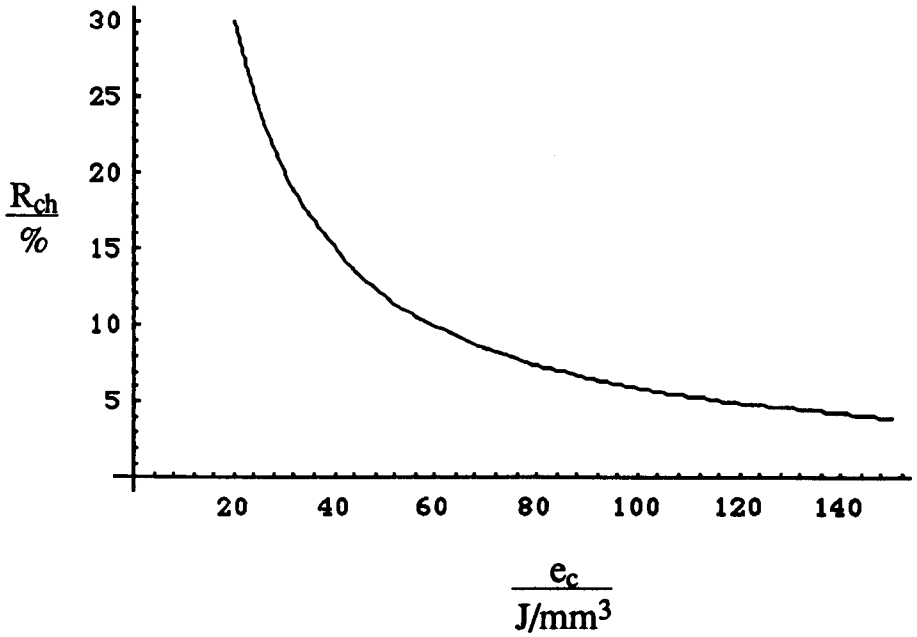

Figure 3.2 : Energy convected to the grinding chips as a percentage of the total grinding energy for different specific energy levels.

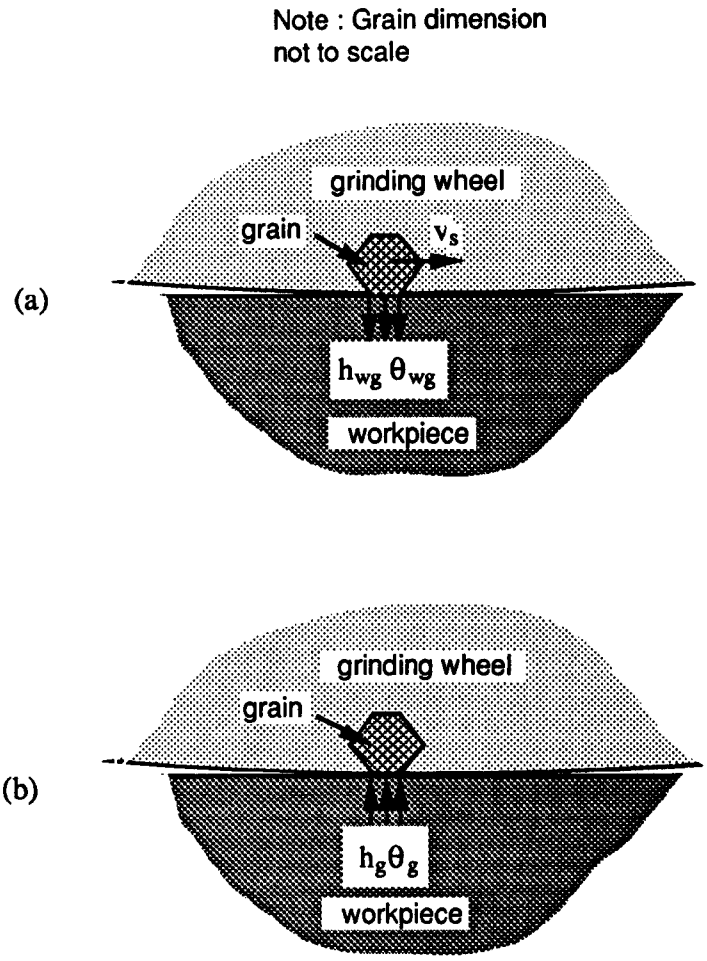

Figure 3.3: a) Heat transfer into the workpiece at a grain
b) Heat transfer into a grain

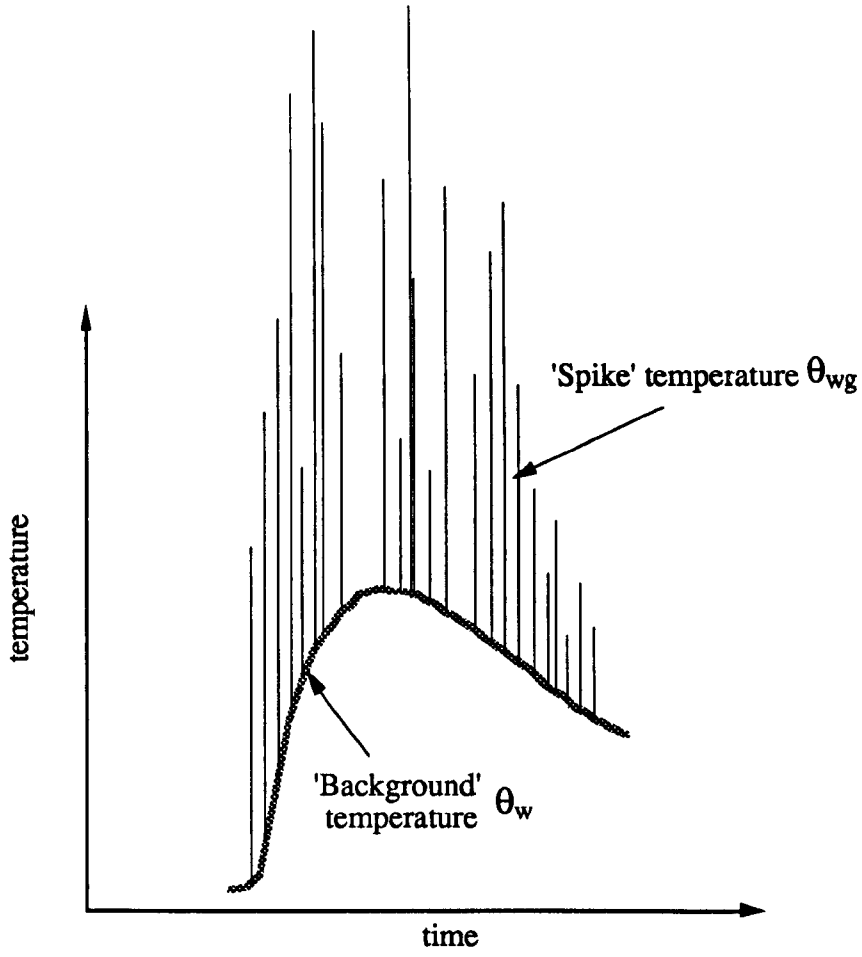

Figure 3.4 : Schematic of temperature / time variation at a point on the workpiece surface.

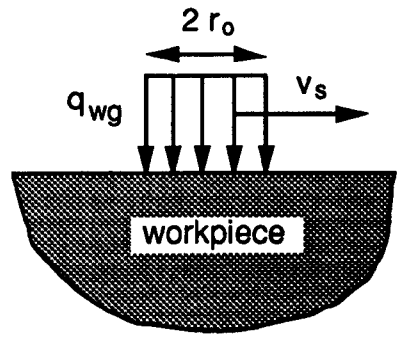

Figure 3.5 : Modelling of workpiece temperature rise under a grain

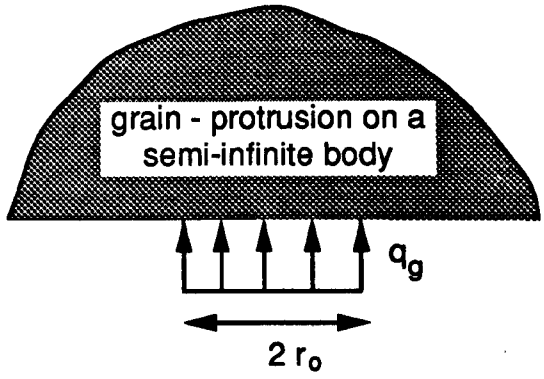

Figure 3.6 : Grain modelled as a stationary semi-infinite body

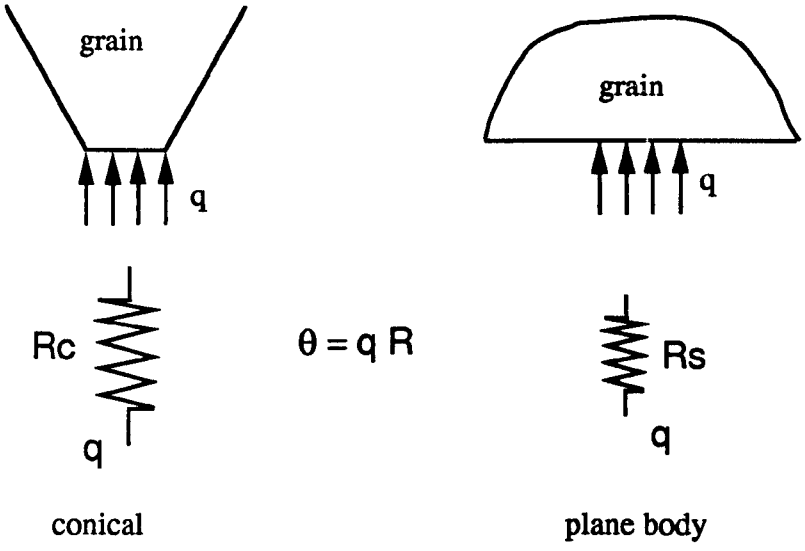

Figure 3.7 : Thermal resistance of a conical and a plane body

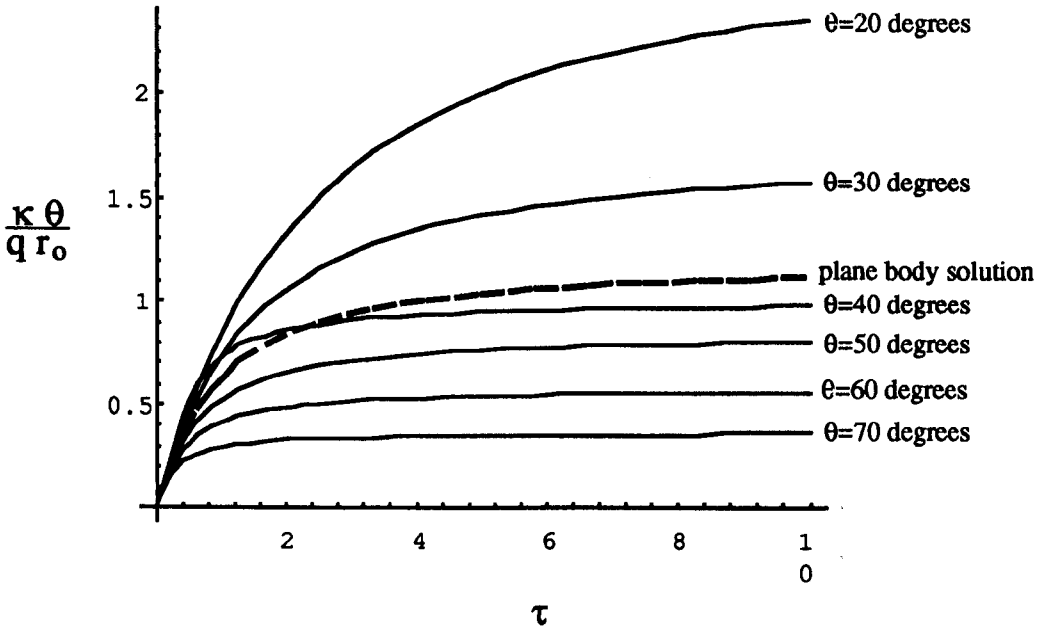

Figure 3.8 : Comparison of plane body and conical body temperature solutions

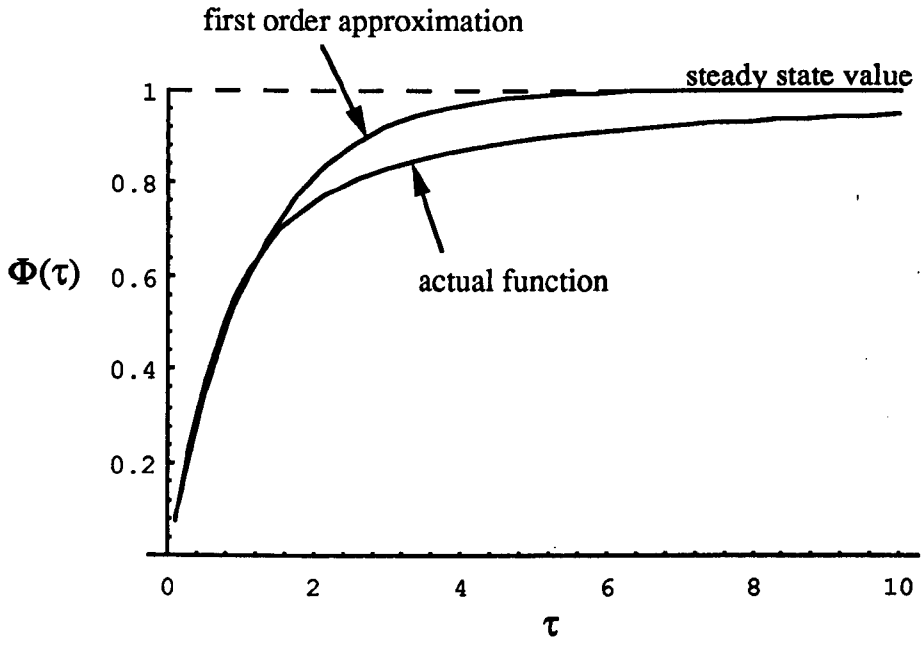

Figure 3.9 : Comparison of transient function $\Phi(\tau)$ and the first order approximation

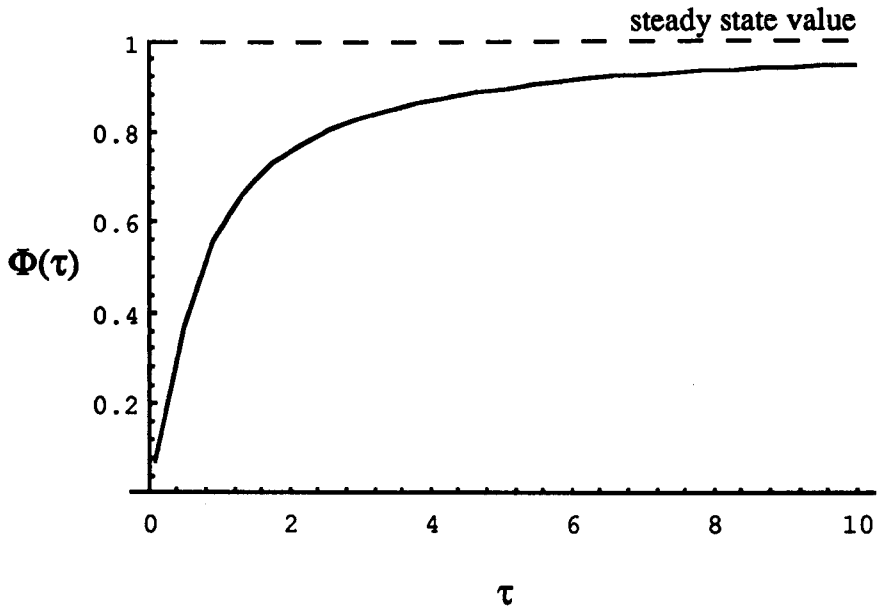

Figure 3.10 : Transient function $\Phi(\tau)$ against dimensionless time

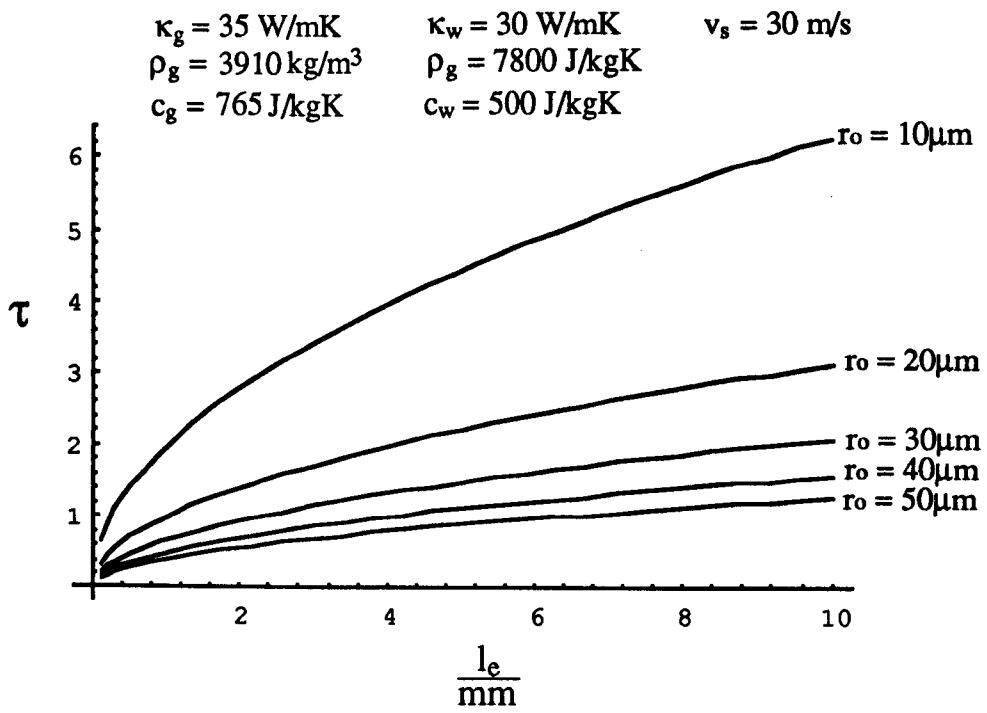

Figure 3.11 : Values of dimensionless time for an alumina wheel

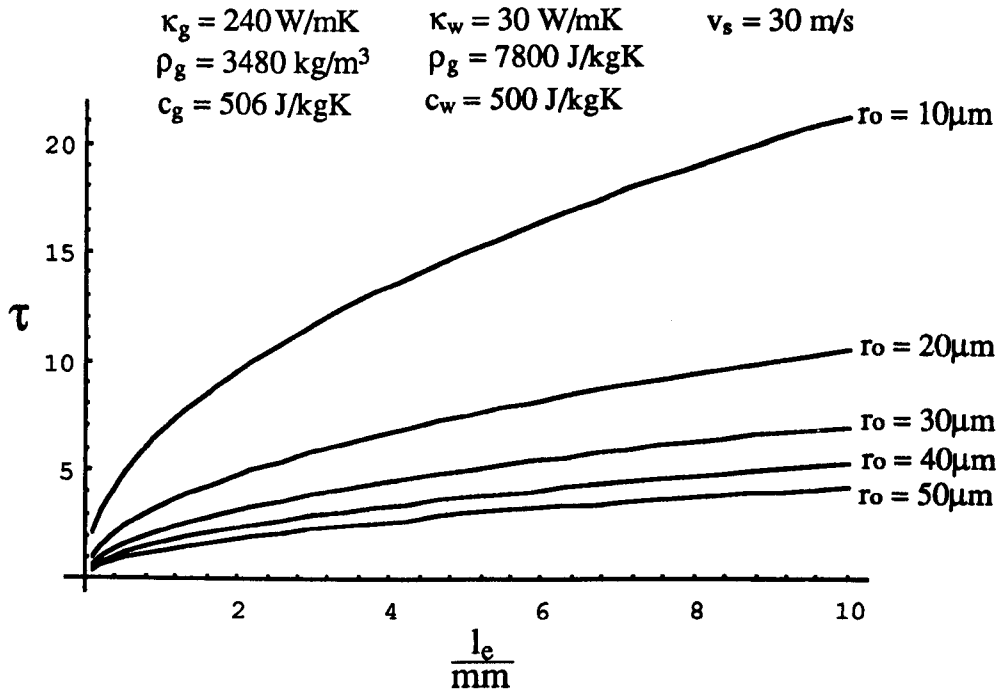

Figure 3.12 : Values of dimensionless time for a CBN wheel

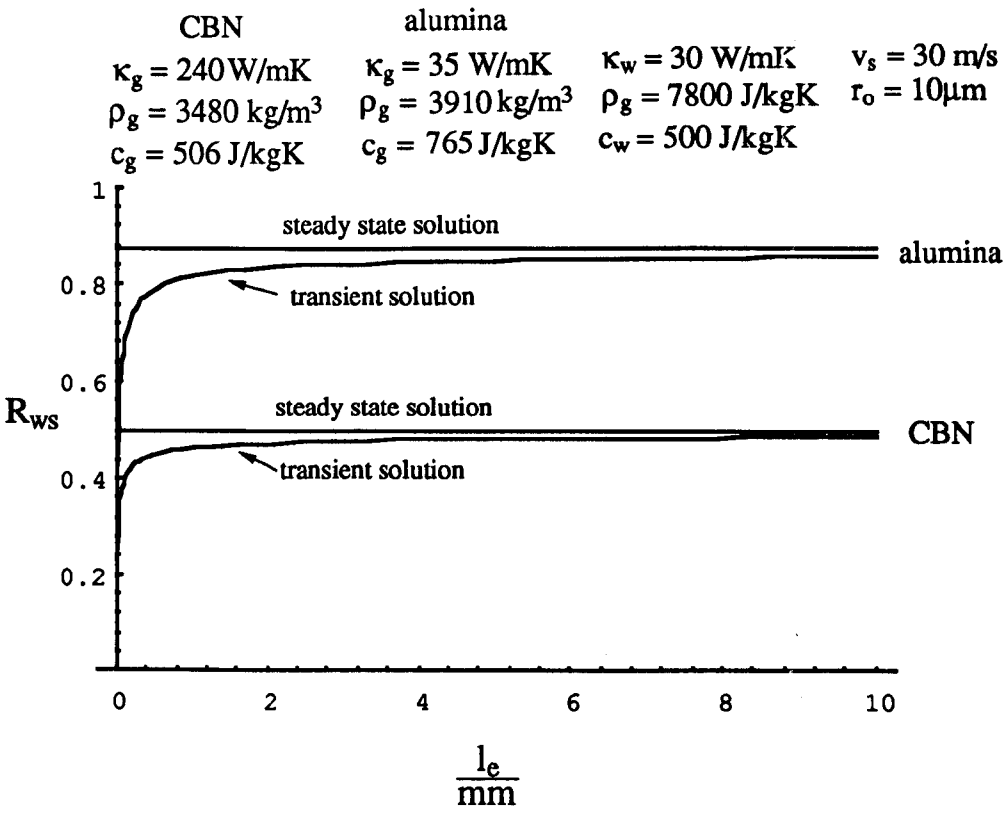

Figure 3.13 : Comparison of steady state and transient partitioning solutions for ro=10μm

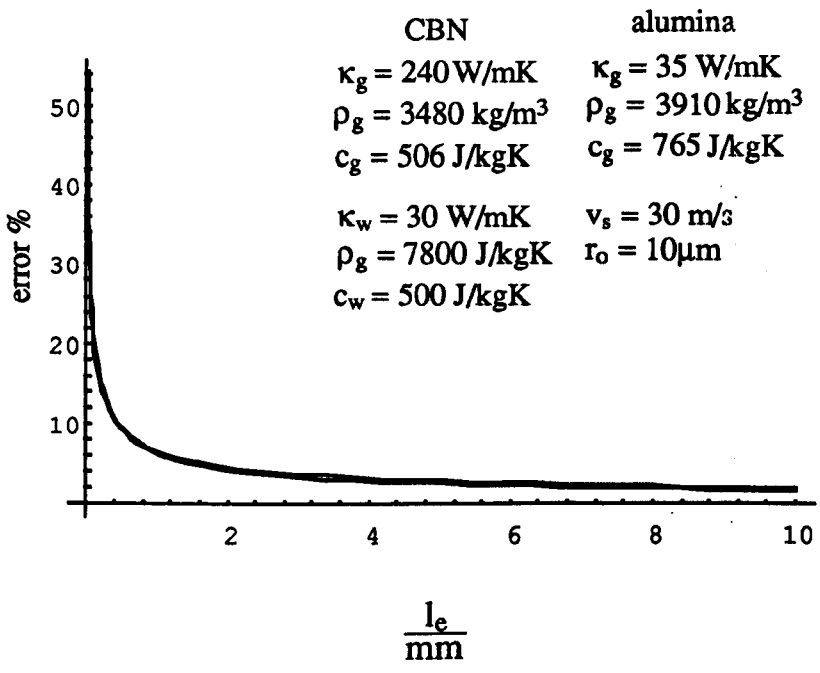

Figure 3.14 : Error in steady state assumption for ro=10μm

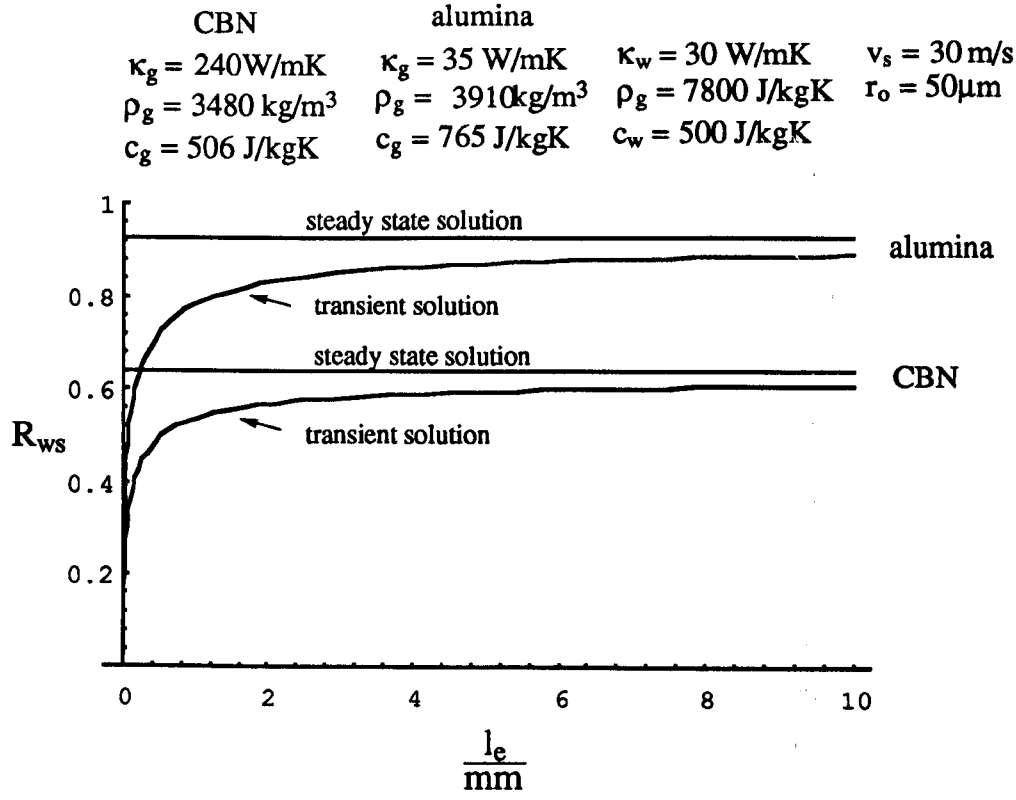

Figure 3.15 : Comparison of steady state and transient partitioning solutions for ro=50μm

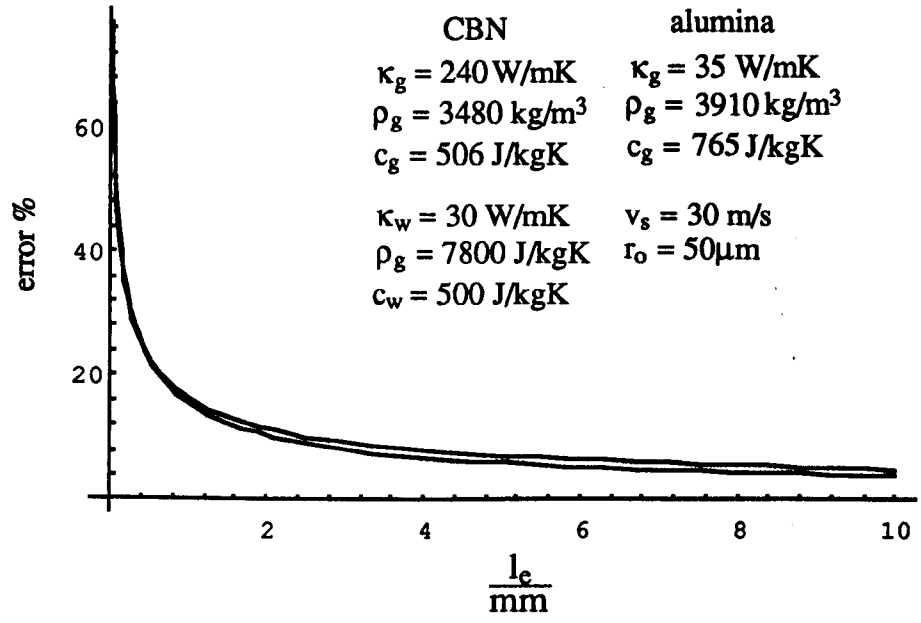

Figure 3.16 : Error in steady state assumption for ro=50μm

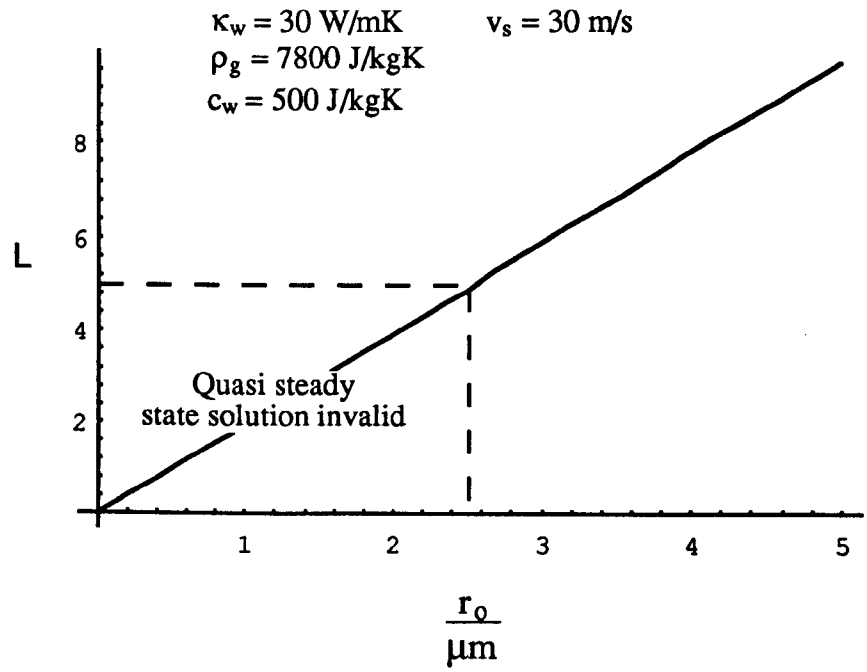

Figure 3.17 : Workpiece Peclet number against wear flat radius

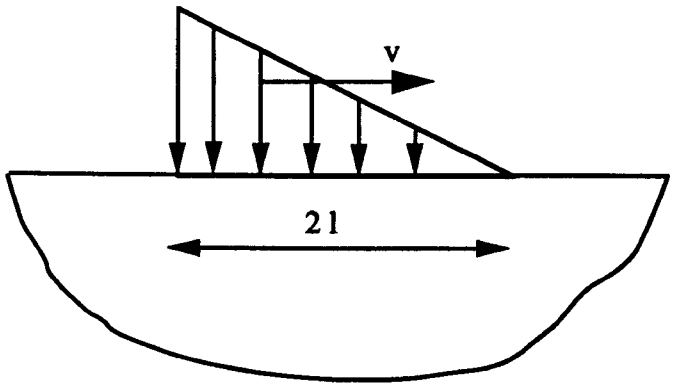

Figure 4.1 : Linear heat flux distribution in the grinding zone

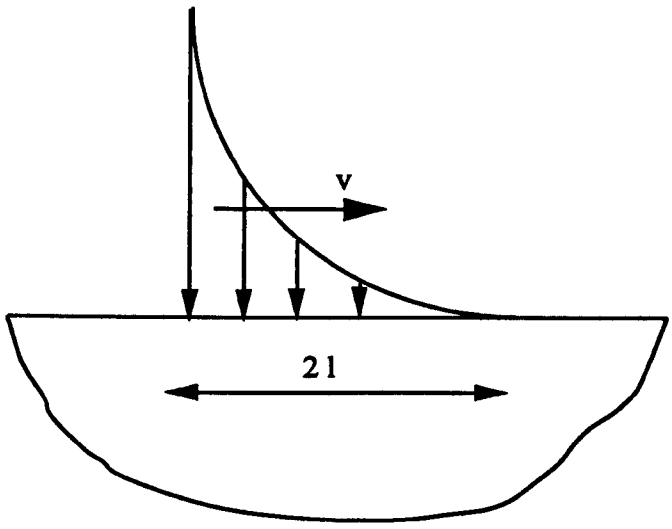

Figure 4.2 : Square law heat flux distribution in the grinding zone

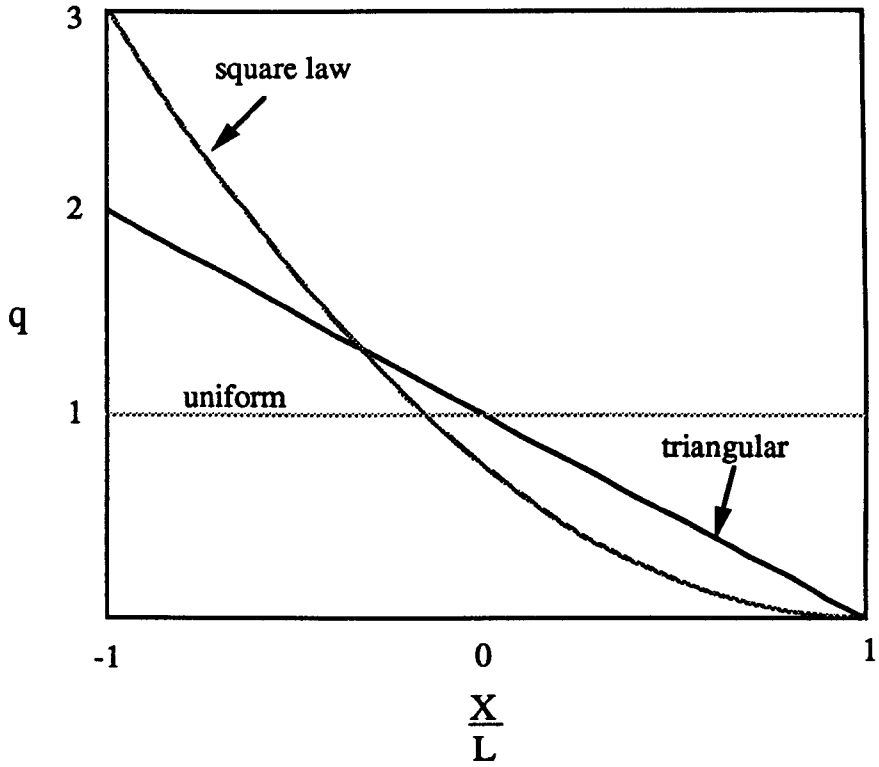

Figure 4.3 : Comparison of uniform, triangular and square law heat flux

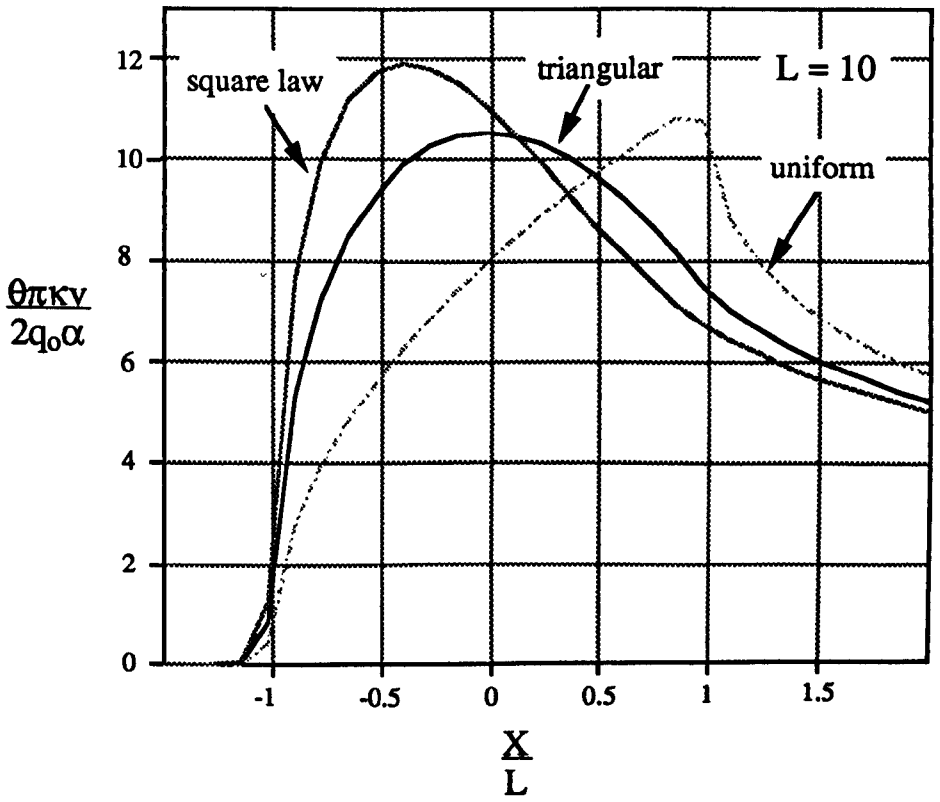

Figure 4.4 : Comparison of the dimensionless temperature for uniform, triangular and square heat flux

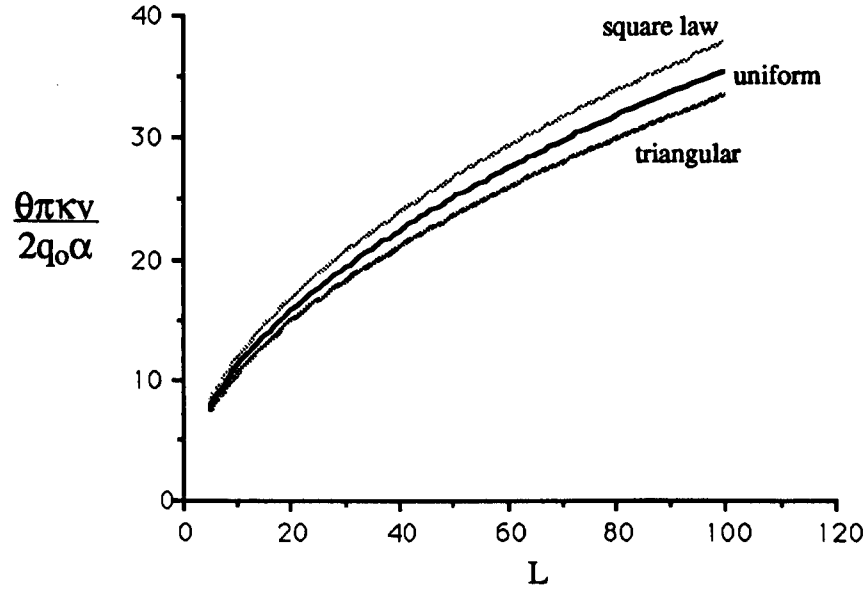

Figure 4.5 : Dimensionless maximum temperature against Peclet number

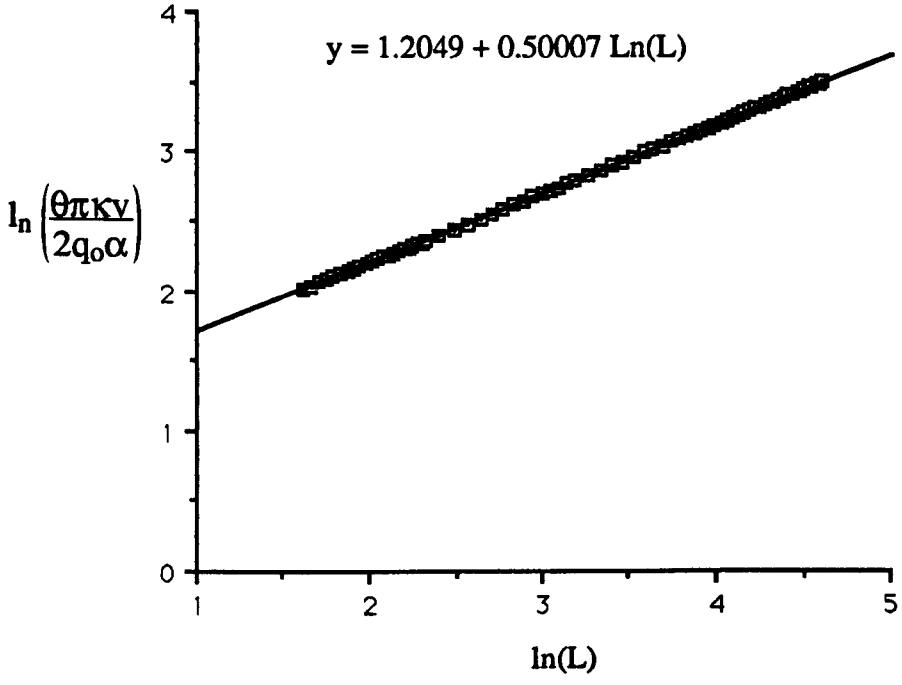

Figure 4.6 : Natural logarithm of dimensionless temperature against natural logarithm of Peclet number for a triangular heat flux

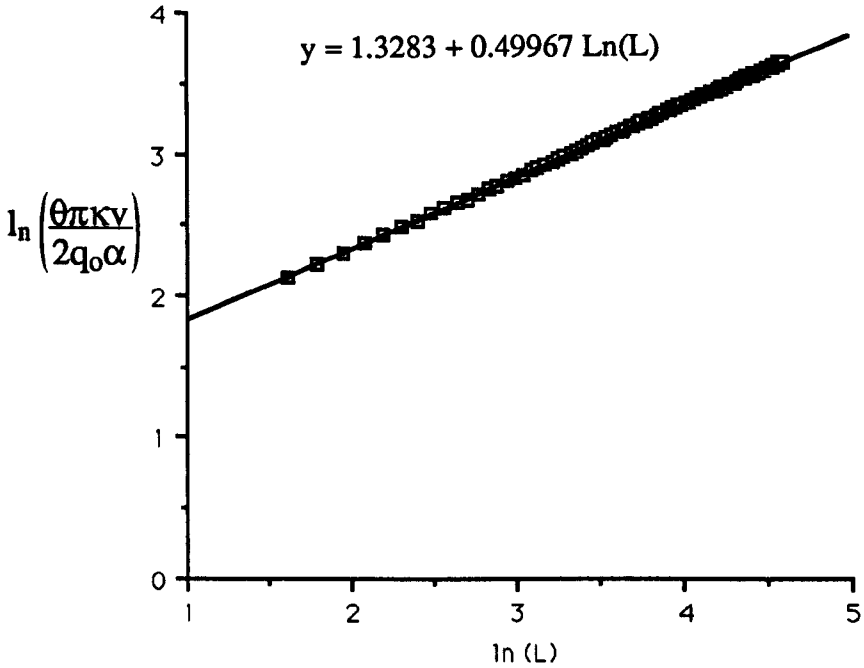

Figure 4.7 : Natural logarithm of dimensionless temperature against nataural logarithm of Peclet number for a square law heat flux

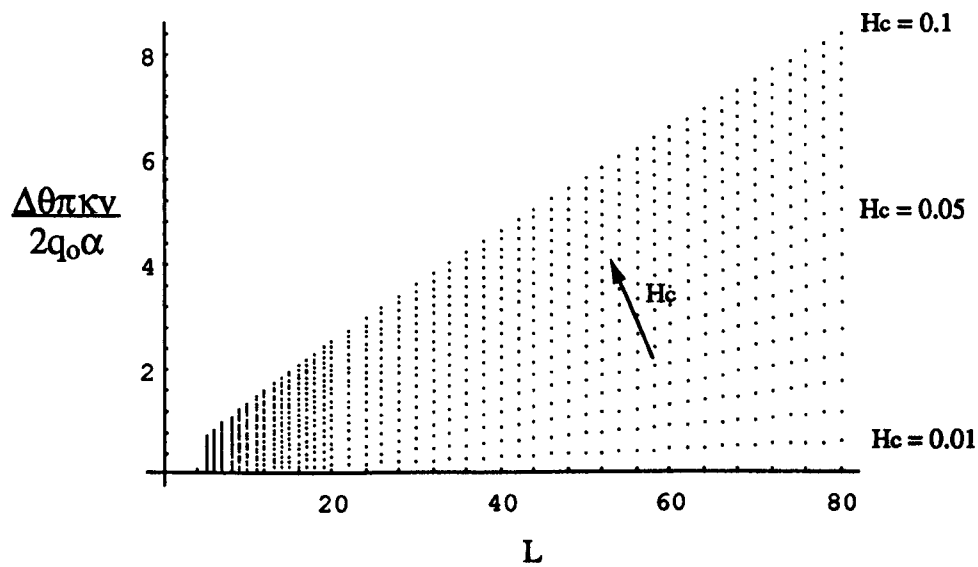

Figure 4.8 : Reduction in maximum dimensionless temperature against Peclet number due to convective cooling for a square law heat flux

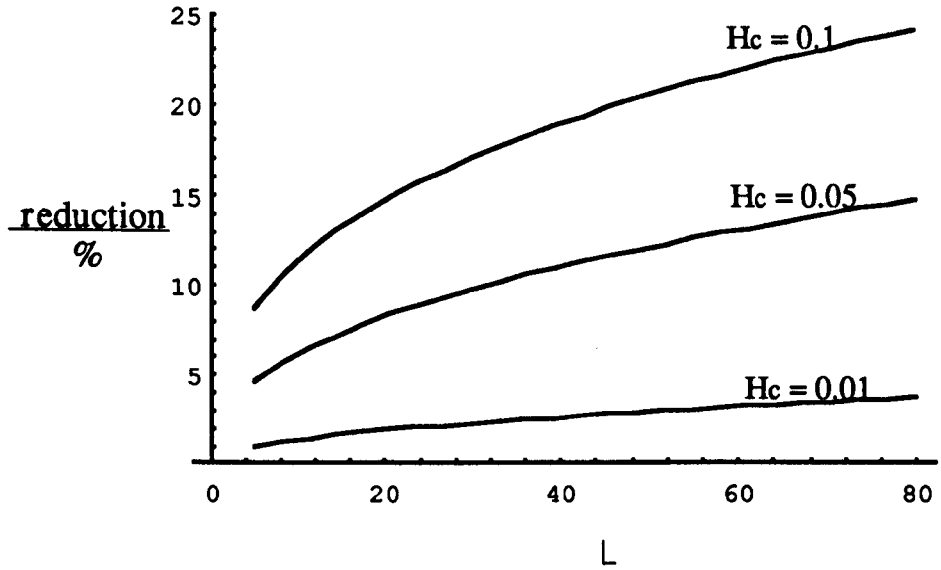

Figure 4.9 : Reduction in maximum temperature against Peclet number due to convective cooling for a square law heat flux

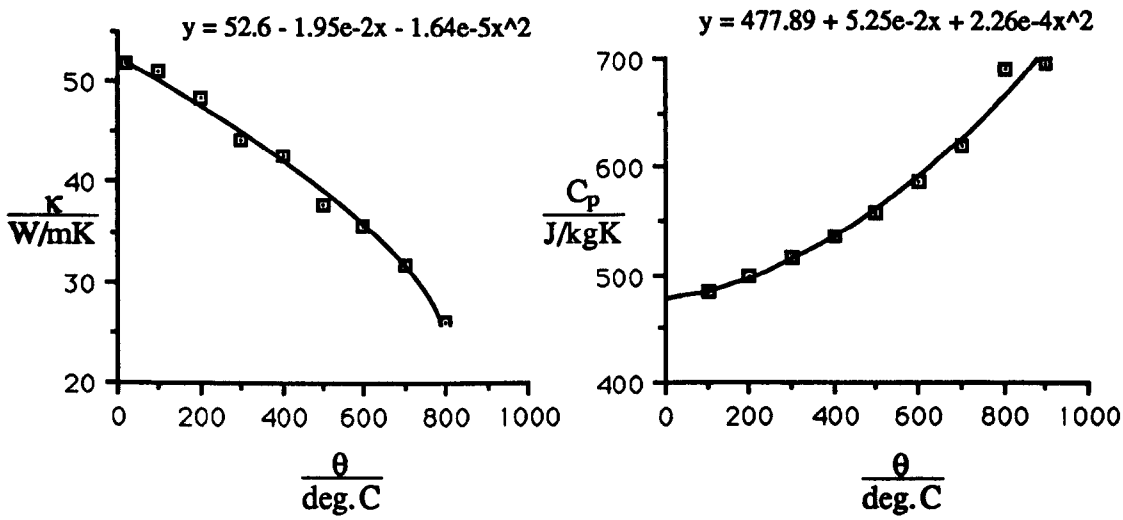

Figure 4.10 : Variation in thermal conductivity and specific heat capacity with temperature for a mild steel

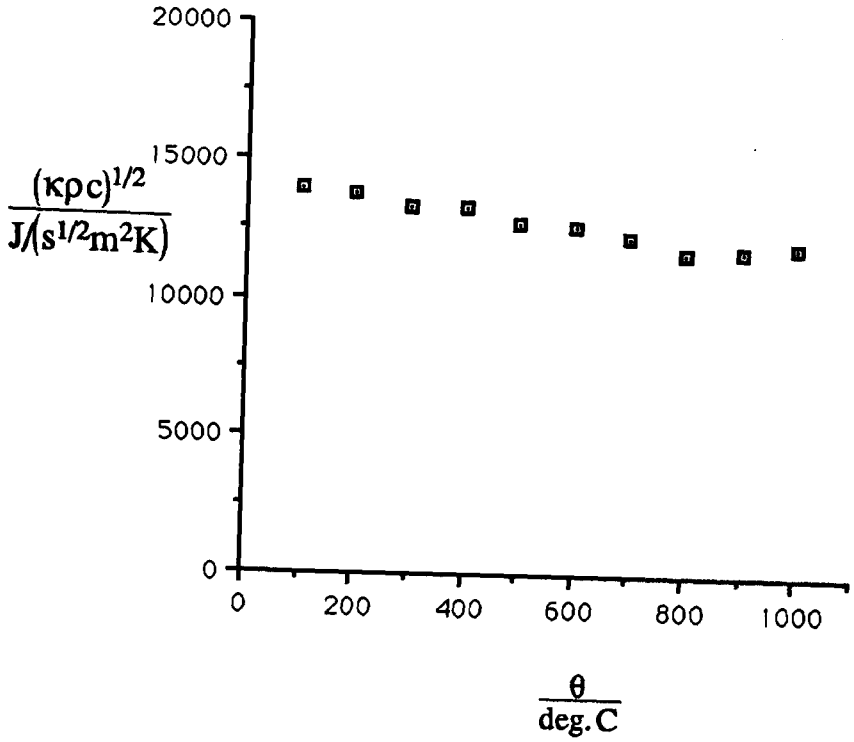

Figure 4.11 : Variation in thermal contact coefficient with temperature for mild steel

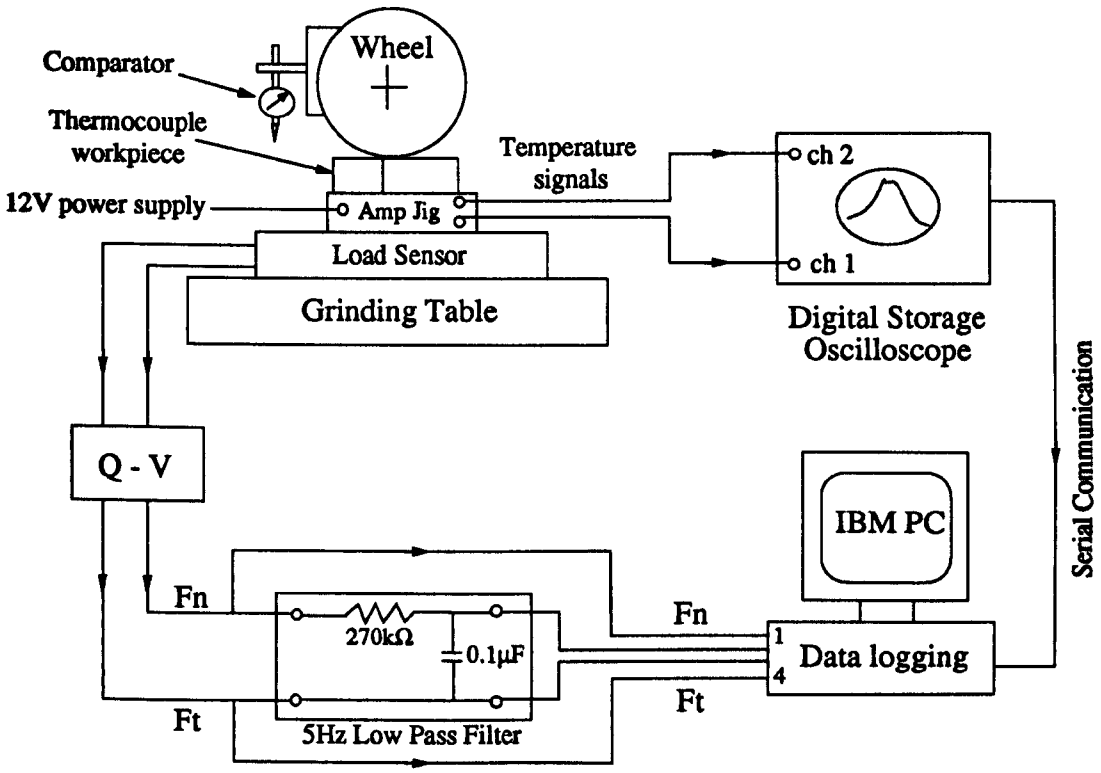

Figure 5.1 : Schematic diagram of the measuring system

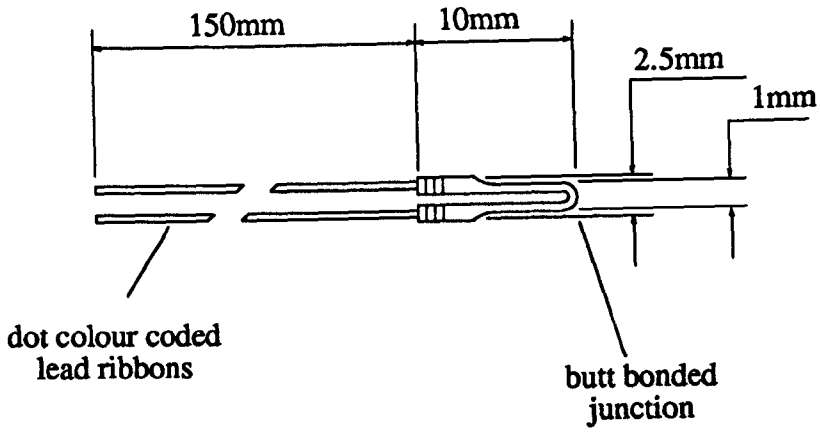

Figure 5.2 : Type K foil thermocouple

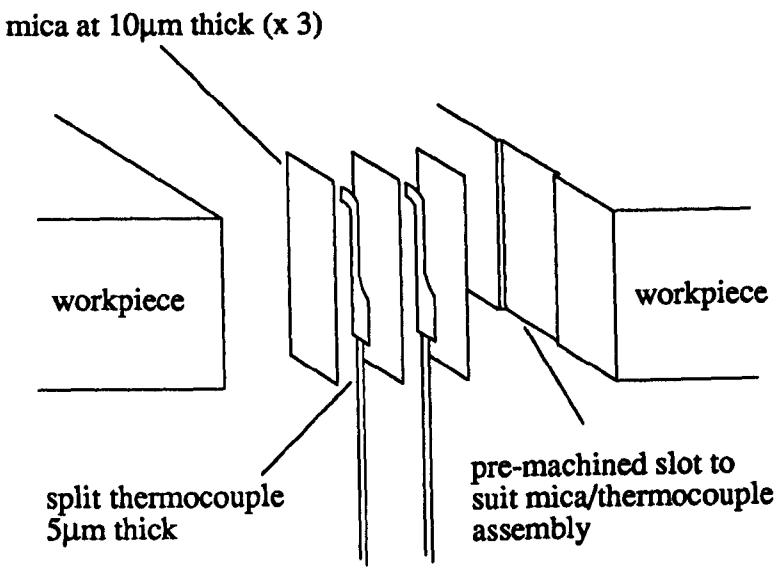

Figure 5.3 : Standard thermocouple assembly

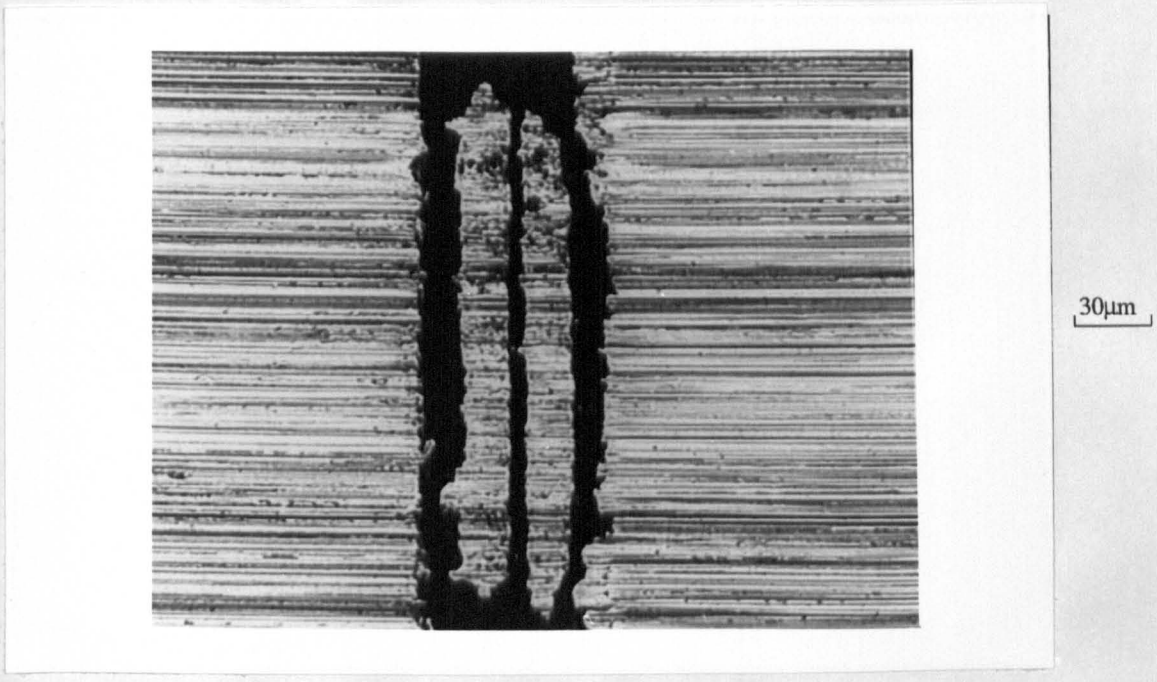

Figure 5.4 : Standard thermocouple measuring junction after assembly

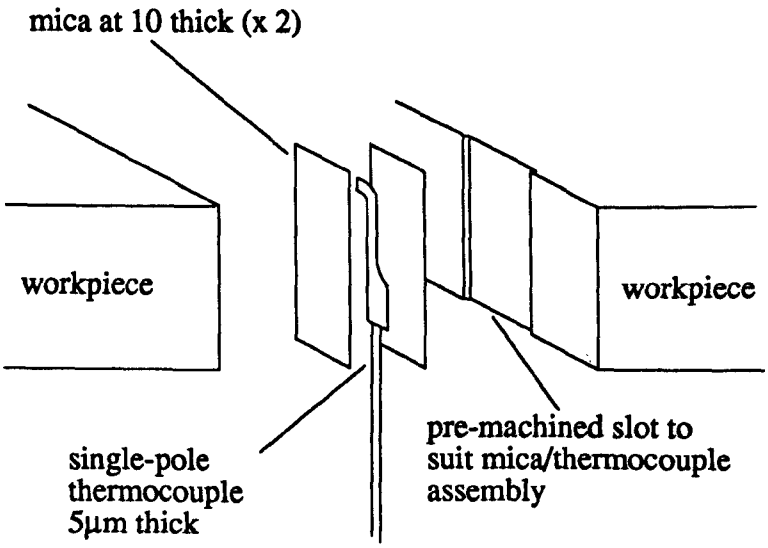

Figure 5.5 : Single pole thermocouple assembly

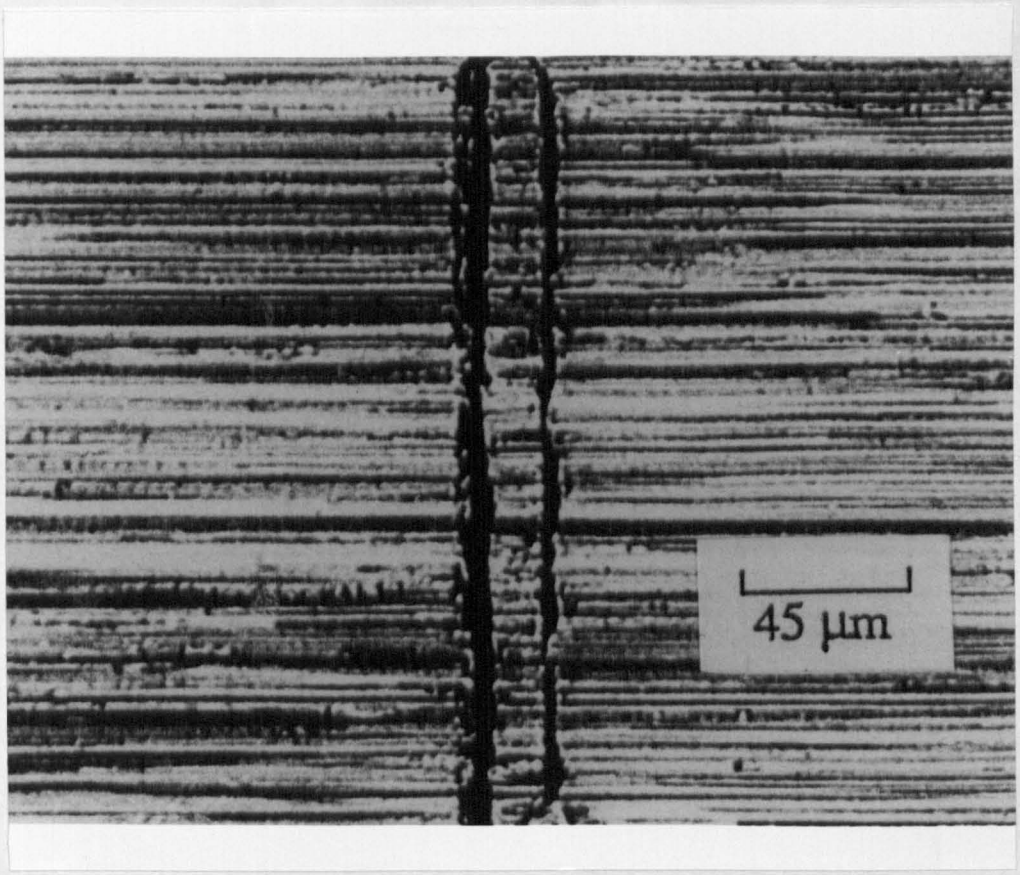

Figure 5.6 : Single pole measuring junction after assembly

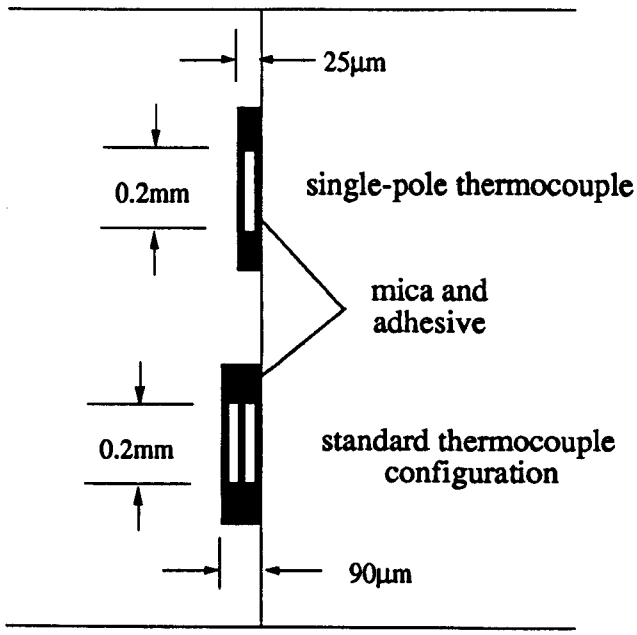

Figure 5.7 : Workpiece assemby

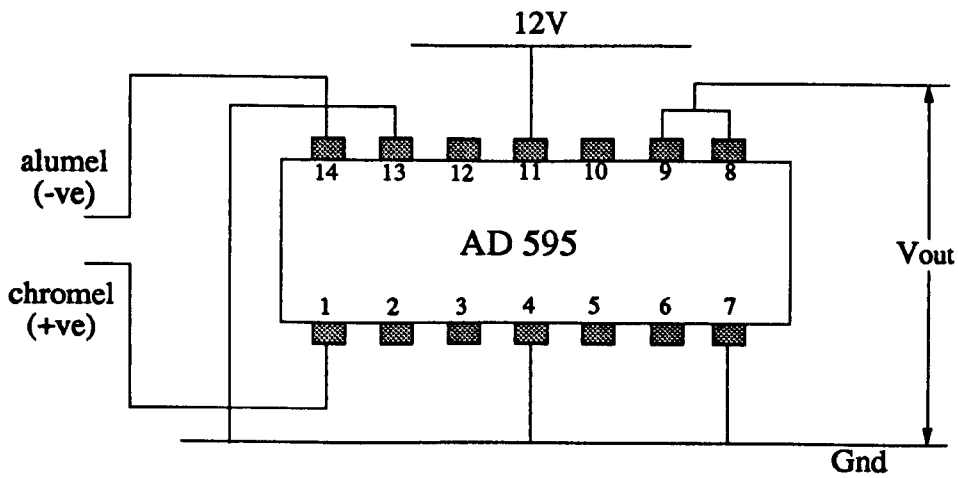

Figure 5.8 : Circuit diagram for the thermocouple amplifier AD595

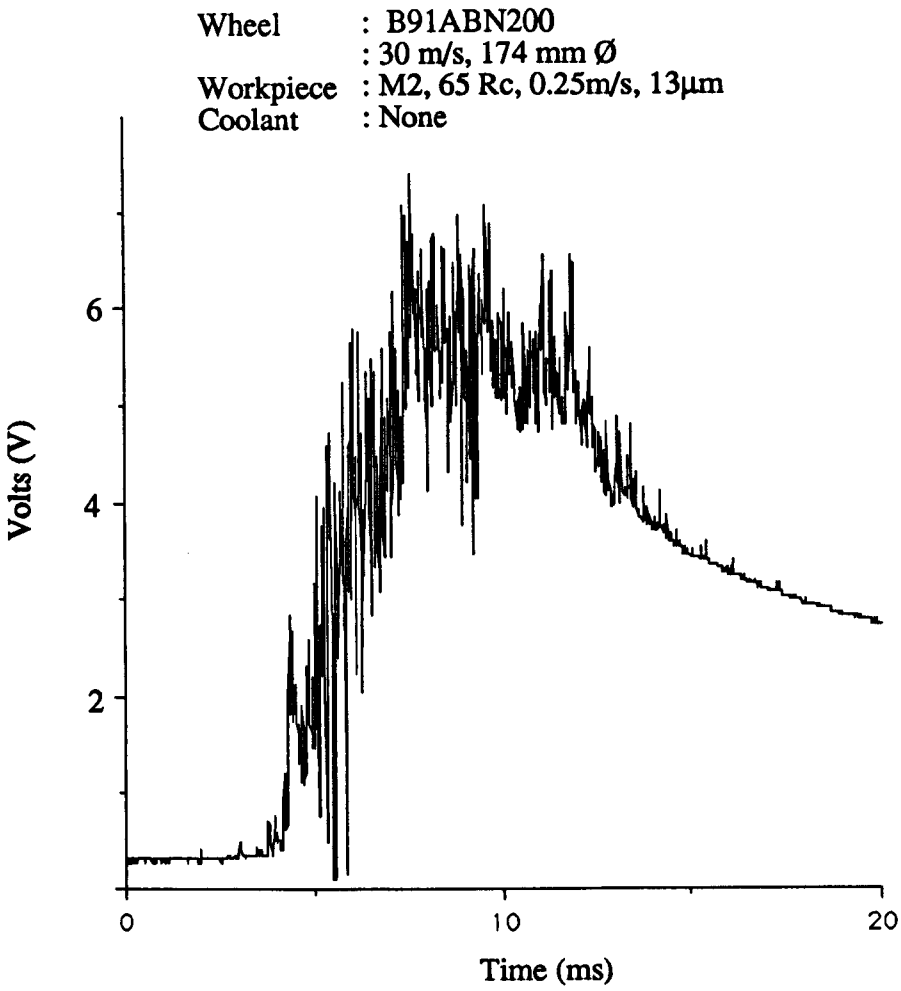

Figure 5.9 : An example of the signal from the standard thermocouple in dry grinding

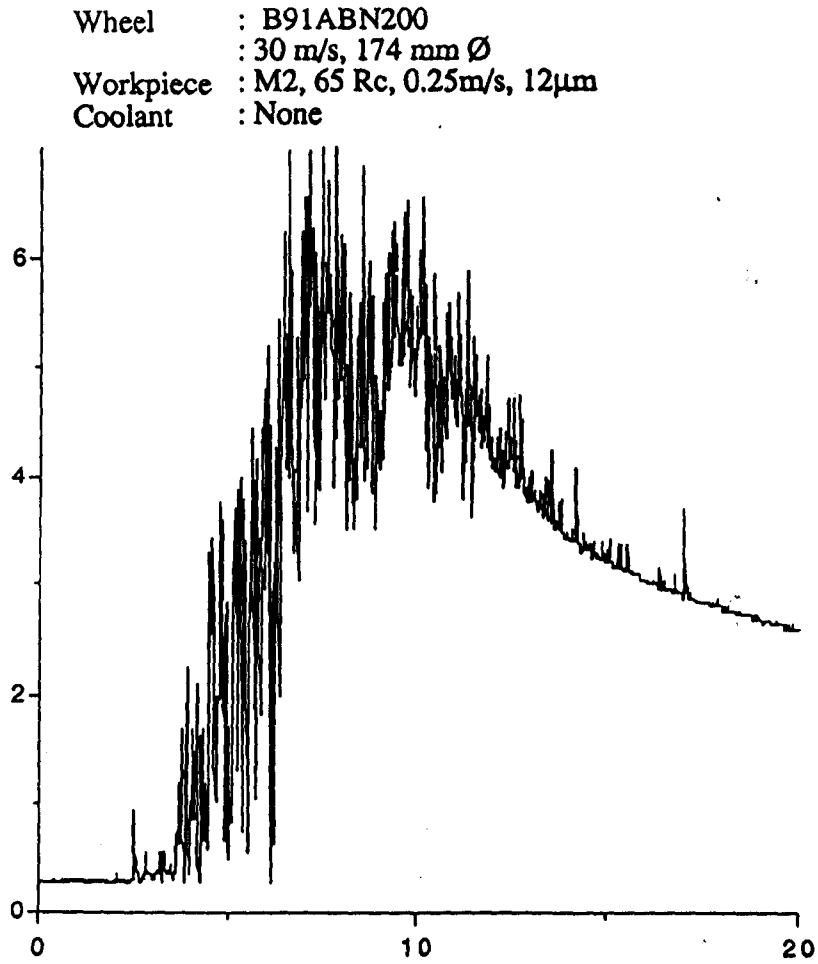

Figure 5.10 : An example of the repeatibility of the measurement using the standard thermocouple in dry grinding

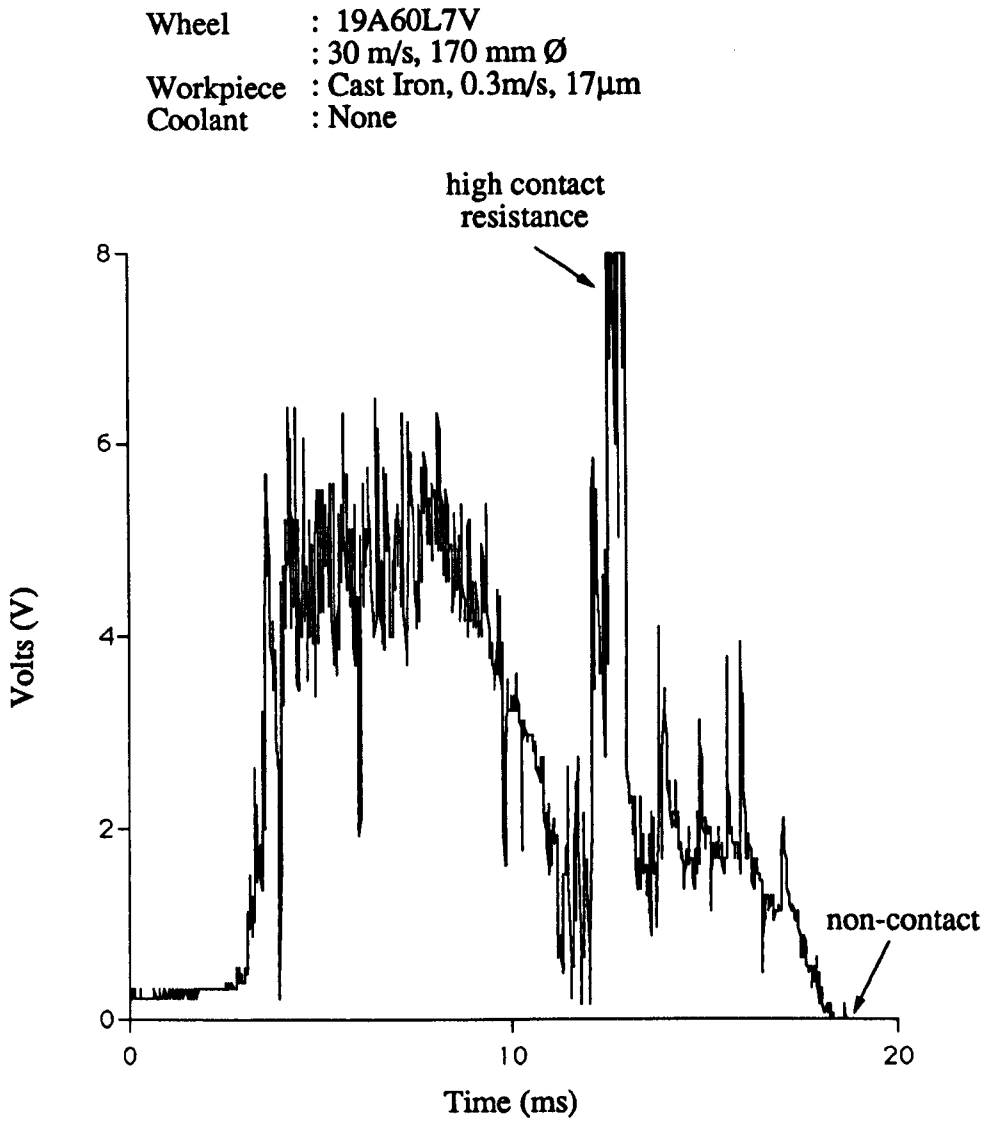

Figure 5.11 : An example of the standard thermocouple signal with poor contact

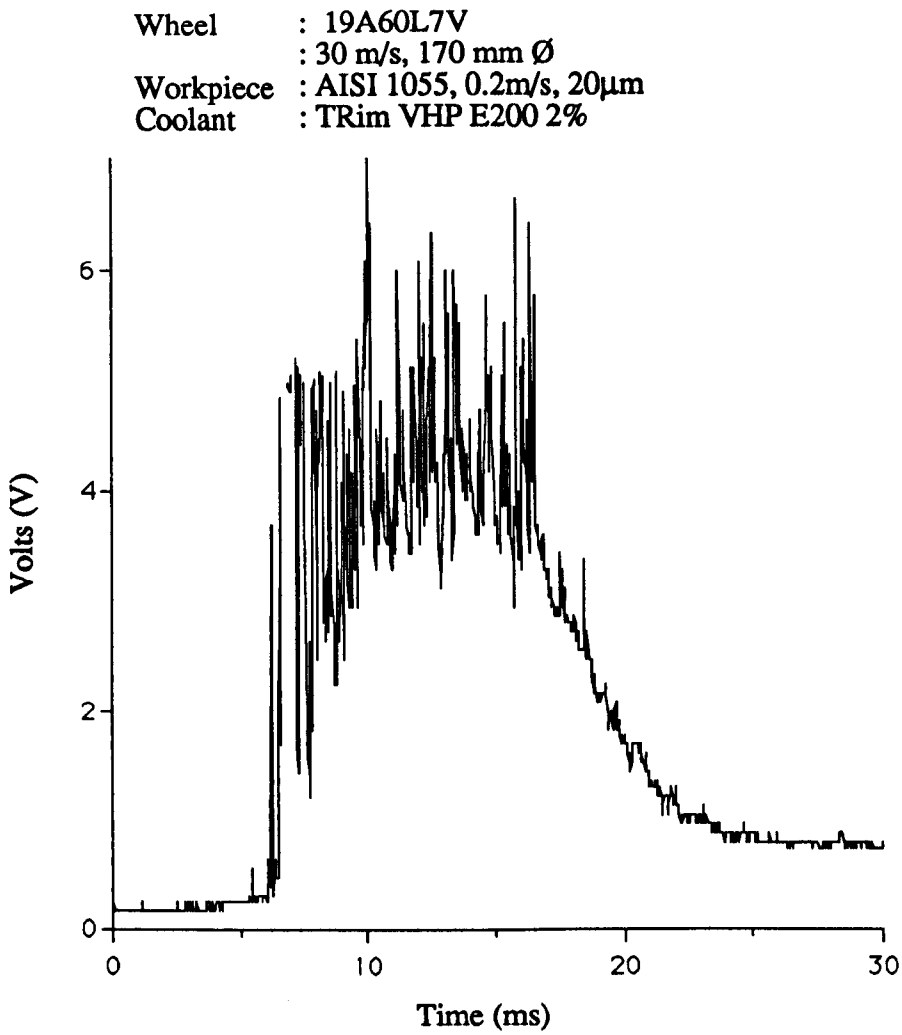

Figure 5.12 : An example of the signal from the standard thermocouple in wet grinding

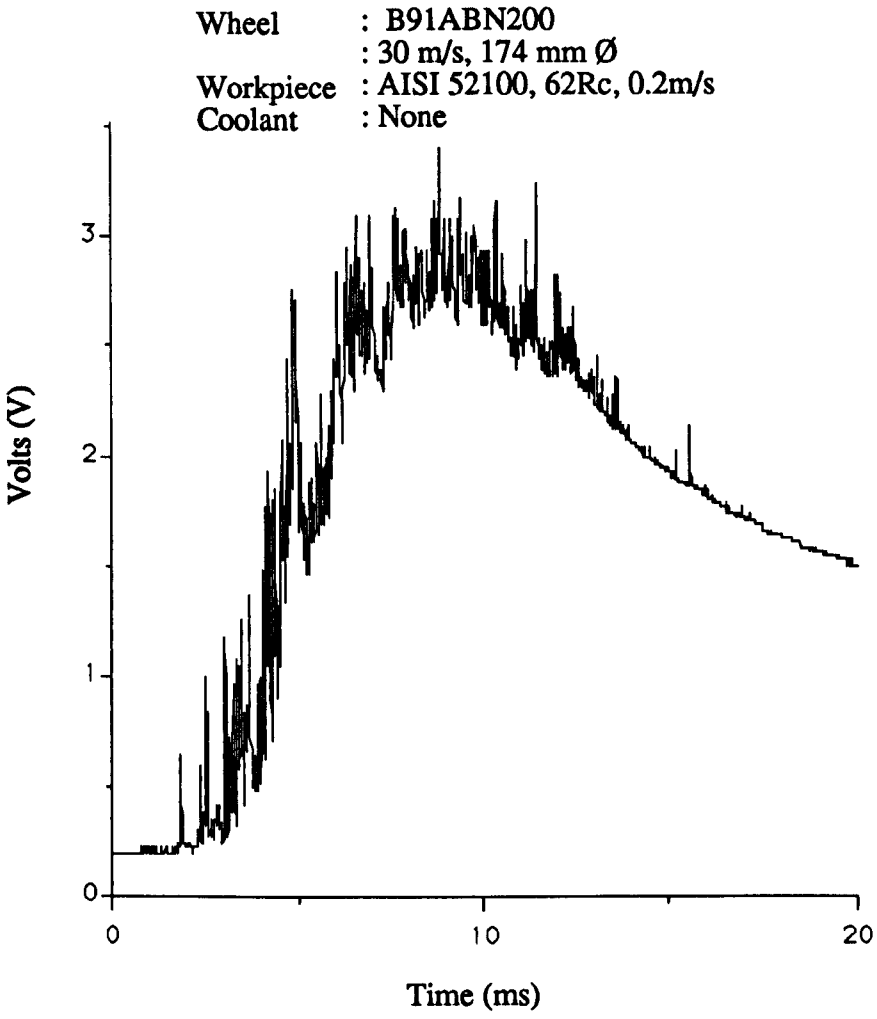

Figure 5.13 : An example of the signal from the single pole thermocouple in dry grinding

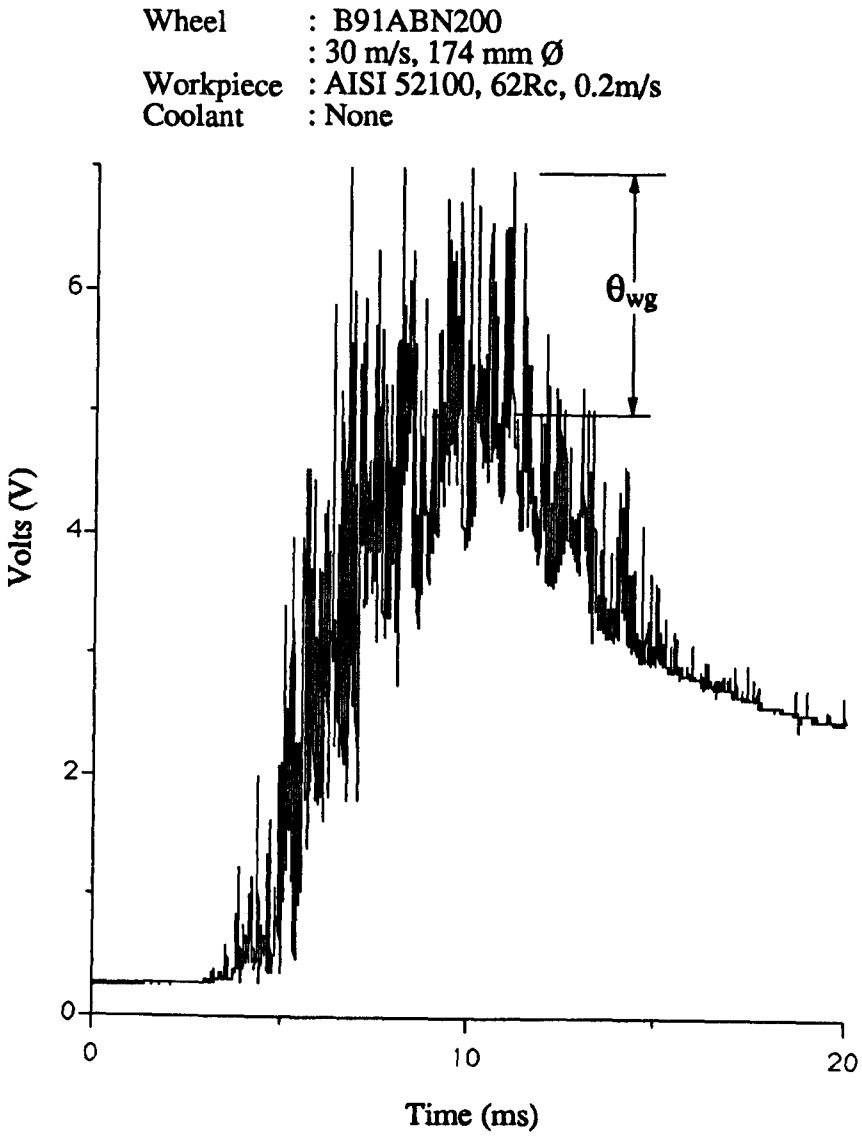

Figure 5.14 : An example of the signal from the standard thermocouple in dry grinding

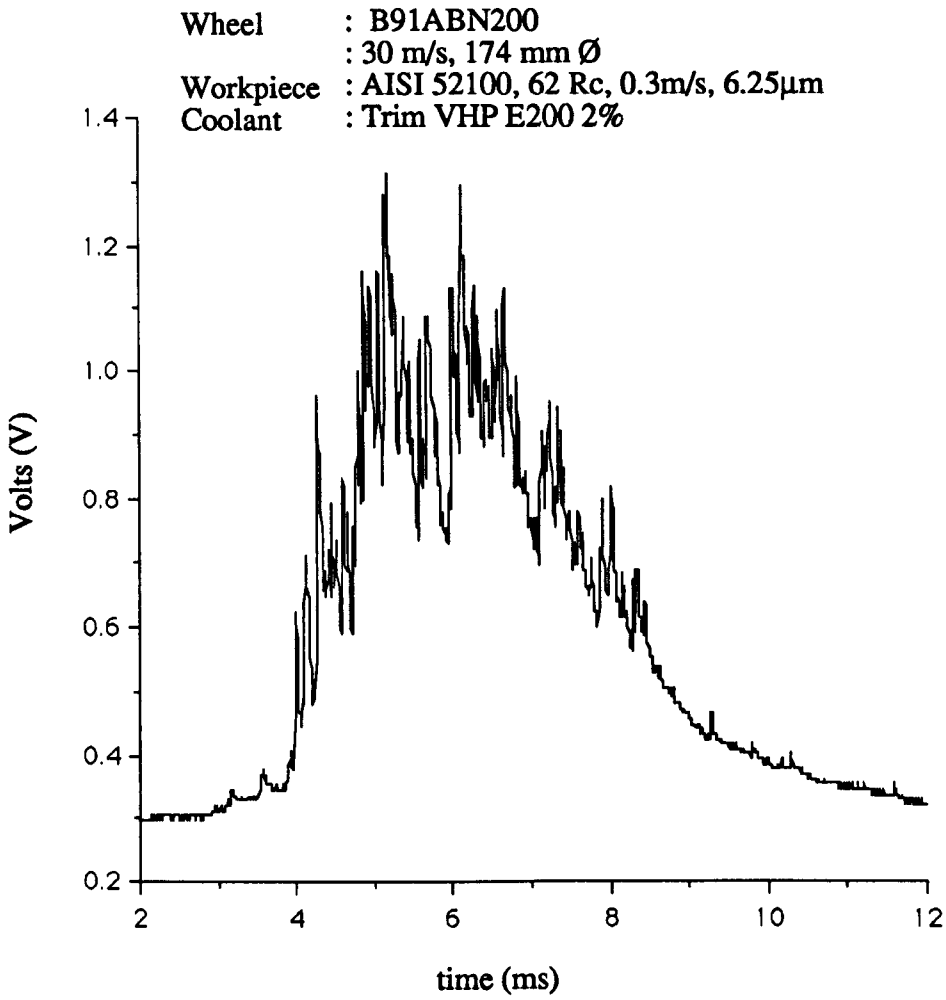

Figure 5.15 : An example of the signal from the single pole thermocouple in wet grinding

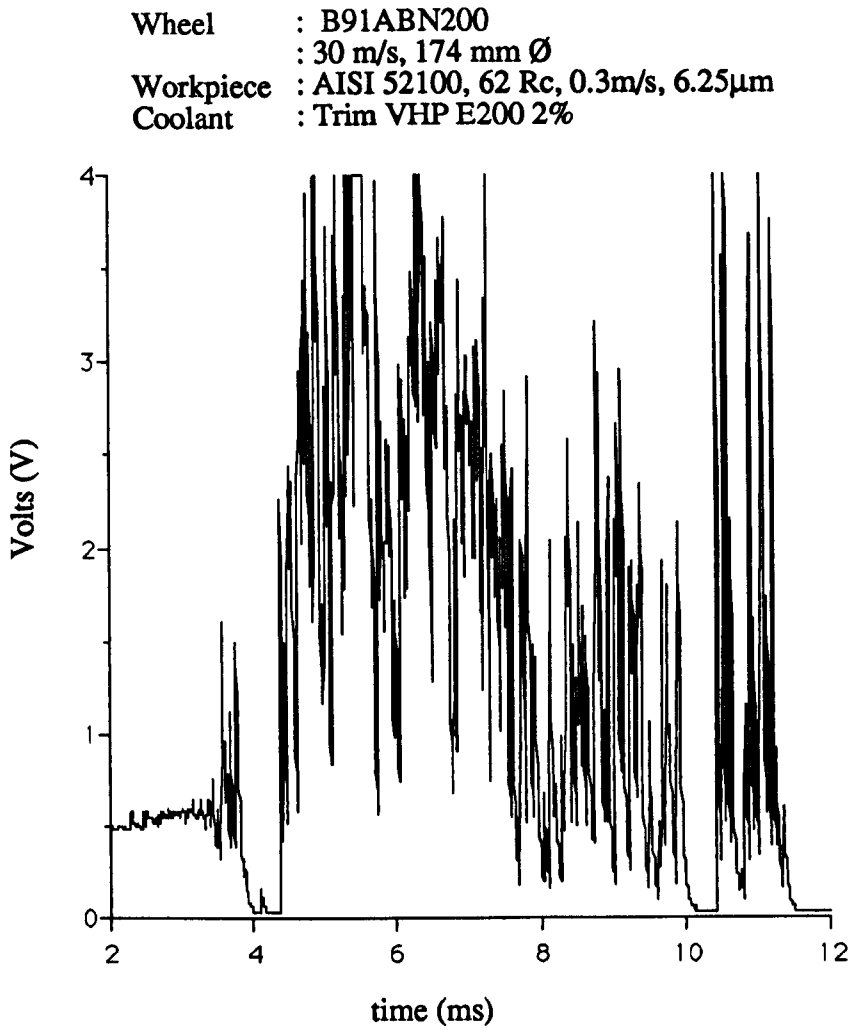

Figure 5.16 : An example of the signal from the standard thermocouple in wet grinding

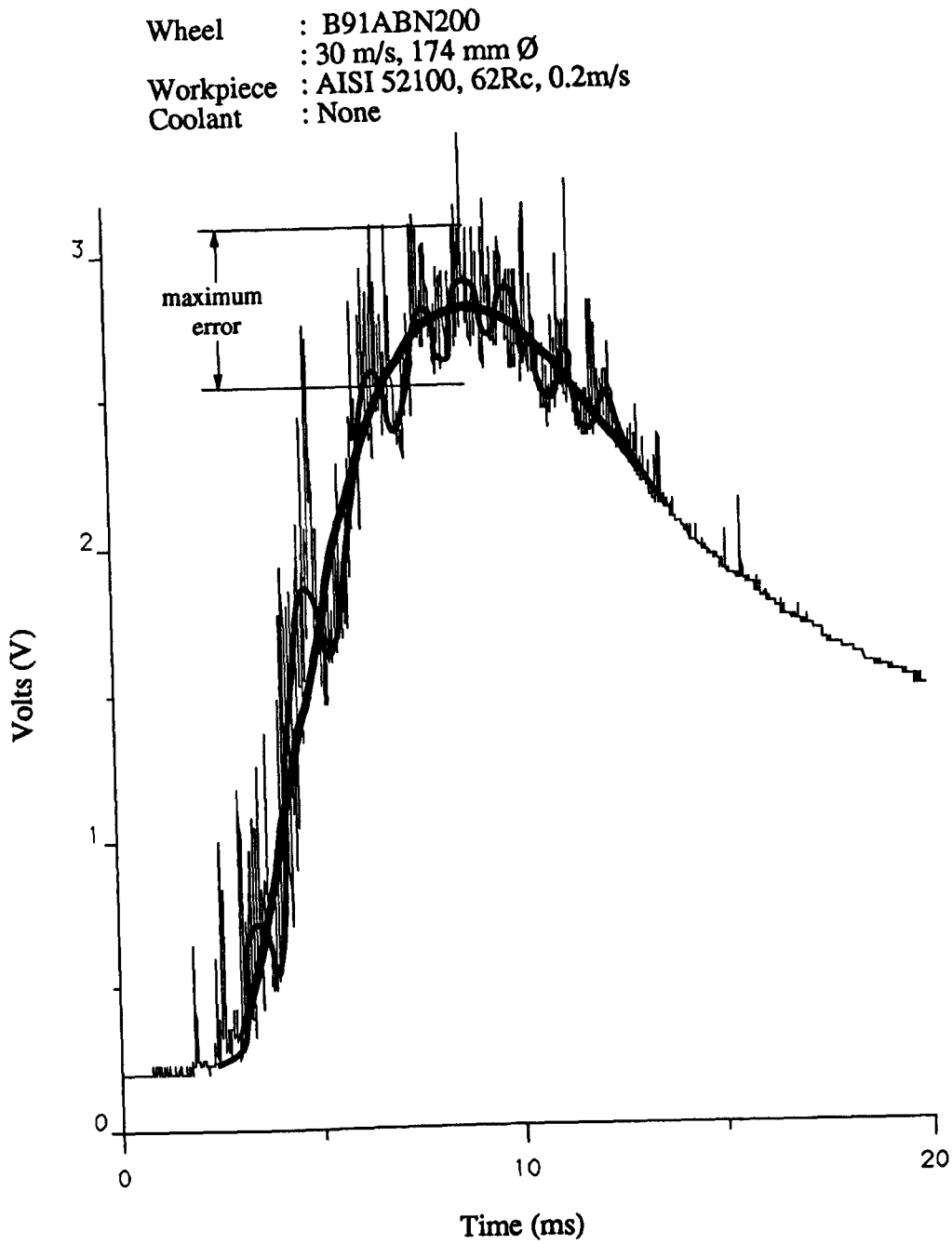

Figure 5.17 : Method used to select the maximum temperature

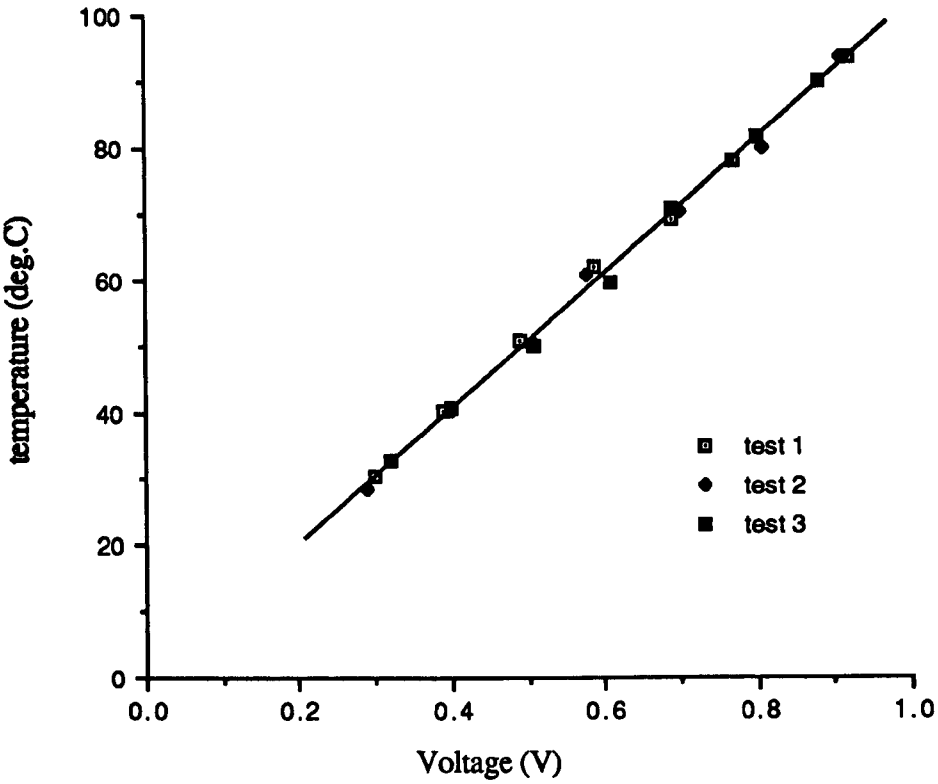

Figure 5.18 : Calibration of the thermocouples using hot water - M2 workpiece

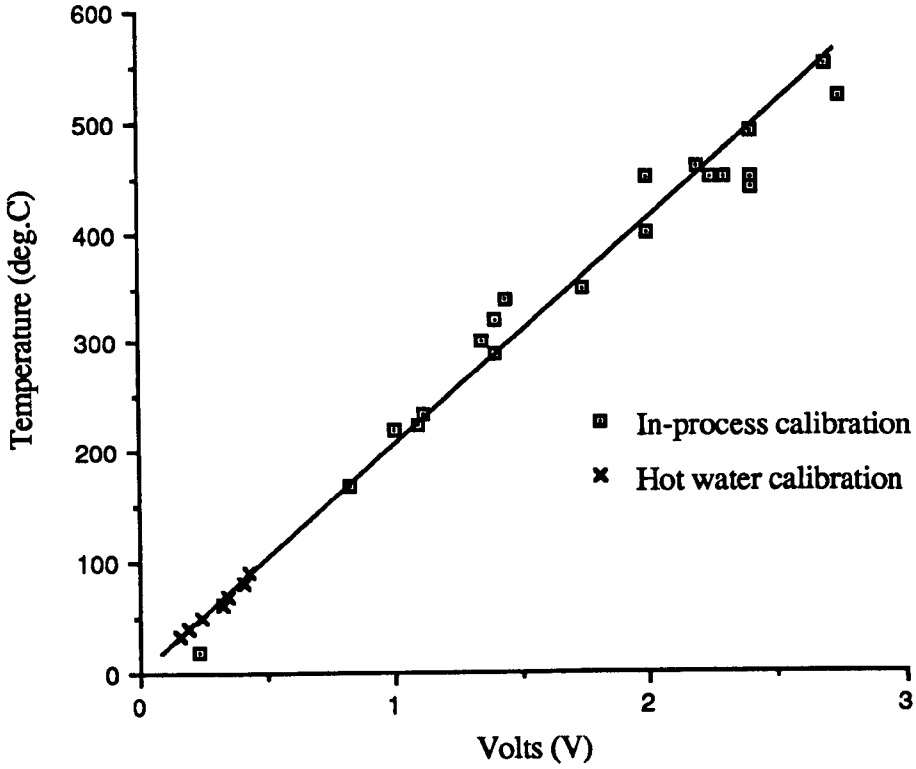

Figure 5.19 : Single pole - AISI 52100 workpiece calibration

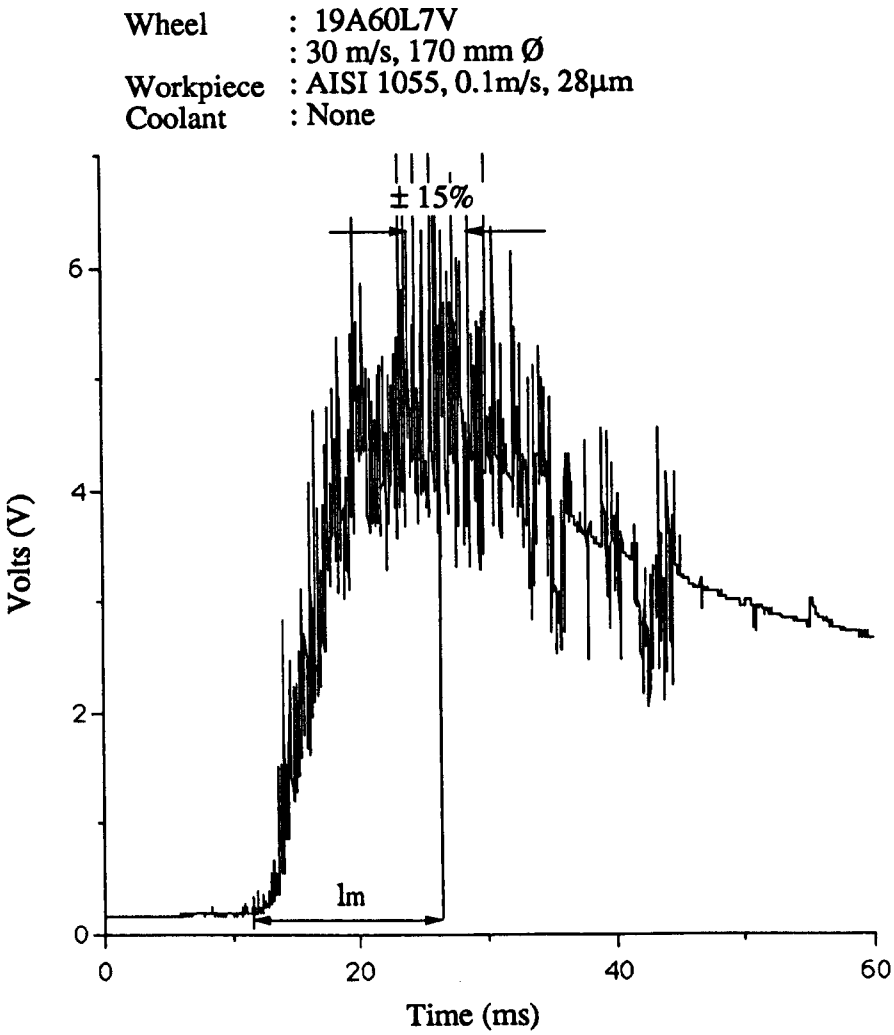

Figure 5.20 : Procedure for selecting the heat source length from the thermocouple signal

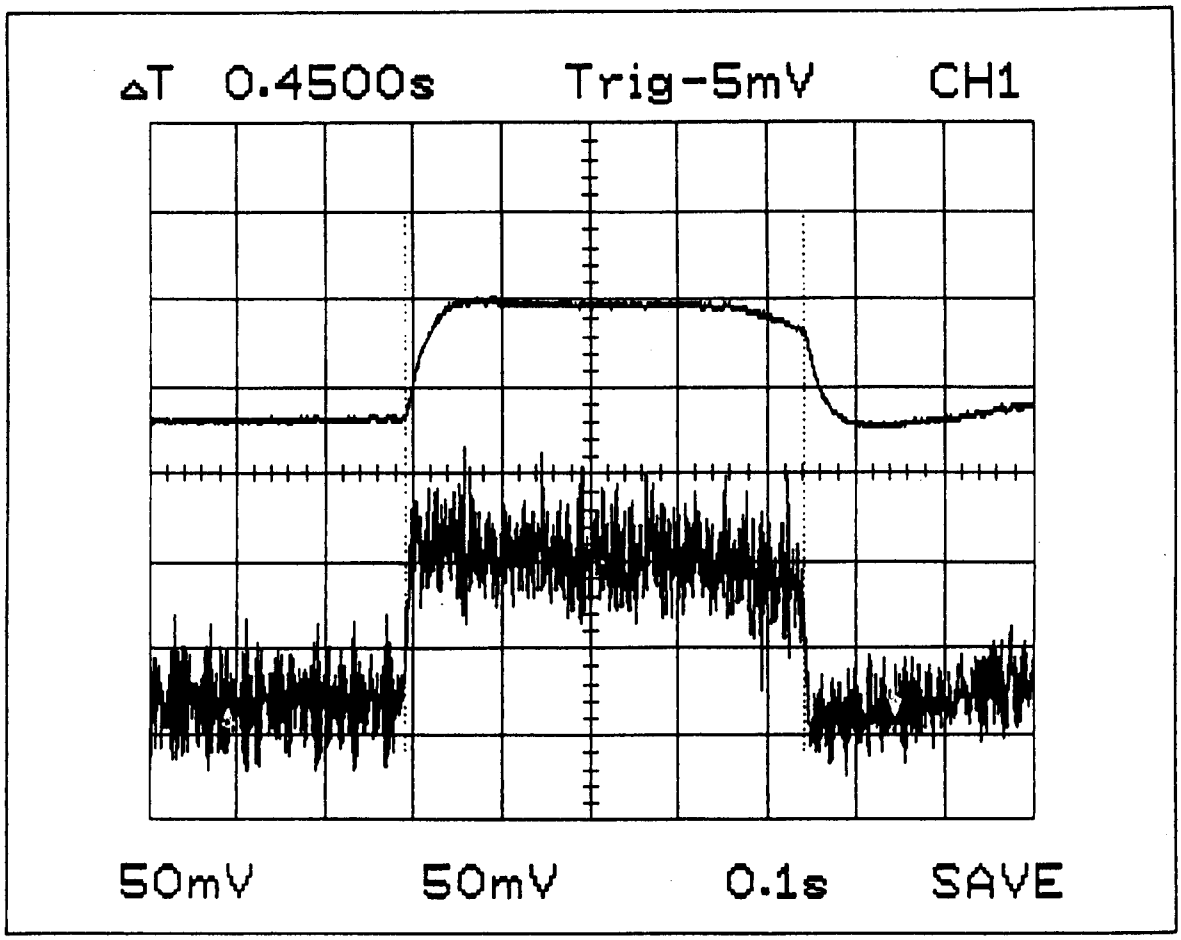

Figure 5.21 : An example of an un-filtered and filtered normal force signal used to measure the workspeed

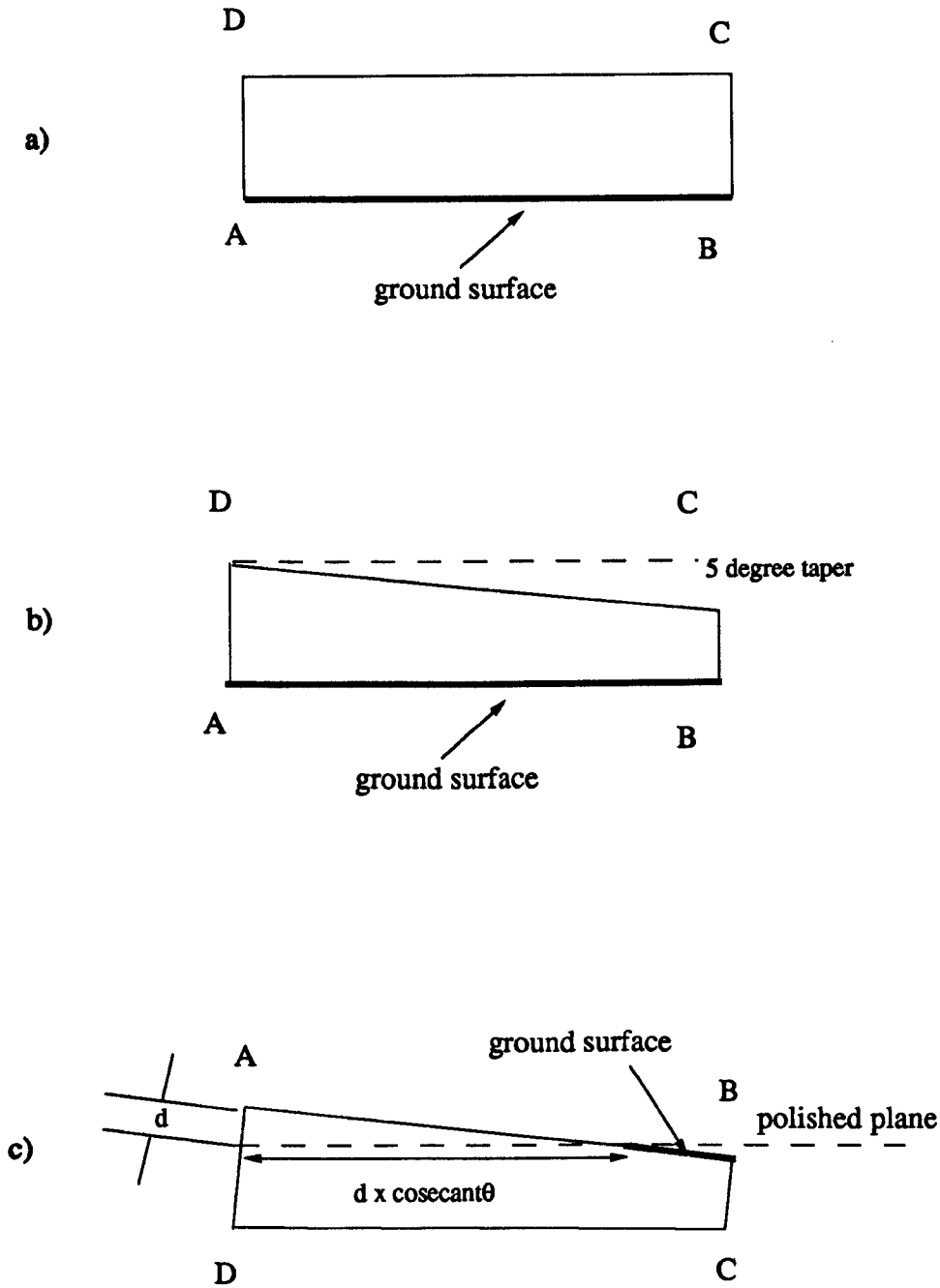

Figure 5.22 : Taper section of ground workpieces

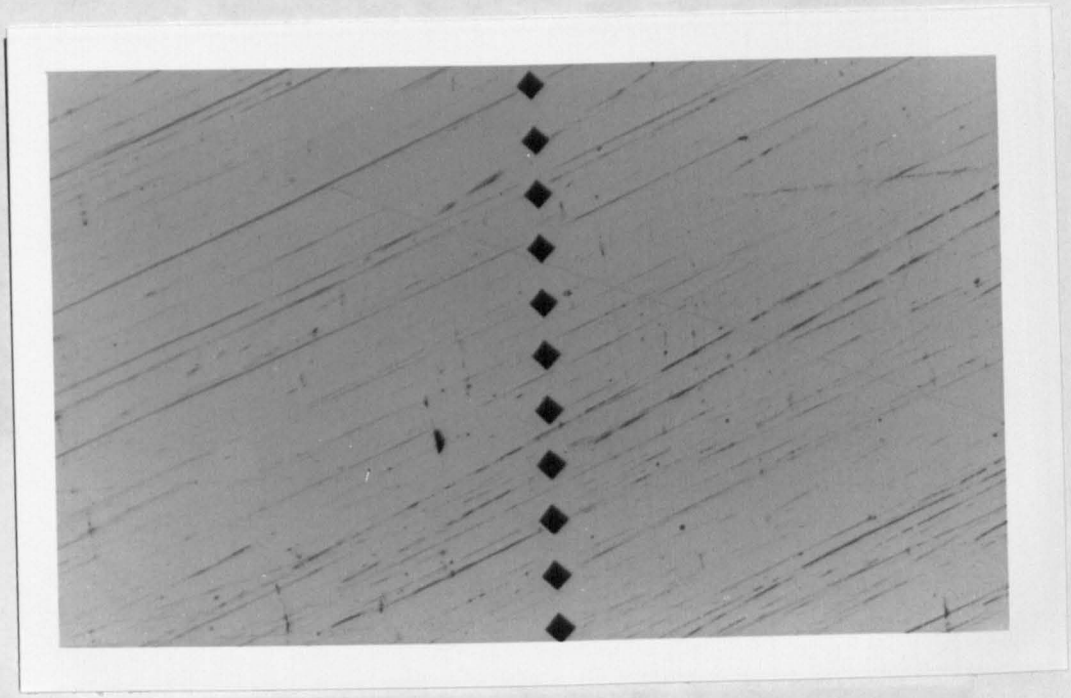

Figure 5.23 : Micro-hardness indentations on a taper section specimen

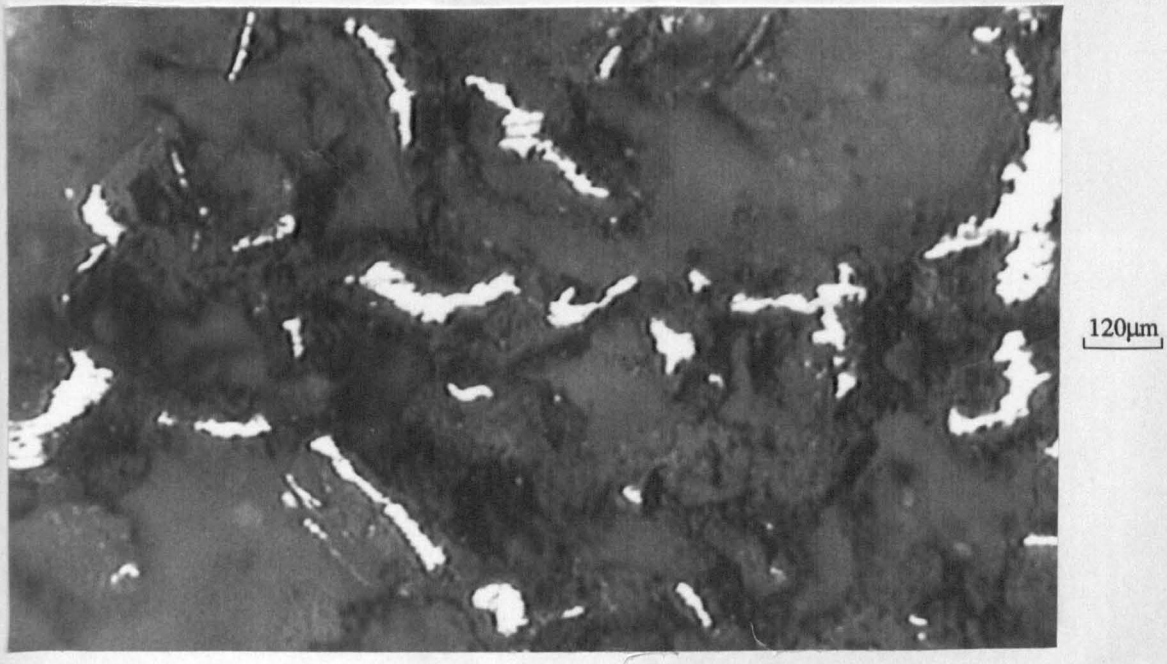

Figure 5.24 : Photograph of the surface of the 19A60K7V alumina wheel

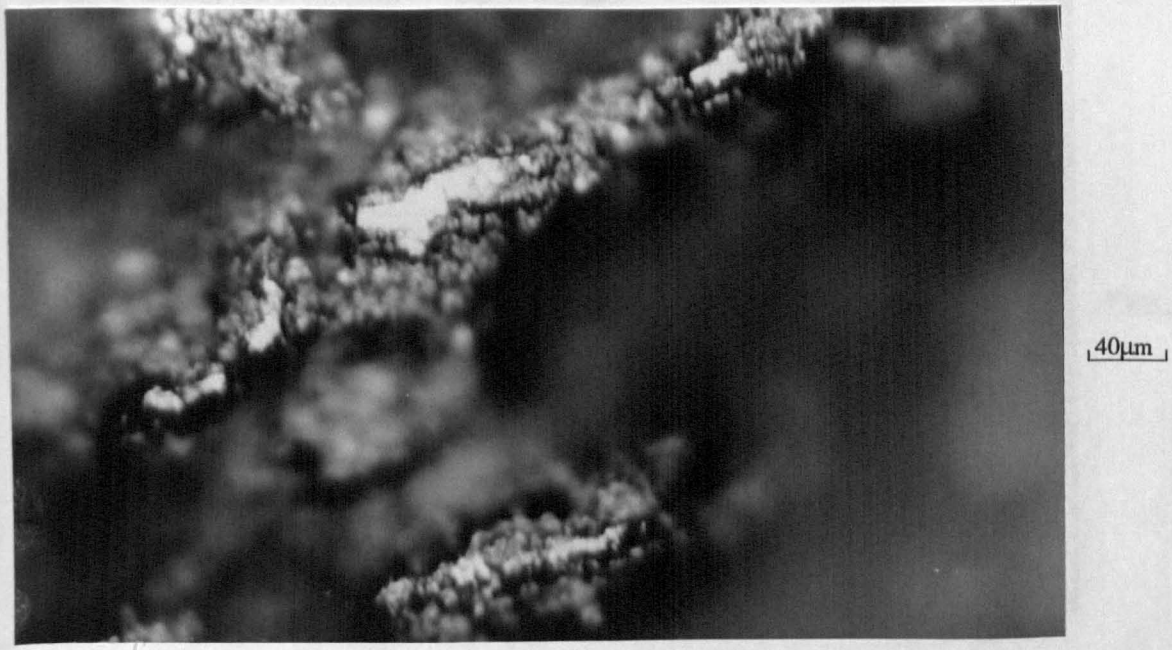

Figure 5.25 : Photograph of the a wear flat on the surface of the A200 alumina wheel - example 1

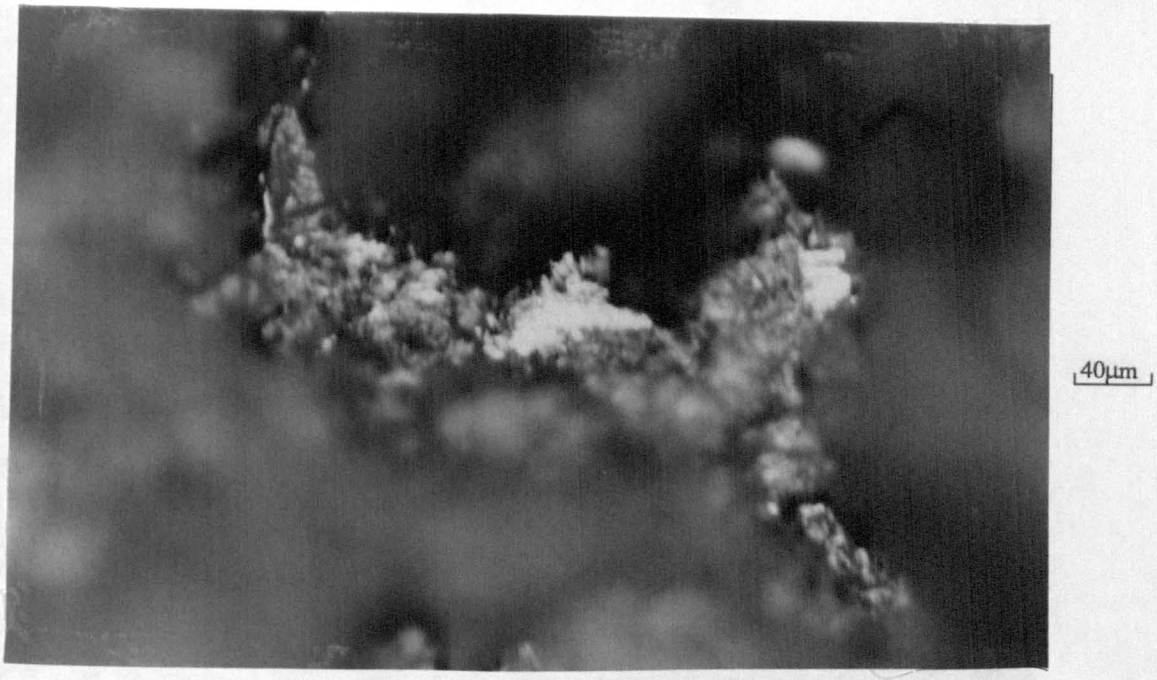

Figure 5.26 : Photograph of the a wear flat on the surface of the A200 alumina wheel - example 2

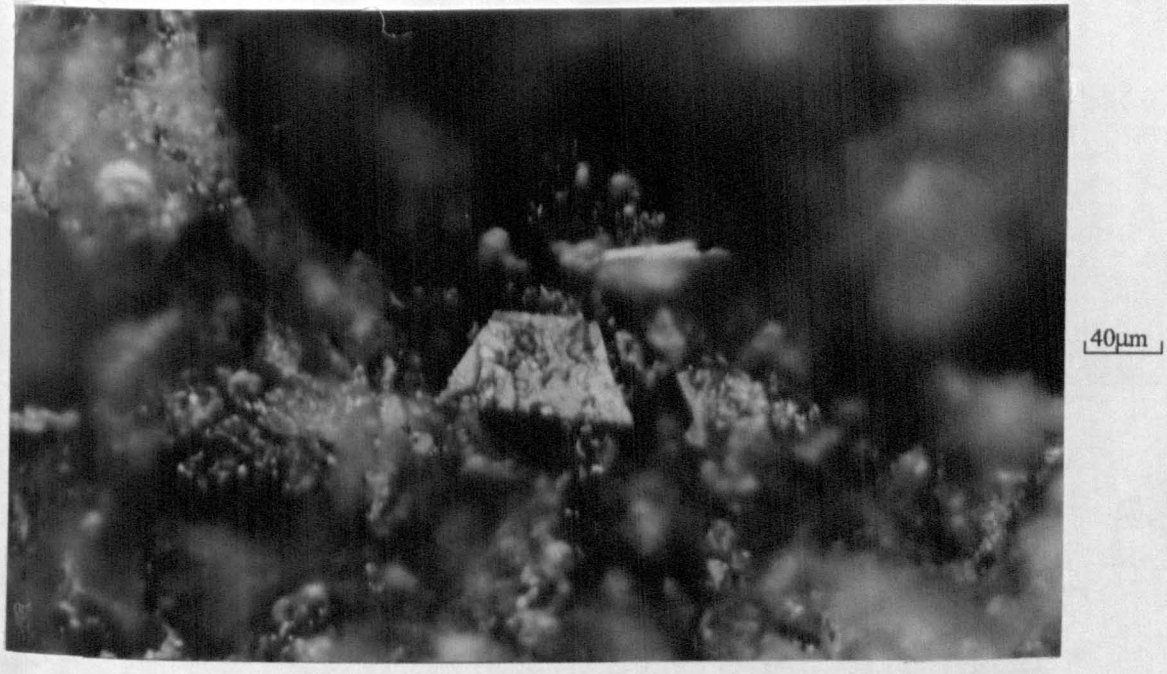

Figure 5.27 : Photograph of the a wear flat on the surface of the B91ABN200 CBN wheel - example 1

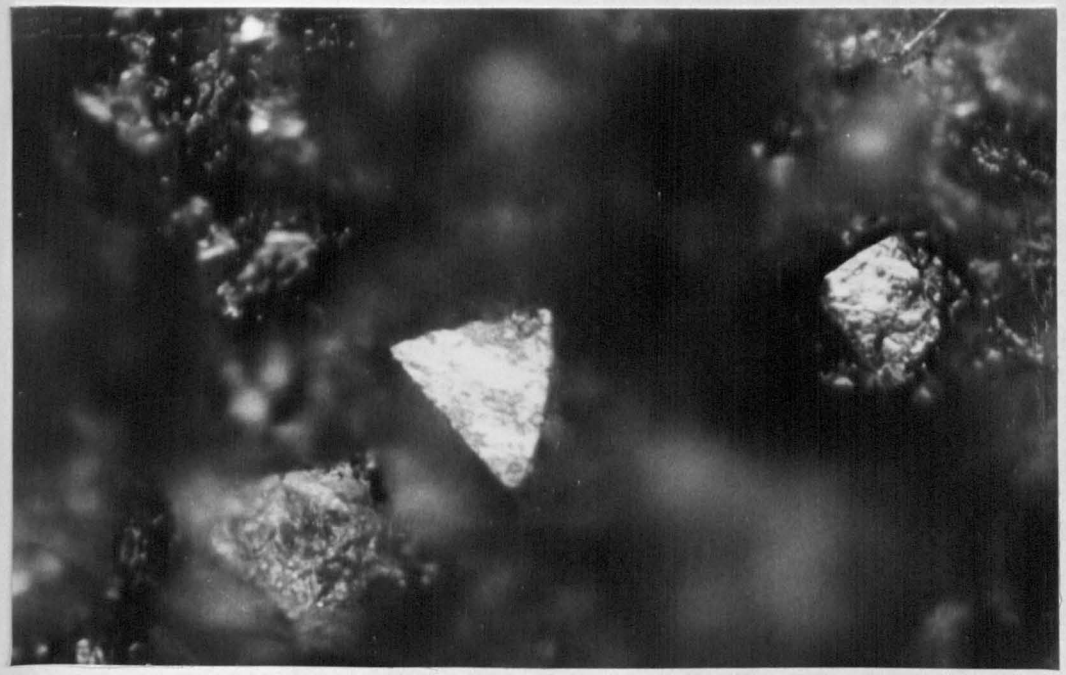

Figure 5.28 : Photograph of the a wear flat on the surface of the B91ABN200 alumina wheel - example 2

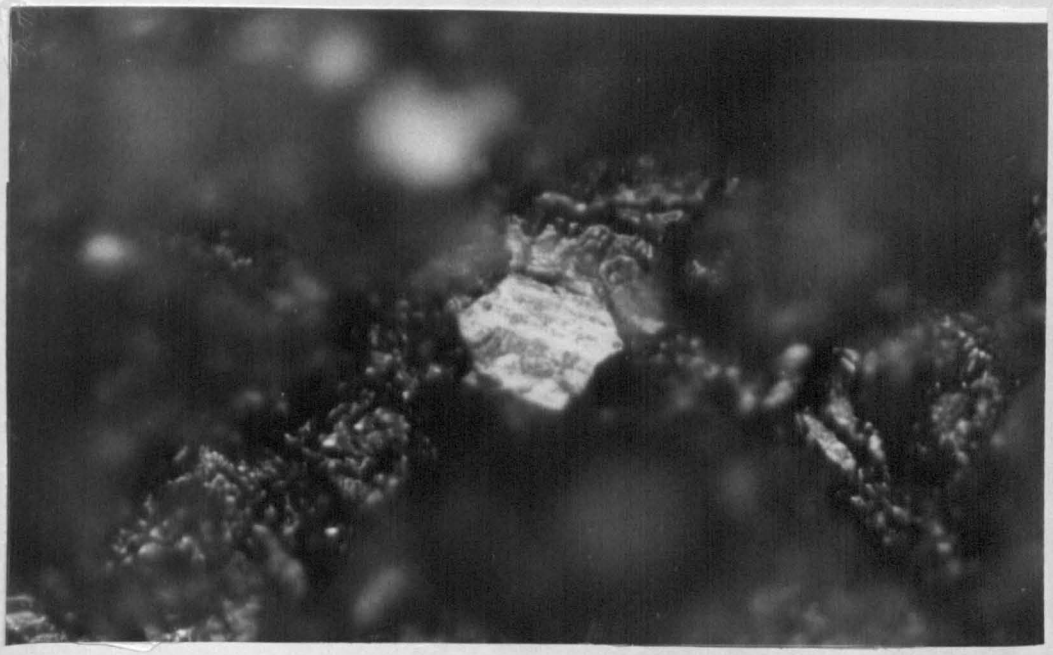

Figure 5.29 : Photograph of the a wear flat on the surface of the B91ABN200 CBN wheel - example 3

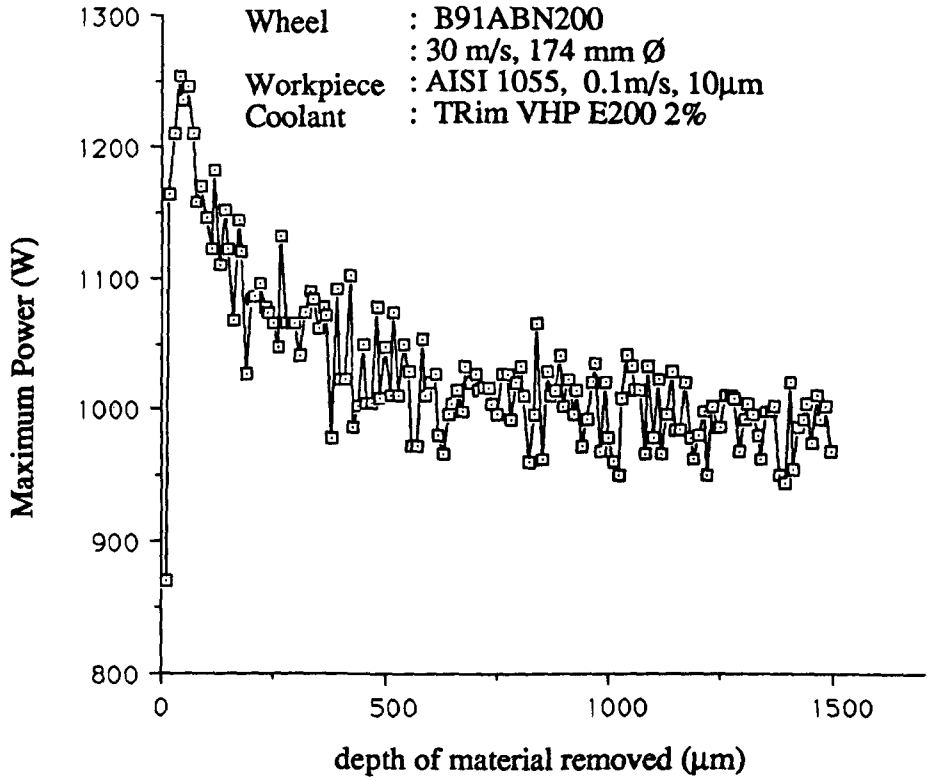

Figure 5.30 : Maximum grinding power against depth of material removed on the stabilsing block

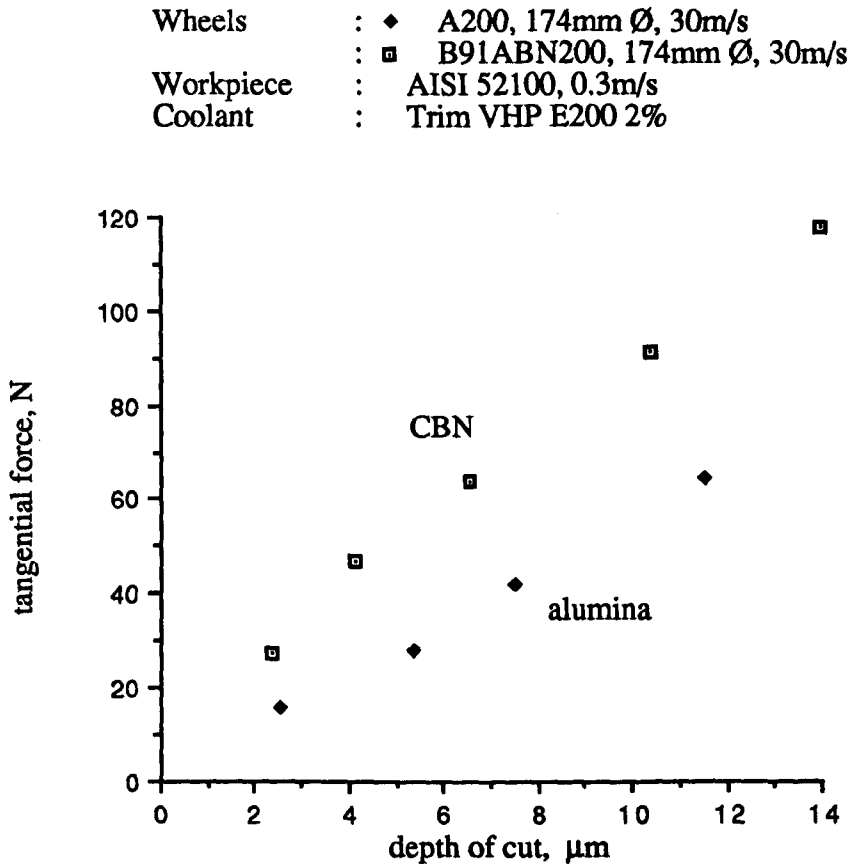

Figure 6.1 : A comparison of the tangential forces against depth of cut for the wet grinding of AISI 52100 with the A200 alumina wheel and the CBN wheel at 0.3m/s

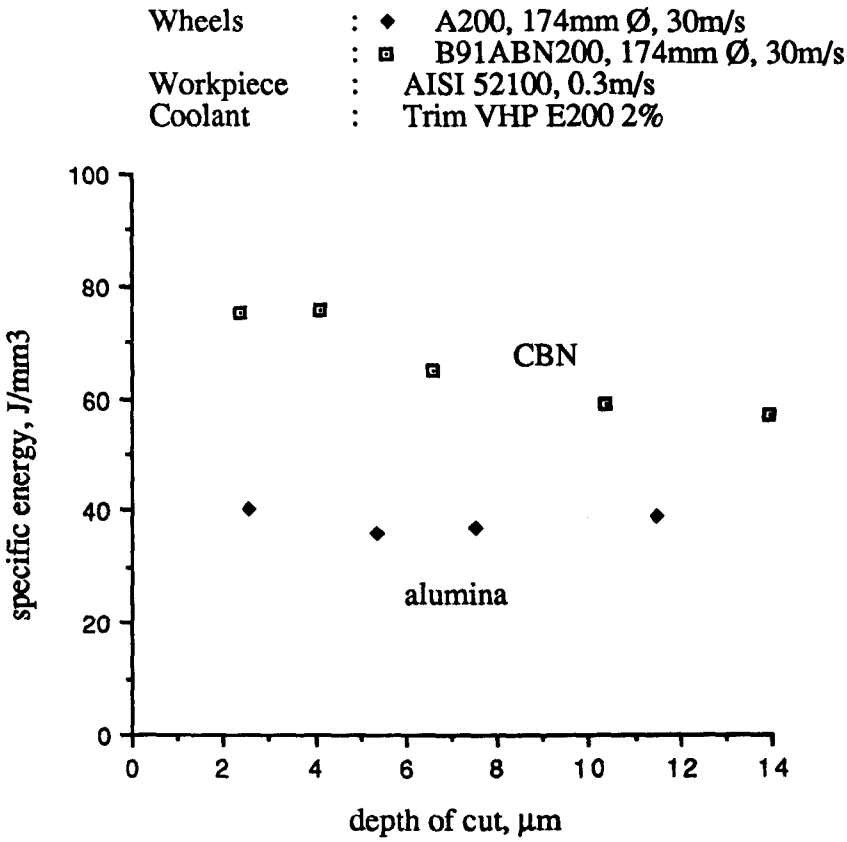

Figure 6.2 : A comparison of the specific energy against depth of cut for the wet grinding of AISI 52100 with the A200 alumina wheel and the CBN wheel at 0.3m/s

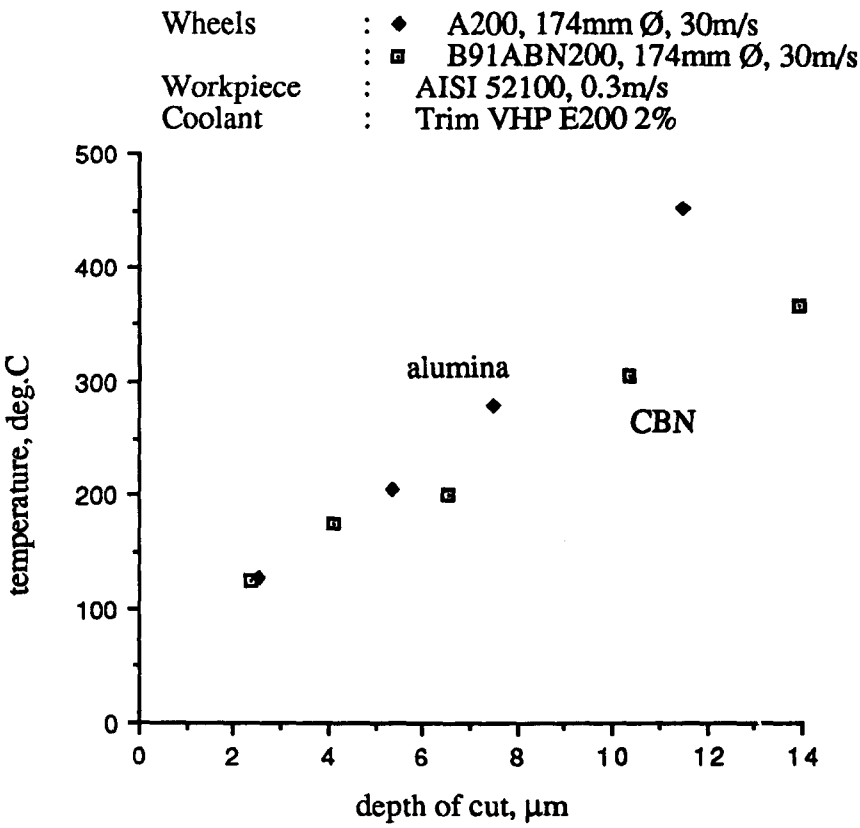

Figure 6.3 : A comparison of the temperatures against depth of cut for the wet grinding of AISI 52100 with the A200 alumina wheel and the CBN wheel at 0.3m/s

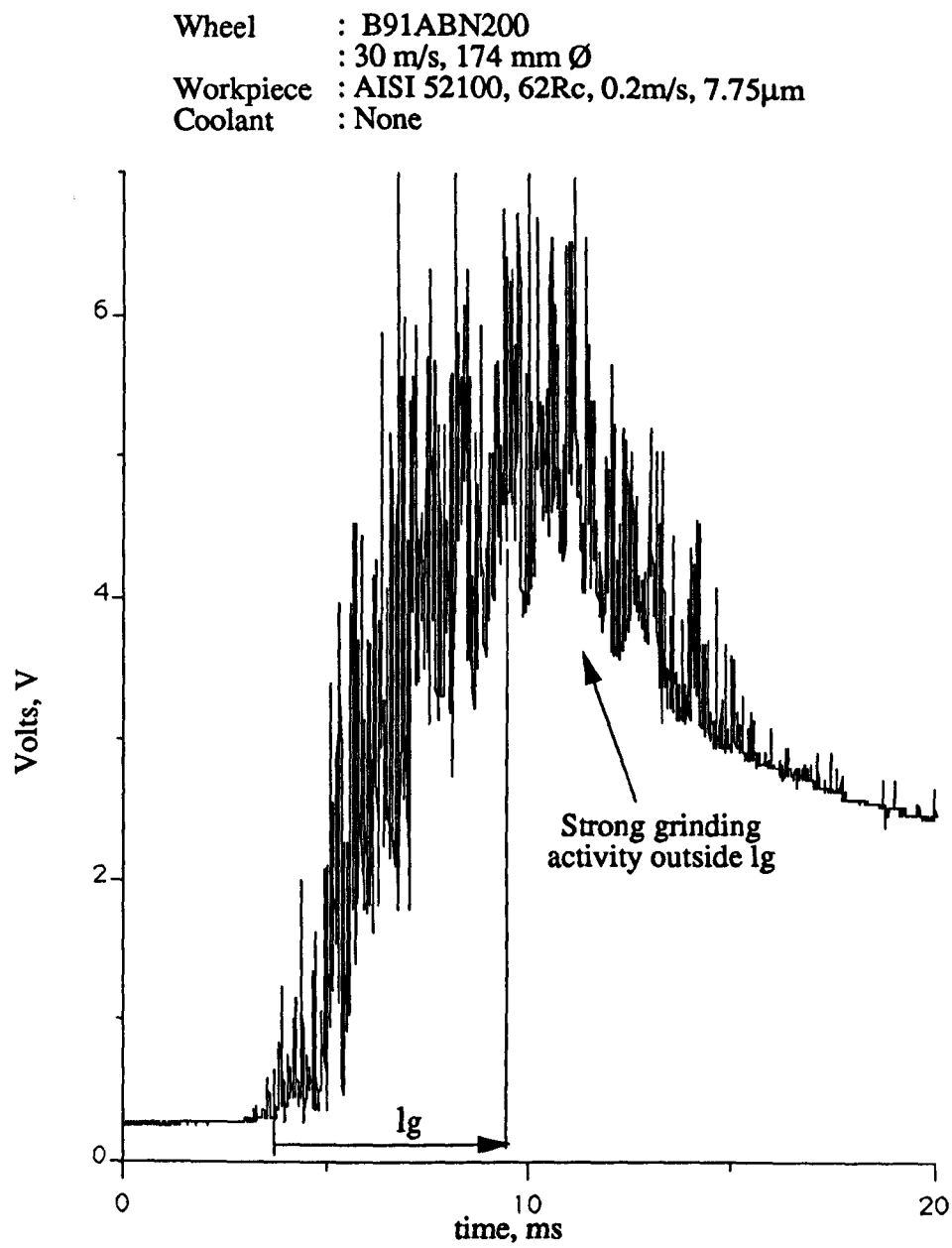

Figure 6.4 : Cutting activity beyond the geometric contact length

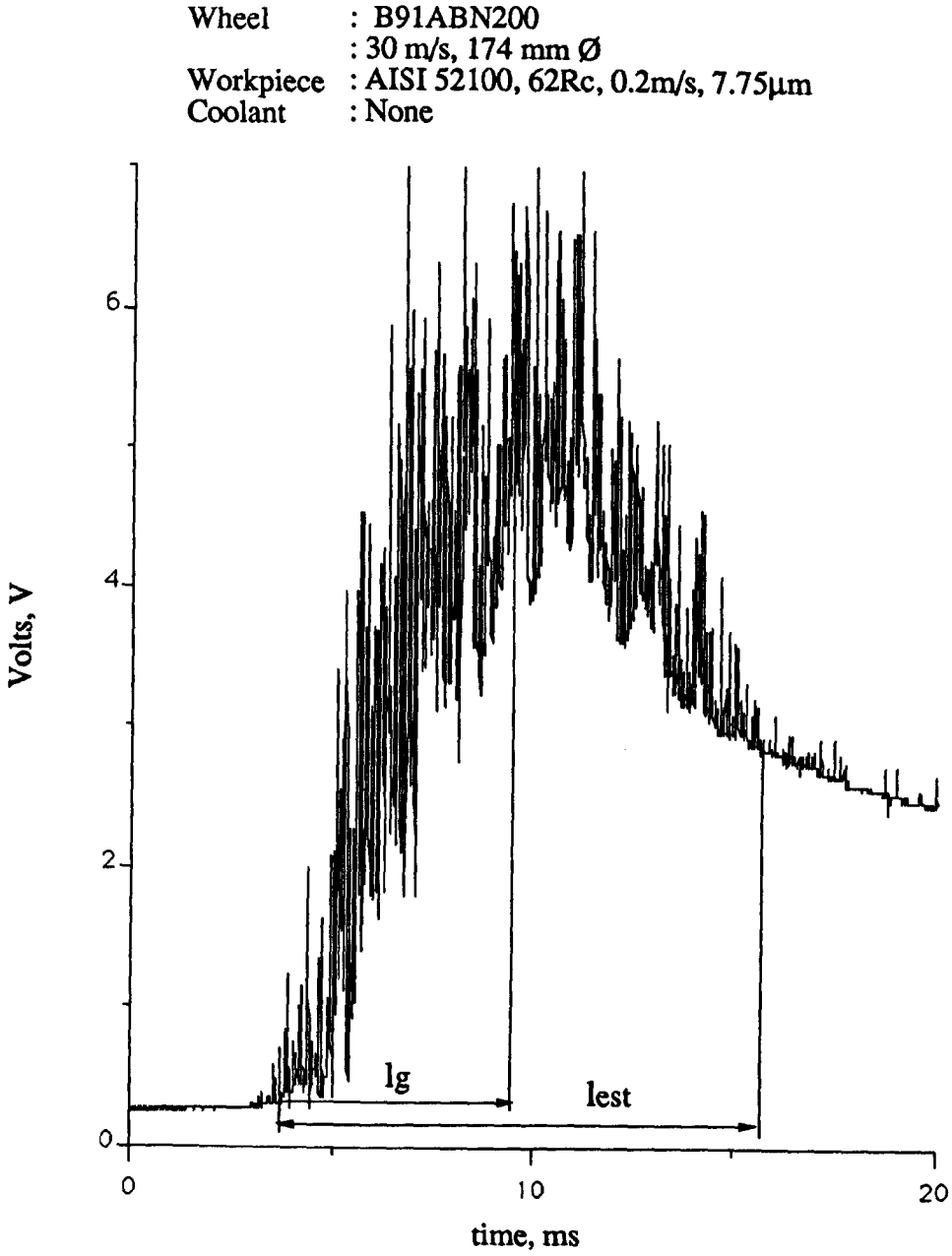

Figure 6.5 : Contact length estimated directly from the signal

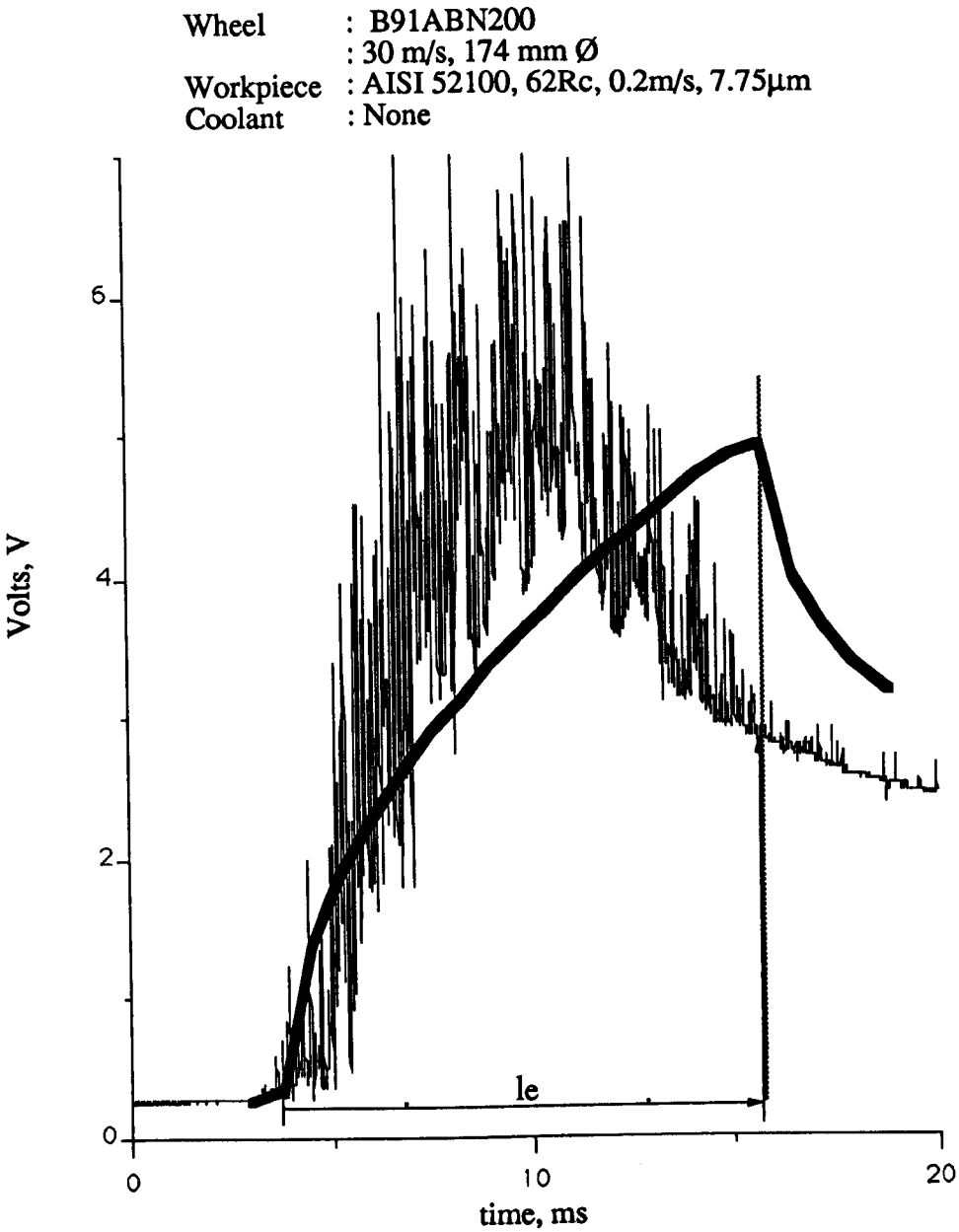

Figure 6.6 : Measured tempearture distribution matched with a uniform heat flux

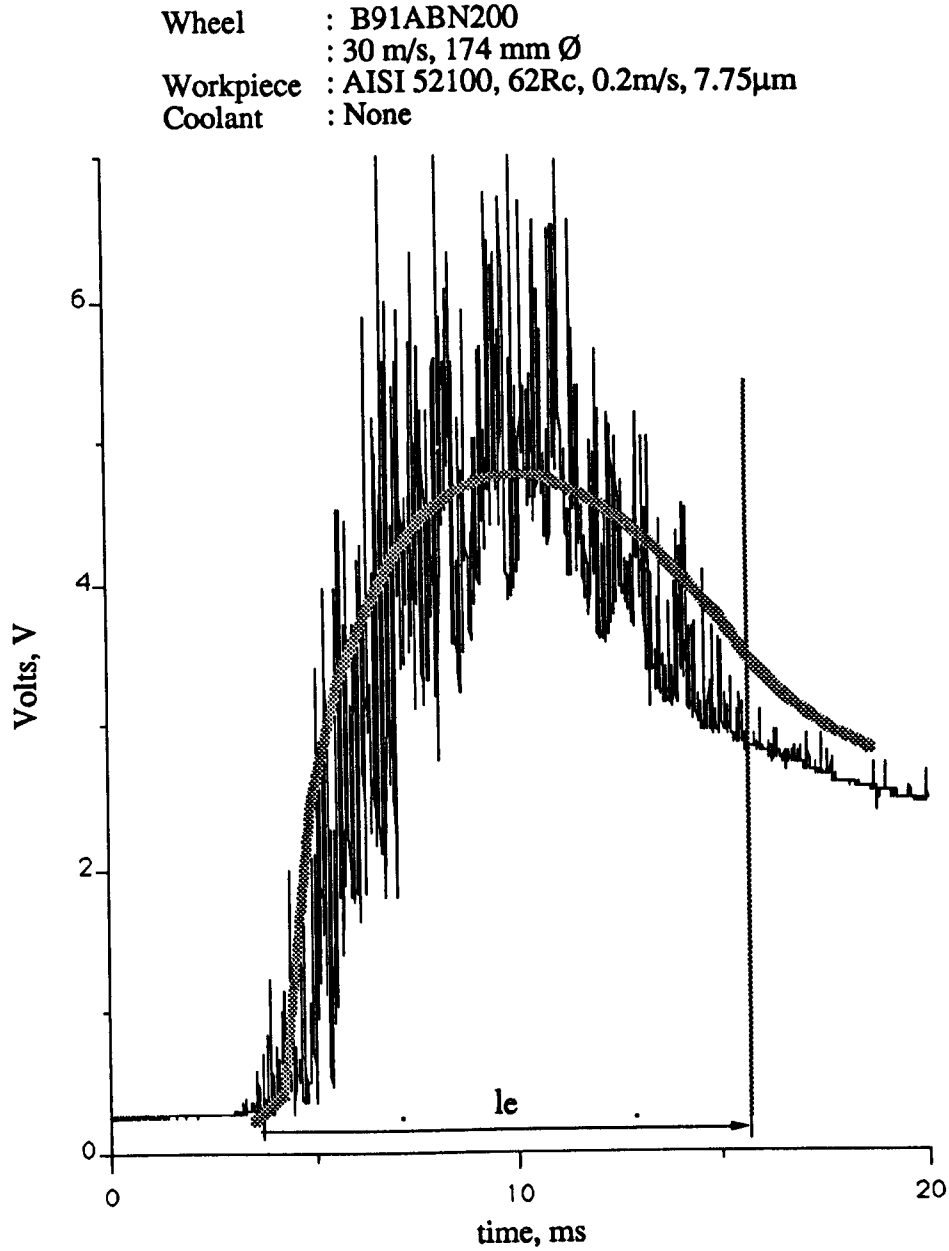

Figure 6.7 : Measured tempearture distribution matched with the triangular heat flux

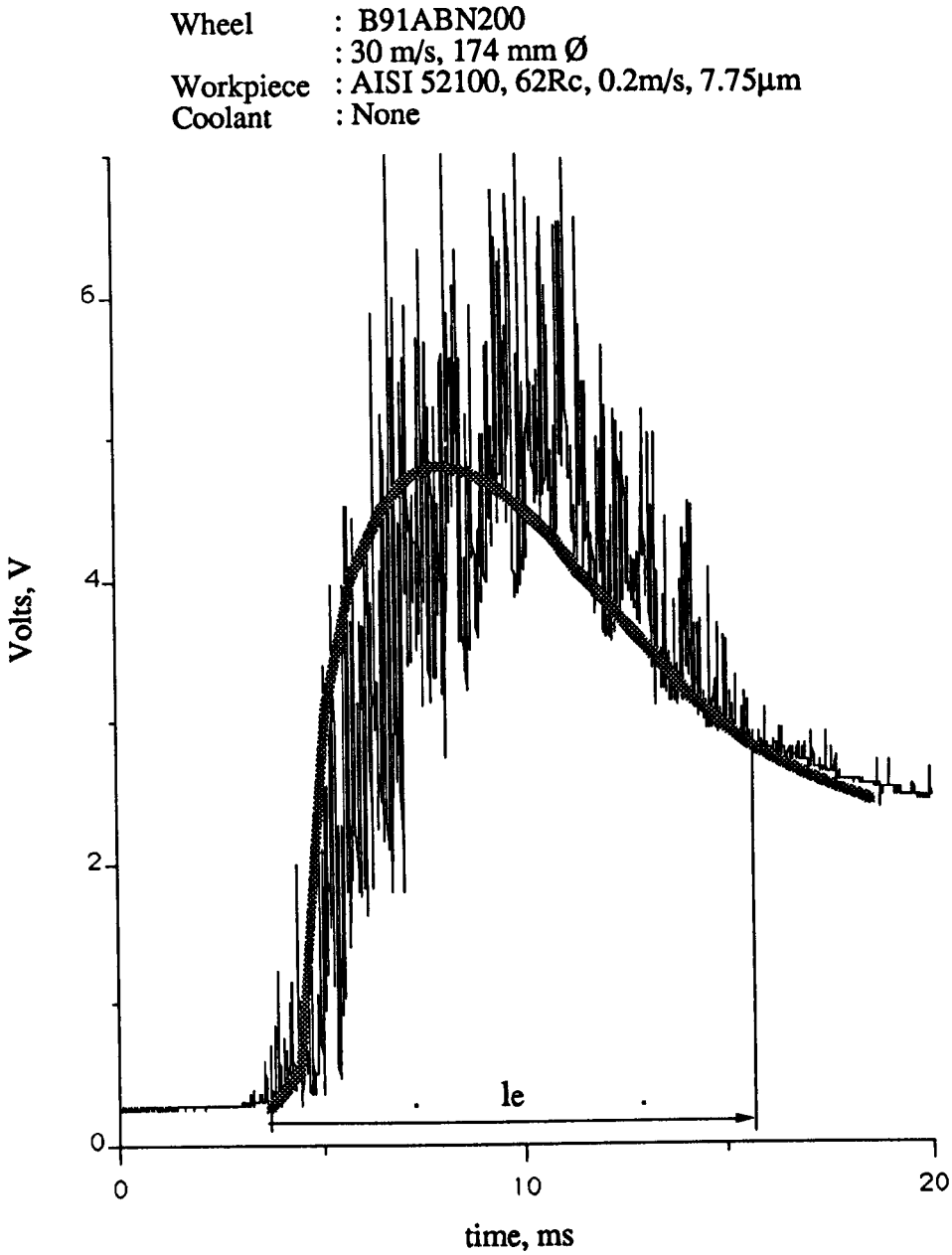

Figure 6.8 : Measured tempearture distribution matched with the square law heat flux

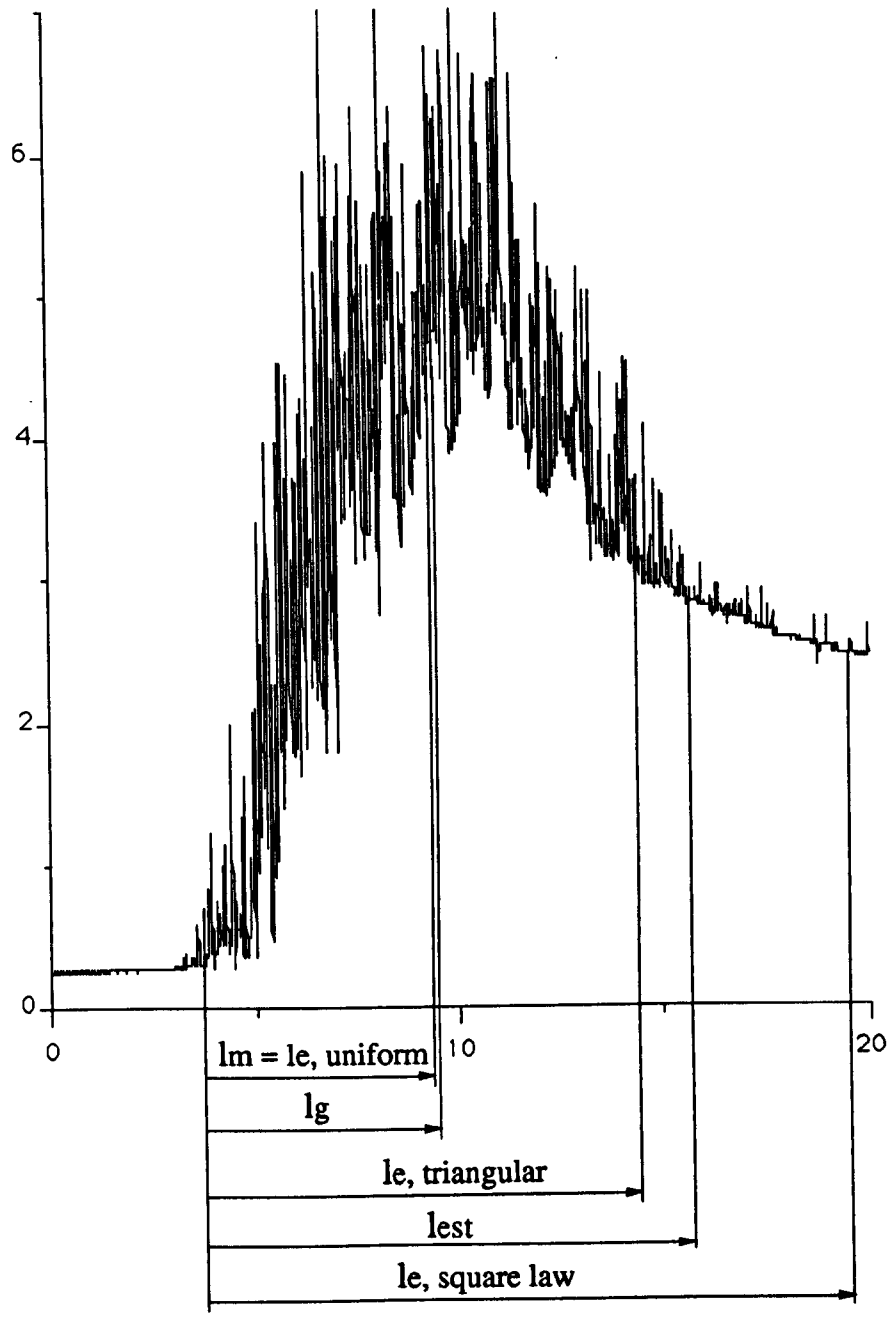

Figure 6.9 : Estimates of the contact length based on the position of the maximum temperature

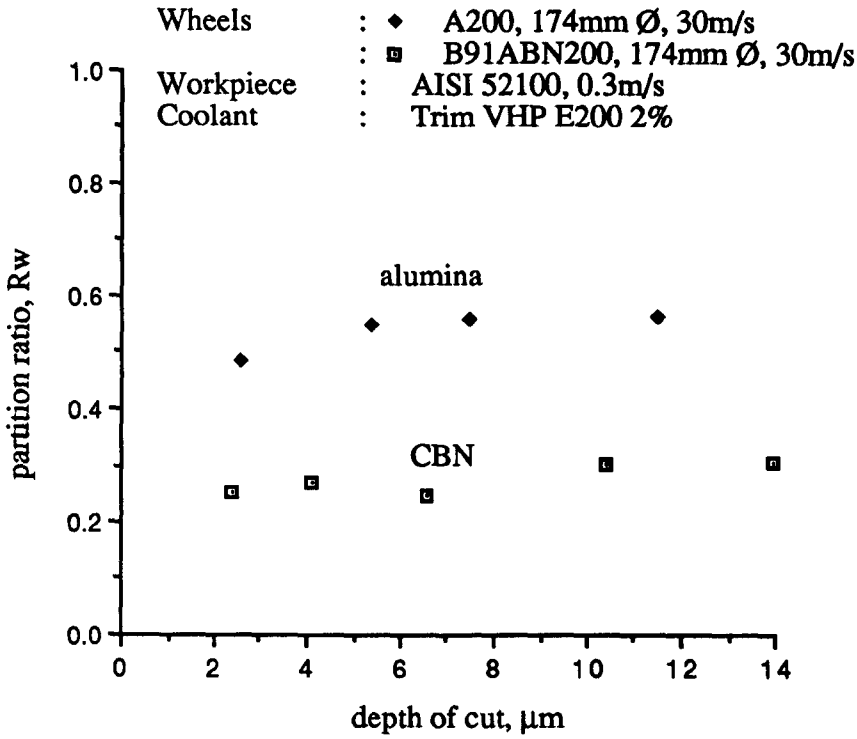

Figure 6.10 : A comparison of the partition ratio based on a uniform heat flux for the wet grinding of AISI 52100 with the A200 alumina wheel and the CBN wheel at 0.3m/s

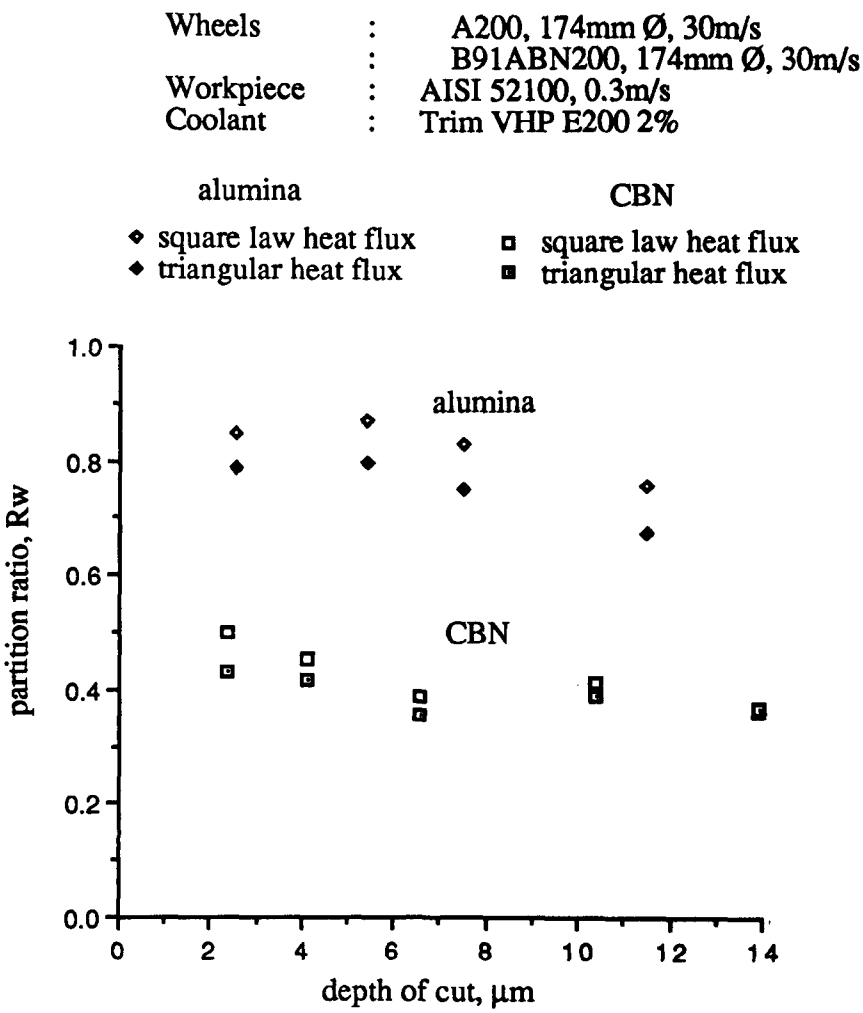

Figure 6.11 : A comparison of the partition ratio based on a triangular and a square law heat flux for the wet grinding of AISI 52100 with the A200 alumina wheel and the CBN wheel at 0.3m/s

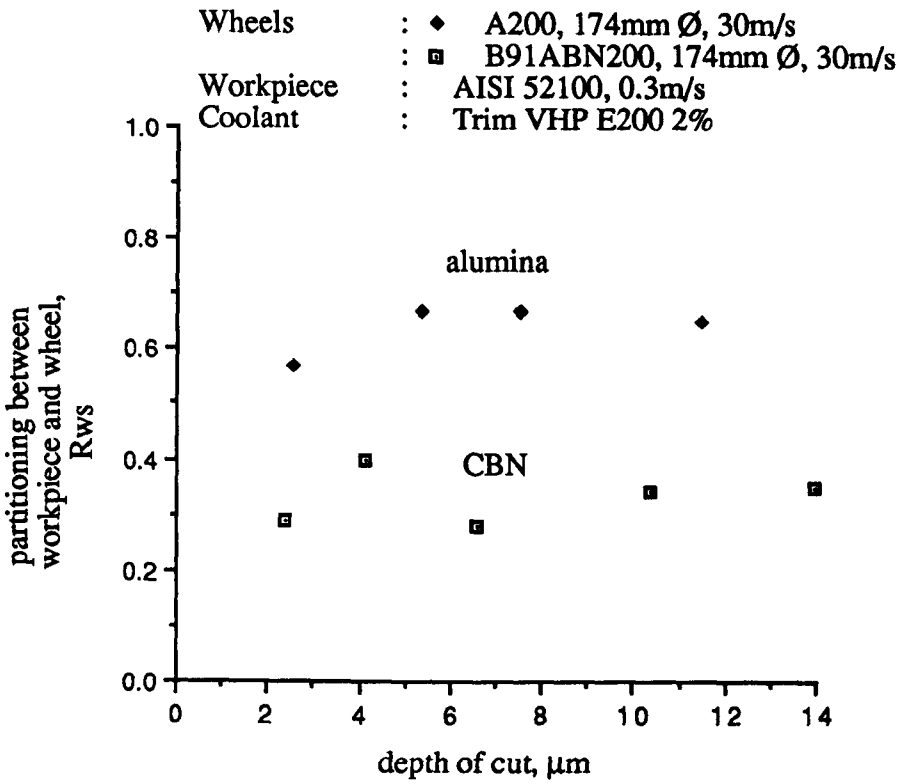

Figure 6.12 : A comparison of the partitioning between the workpiece and wheel based on a uniform heat flux for the wet grinding of AISI 52100 with the A200 alumina wheel and the CBN wheel at 0.3m/s

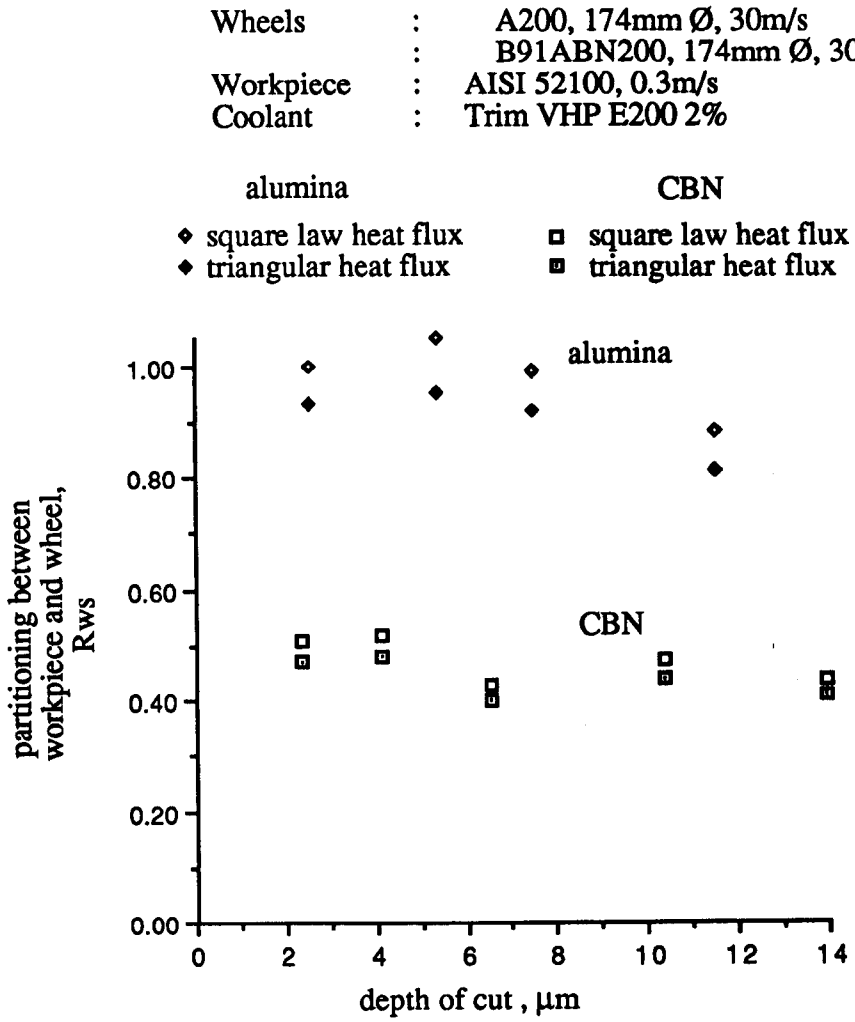

Figure 6.13 : A comparison of the partitioning between the workpiece and wheel based on a square law and a triangular heat flux for the wet grinding of AISI 52100 with the A200 alumina wheel and the CBN wheel at 0.3m/s

Experimental data :

Wheels	: ◆	A200, 174mm Ø, 30m/s
	: ◘	B91ABN200, 174mm Ø, 30m/s
Workpiece	:	AISI 52100, 0.3m/s
Coolant	:	Trim VHP E200 2%

Model data :

Workpiece	Alumina	CBN
κ_w = 34.3 W/mK	κ_g = 36 W/mK	κ_g = 290 W/mK
ρ_w = 7815 kg/m3	ρ_g = 3910 kg/m3	ρ_g = 3480 kg/m3
c_w = 506 J/KgK	c_g = 765 J/KgK	c_g = 506 J/KgK
	Rr = 3.5 ro=15μm	Rr = 4 ro=15μm

ecc = 6J/mm3
——— steady state solution
····· transient solution

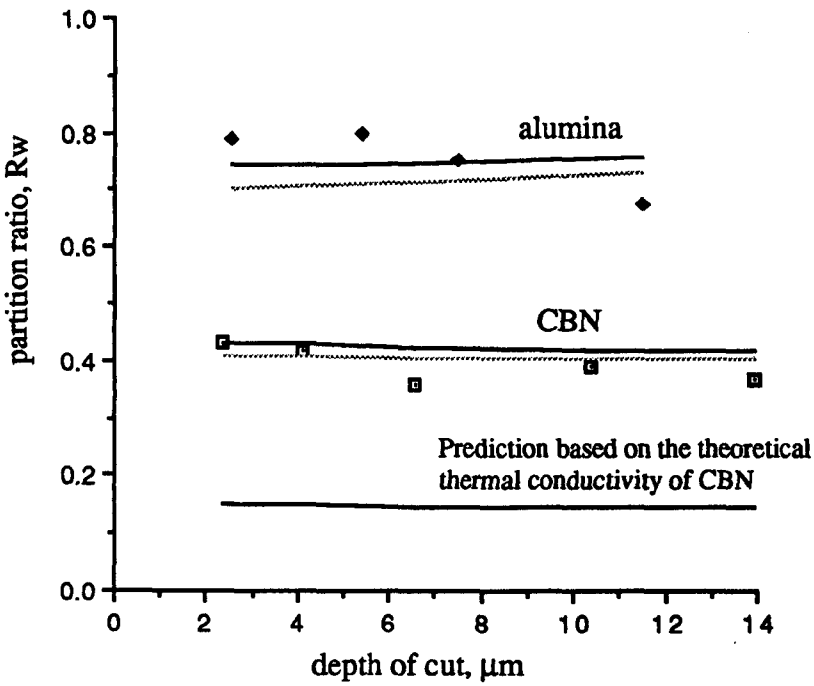

Figure 6.14 : A comparison of the theoretical and measured partition ratios based on a triangular heat flux for the wet grinding of AISI 52100 with the A200 alumina wheel and the CBN wheel at 0.3m/s

Experimental data :

Wheel	: ◆	A200, 174mm Ø, 30m/s
	:	
Workpiece	:	AISI 52100, 0.3m/s
Coolant	:	Trim VHP E200 2%

Model data :

Workpiece	Alumina
κ_w = 34.3 W/mK	κ_g = 36 W/mK
ρ_w = 7815 kg/m3	ρ_g = 3910 kg/m3
c_w = 506 J/KgK	c_g = 765 J/KgK
	Rr = 3.5 ro=15μm

ecc = 6J/mm3

—— steady state solution

..... transient solution

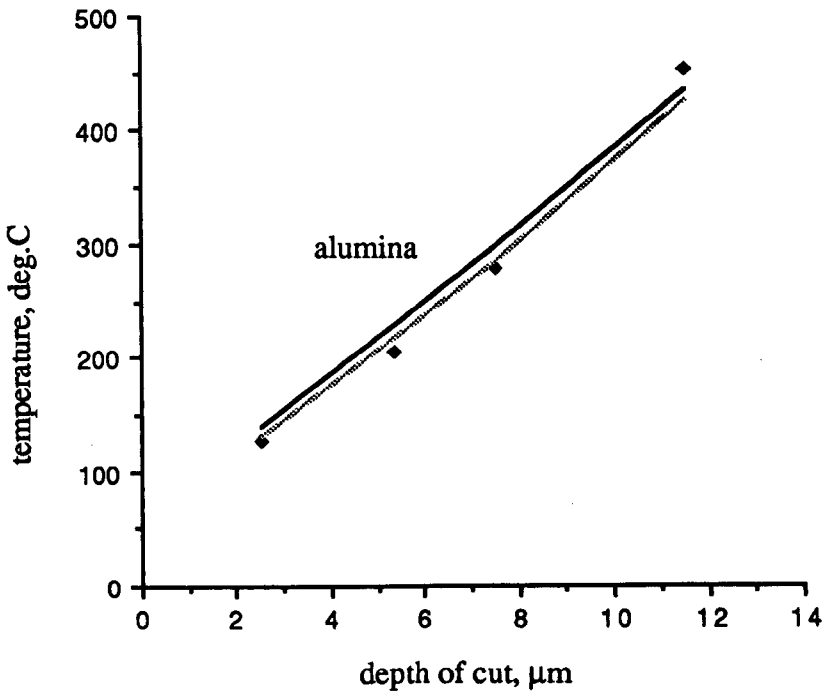

Figure 6.15 : A comparison of the theoretical and measured temperatures for the wet grinding of AISI 52100 with the A200 alumina wheel at 0.3m/s

Experimental data :

Wheel : ▫ B91ABN200, 174mm Ø, 30m/s
:
Workpiece : AISI 52100, 0.3m/s
Coolant : Trim VHP E200 2%

Model data :

Workpiece
κw = 34.3 W/mK
ρw = 7815 kg/m3
cw = 506 J/KgK

CBN
κg = 290 W/mK
ρg = 3480 kg/m3
cg = 506 J/KgK
Rr = 4 ro=15μm

ecc = 6J/mm3
—— steady state solution
····· transient solution

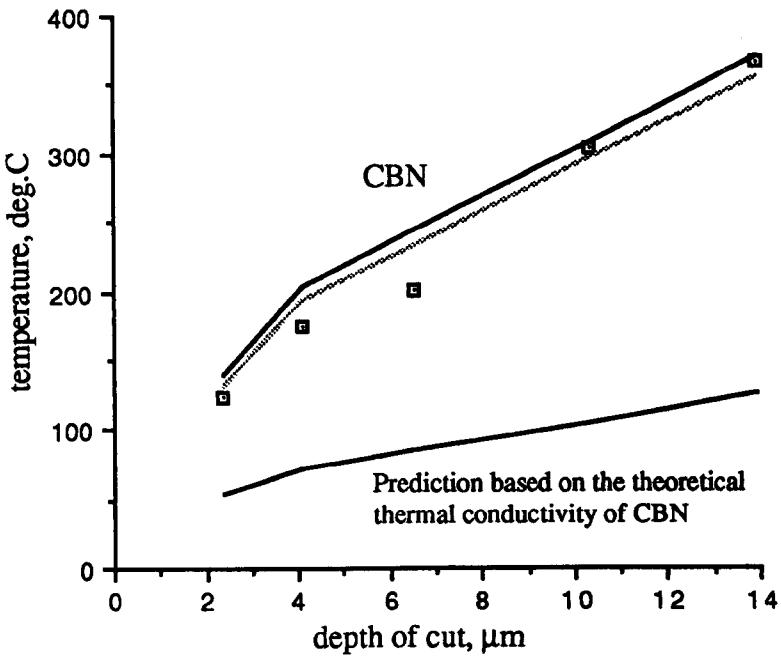

Figure 6.16 : A comparison of the theoretical and measured temperatures for the wet grinding of AISI 52100 with the CBN wheel at 0.3m/s

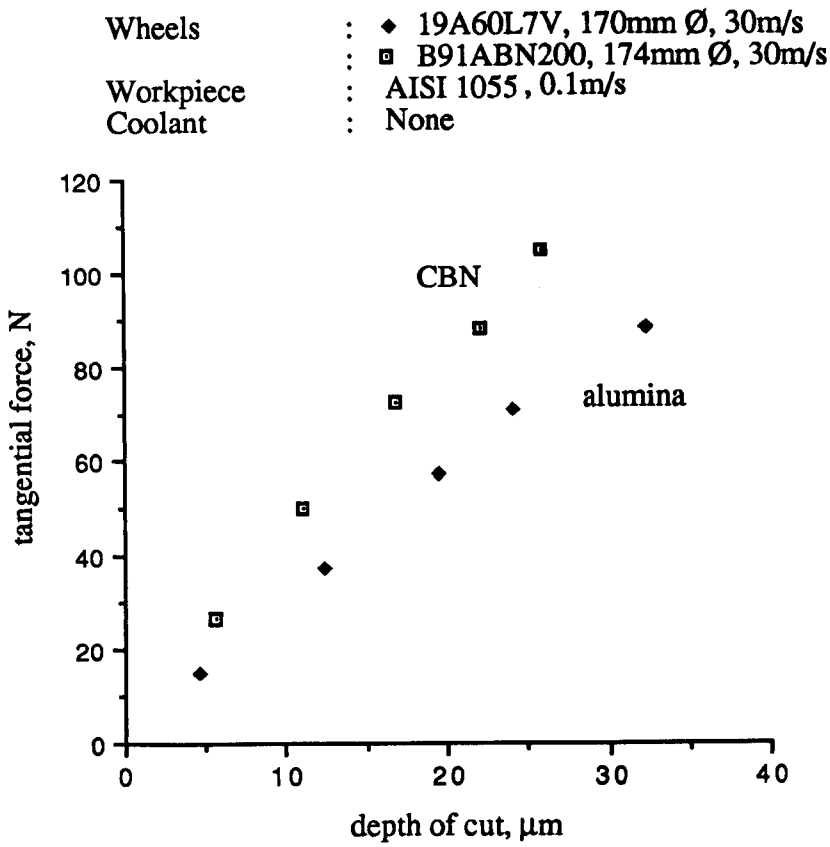

Figure 6.17 : A comparison of the tangential force against depth of cut for the dry grinding of AISI 1055 with the 19A60L7V alumina wheel and the CBN wheel at 0.1m/s

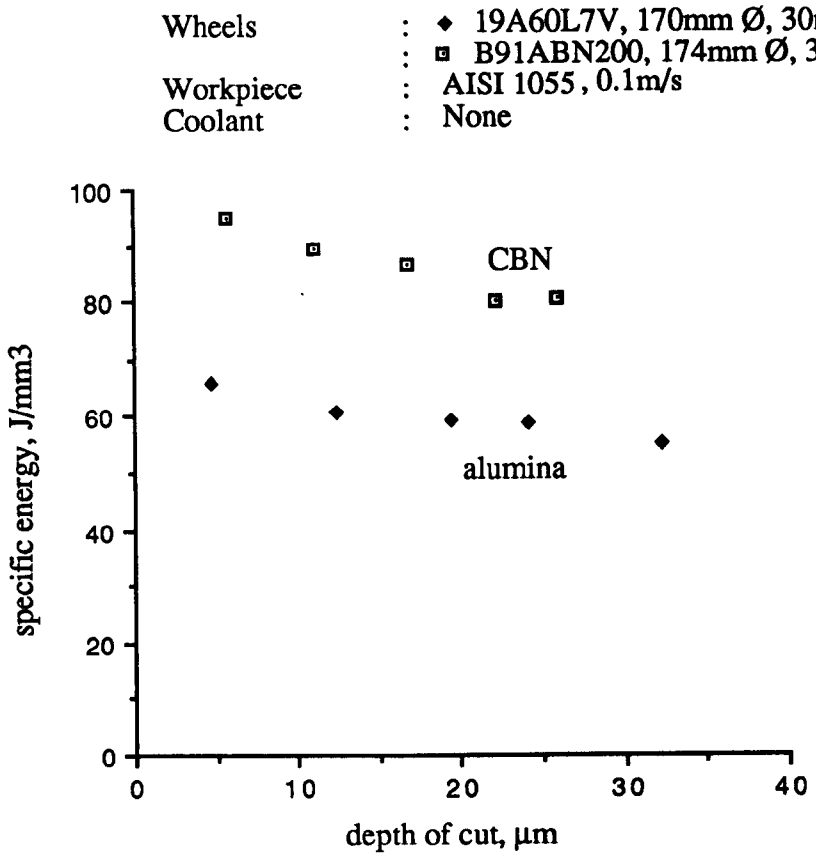

Figure 6.18 : A comparison of the specific energy against depth of cut for the dry grinding of AISI 1055 with the 19A60L7V alumina wheel and the CBN wheel at 0.1m/s

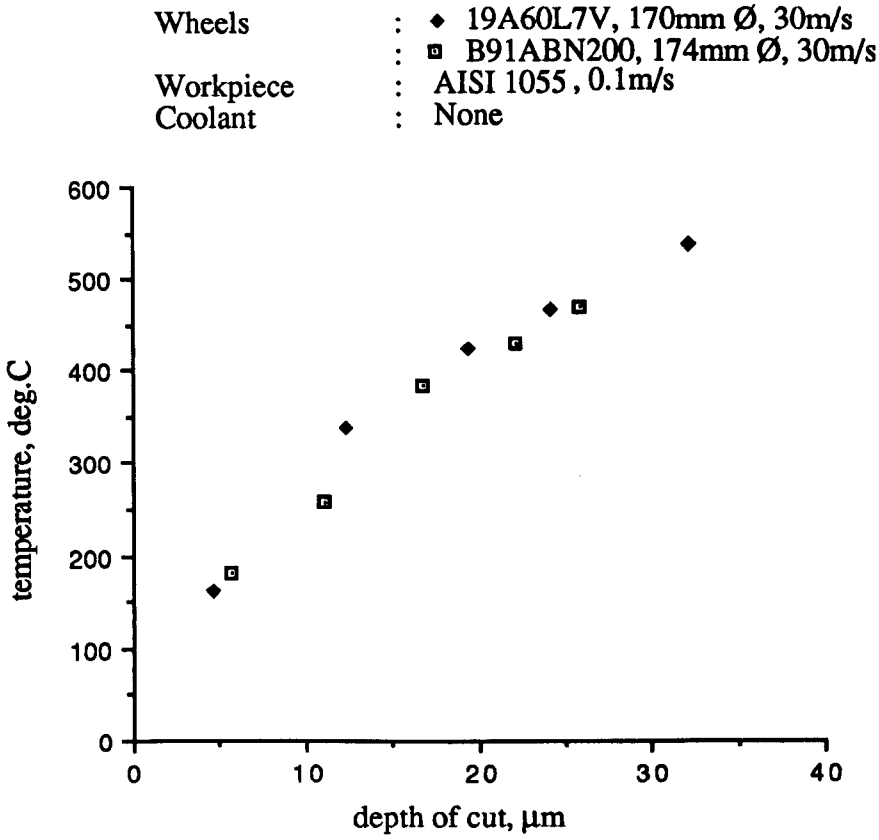

Figure 6.19 : A comparison of the temperature against depth of cut for the dry grinding of AISI 1055 with the 19A60L7V alumina wheel and the CBN wheel at 0.1m/s

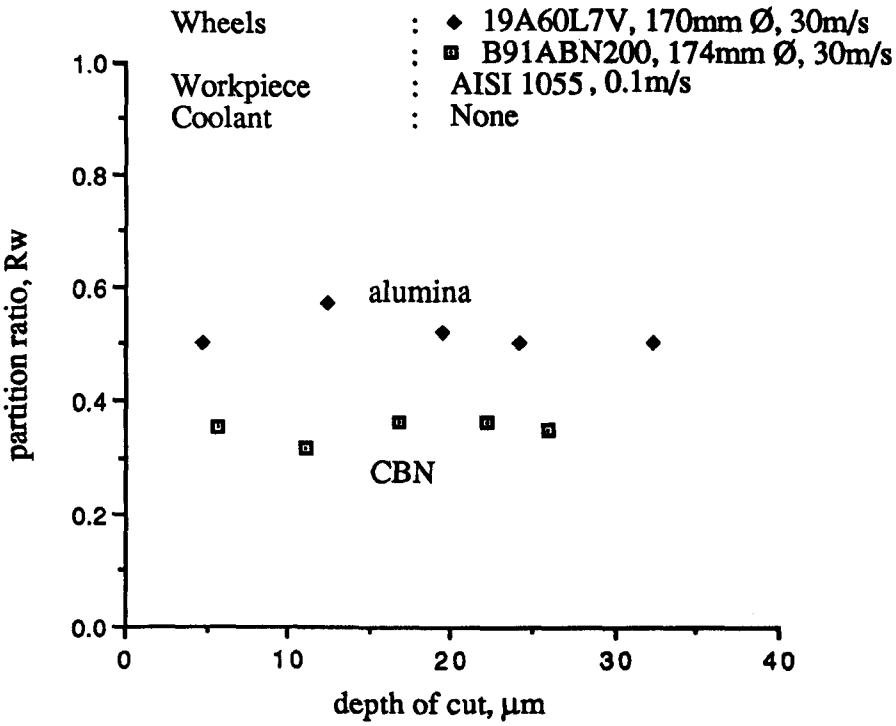

Figure 6.20 : A comparison of the partition ratio based on a uniform heat flux against depth of cut for the dry grinding of AISI 1055 with the 19A60L7V alumina wheel and the CBN wheel at 0.1m/s

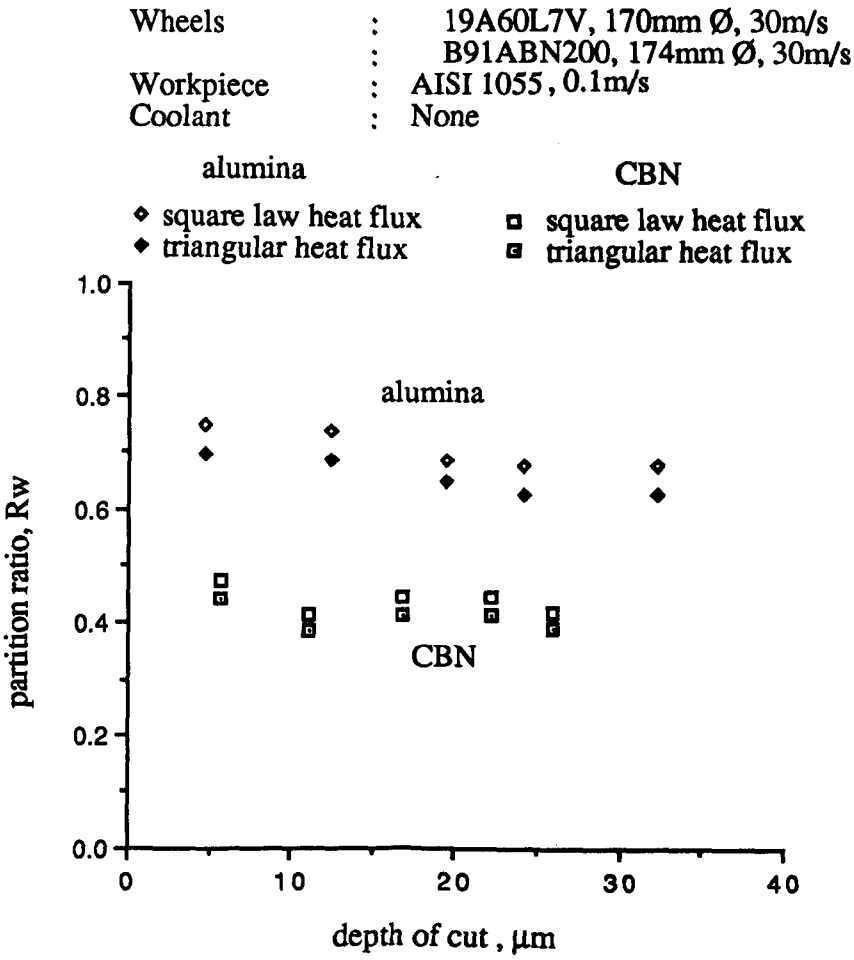

Figure 6.21 : A comparison of the partition ratio based on a triangular and square law heat flux against depth of cut for the dry grinding of AISI 1055 with the 19A60L7V alumina wheel and the CBN wheel at 0.1m/s

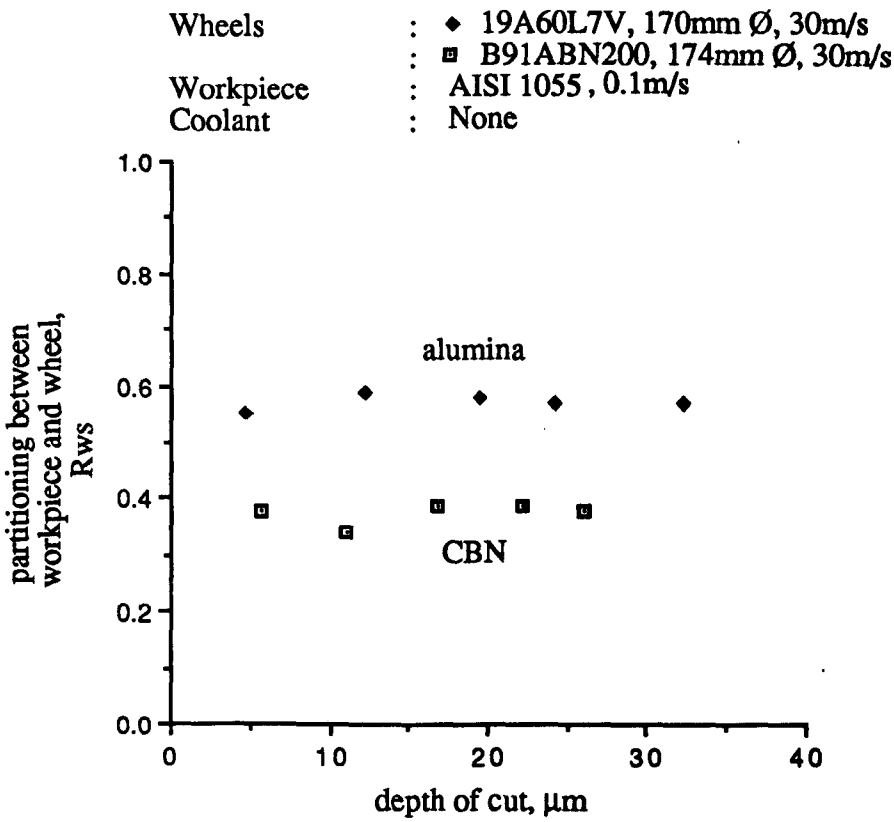

Figure 6.22 : A comparison of the partitioning between the workpiece and wheel based on a uniform heat flux for the dry grinding of AISI 1055 with the 19A60L7V alumina wheel and the CBN wheel at 0.1m/s

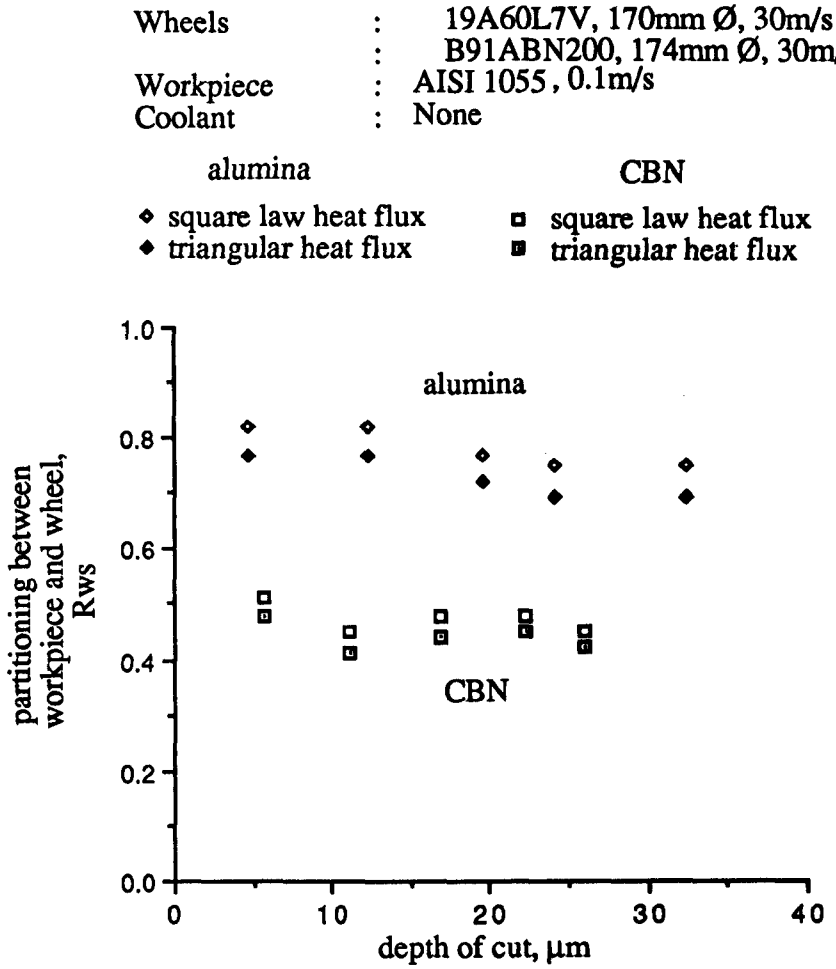

Figure 6.23 : A comparison of the partitioning between the workpiece and wheel based on a triangular and square law heat flux for the dry grinding of AISI 1055 with the 19A60L7V alumina wheel and the CBN wheel at 0.1m/s

Experimental data :

Wheels	:	◆ 19A60L7V, 170mm Ø, 30m/s
	:	◘ B91ABN200, 174mm Ø, 30m/s
Workpiece	:	AISI 1055 , 0.1m/s
Coolant	:	None

Model data :

Workpiece	Alumina	CBN
κw = 42.6 W/mK	κg = 54 W/mK	κg = 325 W/mK
ρw = 7840 kg/m3	ρg = 3910 kg/m3	ρg = 3480kg/m3
cw = 477 J/KgK	cg = 765 J/KgK	cg = 506 J/KgK
	Rr = 6 ro=25μm	Rr = 3.5 ro=15μm

ecc = 6J/mm3

—— steady state solution

transient solution

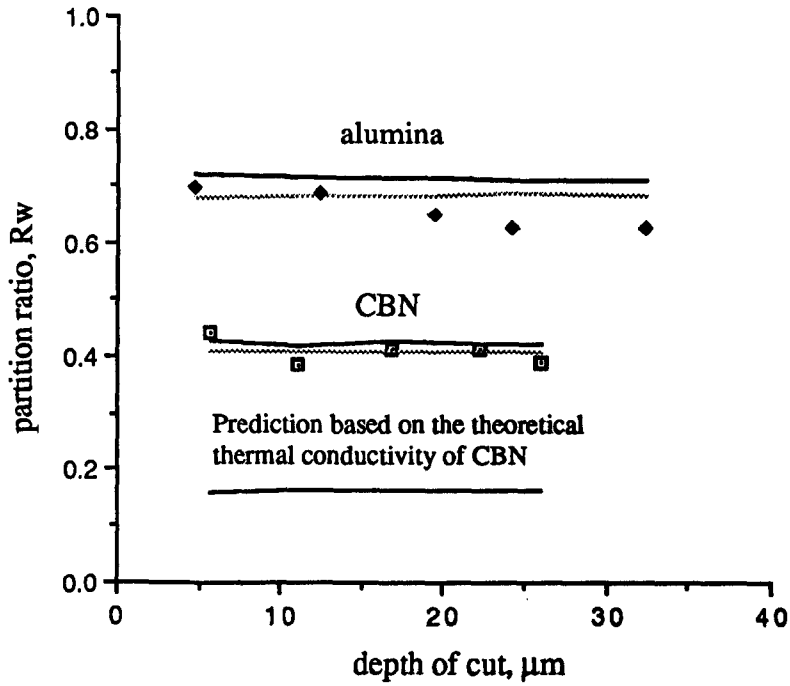

Figure 6.24 : A comparison of the theoretical and measured partition ratios based on a triangular heat flux for the dry grinding of 19A60L7V alumina wheel and the CBN wheel at 0.1m/s

Experimental data :

Wheel	:	◆ 19A60L7V, 170mm Ø, 30m/s
	:	
Workpiece	:	AISI 1055, 0.1m/s
Coolant	:	None

Model data :

Workpiece	Alumina
κ_w = 42.6 W/mK	κ_g = 54 W/mK
ρ_w = 7840 kg/m3	ρ_g = 3910 kg/m3
c_w = 477 J/KgK	c_g = 765 J/KgK
	Rr = 6 ro=25μm

ecc = 6J/mm3

—— steady state solution

transient solution

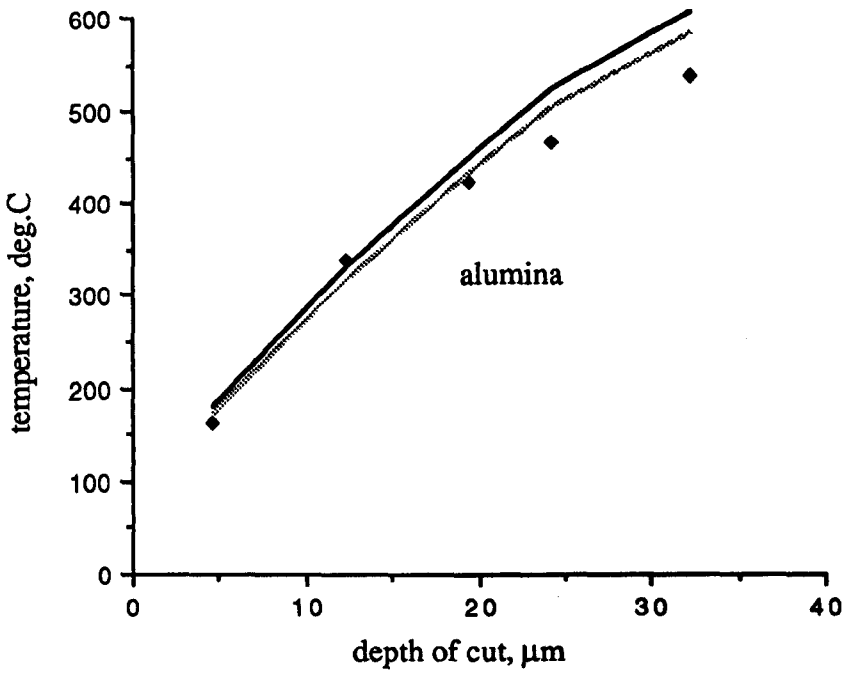

Figure 6.25 : A comparison of the theoretical and measured temperatures for the dry grinding of AISI 1055 with the 19A60L7V alumina wheel at 0.1m/s

Experimental data :

Wheels	:	◆ 19A60L7V, 170mm Ø, 30m/s
	:	◘ B91ABN200, 174mm Ø, 30m/s
Workpiece	:	AISI 1055 , 0.1m/s
Coolant	:	None

Model data :

Workpiece	CBN
κw = 42.6 W/mK	κg = 325 W/mK
ρw = 7840 kg/m3	ρg = 3910 kg/m3
cw = 477 J/KgK	cg = 765 J/KgK
	Rr = 3.5 ro=15μm

ecc = 6J/mm3

—— steady state solution

transient solution

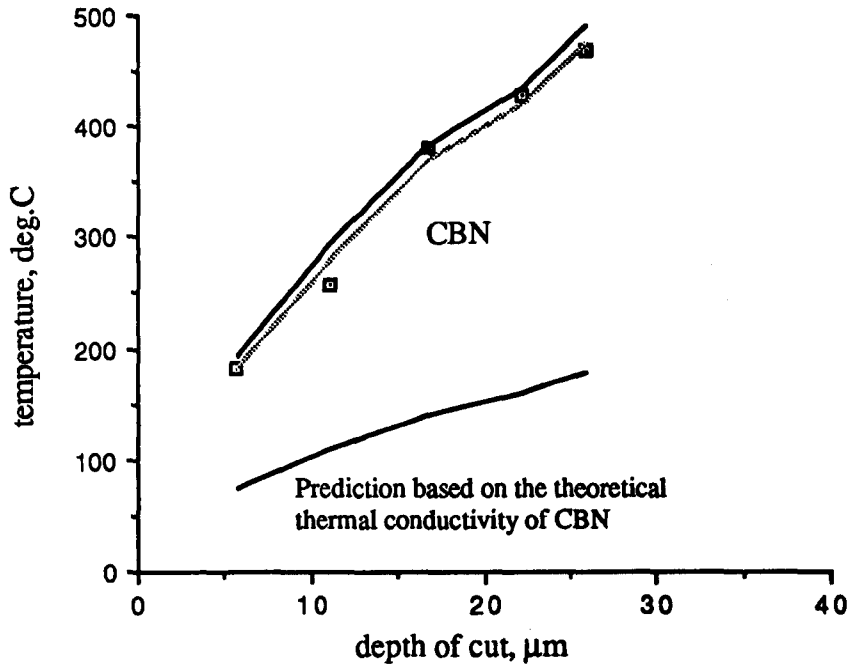

Figure 6.26 : A comparison of the theoretical and measured temperatures for the dry grinding of AISI 1055 with the CBN wheel at 0.1m/s

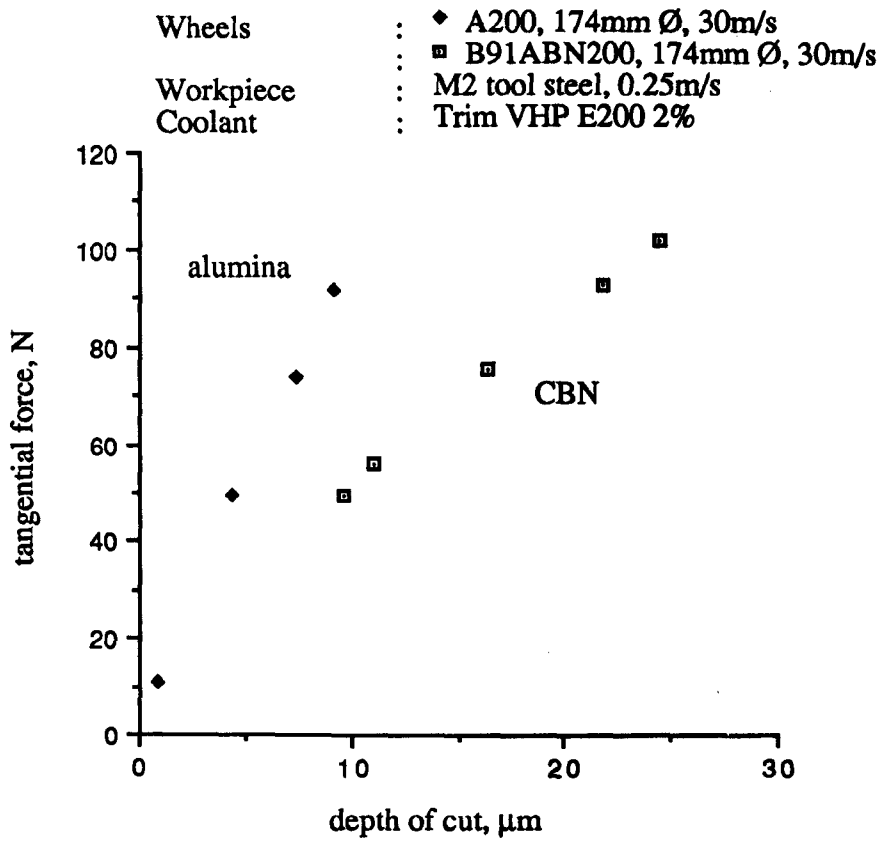

Figure 6.27 : A comparison of the tangential force against depth of cut for the wet grinding of M2 tool steel with the A200 alumina wheel and the CBN wheel at 0.25m/s

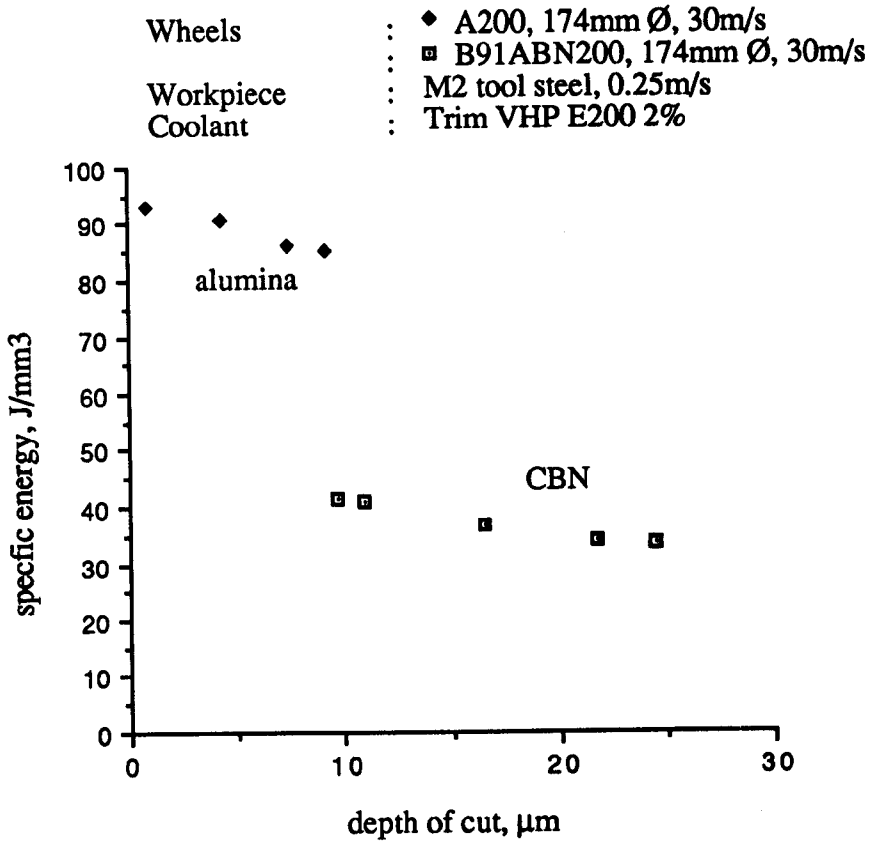

Figure 6.28 : A comparison of the specific energy against depth of cut for the wet grinding of M2 tool steel with the A200 alumina wheel and the CBN wheel at 0.25m/s

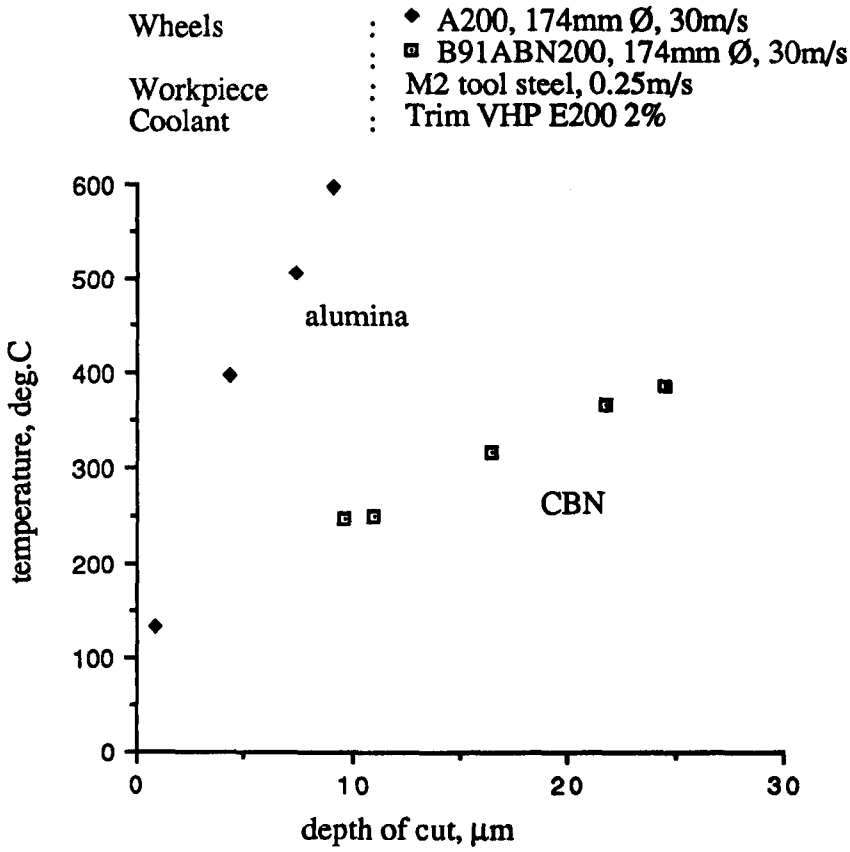

Figure 6.29 : A comparison of the temperature against depth of cut for the wet grinding of M2 tool steel with the A200 alumina wheel and the CBN wheel at 0.25m/s

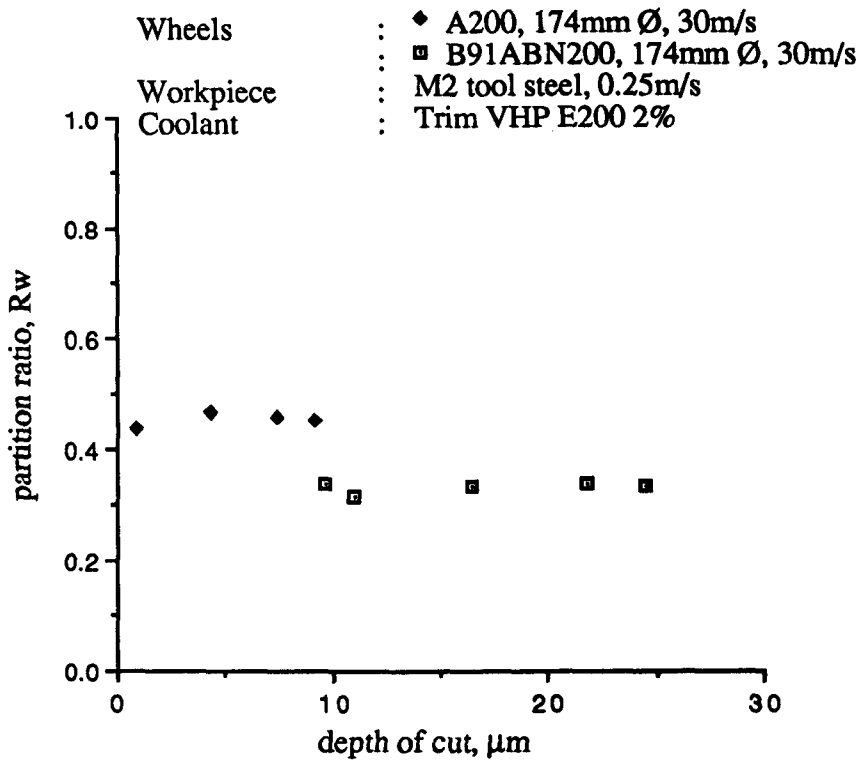

Figure 6.30 : A comparison of the partition ratio based on a uniform heat flux for the wet grinding of M2 tool steel with the A200 alumina wheel and the CBN wheel at 0.25m/s

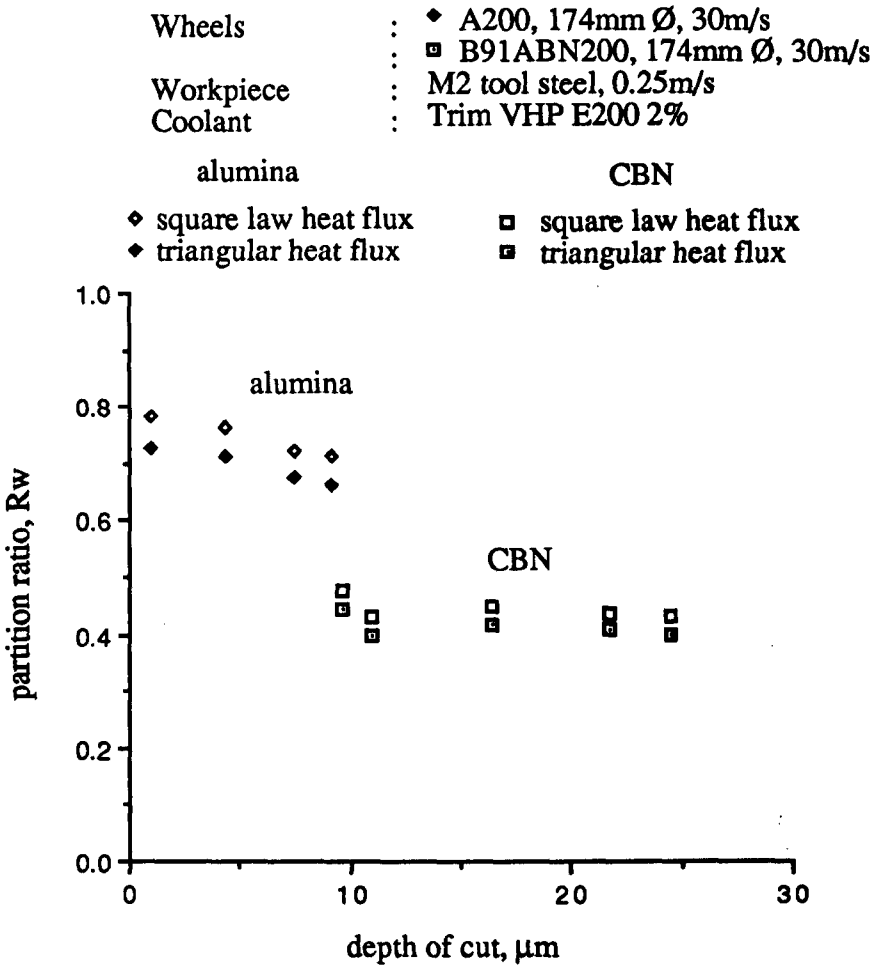

Figure 6.31 : A comparison of the partition ratio based on a triangular and square law heat flux for the wet grinding of M2 tool steel with the A200 alumina wheel and the CBN wheel at 0.25m/s

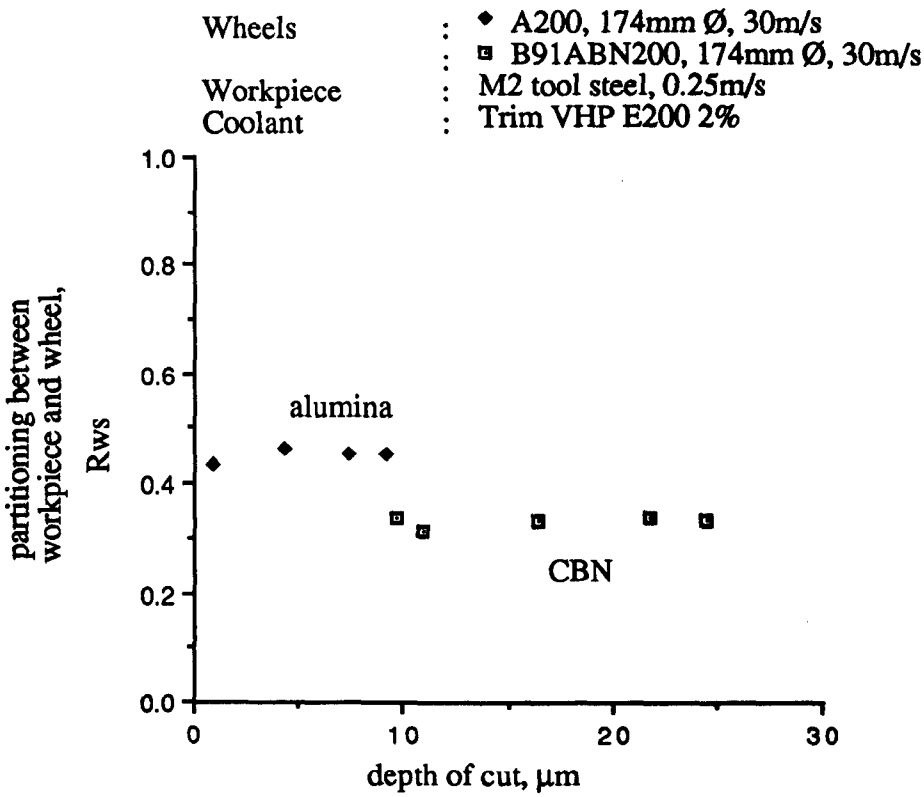

Figure 6.32 : A comparison of the partitioning between the workpiece and wheel based on a uniform heat flux for the wet grinding of M2 tool steel with the A200 alumina wheel and the CBN wheel at 0.25m/s

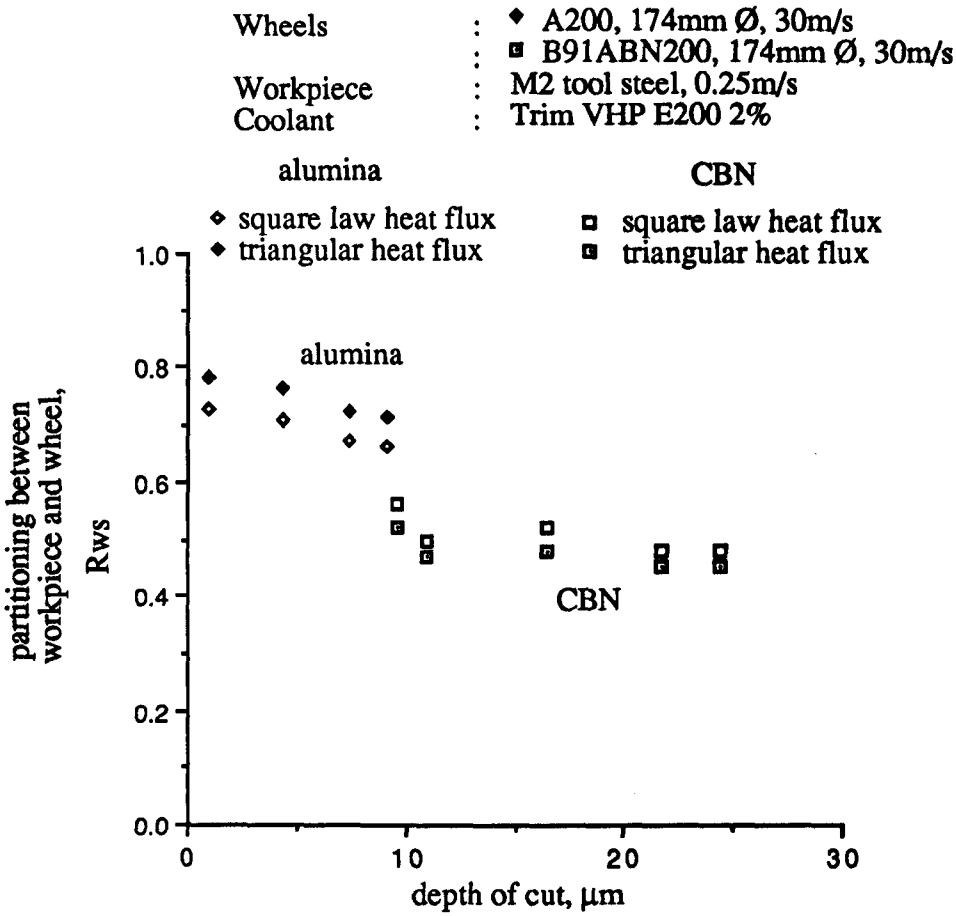

Figure 6.33 : A comparison of the partitioning between the workpiece and wheel based on a triangular and square law heat flux for the wet grinding of M2 tool steel with the A200 alumina wheel and the CBN wheel at 0.25m/s

Experimental data :

Wheel	: ◆	A200, 174mm Ø, 30m/s
	:	
Workpiece	:	M2 tool steel, 0.25m/s
Coolant	:	Trim VHP E200 2%

Model data :

Workpiece	Alumina
κ_w = 23.5 W/mK	κ_g = 51W/mK
ρ_w = 7860kg/m3	ρ_g = 3910 kg/m3
c_w = 515 J/KgK	c_g = 765 J/KgK
	Rr = 3.5 ro=15μm

ecc = 6J/mm3

—— steady state solution

····· transient solution

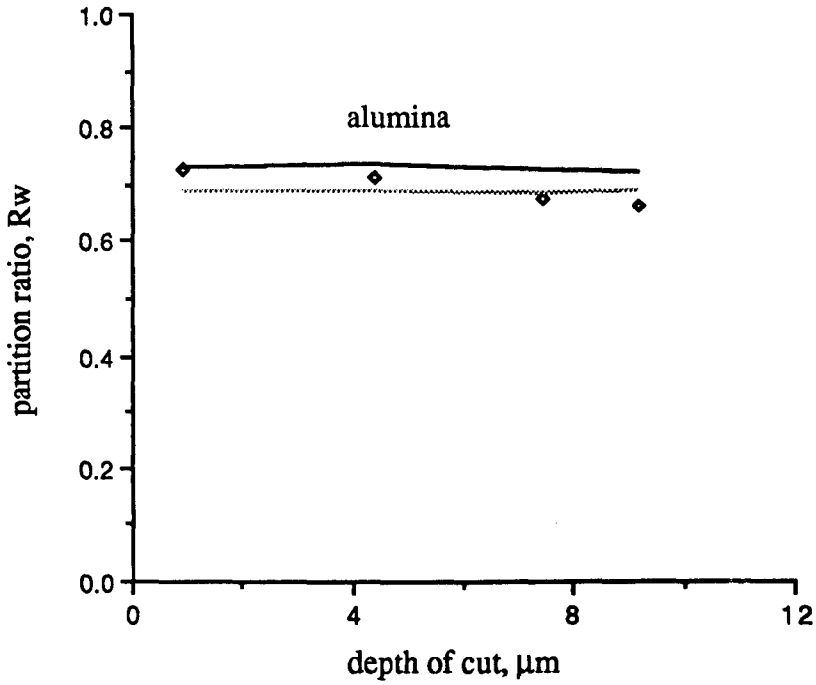

Figure 6.34 : A comparison of the theoretical and measured partition ratios based on a triangular heat flux for the wet grinding of M2 tool steel with the A200 alumina wheel at 0.25m/s

Experimental data :

Wheel	: ◆	A200, 174mm Ø, 30m/s
	:	
Workpiece	:	M2 tool steel, 0.25m/s
Coolant	:	Trim VHP E200 2%

Model data :

Workpiece	Alumina
κ_w = 23.5 W/mK	κ_g = 51W/mK
ρ_w = 7860kg/m3	ρ_g = 3910 kg/m3
c_w = 515 J/KgK	c_g = 765 J/KgK
	Rr = 3.5 ro=15μm

ecc = 6J/mm3

—— steady state solution

..... transient solution

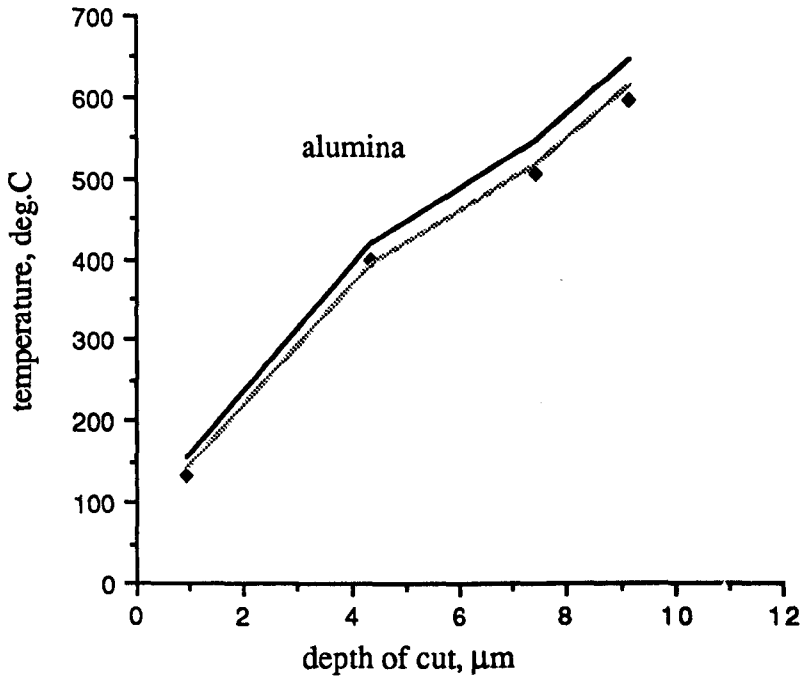

Figure 6.35 : A comparison of the theoretical and measured temperatures for the wet grinding of M2 tool steel with the A200 alumina wheel at 0.25m/s

Experimental data :

Wheel : ▫ B91ABN200, 174mm Ø, 30m/s
:
Workpiece : M2 tool steel, 0.25m/s
Coolant : Trim VHP E200 2%

Model data :

Workpiece
κw = 23.5 W/mK
ρw = 7860kg/m3
cw = 515 J/KgK

CBN
κg = 230 W/mK
ρg = 3480 kg/m3
cg = 506 J/KgK
Rr = 3.5 ro=15μm

ecc = 6J/mm3
—— steady state solution
..... transient solution

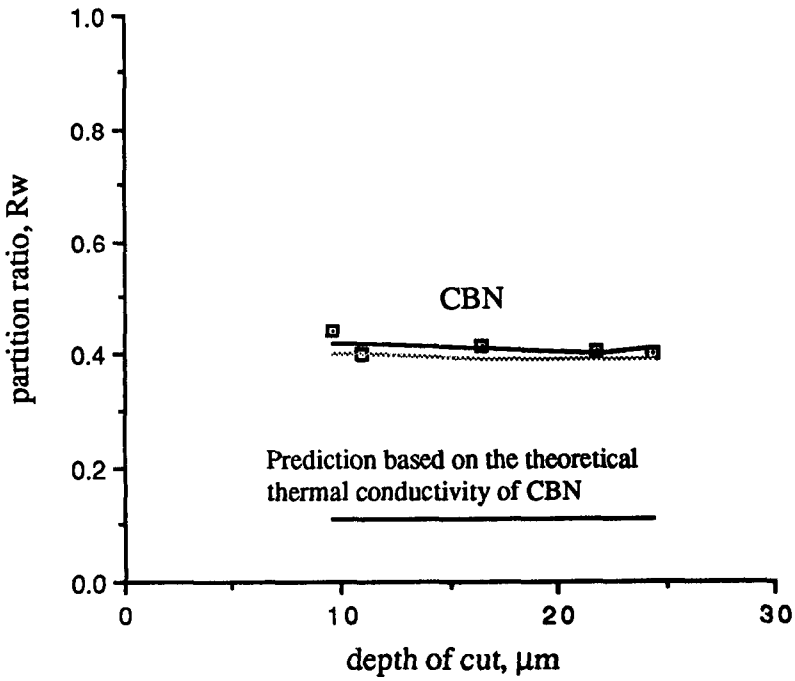

Figure 6.36 : A comparison of the theoretical and measured partition ratios based on a triangular heat flux for the wet grinding of M2 tool steel with the CBN wheel at 0.25m/s

Experimental data :

Wheel	: ◘	B91ABN200, 174mm Ø, 30m/s
	:	
Workpiece	:	M2 tool steel, 0.25m/s
Coolant	:	Trim VHP E200 2%

Model data :

Workpiece	CBN
κ_w = 23.5 W/mK	κ_g = 230 W/mK
ρ_w = 7860kg/m3	ρ_g = 3480 kg/m3
c_w = 515 J/KgK	c_g = 506 J/KgK
	Rr = 3.5 ro=15μm

ecc = 6J/mm3

—— steady state solution

..... transient solution

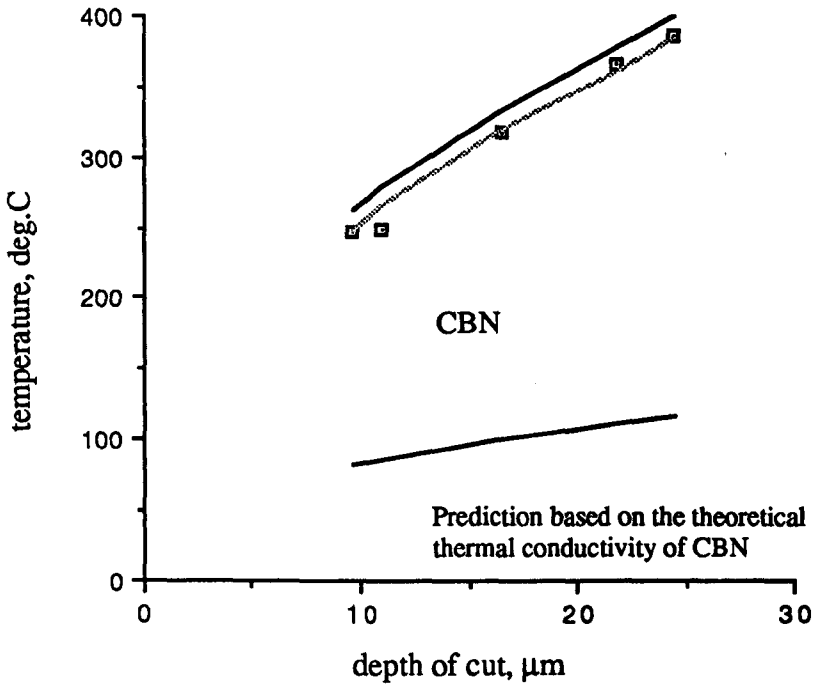

Figure 6.37 : A comparison of the theoretical and measured temperatures for the wet grinding of M2 tool steel with the CBN wheel at 0.25m/s

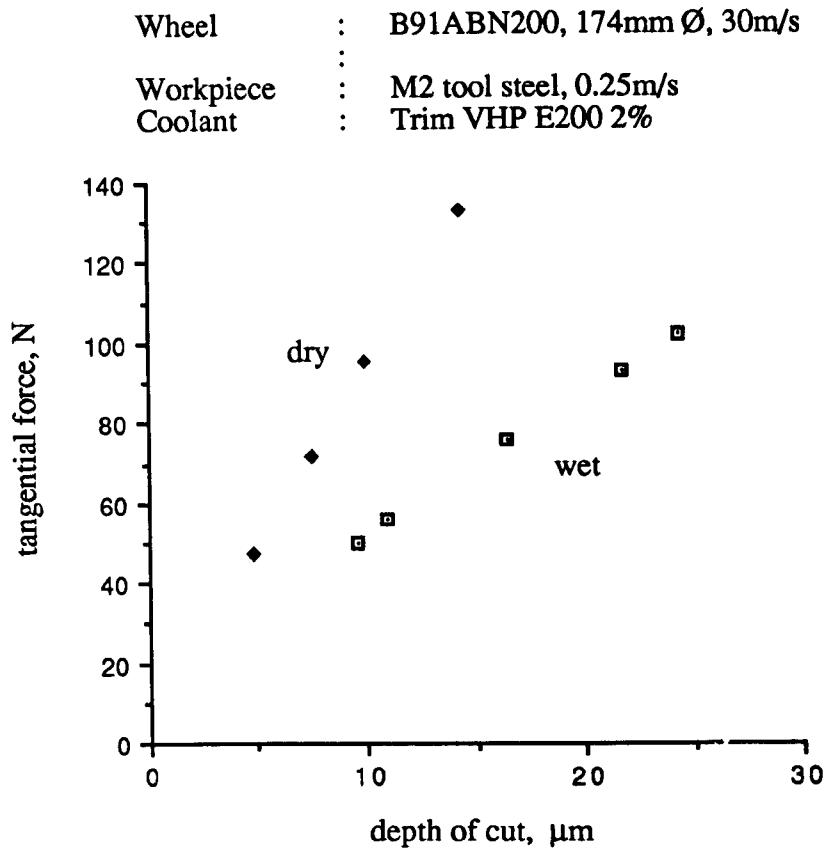

Figure 6.38 : A comparison of the tangential forces against depth of cut for the dry and wet grinding of M2 with the CBN wheel at 0.25m/s

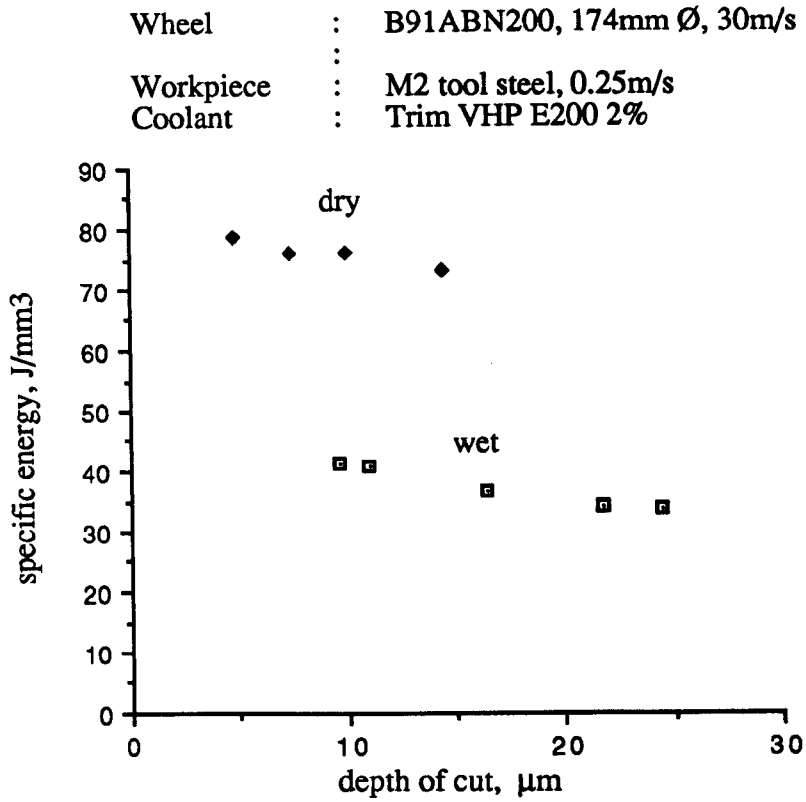

Figure 6.39 : A comparison of the specific energy against depth of cut for the dry and wet grinding of M2 with the CBN wheel at 0.25m/s

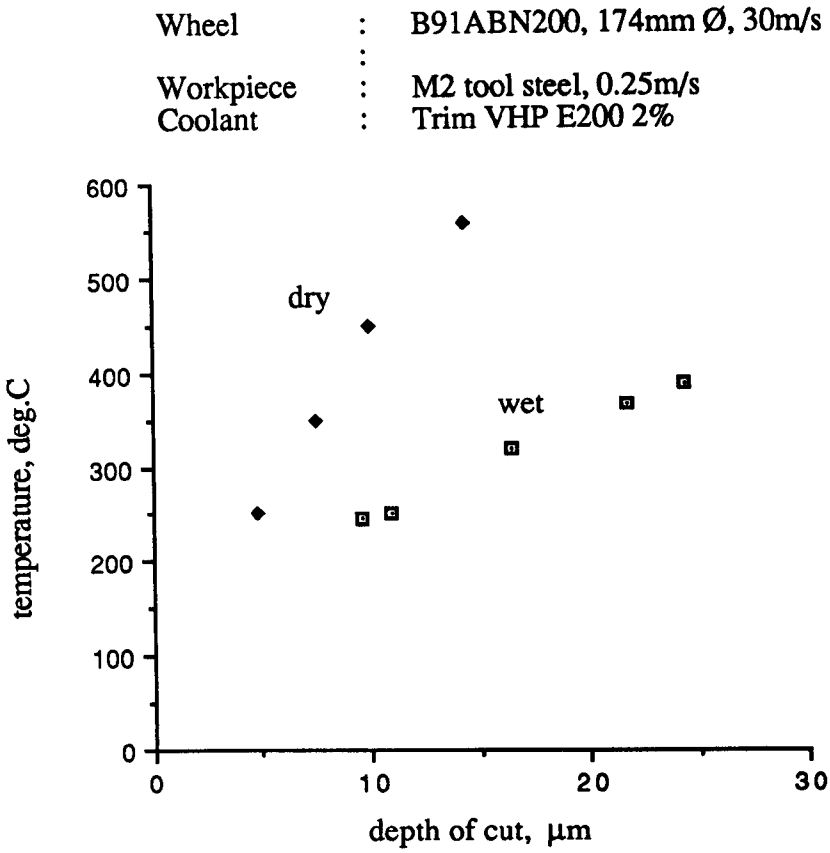

Figure 6.40 : A comparison of the temperature against depth of cut for the dry and wet grinding of M2 with the CBN wheel at 0.25m/s

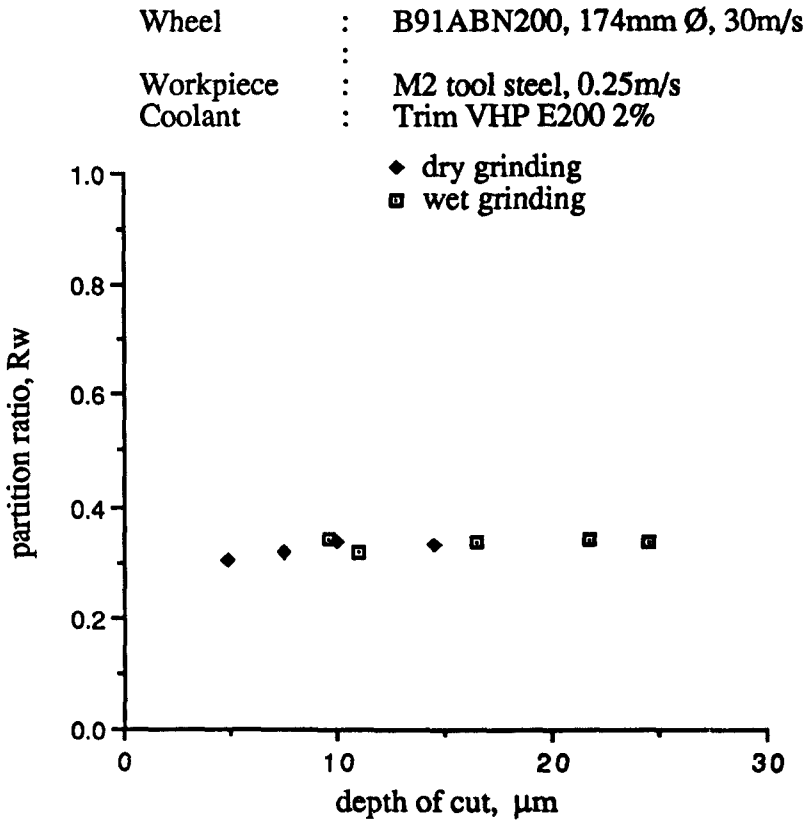

Figure 6.41 : A comparison of the partition ratio based on a uniform heat flux for the dry and wet grinding of M2 with the CBN wheel at 0.25m/s

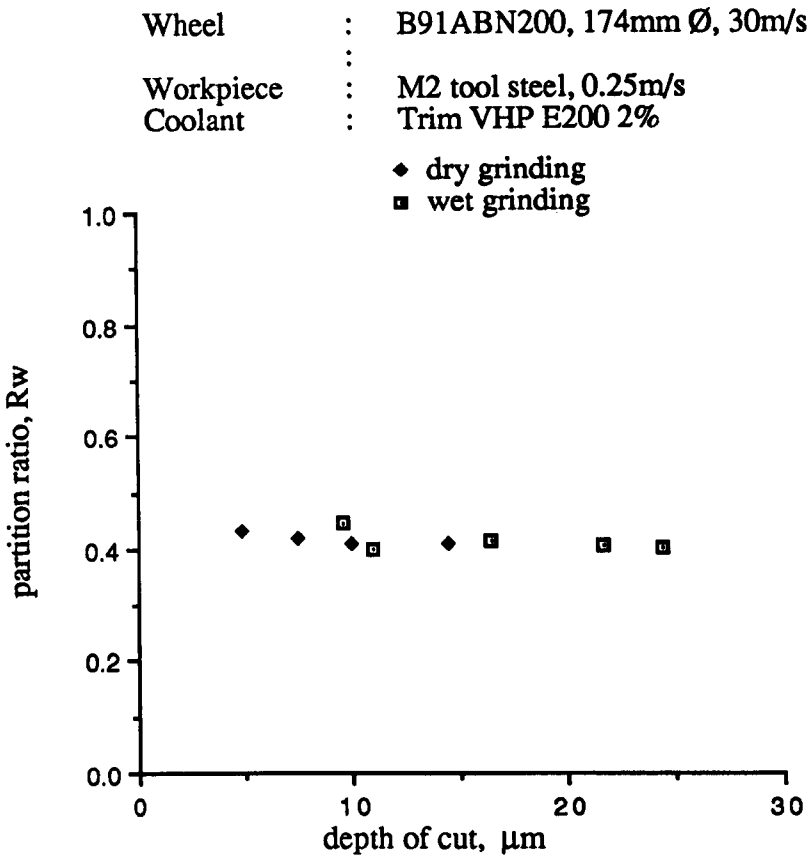

Figure 6.42 : A comparison of the partition ratio based on a triangular heat flux for the dry and wet grinding of M2 with the CBN wheel at 0.25m/s

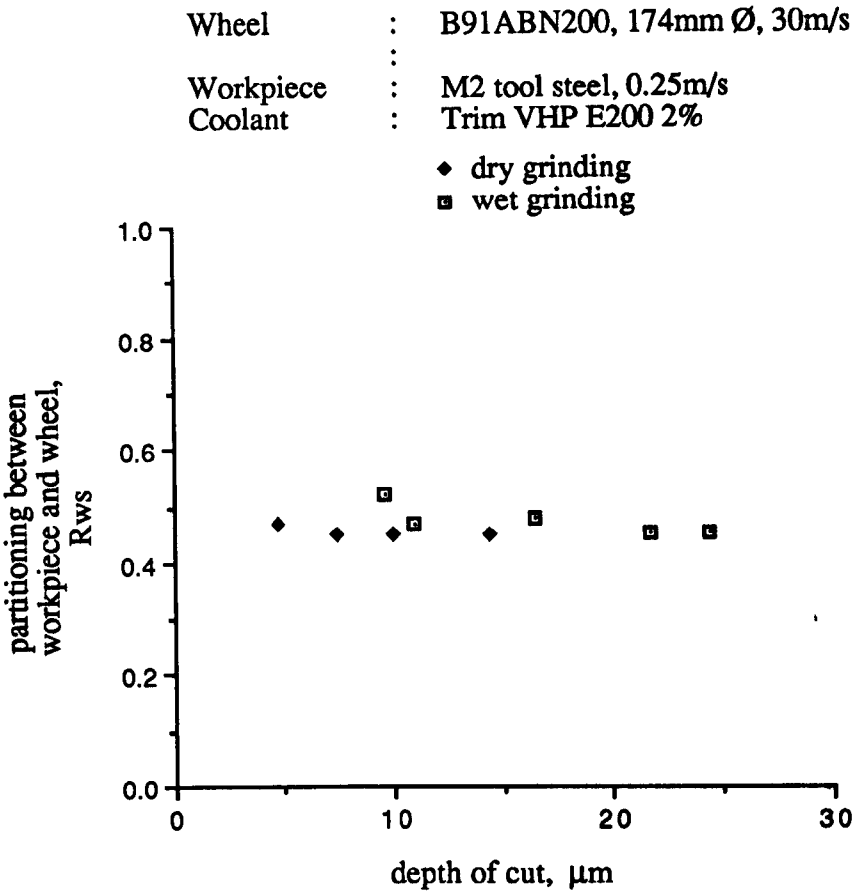

Figure 6.43: A comparison of the partitioning between the workpiece and wheel based on a triangular heat flux for the dry and wet grinding of M2 with the CBN wheel at 0.25m/s

Experimental data :

Wheel	: ▫	B91ABN200, 174mm Ø, 30m/s
	:	
Workpiece	:	M2 tool steel, 0.25m/s
Coolant	:	Trim VHP E200 2%

Model data :

Workpiece	Fluid	CBN
$\kappa w = 23.5$ W/mK	$\kappa g = 0.6$W/mK	$\kappa g = 230$ W/mK
$\rho w = 7860$kg/m3	$\rho g = 1000$kg/m3	$\rho g = 3480$ kg/m3
$cw = 515$ J/KgK	$cg = 4200$J/KgK	$cg = 506$ J/KgK
		$Rr = 3.5$ $ro = 15\mu m$

ecc = 6J/mm3

—— no allowance for chips or fluid

..... allowance for chips only

- - - allowance for chips and fluid

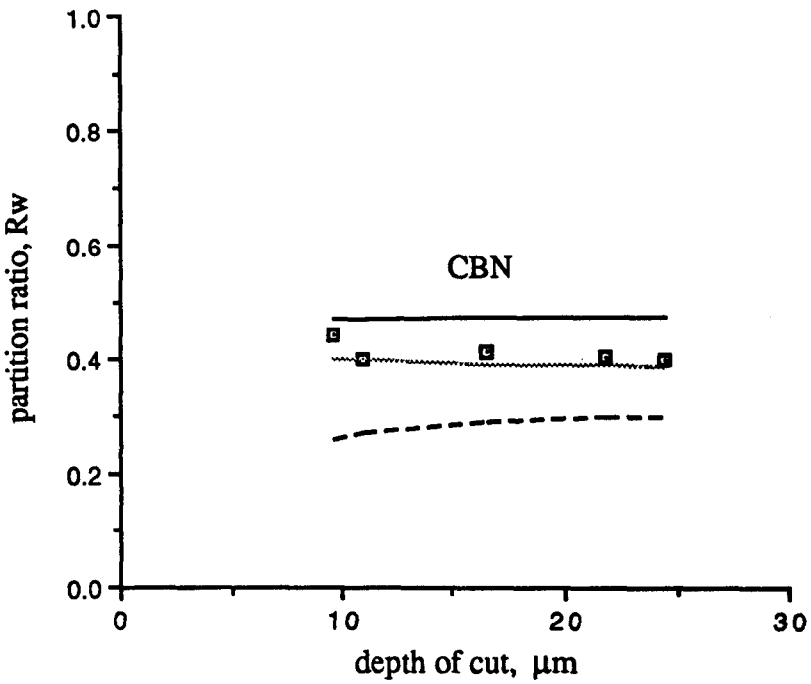

Figure 6.44 : A comparison of the theoretical and measured partition ratios based on a triangular heat flux for wet grinding of M2 with the CBN wheel at 0.25m/s

Experimental data :

Wheel	: ▫	B91ABN200, 174mm Ø, 30m/s
	:	
Workpiece	:	M2 tool steel, 0.25m/s
Coolant	:	Trim VHP E200 2%

Model data :

Workpiece	Fluid	CBN
κw = 23.5 W/mK	κg = 0.6W/mK	κg = 230 W/mK
ρw = 7860kg/m3	ρg = 1000kg/m3	ρg = 3480 kg/m3
cw = 515 J/KgK	cg = 4200J/KgK	cg = 506 J/KgK
		Rr = 3.5 ro=15μm

ecc = 6J/mm3

—— no allowance for chips or fluid

..... allowance for chips only

- - - allowance for chips and fluid

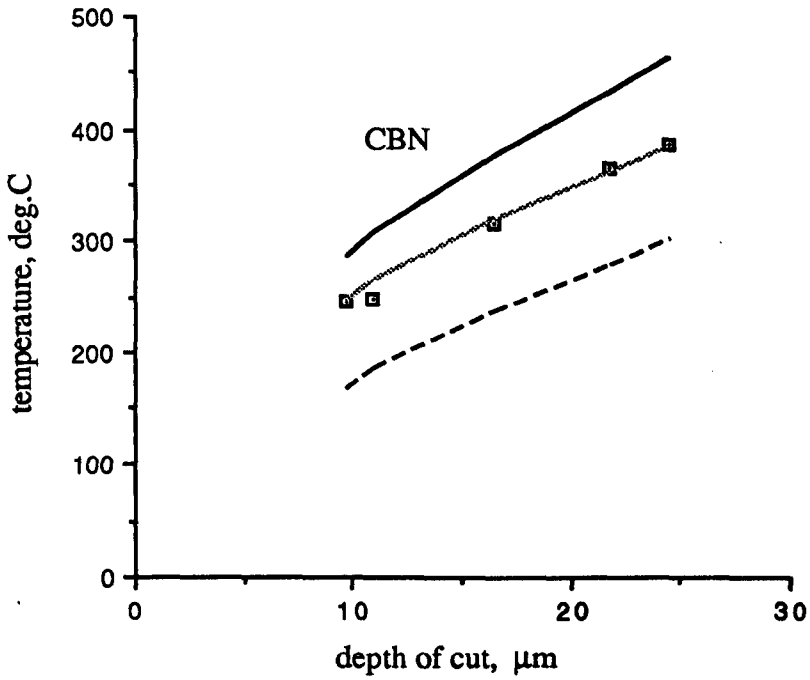

Figure 6.45 : A comparison of the theoretical and measured temperatures for the wet grinding of M2 with the CBN wheel at 0.25m/s

Experimental data :

Wheel	: ◆	B91ABN200, 174mm Ø, 30m/s
	:	
Workpiece	:	M2 tool steel, 0.25m/s
Coolant	:	None

Model data :

Workpiece	Fluid	CBN
κw = 23.5 W/mK	κg = 0.6W/mK	κg = 240W/mK
ρw = 7860kg/m3	ρg = 1000kg/m3	ρg = 3480 kg/m3
cw = 515 J/KgK	cg = 4200J/KgK	cg = 506 J/KgK
		Rr = 3.5 ro=15μm

ecc = 6J/mm3

—— no allowance for chips

····· allowance for chips only

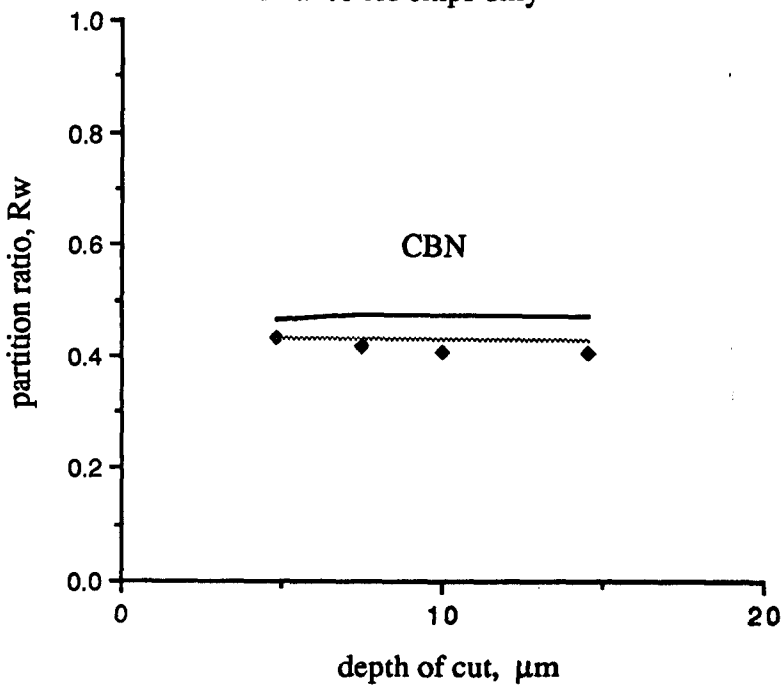

Figure 6.46 : A comparison of the theoretical and measured partition ratios based on a triangular heat flux for the dry grinding of M2 with the CBN wheel at 0.25m/s

Experimental data :

Wheel	: ◆	B91ABN200, 174mm Ø, 30m/s
	:	
Workpiece	:	M2 tool steel, 0.25m/s
Coolant	:	None

Model data :

Workpiece	Fluid	CBN
κ_w = 23.5 W/mK	κ_g = 0.6W/mK	κ_g = 240W/mK
ρ_w = 7860kg/m3	ρ_g = 1000kg/m3	ρ_g = 3480 kg/m3
c_w = 515 J/KgK	c_g = 4200J/KgK	c_g = 506 J/KgK
		Rr = 3.5 ro=15μm

ecc = 6J/mm3

—— no allowance for chips

..... allowance for chips only

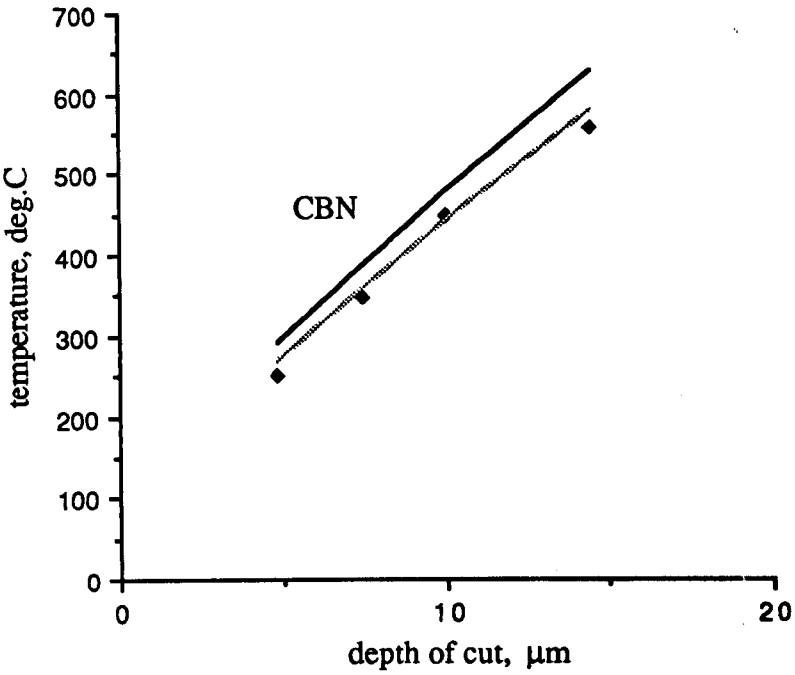

Figure 6.47 : A comparison of the theoretical and measured temperatures for the dry grinding of M2 with the CBN wheel at 0.25m/s

Wheel	:	A200, 174mm Ø, 30m/s
	:	
Workpiece	:	M2 tool steel, 0.25m/s
Coolant	:	Trim VHP E200 2%

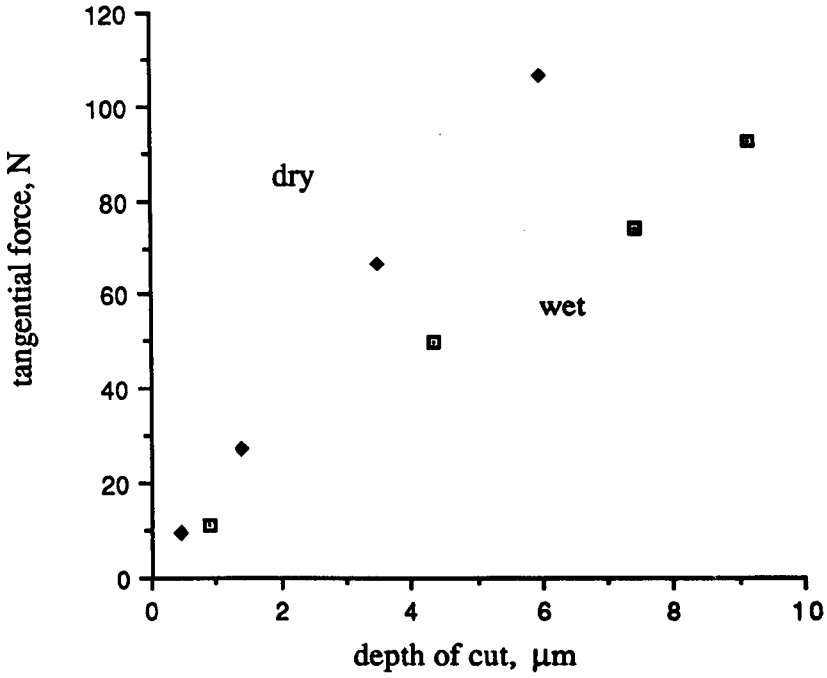

Figure 6.48 : A comparison of the tangential forces against depth of cut for the dry and wet grinding of M2 with the A200 alumina wheel at 0.25m/s

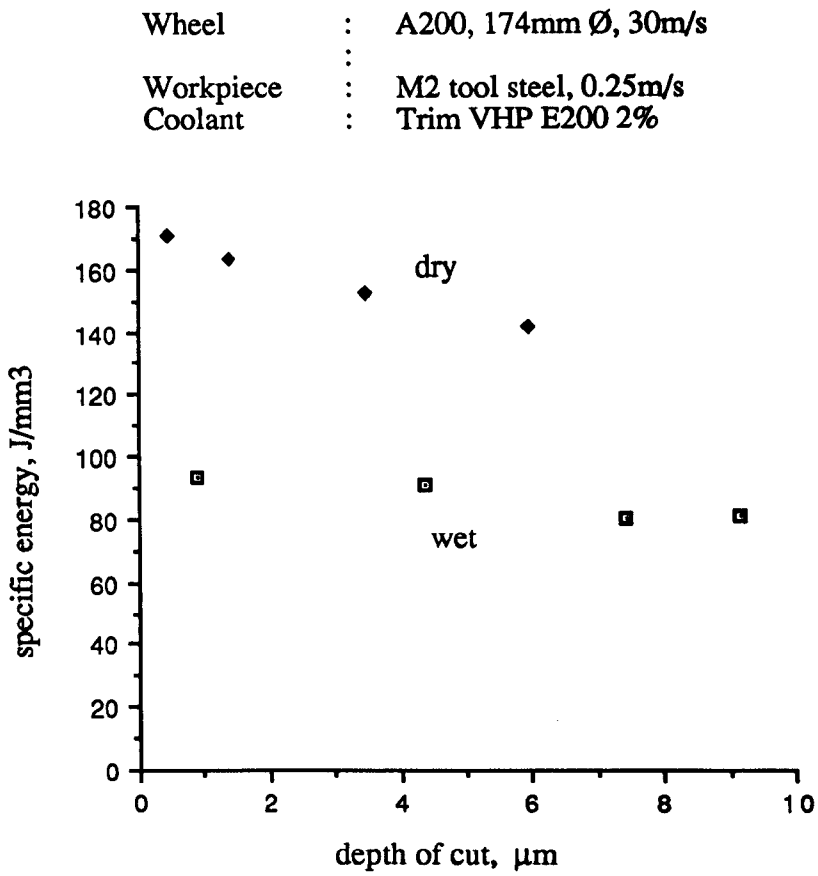

Figure 6.49 : A comparison of the specific energy against depth of cut for the dry and wet grinding of M2 with the A200 alumina wheel at 0.25m/s

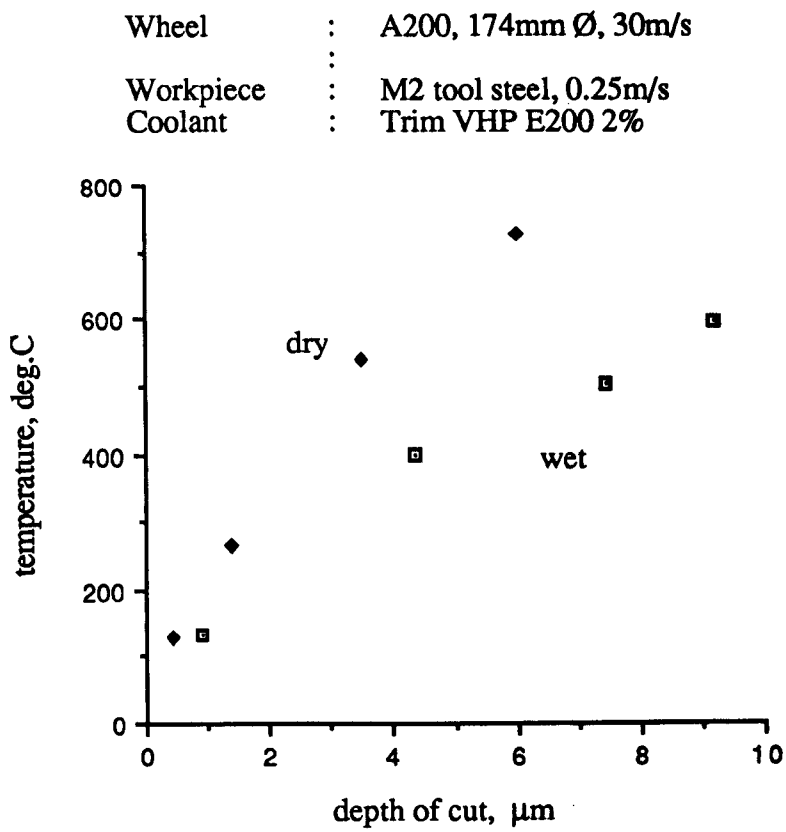

Figure 6.50 : A comparison of the temperatures against depth of cut for the dry and wet grinding of M2 with the A200 alumina wheel at 0.25m/s

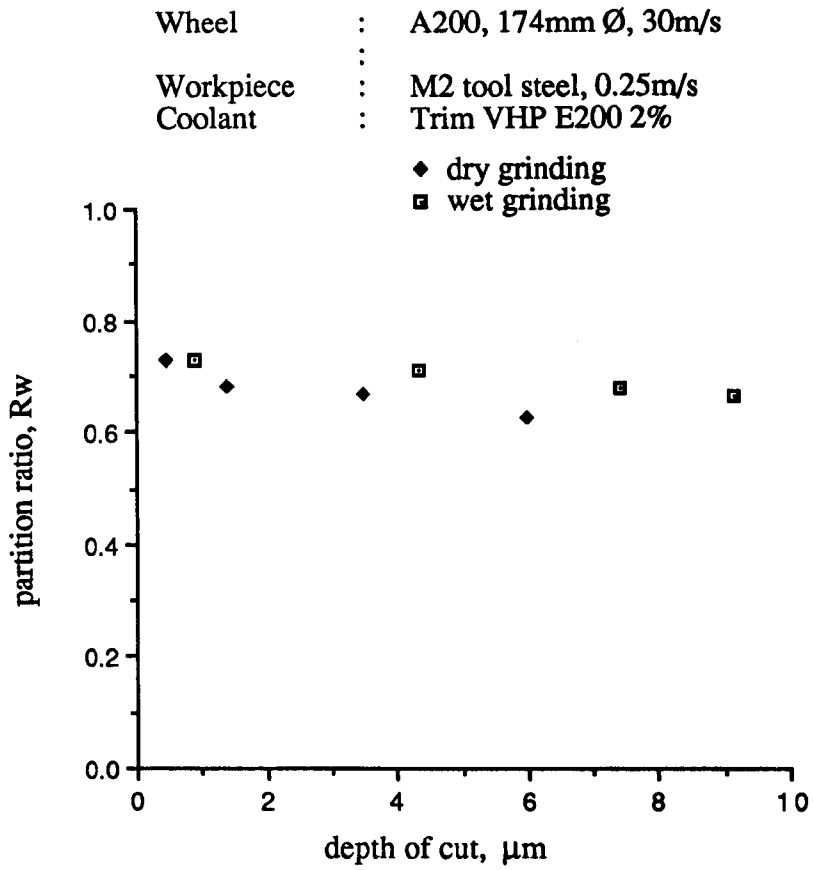

Figure 6.51 : A comparison of the partition ratio based on a triangular heat flux for the dry and wet grinding of M2 with the A200 alumina wheel at 0.25m/s

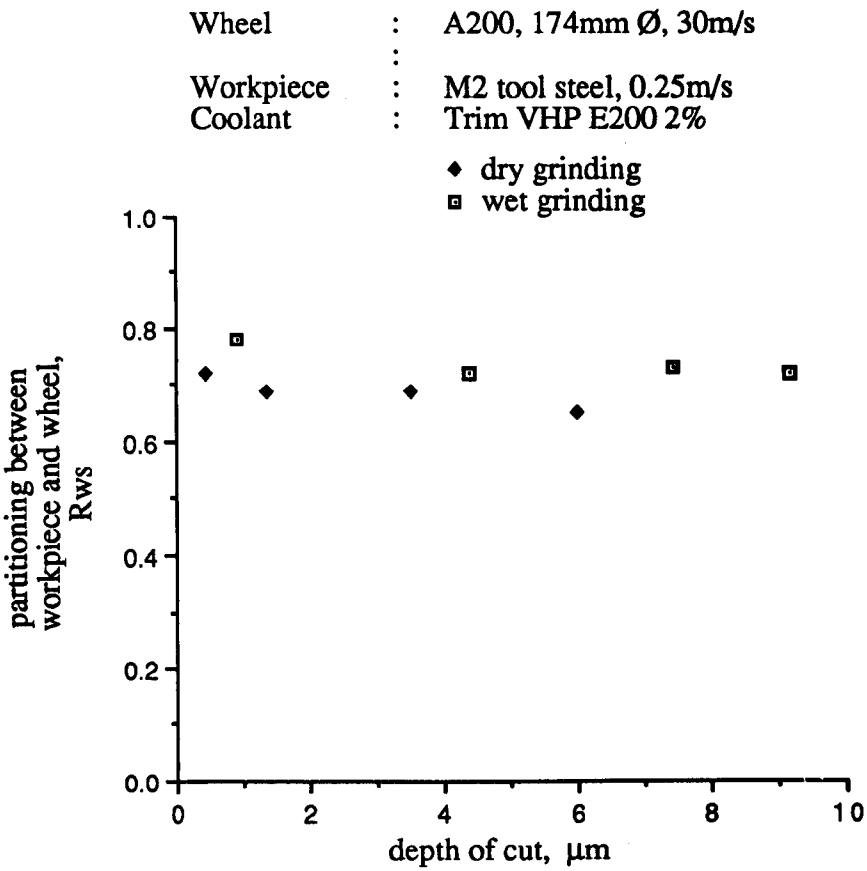

Figure 6.52: A comparison of the partitioning between the workpiece and wheel based on a triangular heat flux triangular heat flux for the dry and wet grinding of M2 with the A200 alumina wheel at 0.25m/s

Experimental data :

Wheel	: ▫	A200, 174mm Ø, 30m/s
	:	
Workpiece	:	M2 tool steel, 0.25m/s
Coolant	:	Trim VHP E200 2%

Model data :

Workpiece	Fluid	Alumina
κ_w = 23.5 W/mK	κ_g = 0.6W/mK	κ_g = 51W/mK
ρ_w = 7860kg/m3	ρ_g = 1000kg/m3	ρ_g = 3910 kg/m3
c_w = 515 J/KgK	c_g = 4200J/KgK	c_g = 765 J/KgK
		Rr = 4.5 ro=15μm

ecc = 6J/mm3

—— no allowance for chips or fluid

..... allowance for chips only

- - - allowance for chips and fluid

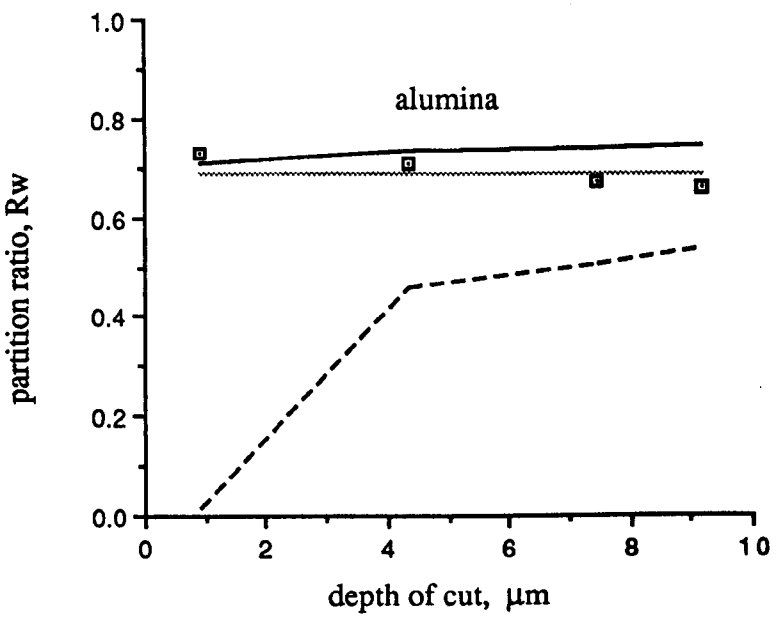

Figure 6.53 : A comparison of the theoretical and measured partition ratios based on a triangular heat flux for wet grinding of M2 with the A200 alumina wheel at 0.25m/s

Experimental data :

Wheel	: ▫	A200, 174mm Ø, 30m/s
	:	
Workpiece	:	M2 tool steel, 0.25m/s
Coolant	:	Trim VHP E200 2%

Model data :

Workpiece	Fluid	Alumina
κ_w = 23.5 W/mK	κ_g = 0.6W/mK	κ_g = 51W/mK
ρ_w = 7860kg/m3	ρ_g = 1000kg/m3	ρ_g = 3910 kg/m3
c_w = 515 J/KgK	c_g = 4200J/KgK	c_g = 765 J/KgK
		Rr = 4.5 ro=15μm

ecc = 6J/mm3

—— no allowance for chips or fluid

····· allowance for chips only

- - - allowance for chips and fluid

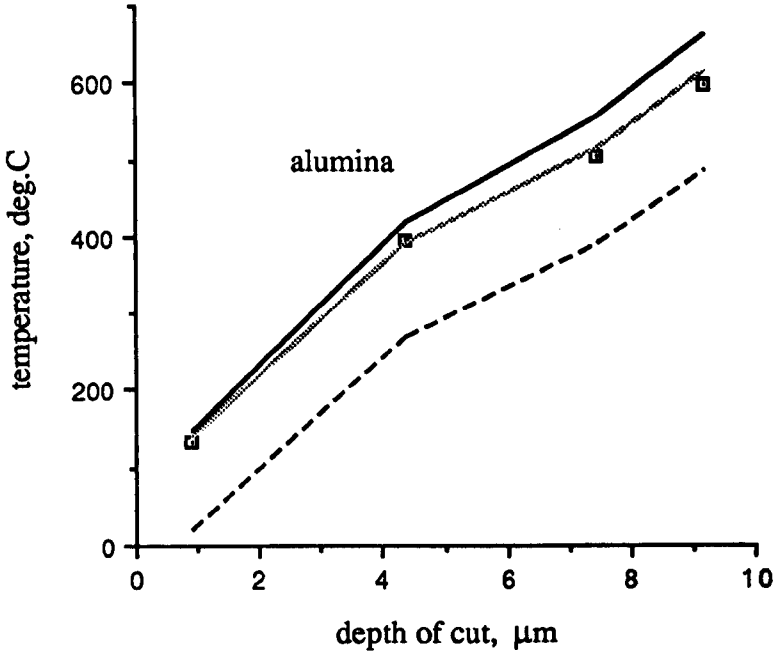

Figure 6.54 : A comparison of the theoretical and measured temperatures for the wet grinding of M2 with the A200 alumina wheel at 0.25m/s

Experimental data :

Wheel	:	◆ A200, 174mm Ø, 30m/s
	:	
Workpiece	:	M2 tool steel, 0.25m/s
Coolant	:	None

Model data :

Workpiece	Fluid	Alumina
κ_w = 23.5 W/mK	κ_g = 0.6W/mK	κ_g = 53 W/mK
ρ_w = 7860kg/m3	ρ_g = 1000kg/m3	ρ_g = 3910 kg/m3
c_w = 515 J/KgK	c_g = 4200J/KgK	c_g = 765 J/KgK
		Rr = 4 ro=15μm

ecc = 6J/mm3

—— no allowance for chips or fluid

..... allowance for chips only

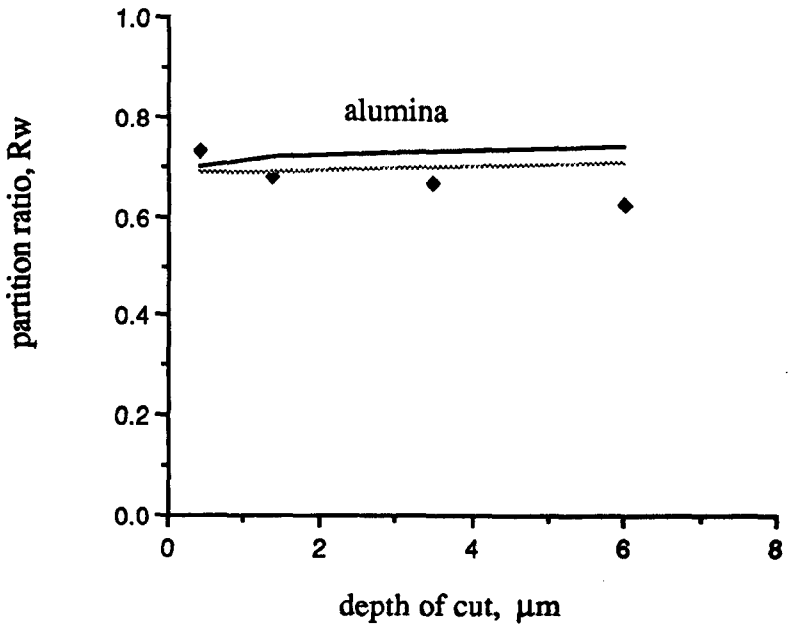

Figure 6.55 : A comparison of the theoretical and measured partition ratios based on a triangular heat flux for the dry grinding of M2 with the A200 alumina wheel at 0.25m/s

Experimental data :

Wheel	:	◆ A200, 174mm Ø, 30m/s
	:	
Workpiece	:	M2 tool steel, 0.25m/s
Coolant	:	None

Model data :

Workpiece	Fluid	Alumina
κ_w = 23.5 W/mK	κ_g = 0.6W/mK	κ_g = 53 W/mK
ρ_w = 7860kg/m3	ρ_g = 1000kg/m3	ρ_g = 3910 kg/m3
c_w = 515 J/KgK	c_g = 4200J/KgK	c_g = 765 J/KgK
		Rr = 4 ro=15μm

ecc = 6J/mm3

—— no allowance for chips or fluid

····· allowance for chips only

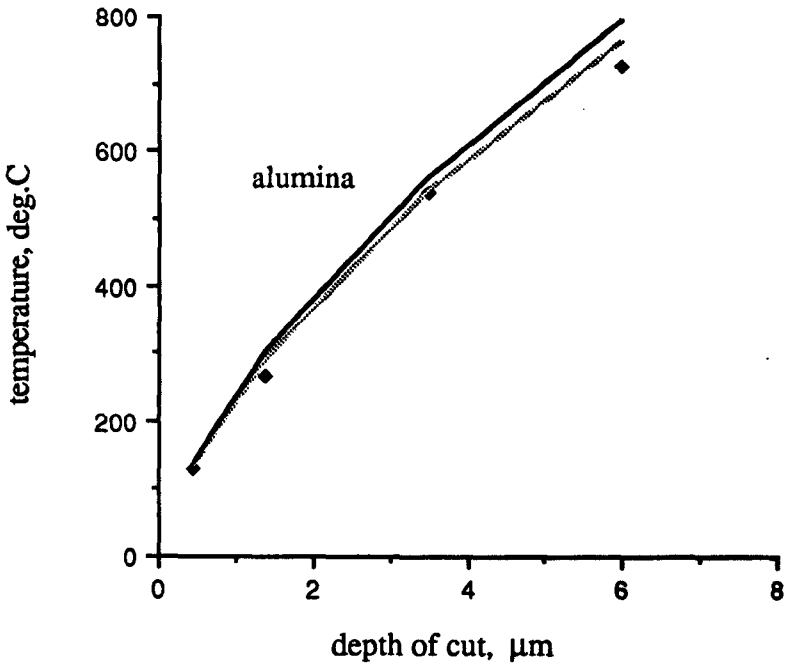

Figure 6.56 : A comparison of the theoretical and measured temperatures for the dry grinding of M2 with the A200 alumina wheel at 0.25m/s

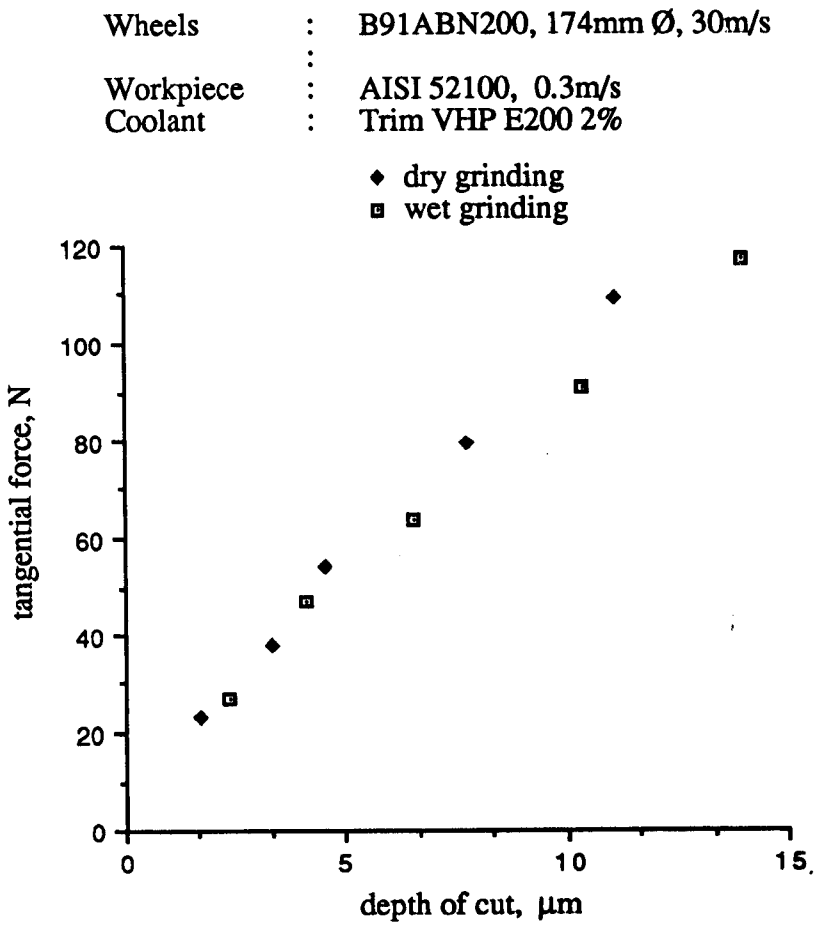

Figure 6.57 : A comparison of the tangential forces against depth of cut for the dry and wet grinding of AISI 52100 with the CBN wheel at 0.3m/s

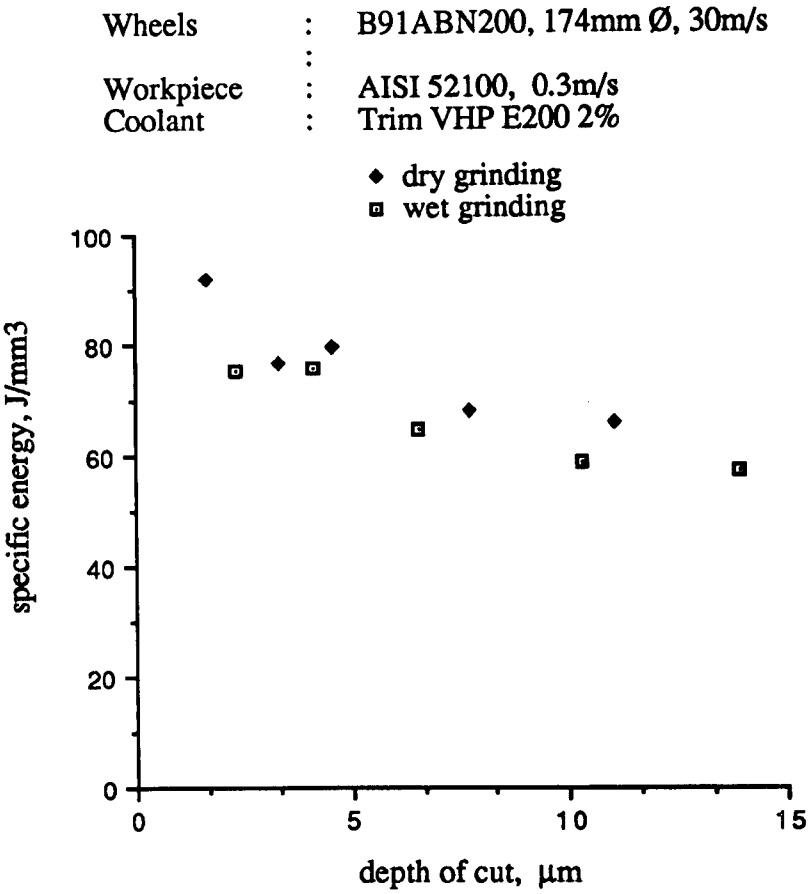

Figure 6.58 : A comparison of the specific energy against depth of cut for the dry and wet grinding of AISI 52100 with the CBN wheel at 0.3m/s

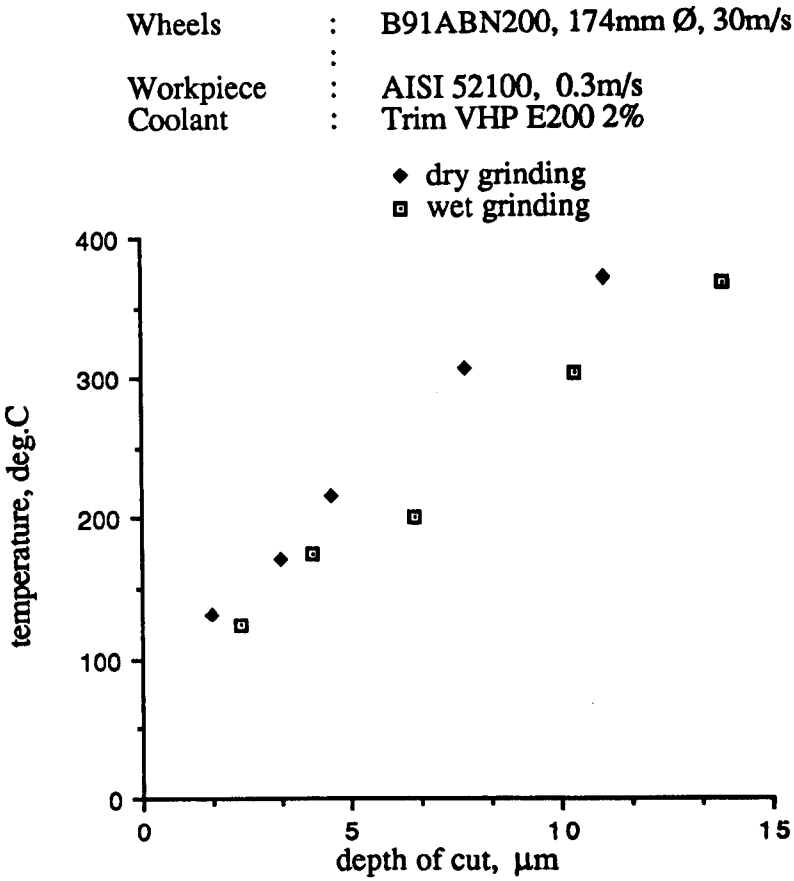

Figure 6.59 : A comparison of the temperature against depth of cut for the dry and wet grinding of AISI 52100 with the CBN wheel at 0.3m/s

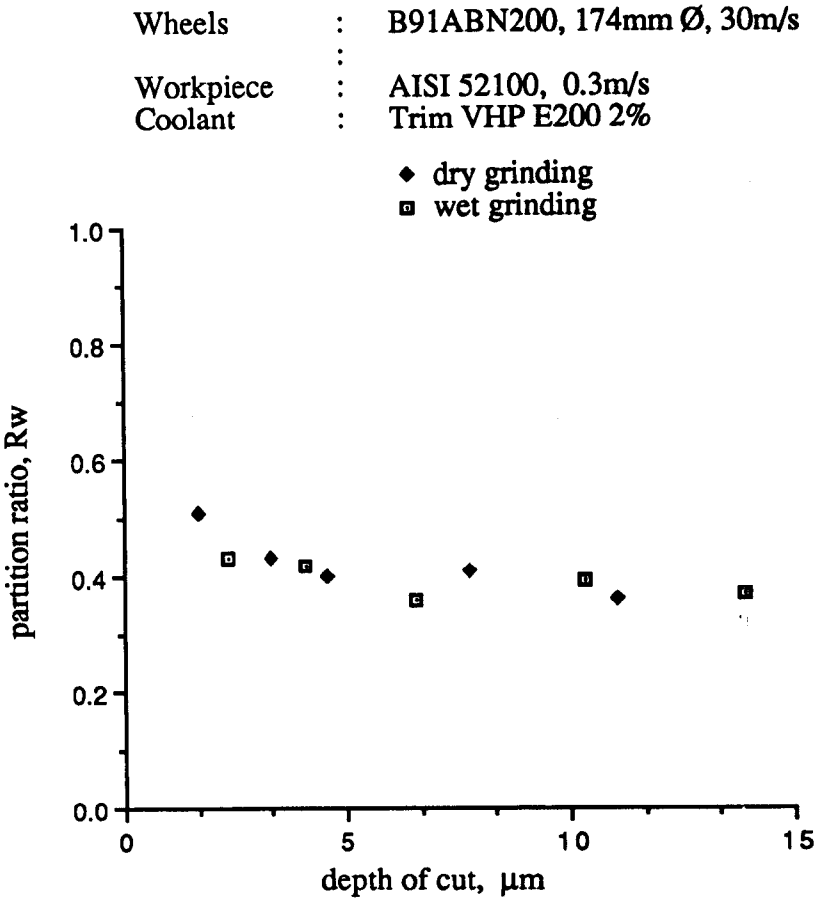

Figure 6.60 : A comparison of the partition ratio based on a triangular heat flux for the dry and wet grinding of AISI 52100 with the CBN wheel at 0.3m/s

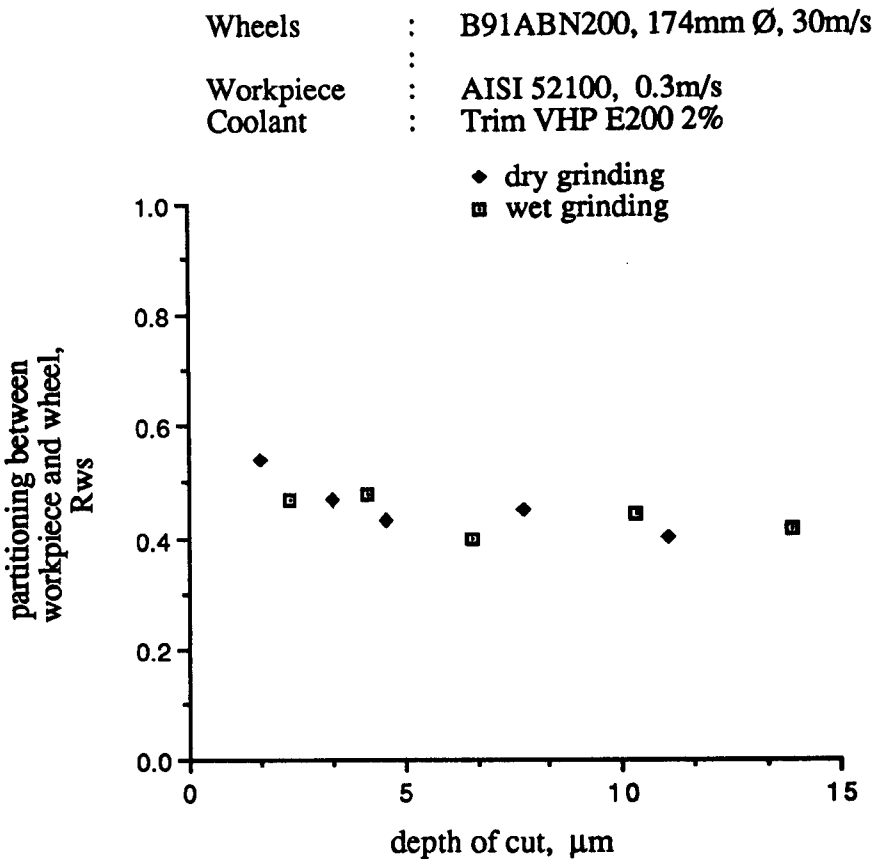

Figure 6.61: A comparison of the partitioning between the workpiece and wheel based on a triangular heat flux triangular heat flux for the dry and wet grinding of AISI 52100 with the CBN wheel at 0.3m/s

Experimental data :

Wheel	: ▫	B91ABN200, 174mm Ø, 30m/s
	:	
Workpiece	:	AISI 52100, 0.3m/s
Coolant	:	Trim VHP E200 2%

Model data :

Workpiece	Fluid	CBN
κ_w = 34.3W/mK	κ_g = 0.6W/mK	κ_g = 290 W/mK
ρ_w = 7815kg/m3	ρ_g = 1000kg/m3	ρ_g = 3480 kg/m3
c_w = 506 J/KgK	c_g = 4200J/KgK	c_g = 506 J/KgK
		Rr = 3.5 ro=15μm

ecc = 6J/mm3

—— no allowance for chips or fluid

..... allowance for chips only

- - - allowance for chips and fluid

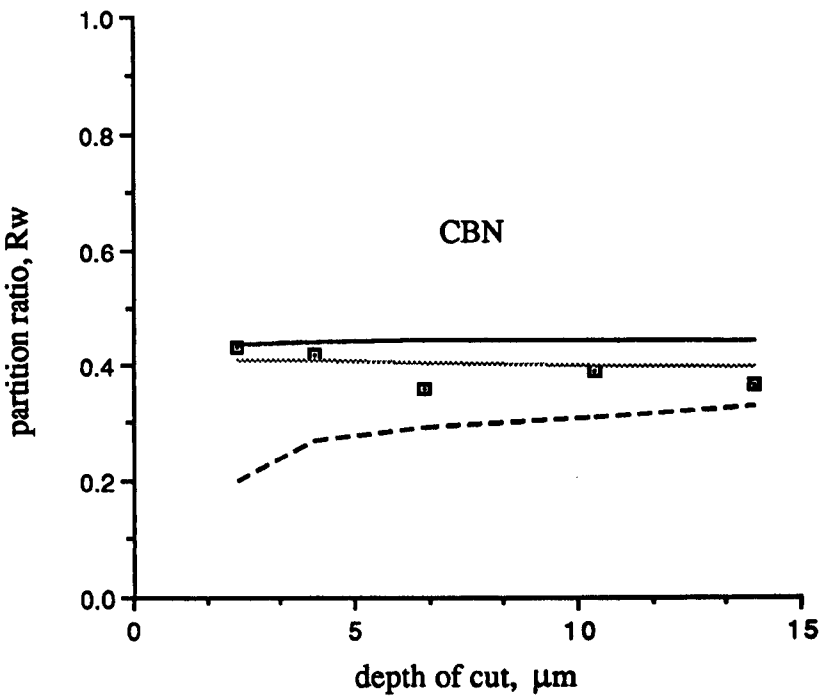

Figure 6.62 : A comparison of the theoretical and measured partition ratios based on a triangular heat flux for the wet grinding of AISI 52100 with the CBN wheel at 0.3m/s

Experimental data :

Wheel	: ▫	B91ABN200, 174mm Ø, 30m/s
	:	
Workpiece	:	AISI 52100, 0.3m/s
Coolant	:	Trim VHP E200 2%

Model data :

Workpiece	Fluid	CBN
κ_w = 34.3W/mK	κ_g = 0.6W/mK	κ_g = 290 W/mK
ρ_w = 7815kg/m3	ρ_g = 1000kg/m3	ρ_g = 3480 kg/m3
c_w = 506 J/KgK	c_g = 4200J/KgK	c_g = 506 J/KgK
		Rr = 3.5 ro=15μm

ecc = 6J/mm3

—— no allowance for chips or fluid

····· allowance for chips only

- - - allowance for chips and fluid

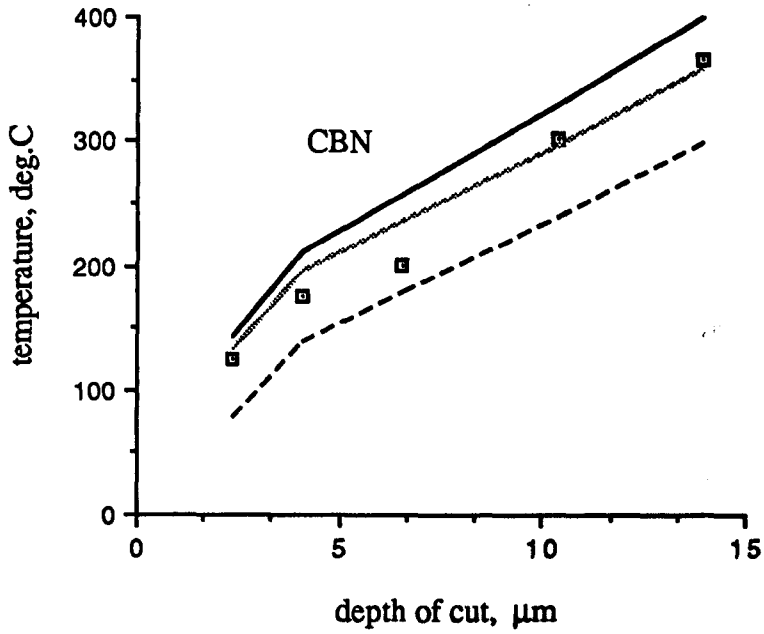

Figure 6.63 : A comparison of the theoretical and measured temperatures for the wet grinding of AISI 52100 with the CBN wheel at 0.3m/s

Experimental data :

Wheel	: ◆	B91ABN200, 174mm Ø, 30m/s
	:	
Workpiece	:	AISI 52100, 0.3m/s
Coolant	:	None

Model data :

Workpiece	Fluid	CBN
κ_w = 34.3W/mK	κ_g = 0.6W/mK	κ_g = 260W/mK
ρ_w = 7815kg/m3	ρ_g = 1000kg/m3	ρ_g = 3480 kg/m3
c_w = 506J/KgK	c_g = 4200J/KgK	c_g = 506 J/KgK
		Rr = 3.5 ro=15μm

ecc = 6J/mm3

—— no allowancefor chips

..... allowance for chips only

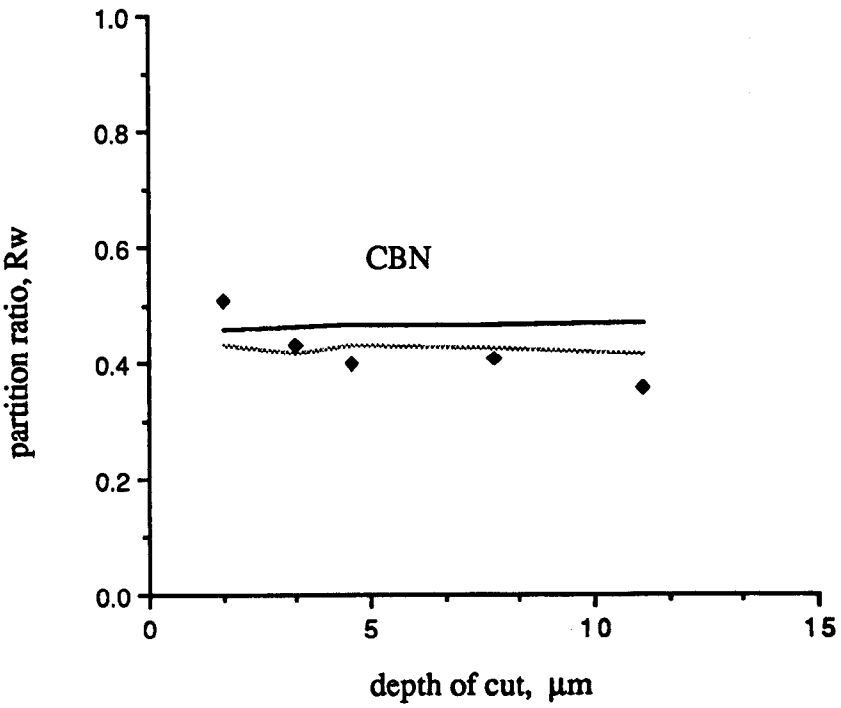

Figure 6.64 : A comparison of the theoretical and measured partition ratios based on a triangular heat flux for the dry grinding of AISI 52100 with the CBN wheel at 0.3m/s

Experimental data :

Wheel	: ◆	B91ABN200, 174mm Ø, 30m/s
	:	
Workpiece	:	AISI 52100, 0.3m/s
Coolant	:	None

Model data :

Workpiece	Fluid	CBN
$\kappa w = 34.3 W/mK$	$\kappa g = 0.6 W/mK$	$\kappa g = 260 W/mK$
$\rho w = 7815 kg/m3$	$\rho g = 1000 kg/m3$	$\rho g = 3480\ kg/m3$
$cw = 506 J/KgK$	$cg = 4200 J/KgK$	$cg = 506\ J/KgK$
		$Rr = 3.5 \quad ro = 15 \mu m$

ecc = 6J/mm3

—— no allowancefor chips

····· allowance for chips only

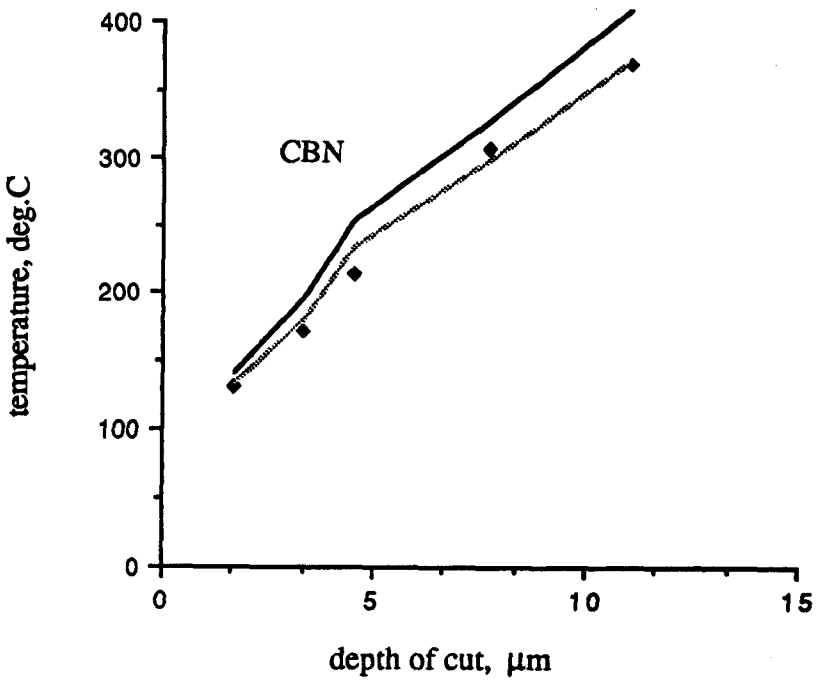

Figure 6.65 : A comparison of the theoretical and measured temperatures for the dry grinding of AISI 52100 with the CBN wheel at 0.3m/s

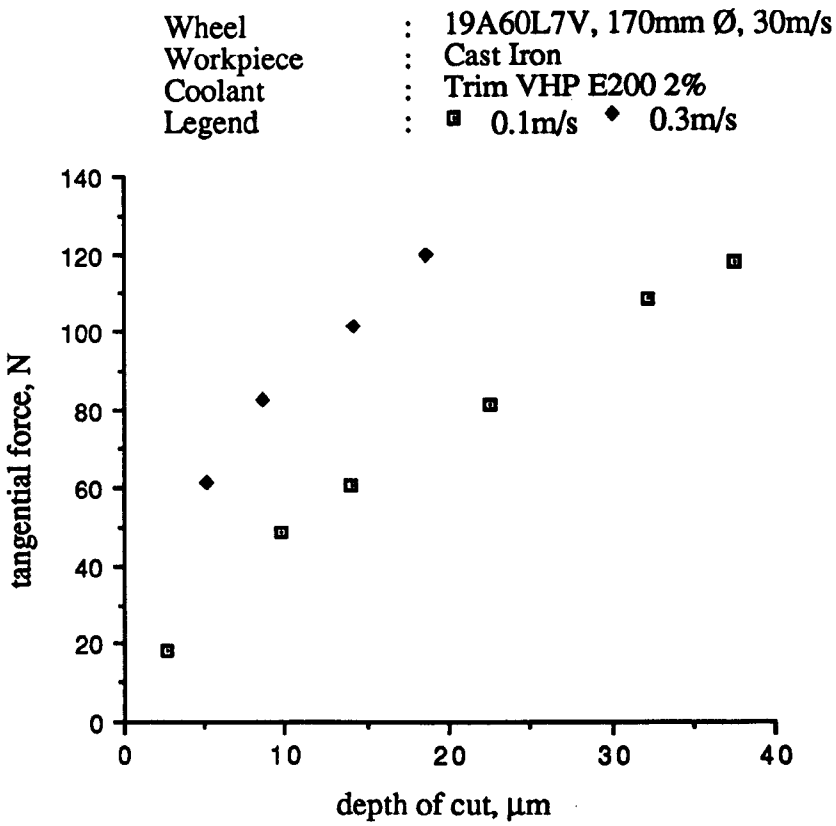

Figure 6.66 : A comparison of the tangential force against depth of cut for the wet grinding of cast iron with the 19A60L7V alumina wheel at 0.1 and 0.3 m/s

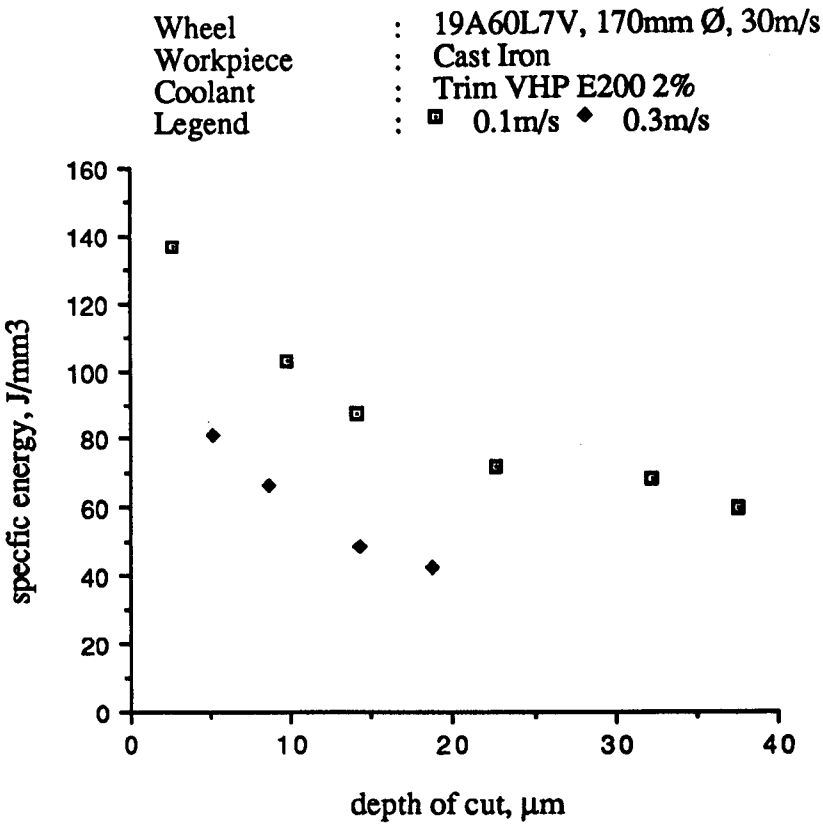

Figure 6.67 : Specific energy against depth of cut for the wet grinding of cast iron with the 19A60L7V alumina wheel at 0.1 and 0.3 m/s

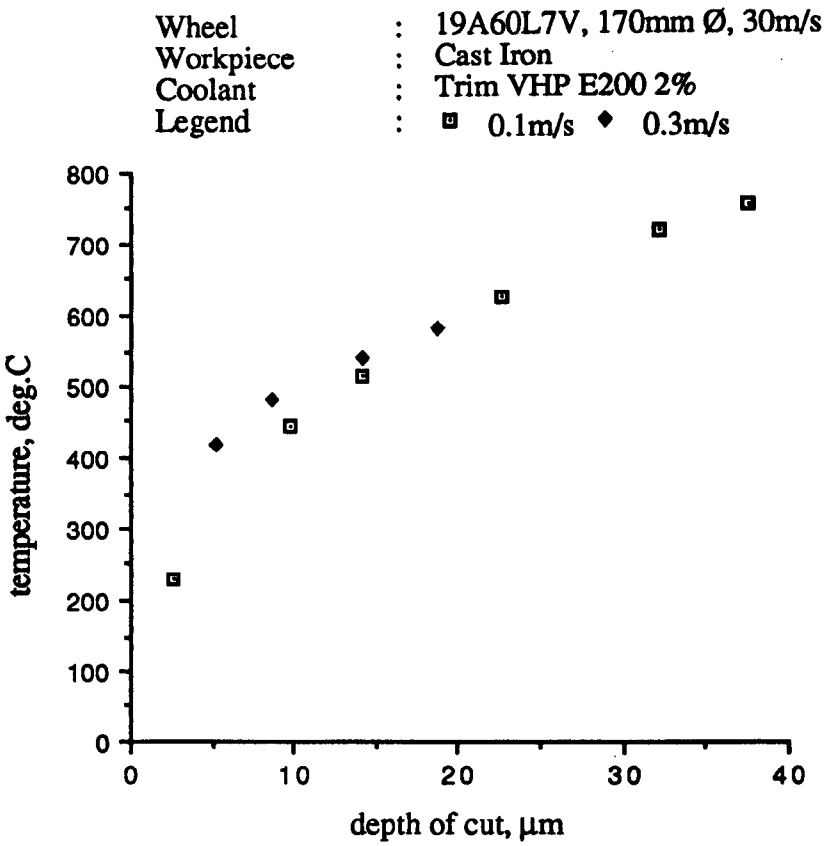

Figure 6.68 : A comparison of temperature against depth of cut for the wet grinding of cast iron with the 19A60L7V alumina wheel at 0.1 and 0.3 m/s

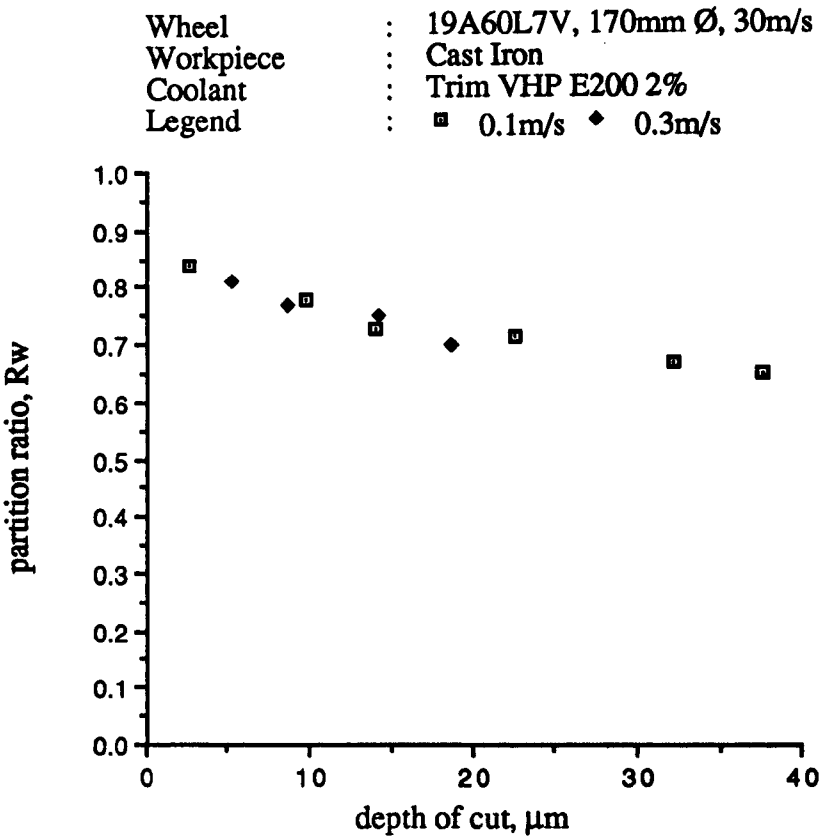

Figure 6.69 : A comparison of the partition ratio based on a triangular heat flux for the wet grinding of cast iron with the 19A60L7V alumina wheel at 0.1m/s and 0.3m/s

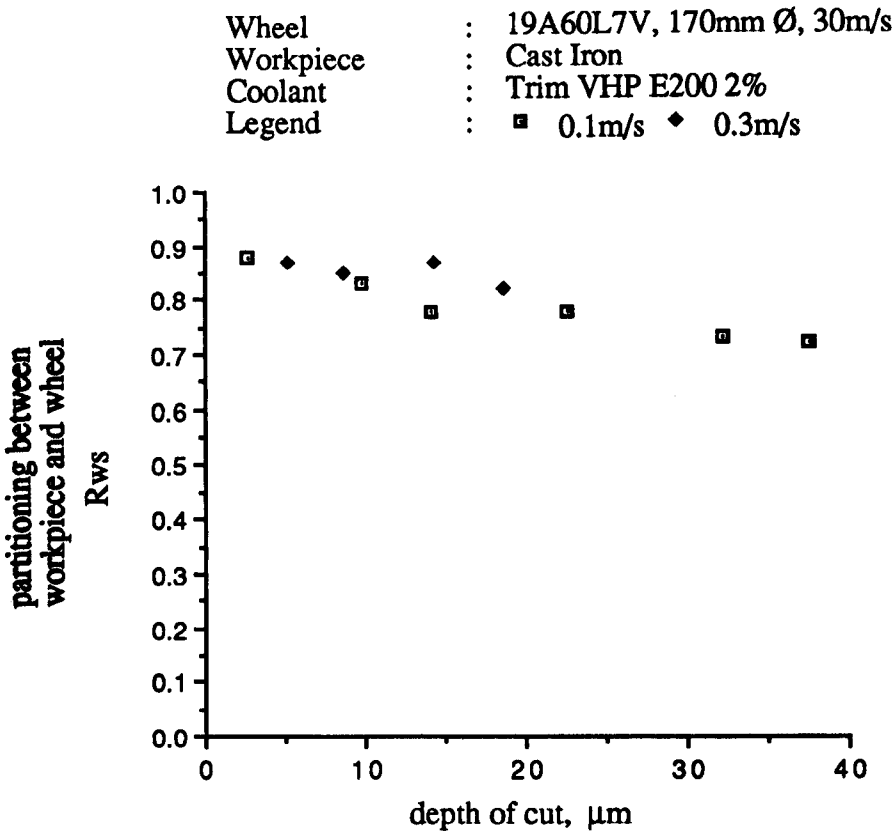

Figure 6.70 : A comparison of the partitioning between the workpiece and grinding wheel based on a triangular heat flux for the wet grinding of cast iron with the 19A60L7V alumina wheel at 0.1m/s and 0.3m/s

Experimental data :

Wheel	:	19A60L7V, 170mm Ø, 30m/s
Workpiece	:	Cast Iron
Coolant	:	Trim VHP E200 2%
Legend	:	▫ 0.1m/s

Model data :

Workpiece	Alumina
κ_w = 53.7 W/mK	κ_g = 45 W/mK
ρ_w = 7300 kg/m3	ρ_g = 3910 kg/m3
c_w = 511 J/KgK	c_g = 765 J/KgK
	Rr = 4 ro=25μm

ecc = 6J/mm3

—— steady state solution

transient solution

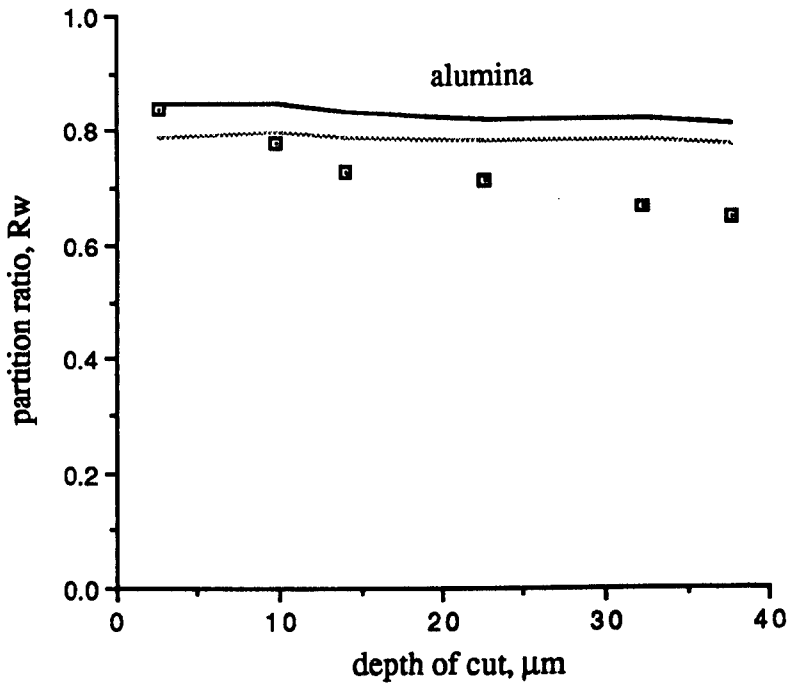

Figure 6.71: A comparison of the theoretical and measured partition ratios based on a triangular heat flux for the wet grinding of cast iron with the 19A60L7V alumina wheel at 0.1m/s

Experimental data :

Wheel	:	19A60L7V, 170mm Ø, 30m/s
Workpiece	:	Cast Iron
Coolant	:	Trim VHP E200 2%
Legend	:	▫ 0.1m/s

Model data :

Workpiece	Alumina
$\kappa w = 53.7$ W/mK	$\kappa g = 45$ W/mK
$\rho w = 7300$ kg/m3	$\rho g = 3910$ kg/m3
$cw = 511$ J/KgK	$cg = 765$ J/KgK
	Rr = 4 ro=25μm

ecc = 6J/mm3

—— steady state solution

····· transient solution

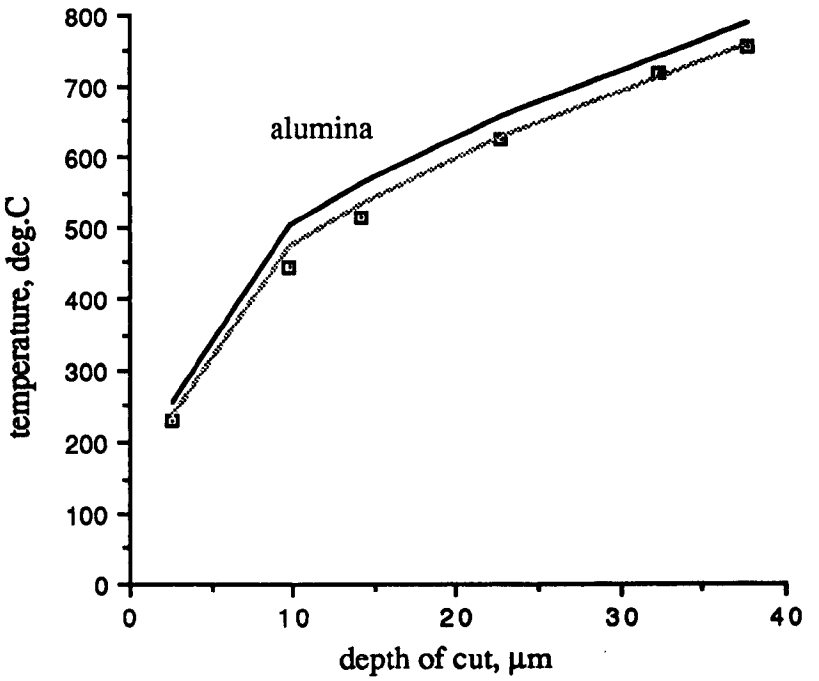

Figure 6.72 : A comparison of the theoretical and measured temperatures for the wet grinding of cast iron with the 19A60L7V alumina wheel at 0.1m/s

Experimental data :

Wheel	:	19A60L7V, 170mm Ø, 30m/s
Workpiece	:	Cast Iron
Coolant	:	Trim VHP E200 2%
Legend	:	◆ 0.3m/s

Model data :

Workpiece	Alumina
$\kappa w = 53.7$ W/mK	$\kappa g = 41$ W/mK
$\rho w = 7300$ kg/m3	$\rho g = 3910$ kg/m3
$cw = 511$ J/KgK	$cg = 765$ J/KgK
	Rr = 3 ro=25μm

ecc = 6J/mm3

—— steady state solution

..... transient solution

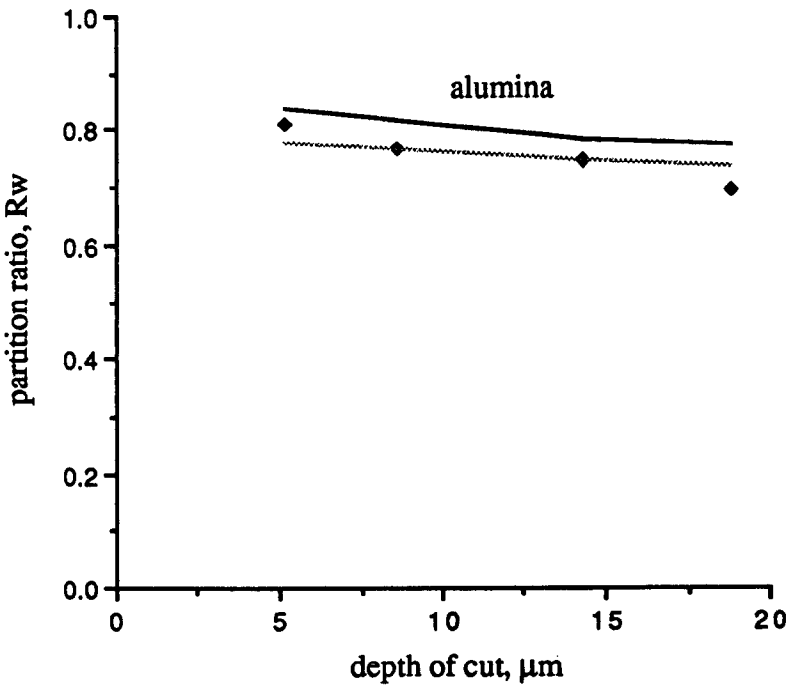

Figure 6.73 : A comparison of the theoretical and measured partition ratios based on a triangular heat flux for the wet grinding of cast iron with the 19A60L7V alumina wheel at 0.3m/s

Experimental data :

Wheel	:	19A60L7V, 170mm Ø, 30m/s
Workpiece	:	Cast Iron
Coolant	:	Trim VHP E200 2%
Legend	:	◆ 0.3m/s

Model data :

Workpiece	Alumina
$\kappa w = 53.7$ W/mK	$\kappa g = 41$ W/mK
$\rho w = 7300$ kg/m3	$\rho g = 3910$ kg/m3
$cw = 511$ J/KgK	$cg = 765$ J/KgK
	Rr = 3 ro=25μm

ecc = 6J/mm3

—— steady state solution

····· transient solution

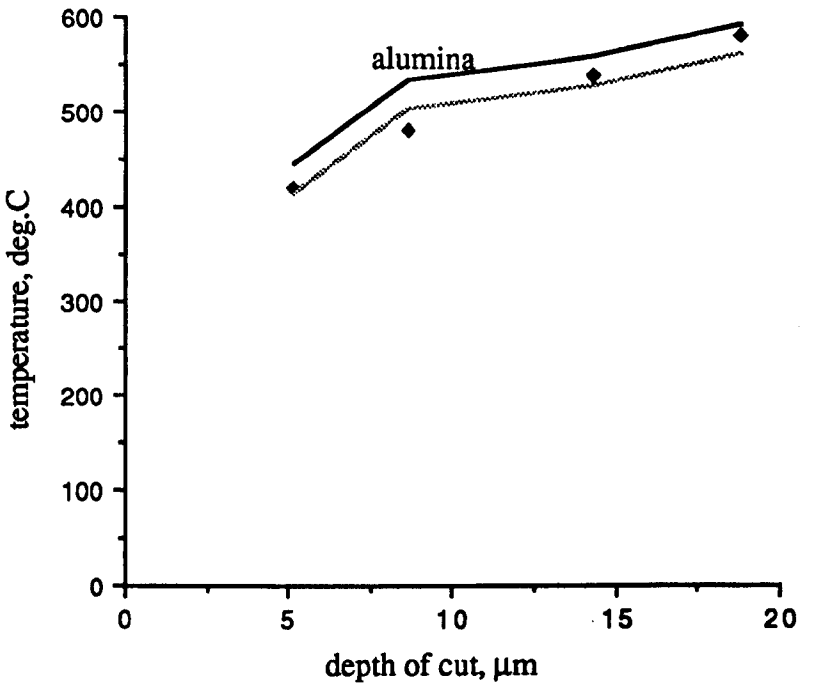

Figure 6.74 : A comparison of the theoretical and measured temperatures for the wet grinding of cast iron with the 19A60L7V alumina wheel at 0.3m/s

Experimental data :

Wheel	:	19A60L7V, 170mm Ø, 30m/s
Workpiece	:	Cast Iron
Coolant	:	Trim VHP E200 2%
Legend	:	▫ 0.1m/s

Model data :

Workpiece	Alumina
κw = 53.7 W/mK	Actual effective (κρc)s^1/2 = 230 J/(s^1/2 m^2K)
ρw = 7300 kg/m3	Average effective (κρc)s^1/2 = 196 J/(s^1/2 m^2K)
cw = 511 J/KgK	Steady state (κρc)s^1/2 = 514 J/(s^1/2 m^2K)

ecc = 6J/mm3

——— actual wheel thermal properties

..... average wheel thermal properties

– – – steady state measured wheel thermal properties

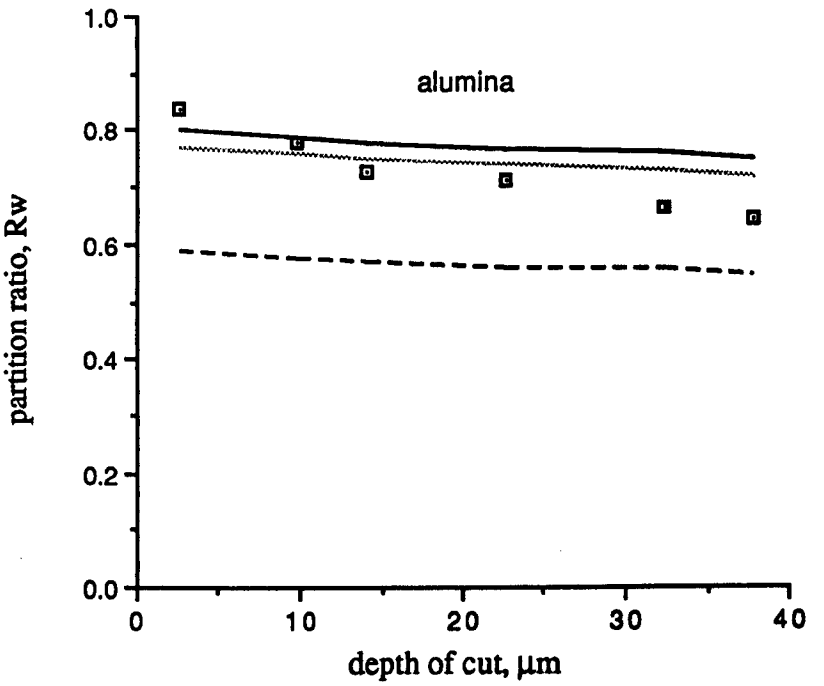

Figure 6.75 : A comparison of the measured and theoretical partition ratios based on the wheel contact analysis for the wet grinding of cast iron with the 19A60L7V alumina wheel at 0.1m/s

Experimental data :

Wheel	:	19A60L7V, 170mm Ø, 30m/s
Workpiece	:	Cast Iron
Coolant	:	Trim VHP E200 2%
Legend	:	◆ 0.3m/s

Model data :

Workpiece	Actual effective (κρc)s^1/2 = 230 J/(s^1/2 m^2K)
ρw = 7300 kg/m3	Average effective (κρc)s^1/2 = 196 J/(s^1/2 m^2K)
cw = 511 J/KgK	Steady state (κρc)s^1/2 = 514 J/(s^1/2 m^2K)

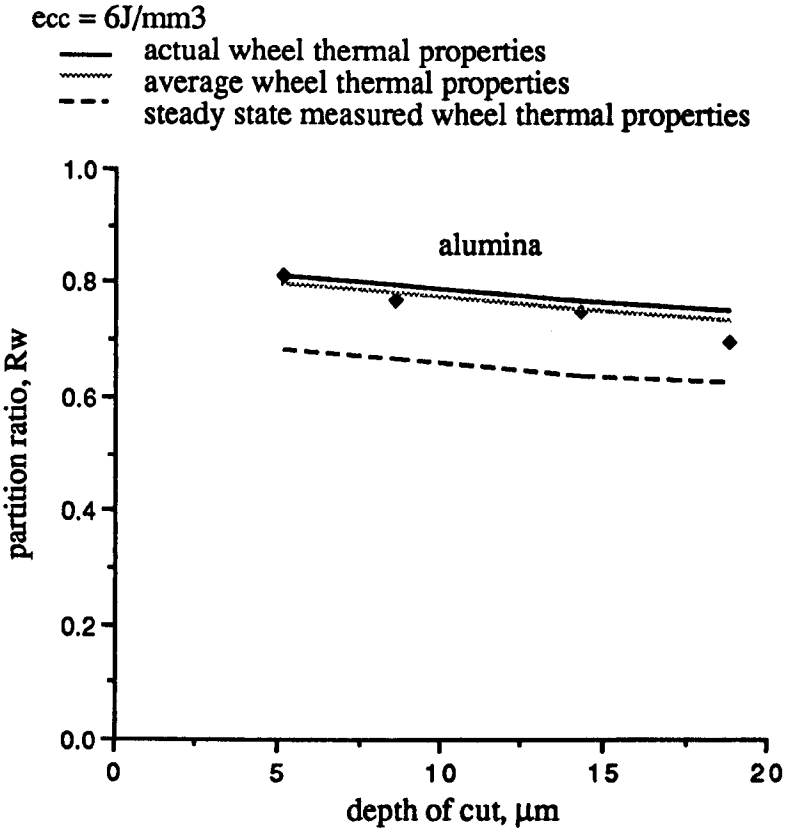

Figure 6.76 : A comparison of the measured and theoretical partition ratios based on the wheel contact analysis for the wet grinding of cast iron with the 19A60L7V alumina wheel at 0.3m/s

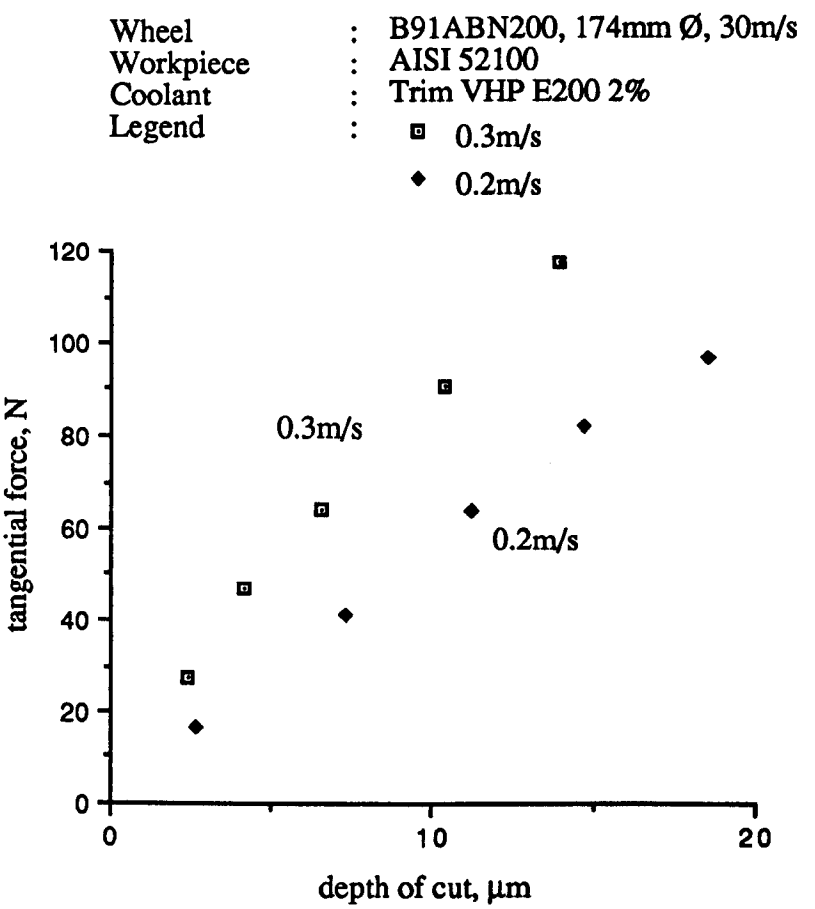

Figure 6.77 : A comparison of the tangential force against depth of cut for the wet grinding of AISI 52100 with the CBN wheel at 0.2m/s and 0.3m/s

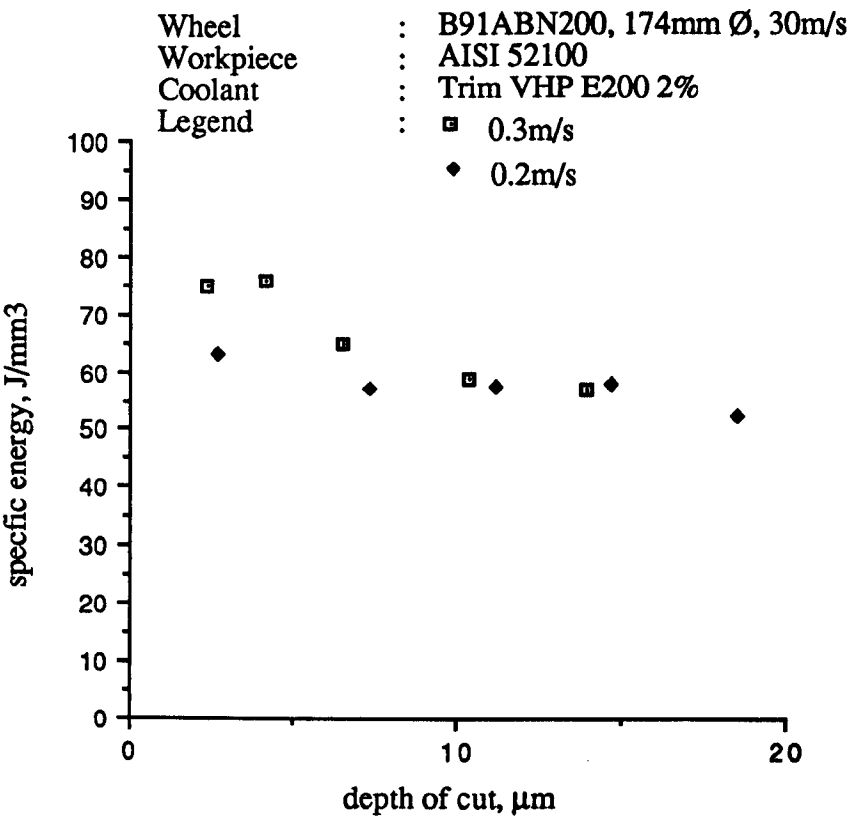

Figure 6.78 : A comparison of the specific energy against depth of cut for the wet grinding of AISI 52100 with the CBN wheel at 0.2m/s and 0.3m/s

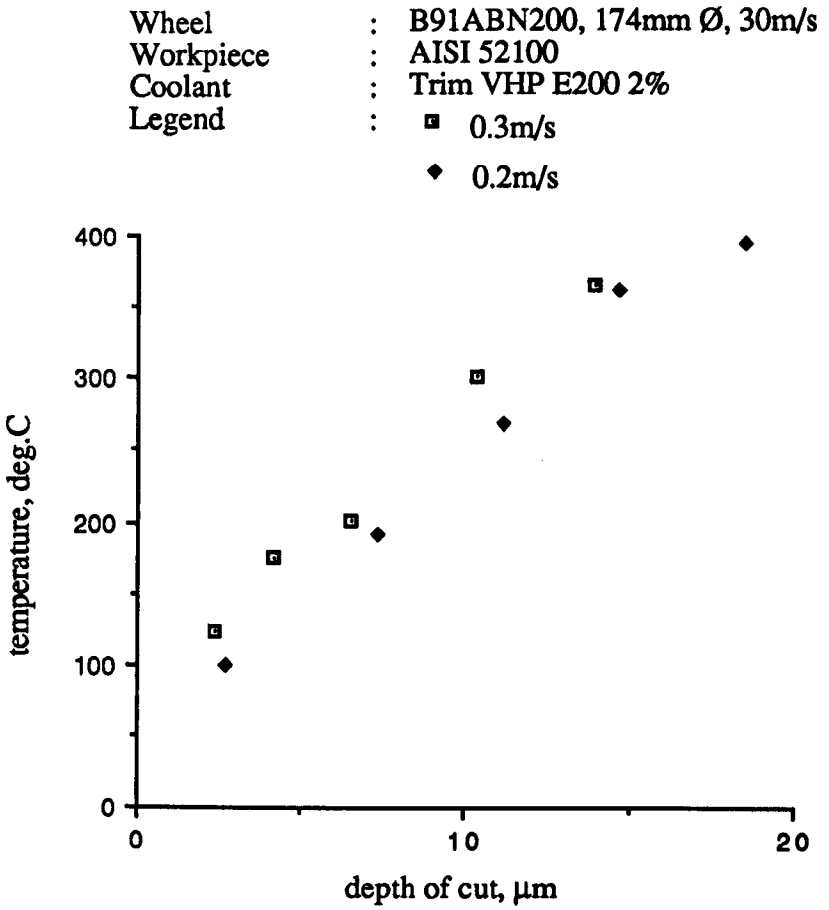

Figure 6.79 : A comparison of the temperatures against depth of cut for the wet grinding of AISI 52100 with the CBN wheel at 0.2m/s and 0.3m/s

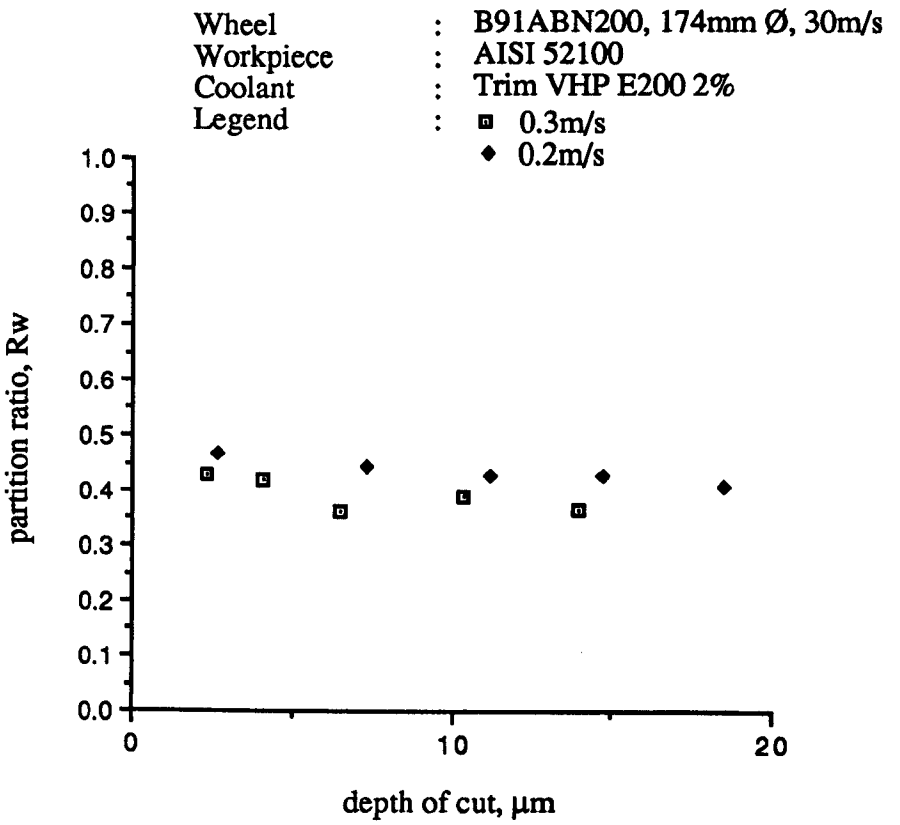

Figure 6.80 : A comparison of the partition ratio based on a triangular heat flux for the wet grinding of AISI 52100 with the CBN wheel at 0.2m/s and 0.3m/s

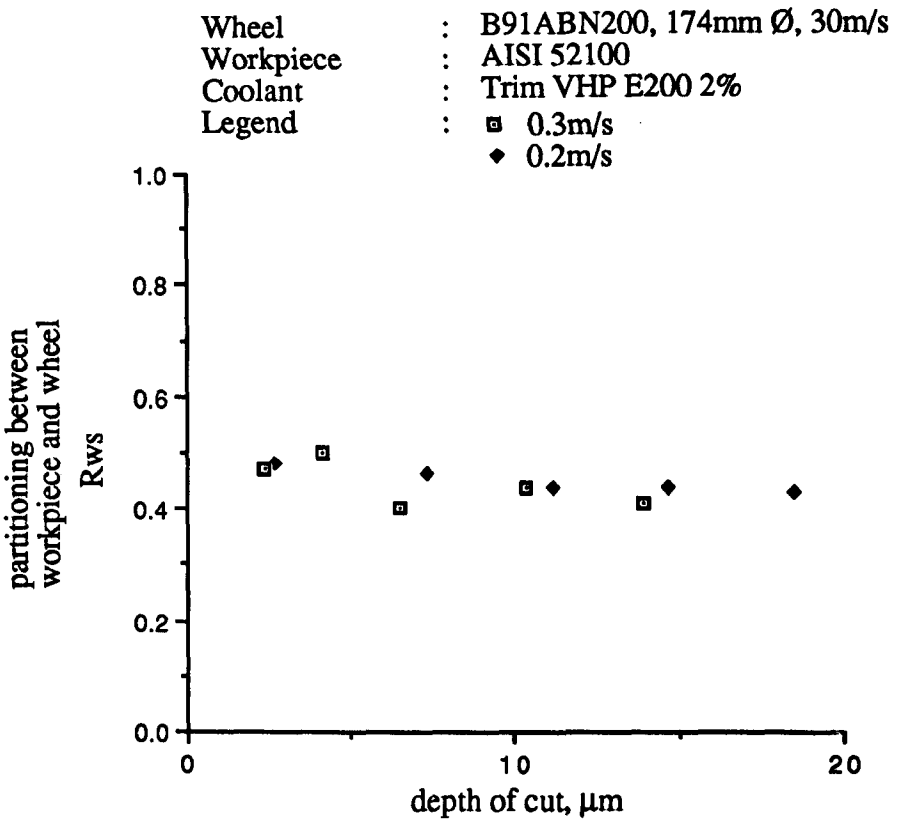

Figure 6.81 : A comparison of the partitioning between the workpiece and wheel based on a triangular heat flux for the wet grinding of AISI 52100 with the CBN wheel at 0.2m/s and 0.3m/s

Experimental data :

Wheel : ◆ B91ABN200, 174mm Ø, 30m/s
Workpiece : AISI 52100, 0.2m/s
Coolant : Trim VHP E200 2%

Model data :

Workpiece

κ_w = 34.3 W/mK
ρ_w = 7815 kg/m3
c_w = 506 J/KgK

Grain contact analysis

κ_g = 274 W/mK
ρ_g = 3480 kg/m3
c_g = 506 J/KgK
Rr = 3.5 ro = 15μm

Wheel contact analysis

Actual $(\kappa\rho c)s^{1/2}$ = 1140 J/(s^1/2 m^2K)
Average $(\kappa\rho c)s^{1/2}$ = 1360 J/(s^1/2 m^2K)

ecc = 6J/mm3

..... grain contact analysis
—— wheel contact analysis - actual wheel thermal properties
- - - wheel contact analysis - average wheel thermal properties

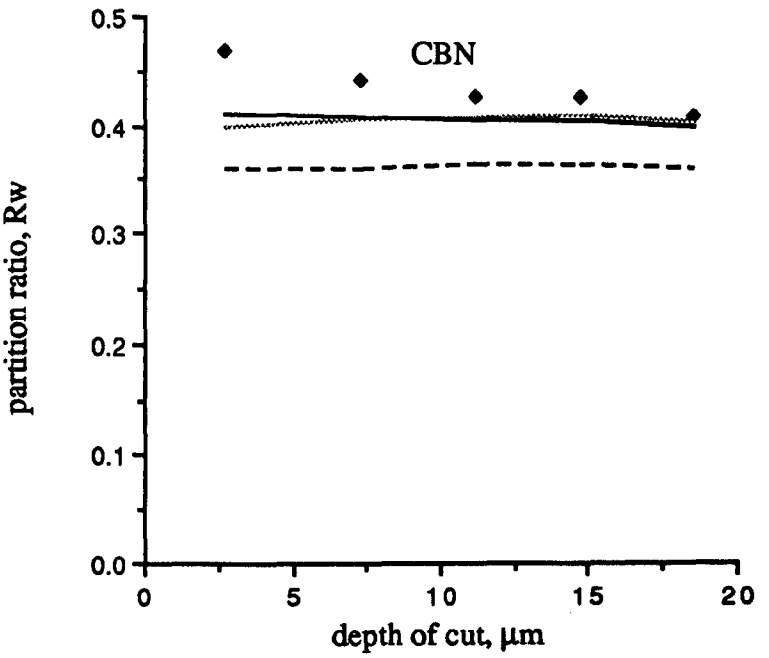

Figure 6.82 : A comparison of the measured and theoretical partition ratios based on the grain contact analysis and the wheel contact analysis for the wet grinding of AISI 52100 with the CBN wheel at 0.2m/s

Experimental data :

Wheel : ◆ B91ABN200, 174mm Ø, 30m/s
Workpiece : AISI 52100, 0.2m/s
Coolant : Trim VHP E200 2%

Model data :

Workpiece

$\kappa w = 34.3$ W/mK
$\rho w = 7815$ kg/m3
$cw = 506$ J/KgK

Grain contact analysis

$\kappa g = 274$ W/mK
$\rho g = 3480$ kg/m3
$cg = 506$ J/KgK
$Rr = 3.5$ $ro = 15\mu m$

Wheel contact analysis

Actual $(\kappa\rho c)s^{1/2} = 1140$ J/(s^1/2 m^2K)
Average $(\kappa\rho c)s^{1/2} = 1360$ J/(s^1/2 m^2K)

ecc = 6J/mm3

..... grain contact analysis
——— wheel contact analysis - actual wheel thermal properties
– – – wheel contact analysis - average wheel thermal properties

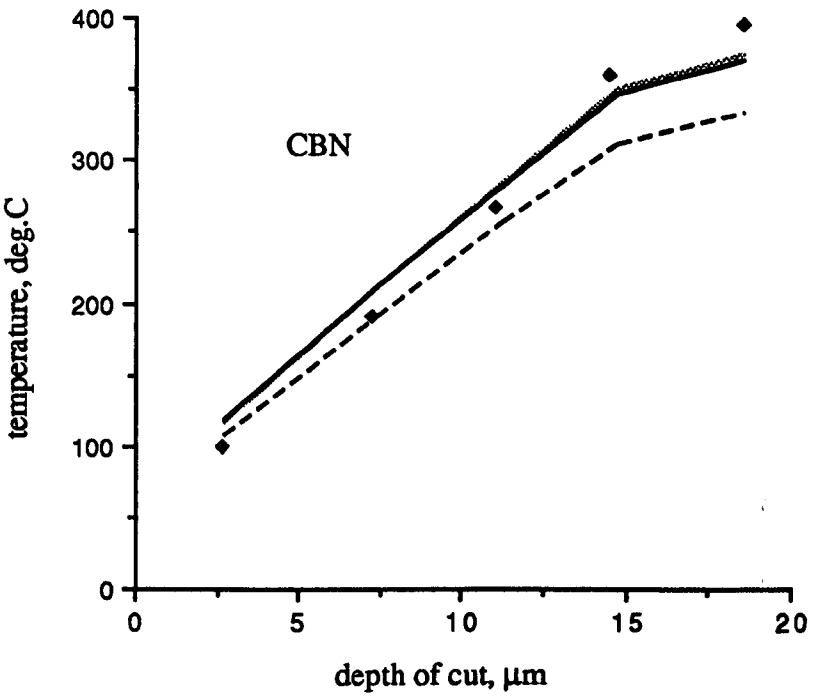

Figure 6.83 : A comparison of the measured and theoretical temperatures based on the grain contact analysis and the wheel contact analysis for the wet grinding of AISI 52100 with the CBN wheel at 0.2m/s

Experimental data :

Wheel : ▫ B91ABN200, 174mm Ø, 30m/s
Workpiece : AISI 52100, 0.3m/s
Coolant : Trim VHP E200 2%

Model data :

Workpiece

κ_w = 34.3 W/mK
ρ_w = 7815 kg/m3
c_w = 506 J/KgK

Grain contact analysis

κ_g = 290 W/mK
ρ_g = 3480 kg/m3
c_g = 506 J/KgK
Rr = 4 ro = 15μm

Wheel contact analysis

Actual $(\kappa\rho c)s^{1/2}$ = 1581 J/(s^1/2 m^2K)
Average $(\kappa\rho c)s^{1/2}$ = 1360 J/(s^1/2 m^2K)

ecc = 6J/mm3

..... grain contact analysis
—— wheel contact analysis - actual wheel thermal properties
- - - wheel contact analysis - average wheel thermal properties

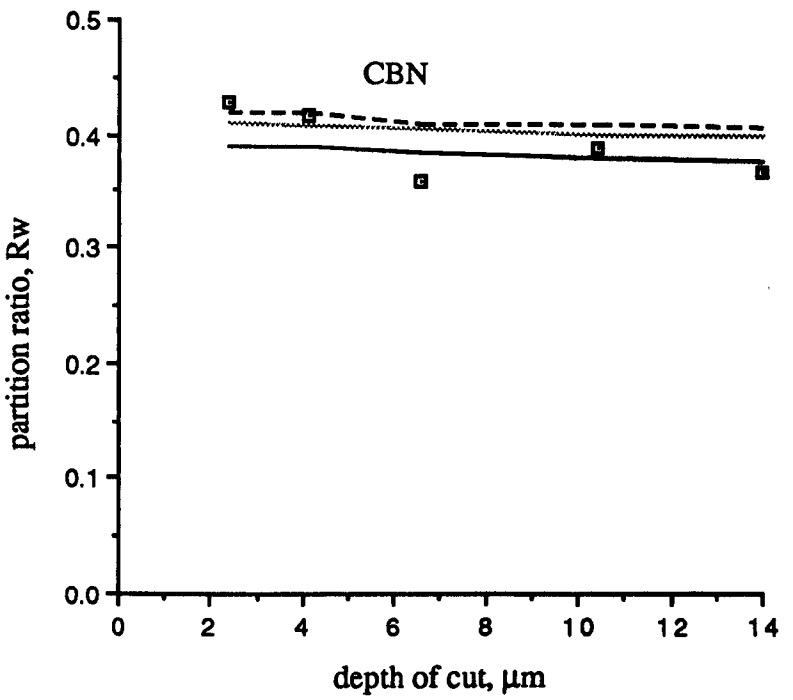

Figure 6.84 : A comparison of the measured and theoretical partitions based on the grain contact analysis and the wheel contact analysis for the wet grinding of AISI 52100 with the CBN wheel at 0.3m/s

Experimental data :

Wheel : ▪ B91ABN200, 174mm Ø, 30m/s
Workpiece : AISI 52100, 0.3m/s
Coolant : Trim VHP E200 2%

Model data :

Workpiece

κ_w = 34.3 W/mK
ρ_w = 7815 kg/m3
c_w = 506 J/KgK

Grain contact analysis

κ_g = 290 W/mK
ρ_g = 3480 kg/m3
c_g = 506 J/KgK
Rr = 4 ro = 15μm

Wheel contact analysis

Actual $(\kappa\rho c)s^{1/2}$ = 1581 J/(s^1/2 m^2K)
Average $(\kappa\rho c)s^{1/2}$ = 1360 J/(s^1/2 m^2K)

ecc = 6J/mm3

..... grain contact analysis
——— wheel contact analysis - actual wheel thermal properties
– – – wheel contact analysis - average wheel thermal properties

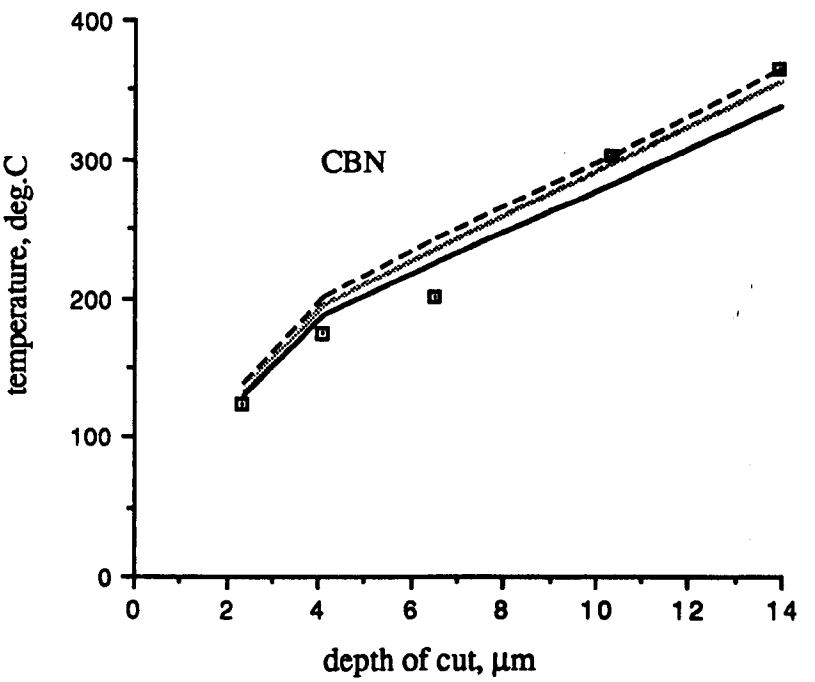

Figure 6.85 : A comparison of the measured and theoretical temperatures based on the grain contact analysis and the wheel contact analysis for the wet grinding of AISI 52100 with the CBN wheel at 0.3m/s

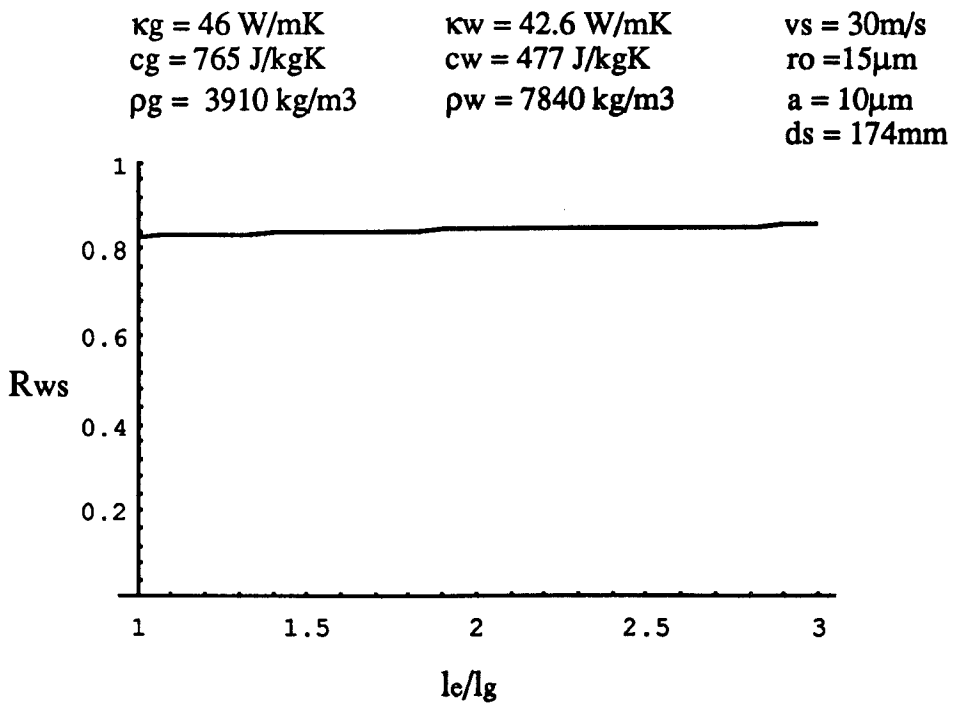

Figure 6.86 : Theoretical energy partioning between the workpiece and wheel against the contact length ratio for an alumina wheel

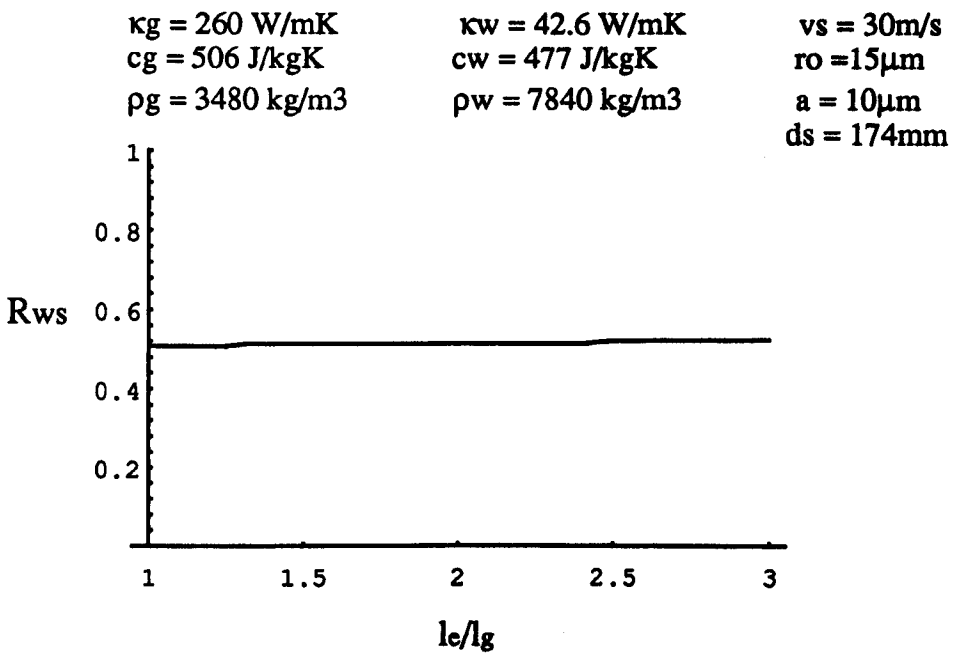

Figure 6.87 : Theoretical energy partioning between the workpiece and wheel against the contact length ratio for a CBN wheel

Experimental data :

Wheel	:	◆ 19A60L7V, 170mm Ø, 30m/s
	:	
Workpiece	:	AISI 1055, 0.1m/s
Coolant	:	None

Model data :

Workpiece	Alumina
κ_w = 42.6 W/mK	κ_g = 54 W/mK
ρ_w = 7840 kg/m3	ρ_g = 3910 kg/m3
c_w = 477 J/KgK	c_g = 765 J/KgK
	Rr = 6 ro=25μm

ecc = 6J/mm3

—— geometric contact length

····· real contact length

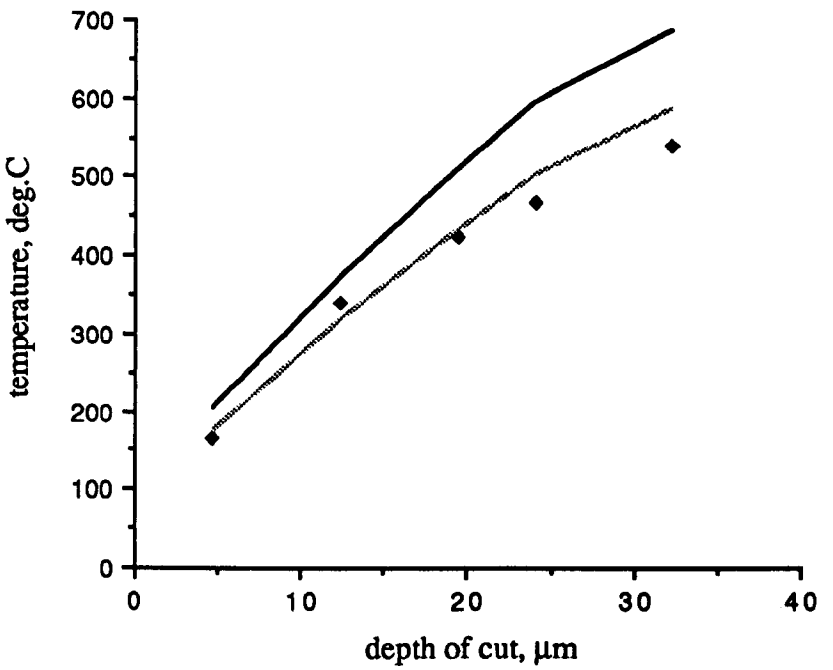

Figure 6.88 : A comparison of the theoretical prediction based on the geometric contact length and the real contact length

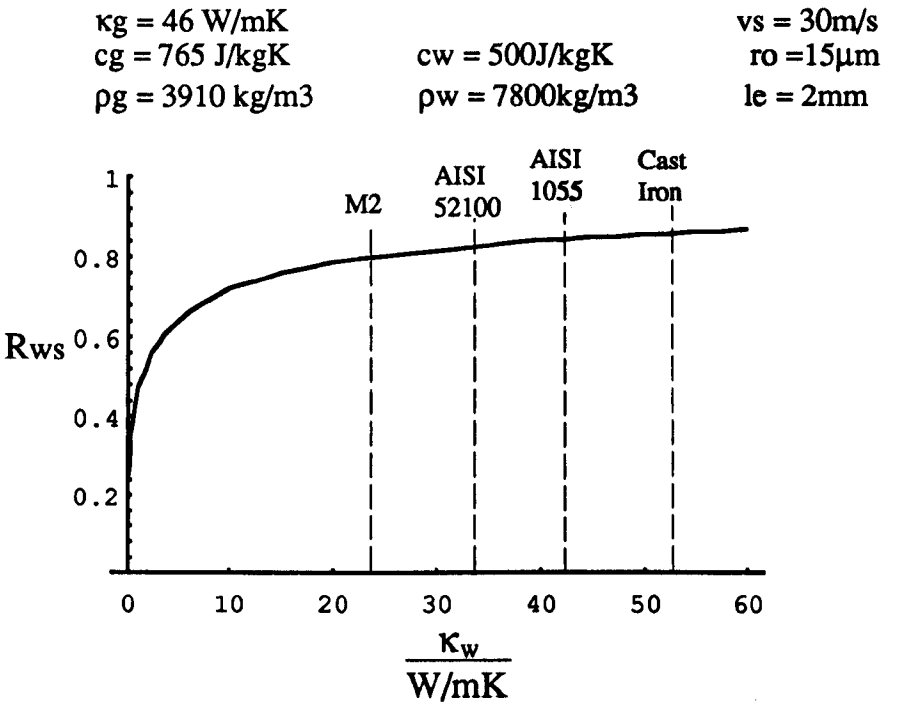

Figure 6.89 : Energy partitioning between workpiece and wheel against workpiece thermal conductivity for alumina grinding

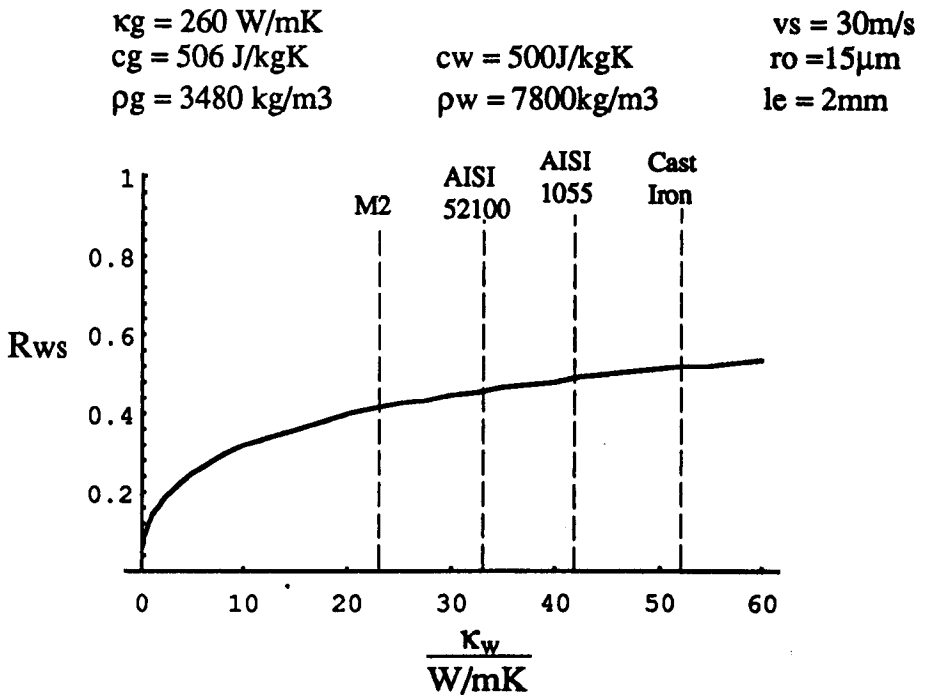

Figure 6.90 : Energy partitioning between workpiece and wheel against workpiece thermal conductivity for CBN grinding

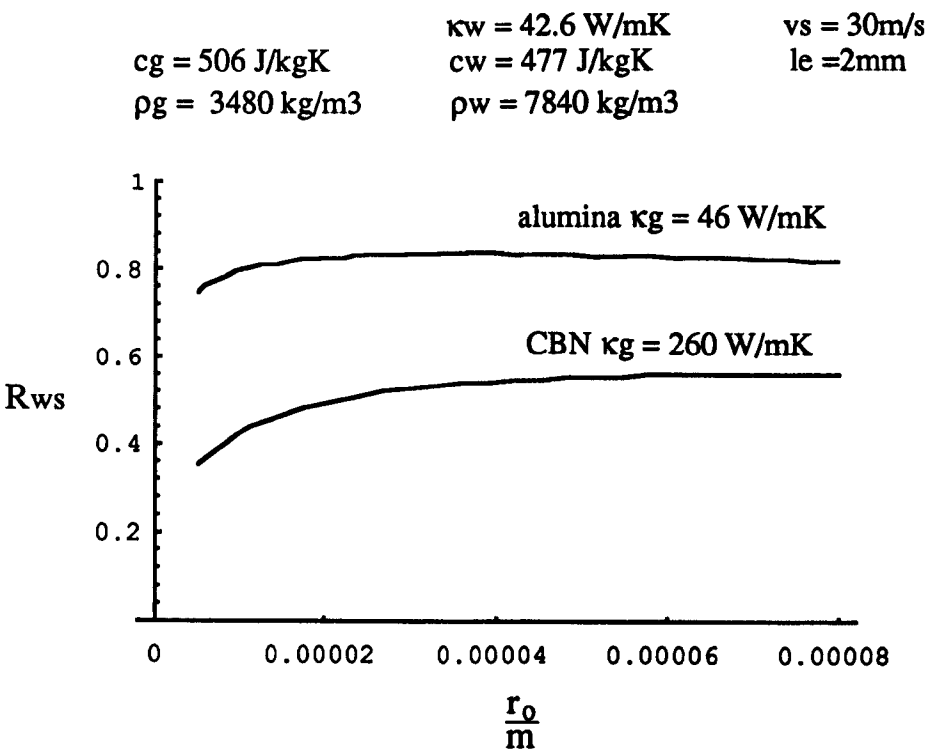

Figure 6.91 : Energy partitioning between the workpiece and wheel against wear flat radius

Experimental data :

Wheel	: ▫	A200, 174mm Ø, 30m/s
	:	
Workpiece	:	M2 tool steel, 0.25m/s
Coolant	:	Trim VHP E200 2%

Model data :

Workpiece	Actual values	Average values
κ_w = 23.5 W/mK	κ_g = 51W/mK	κ_g = 46W/mK
ρ_w = 7860kg/m3	ρ_g = 3910 kg/m3	ρ_g = 3910kg/m3
c_w = 515 J/KgK	c_g = 765 J/KgK	c_g = 765 J/KgK
	Rr = 3.5	Rr = 4

ro=15μm
ecc = 6J/mm3

—— average values of κ_g and Rr

····· actual values of κ_g and Rr

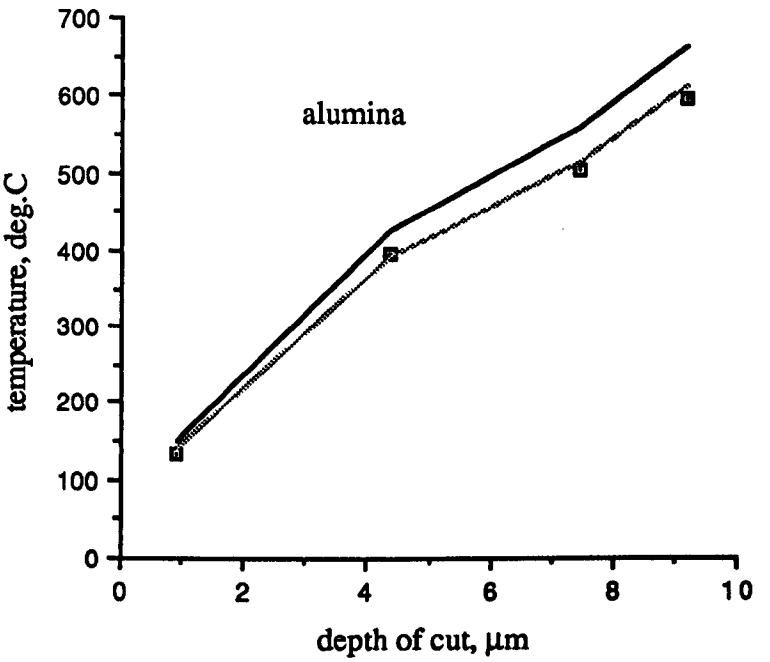

Figure 6.92 : The theoretical prediction using the average value of grain thermal conductivity and roughness factor for alumina

Experimental data :

Wheel : ◆ A200, 174mm Ø, 30m/s
:
Workpiece : M2 tool steel, 0.25m/s
Coolant : None

Model data :

Workpiece	Actual values	Average values
κ_w = 23.5 W/mK	κ_g = 240 W/mK	κ_g = 260 W/mK
ρ_w = 7860kg/m3	ρ_g = 3480kg/m3	ρ_g = 3480kg/m3
c_w = 515 J/KgK	c_g = 506 J/KgK	c_g = 506 J/KgK
	Rr = 3.5	Rr = 4

ro=15μm
ecc = 6J/mm3

—— average values of κ_g and Rr
····· actual values of κ_g and Rr

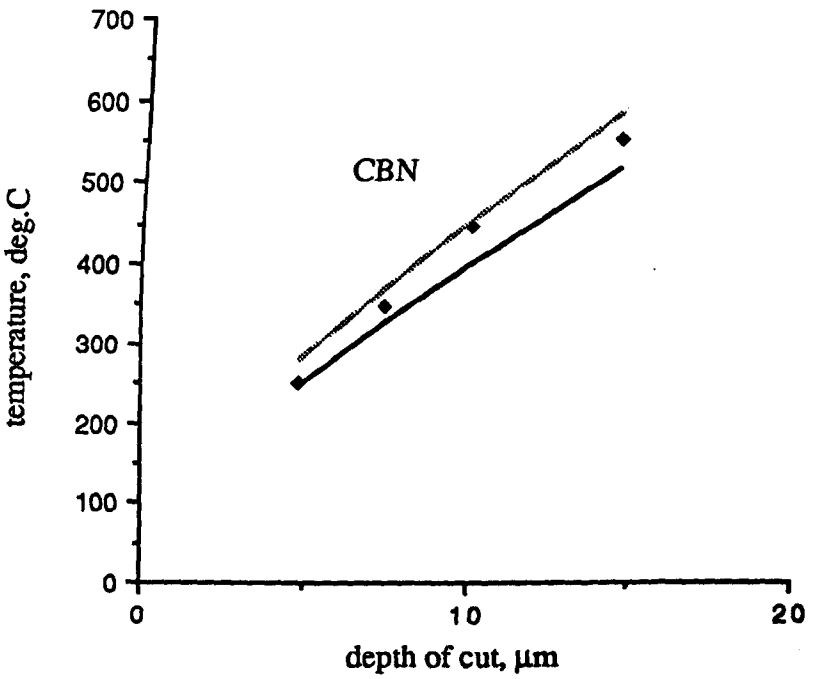

Figure 6.93 : The theoretical prediction using the average value of grain thermal conductivity and roughness factor for CBN

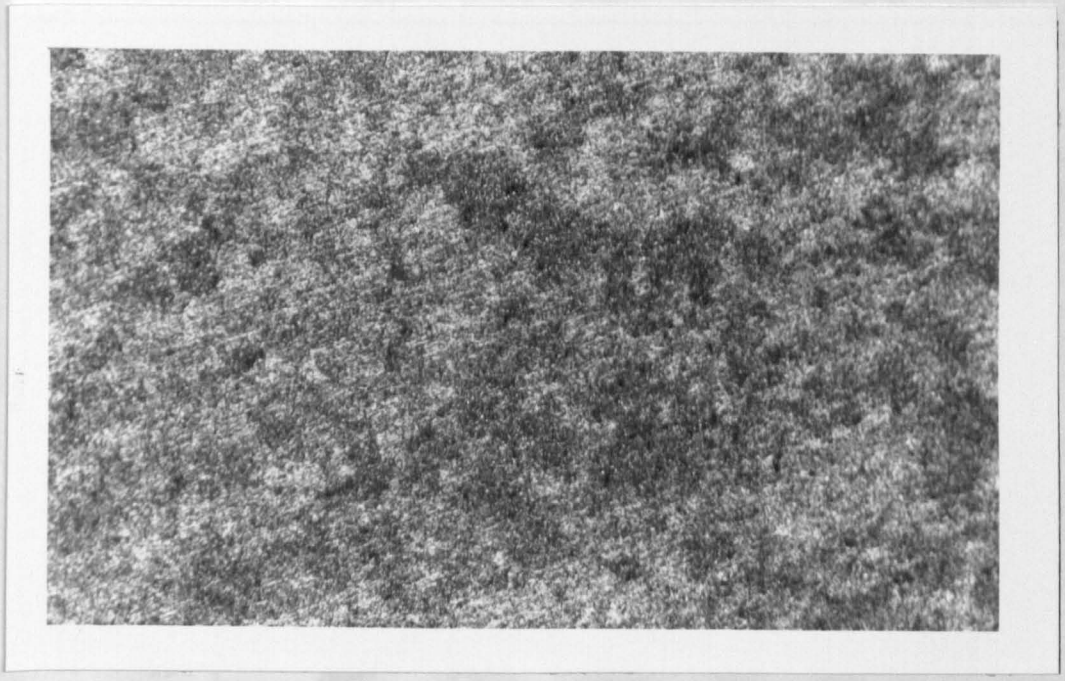

Figure 7.1 : Microstructure of AISI 51200

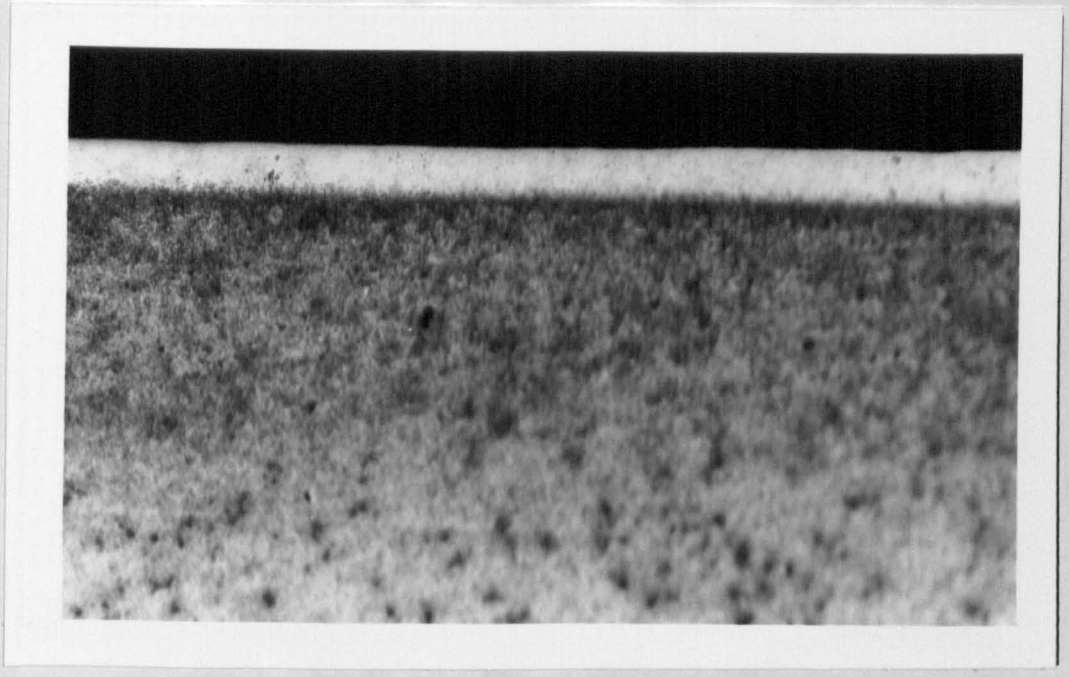

Figure 7.2 : Microstructure of an abusively ground AISI 51200 workpiece with dark blue temper colours

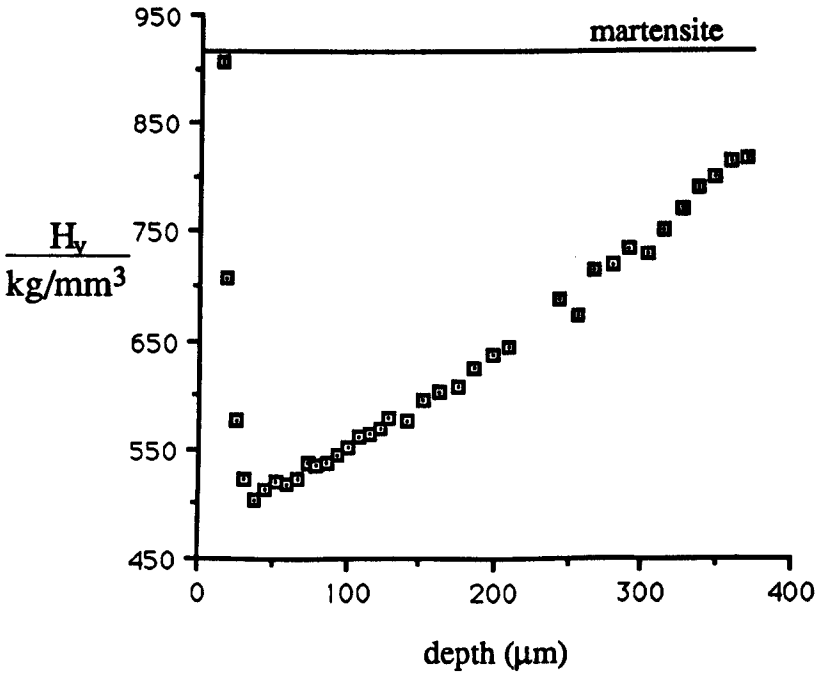

Figure 7.3 : Microhardness against depth below the surface for AISI 52100 ground with dark blue temper colours on the surface

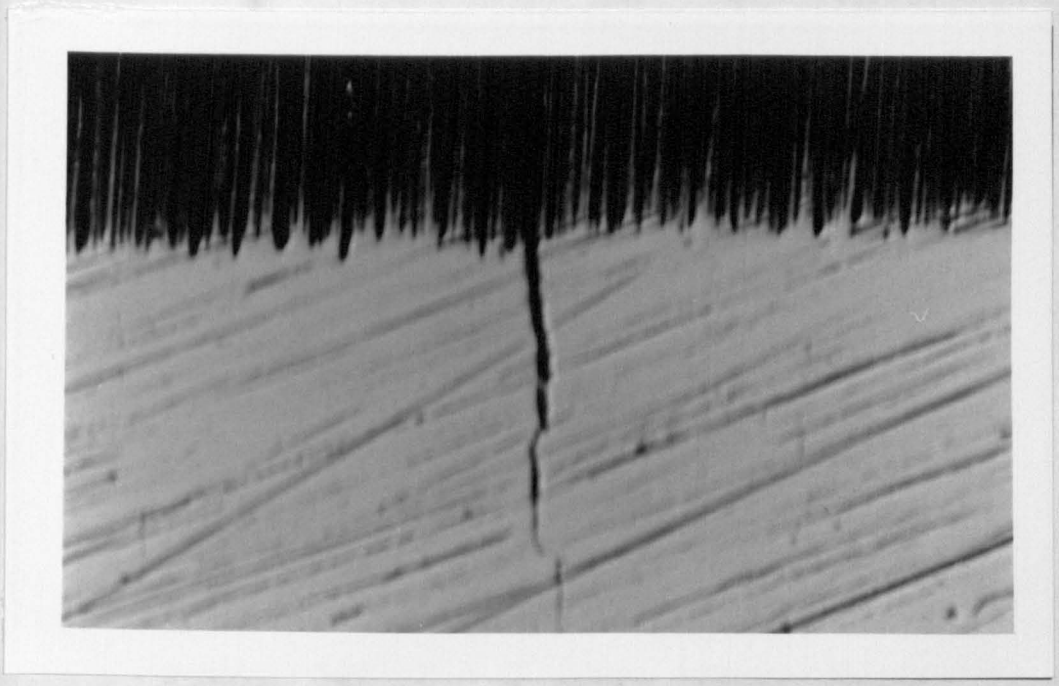

Figure 7.4 : Example of a microcrack in an abusively ground AISI 52100 workpiece with blue temper colours

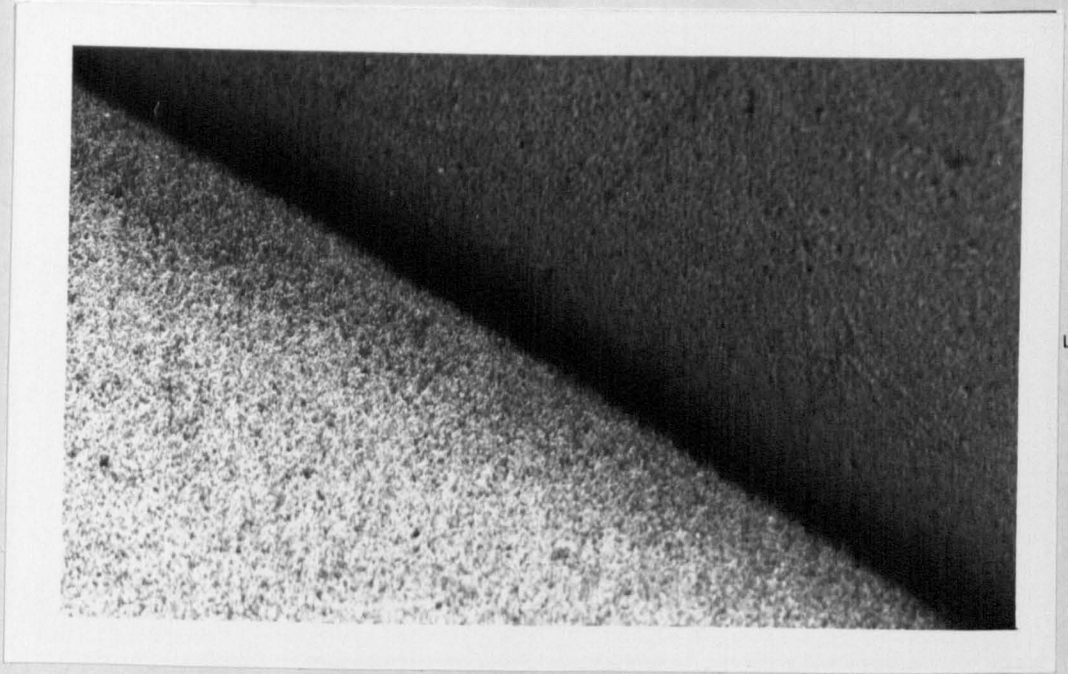

Figure 7.5 : Microstructure of AISI 51200 workpiece ground with straw temper colours

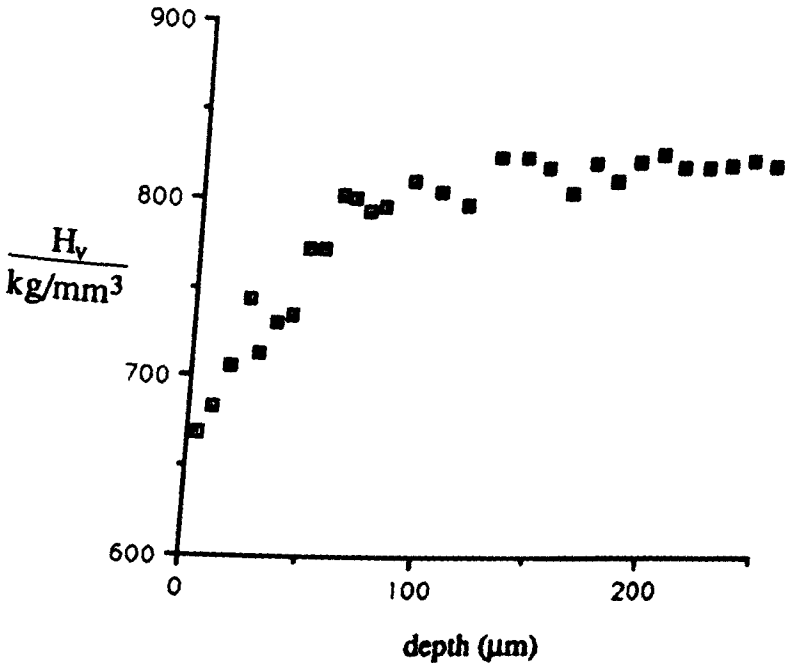

Figure 7.6 : Microhardness against depth below the surface for AISI 52100 ground with straw temper colours on the surface

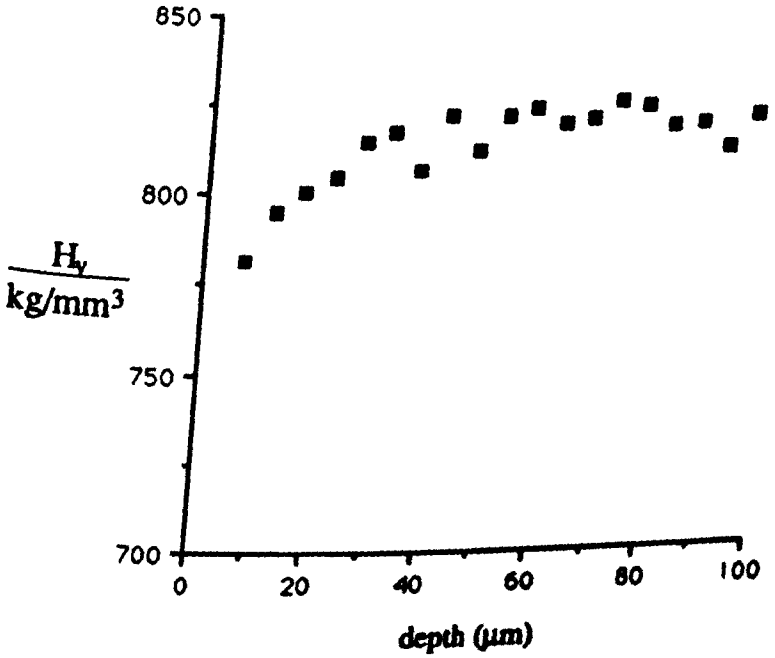

Figure 7. 7 : Microhardness against depth below the surface for AISI 52100 ground with no visible colours on the surface

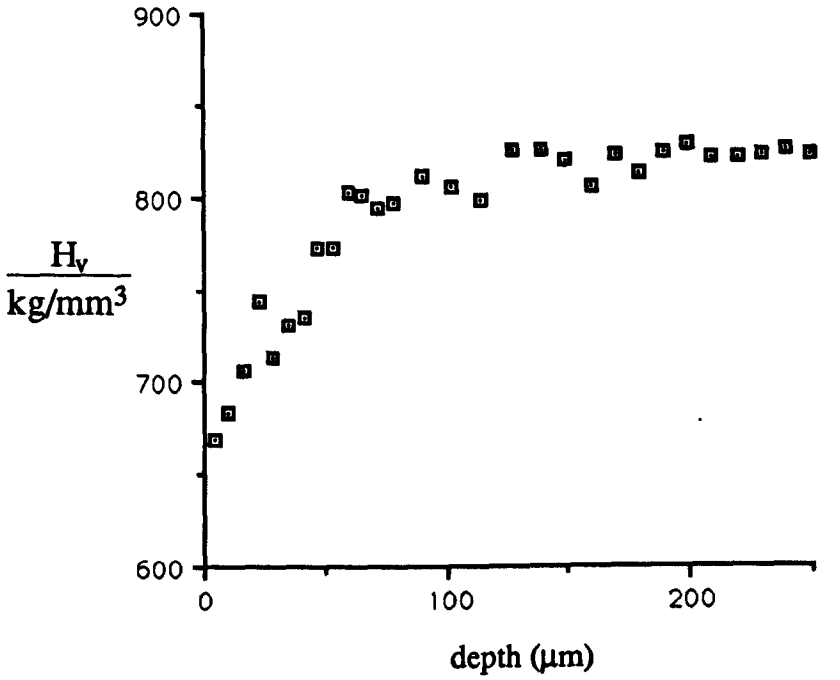

Figure 7.6 : Microhardness against depth below the surface for AISI 52100 ground with straw temper colours on the surface

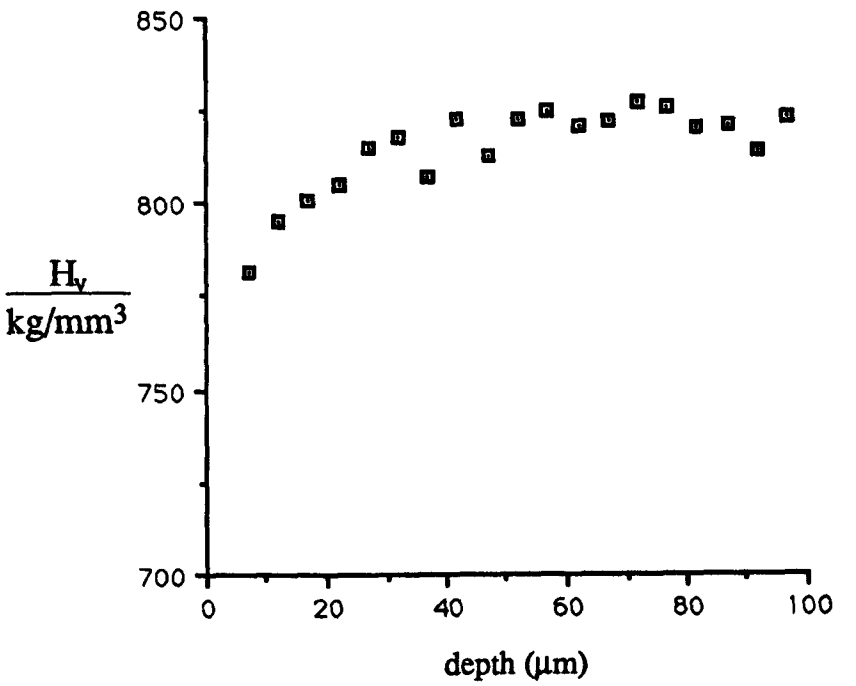

Figure 7. 7 : Microhardness against depth below the surface for AISI 52100 ground with no visible colours on the surface

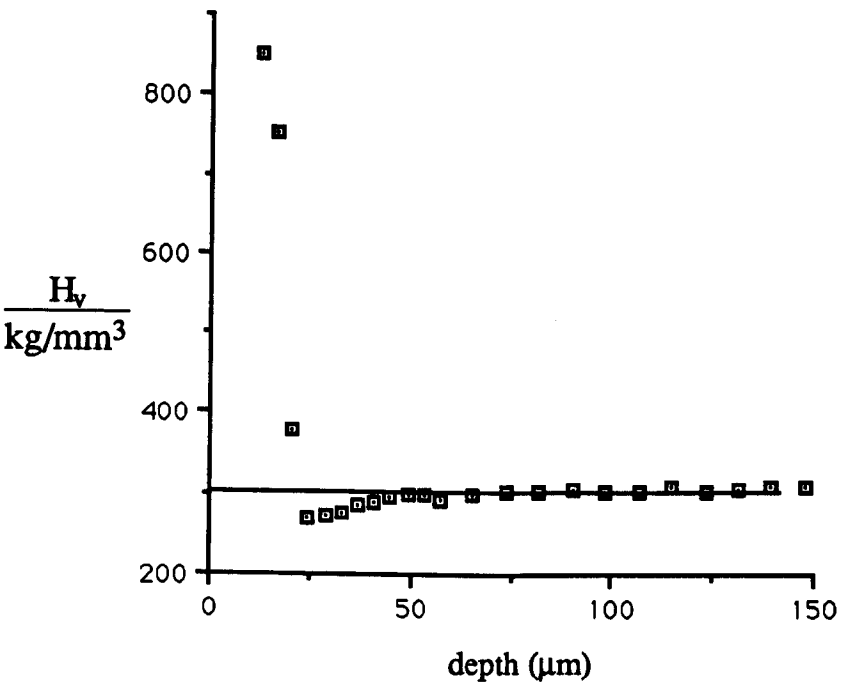

Figure 7.8 : Microhardness against depth below the surface for AISI 1055 ground with dark blue temper colours on the surface

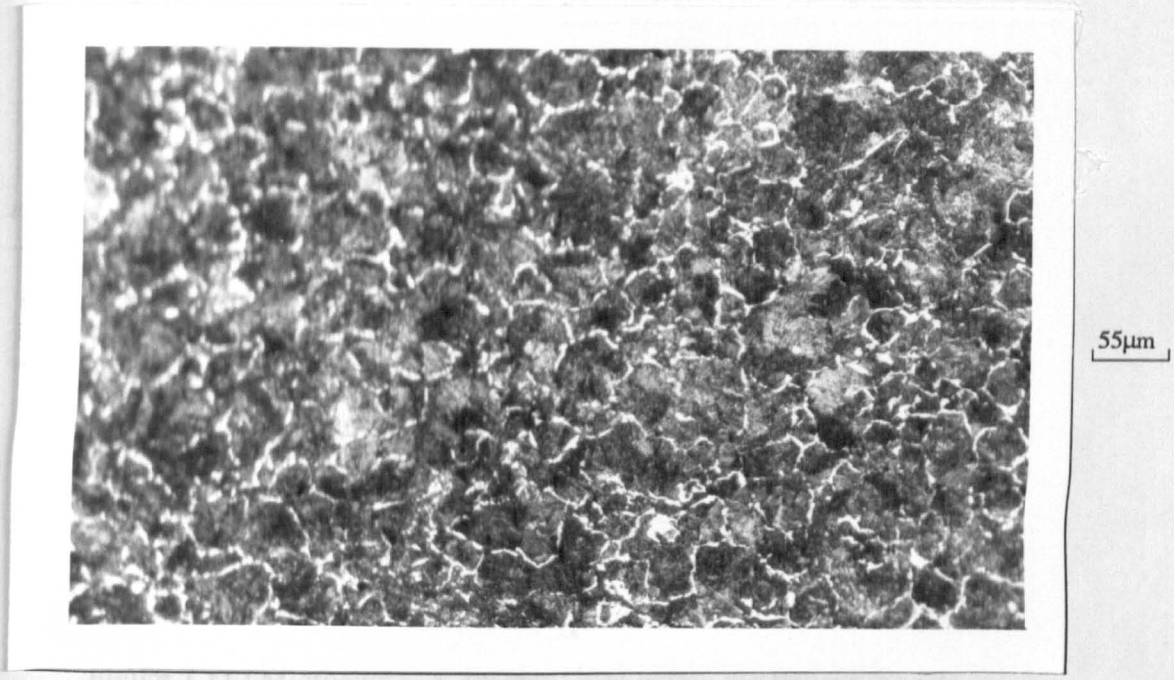

Figure 7.9 : Microstructure of AISI 1055

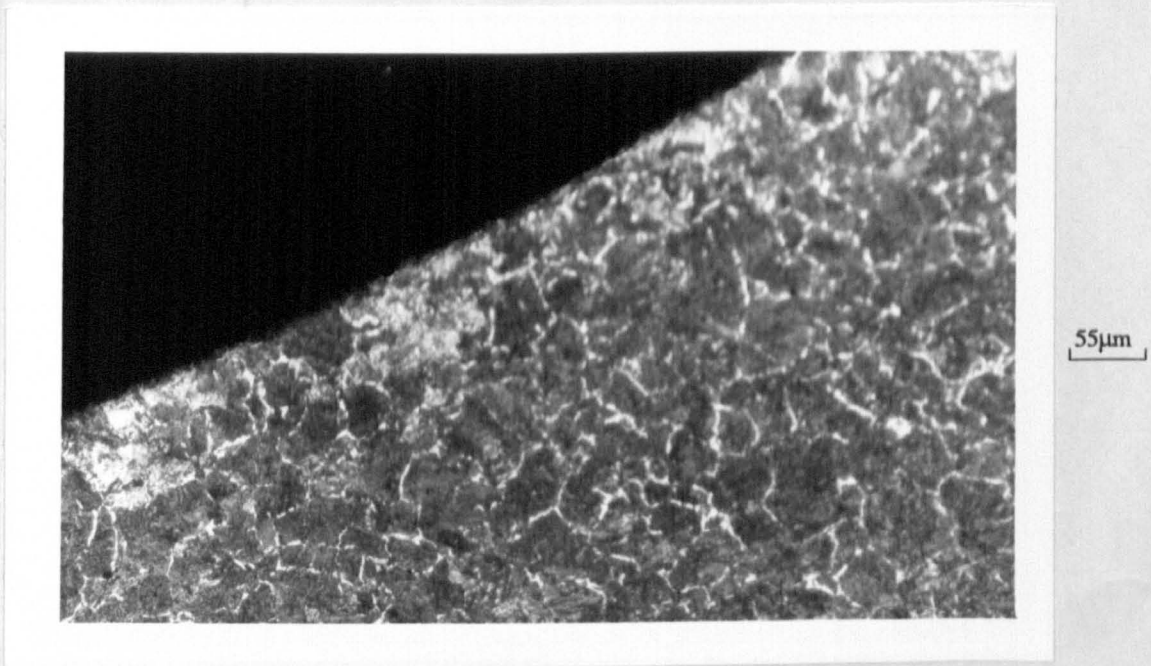

Figure 7.10 : Microstructure of AISI 1055 workpiece ground with straw temper colours

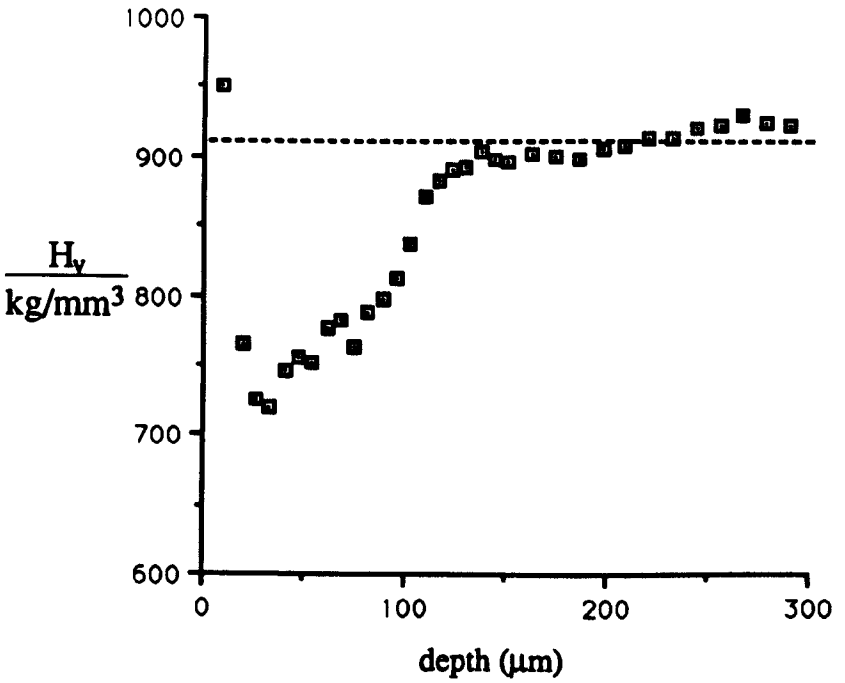

Figure 7.11 : Microhardness against depth below the surface for M2 tool steel ground with dark blue temper colours on the surface

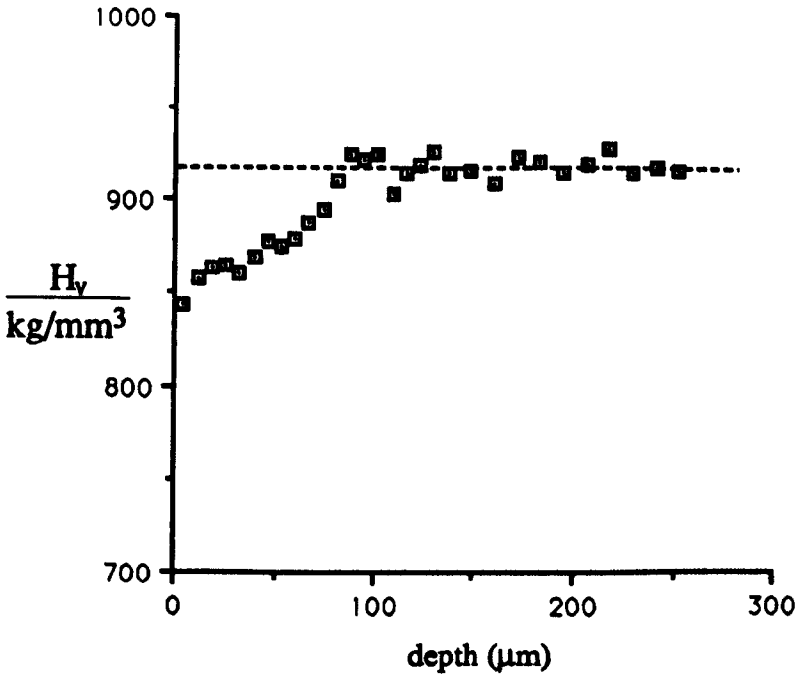

Figure 7.12 : Microhardness against depth below the surface for M2 tool steel ground with straw temper colours on the surface

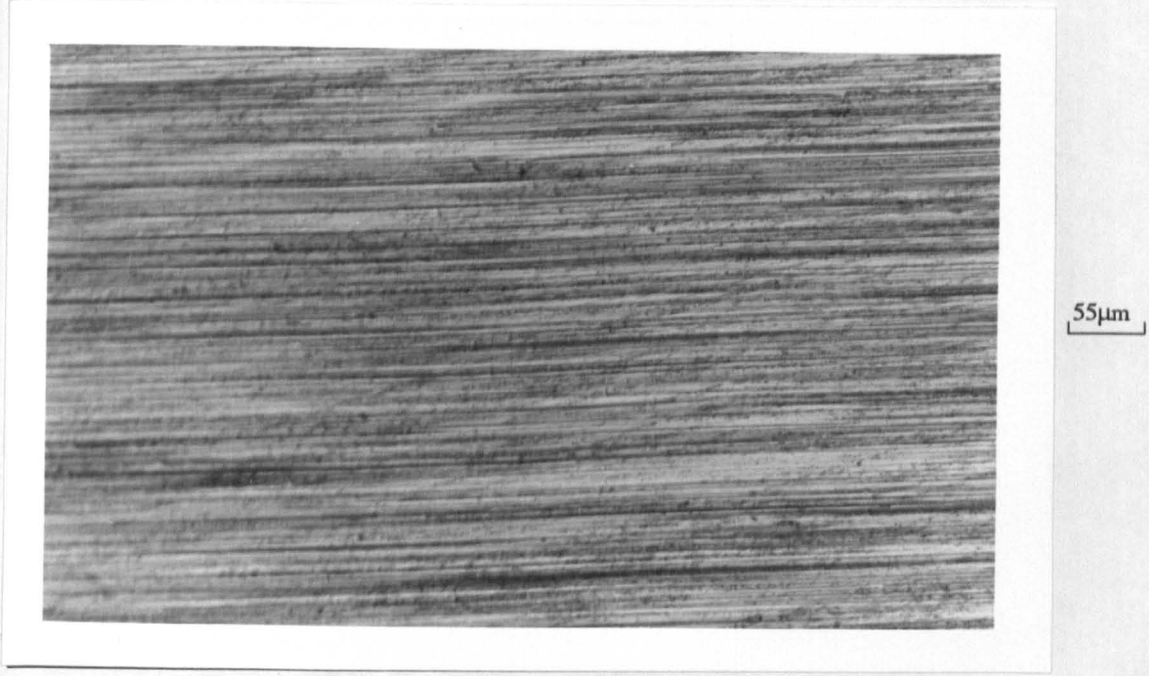

Figure 7.13 : Morphology of a ground surface with no visible thermal damage - AISI 52100 workpiece

Figure 7.14 : Morphology of a ground surface with straw temper colours - AISI 52100 workpiece example 1

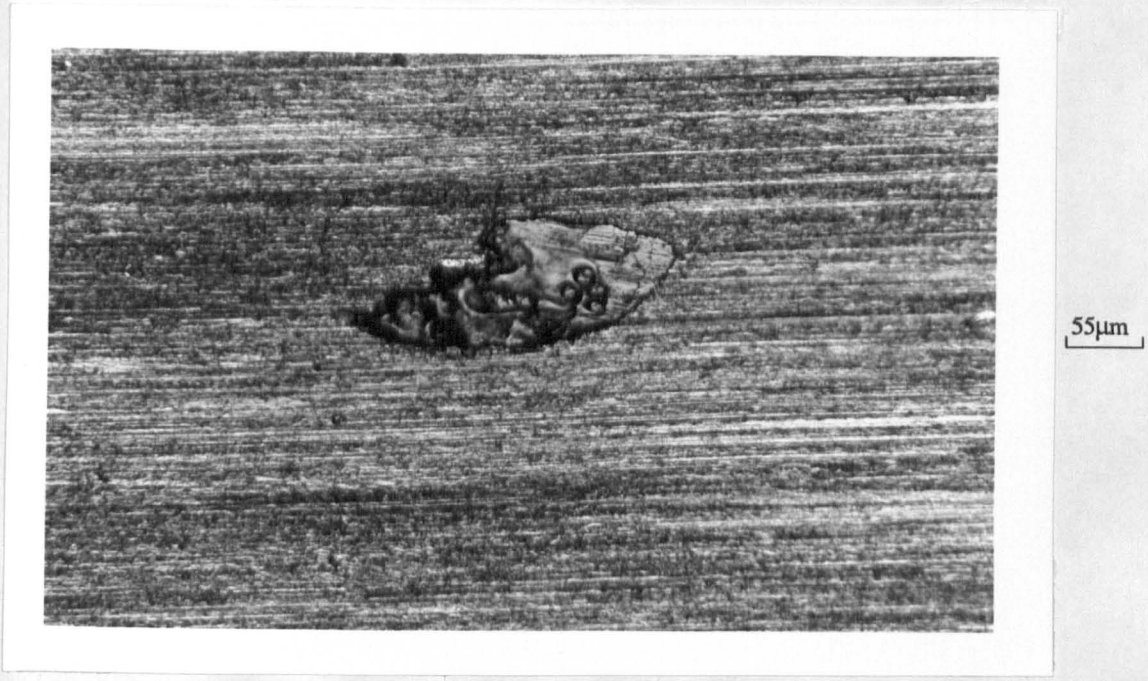

Figure 7.15 : Morphology of a ground surface with straw temper colours - AISI 52100 workpiece example 2

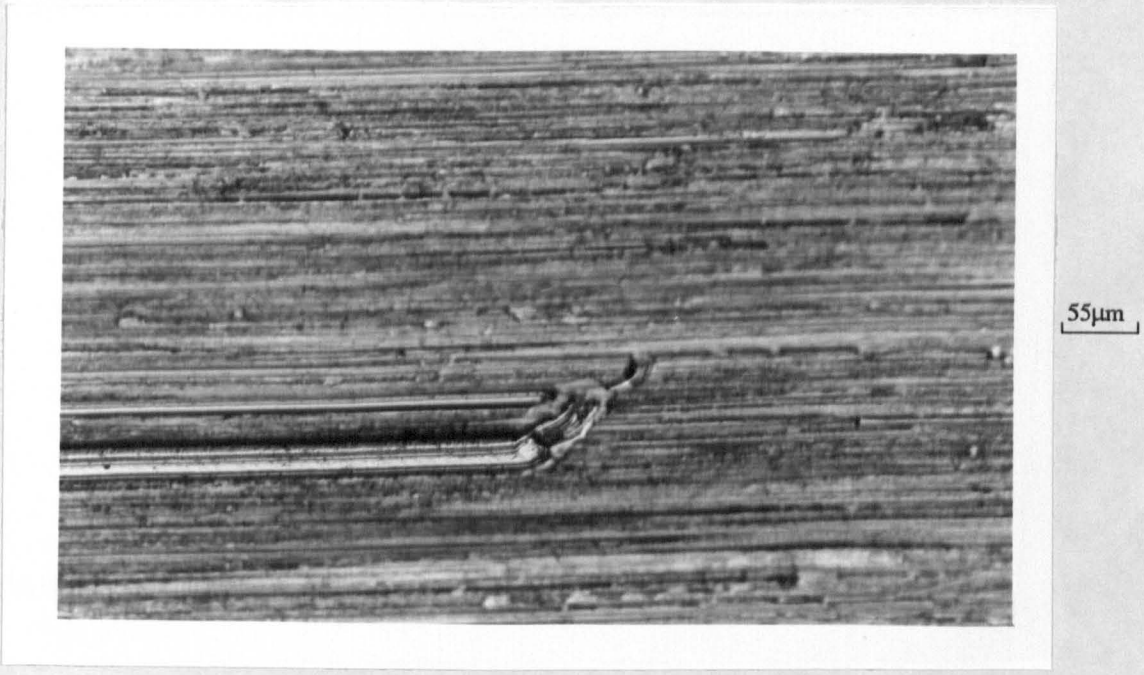

Figure 7.16 : Morphology of a ground surface with straw temper colours - AISI 52100 workpiece example 3

Figure 7.17 : Morphology of a ground surface with straw temper colours - AISI 52100 workpiece example 4

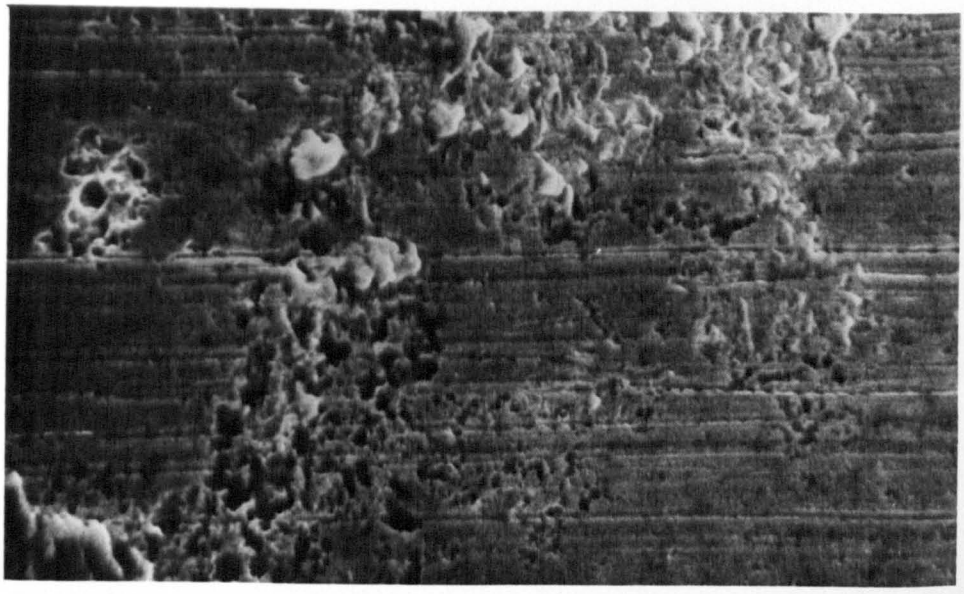

Figure 7.18 : Blistered oxide layer on a ground surface with temper colours as viewed under an SEM [59]

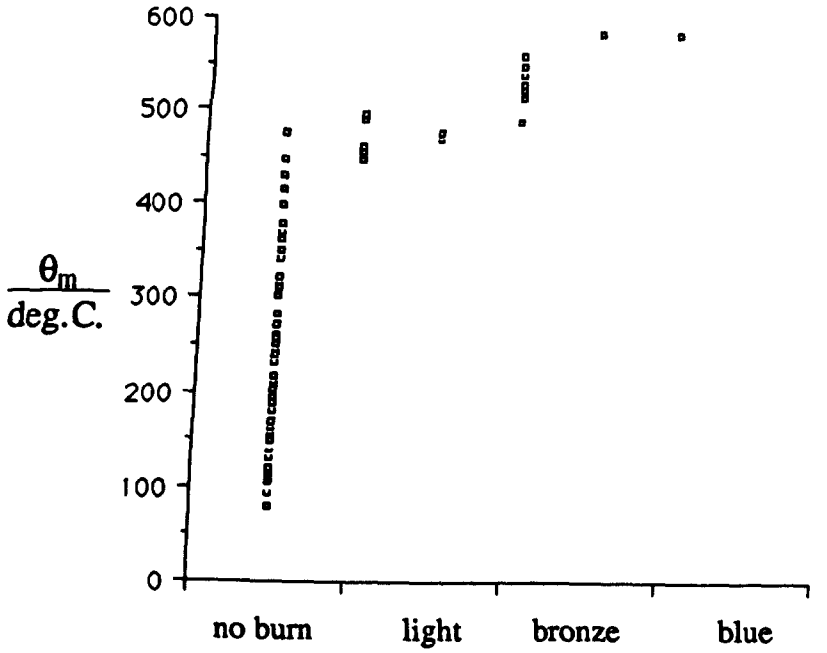

Figure 7.19 : Temperature against visible burn for AISI 52100

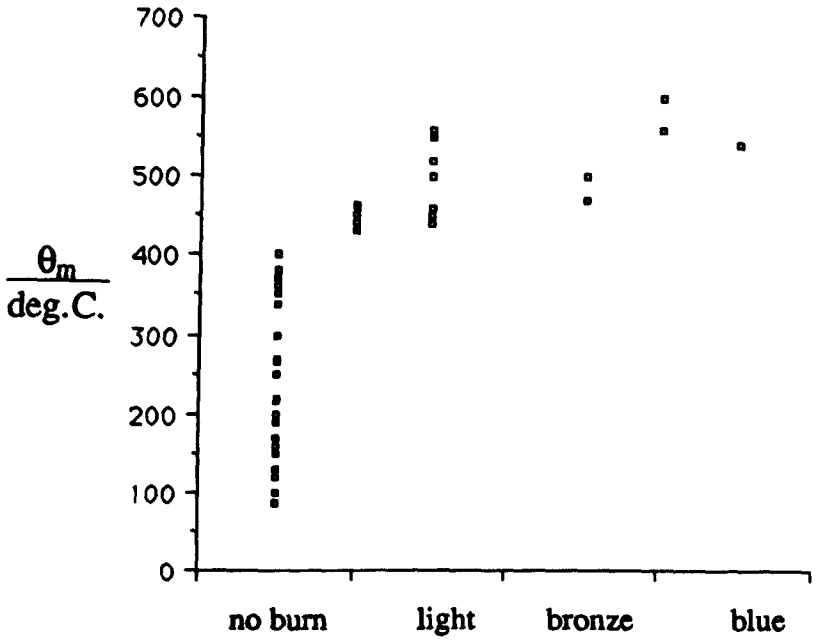

Figure 7.20 : Temperature against visible burn for AISI 1055

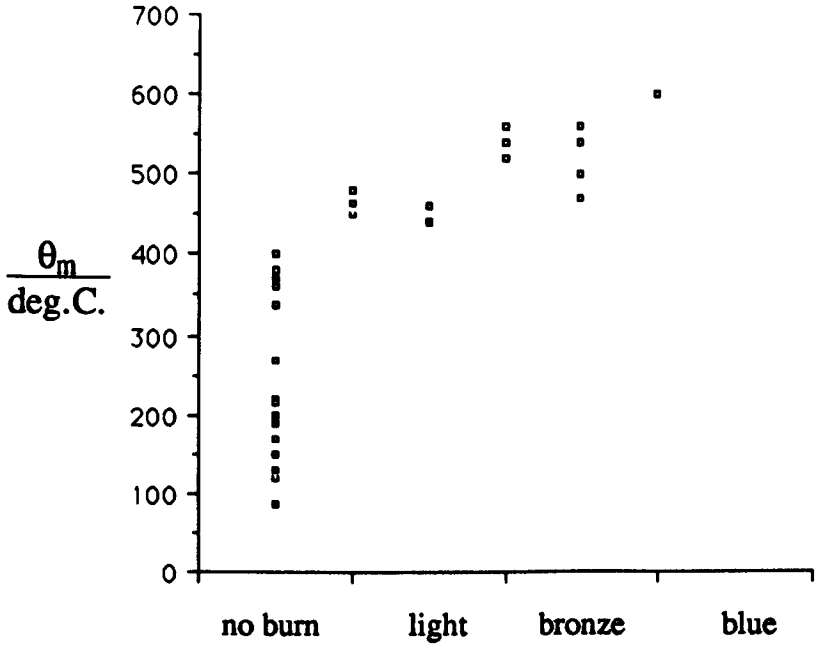

Figure 7.21 : Temperature against visible burn for M2

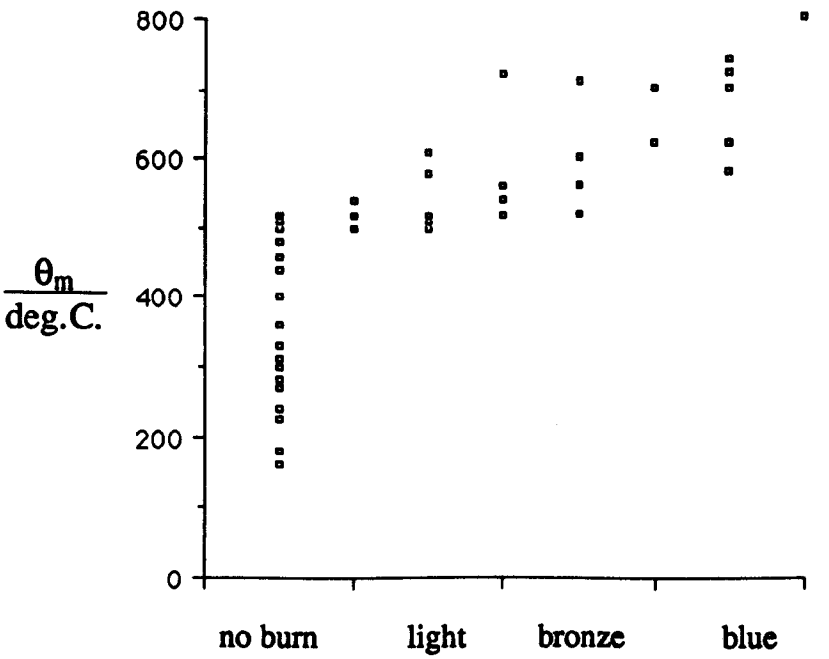

Figure 7.22 : Temperature against visible burn for cast iron

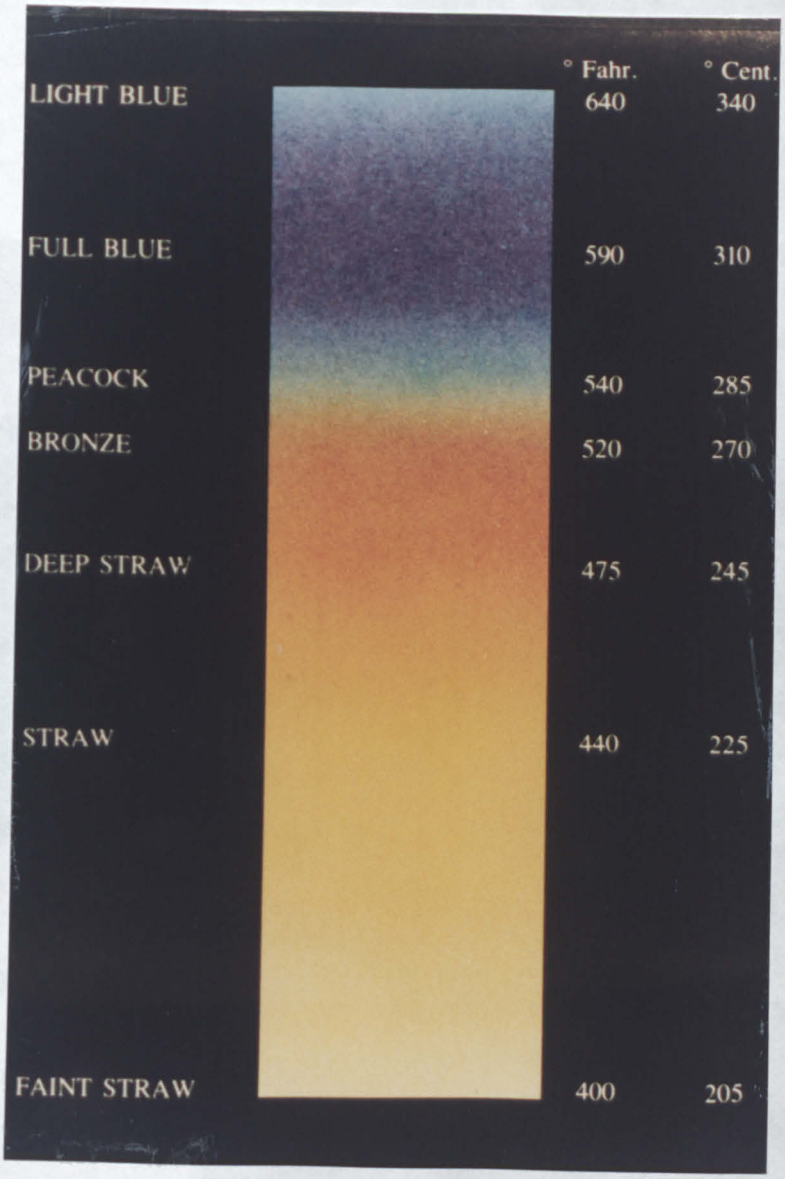

Figure 7.23 : Steady state heat treatment temperatures

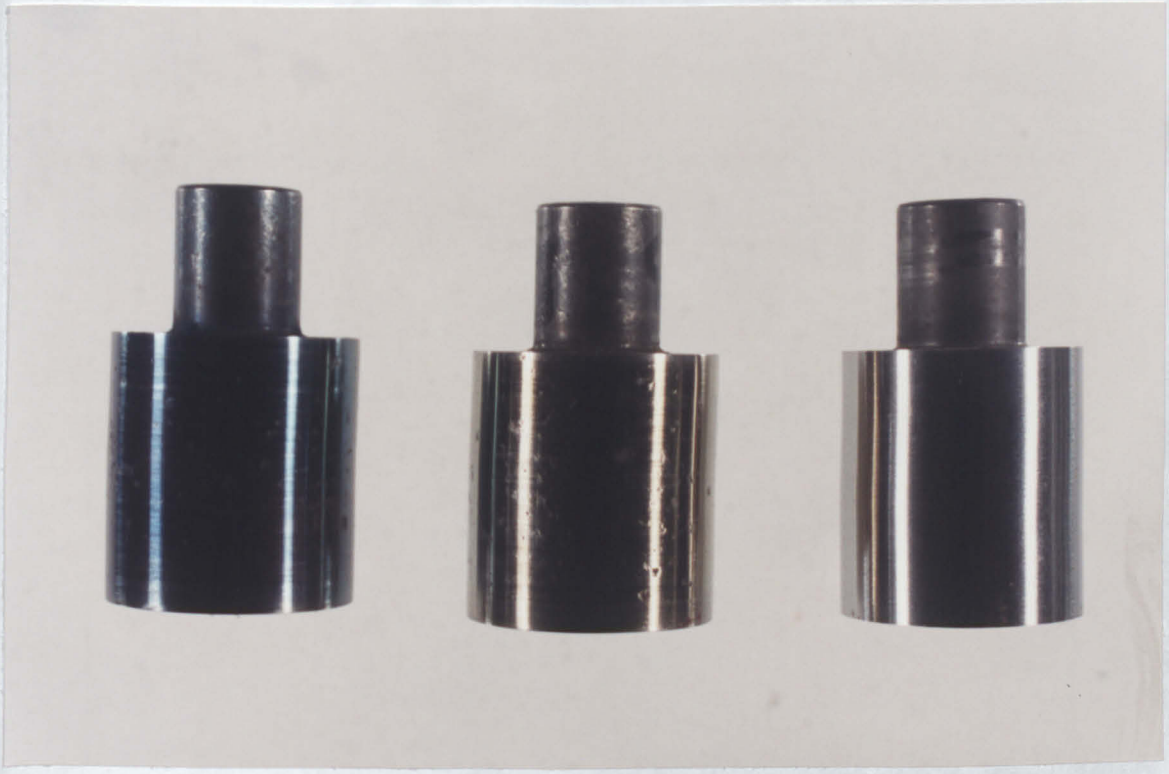

Figure 7.24 : Example of non visible thermal damage, straw temper damage and blue temper damage

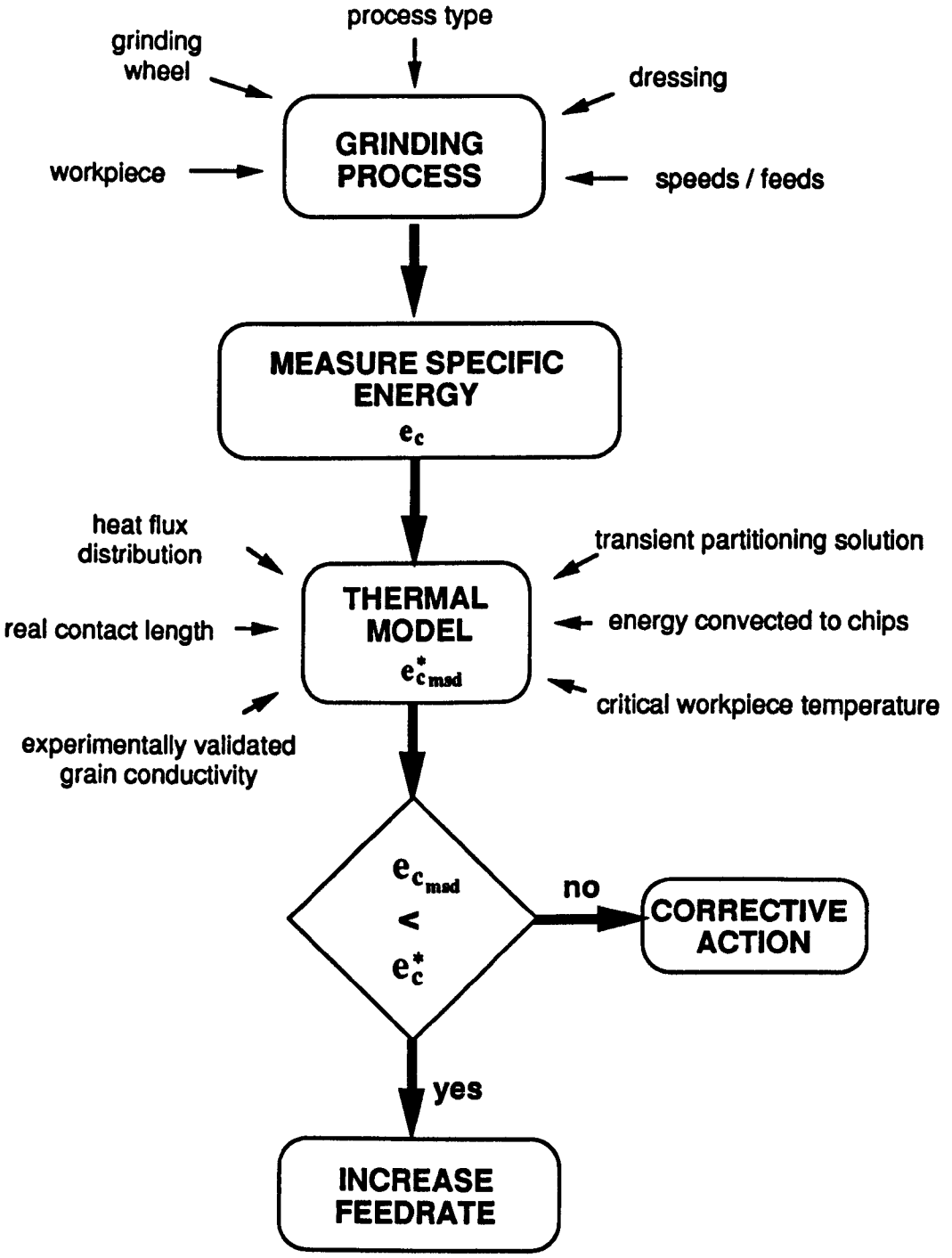

Figure 8.1 : Strategy for the prevention of thermal damage in grinding

Plate 1 Instrumented workpiece, amplifier and load cell

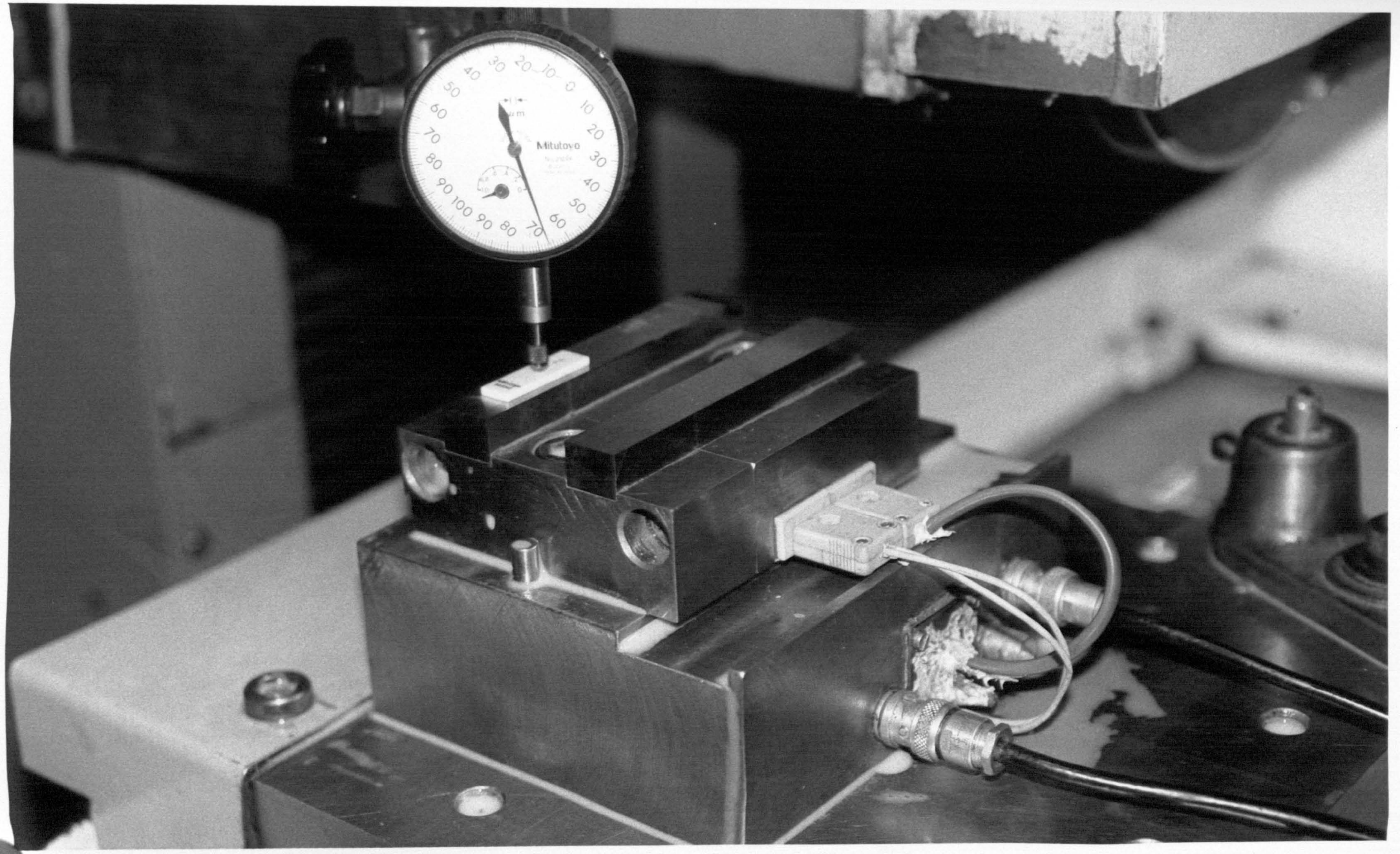
Mitutoyo

Plate 2 Example of the single pass grinding test

Plate 3 Instrumentation

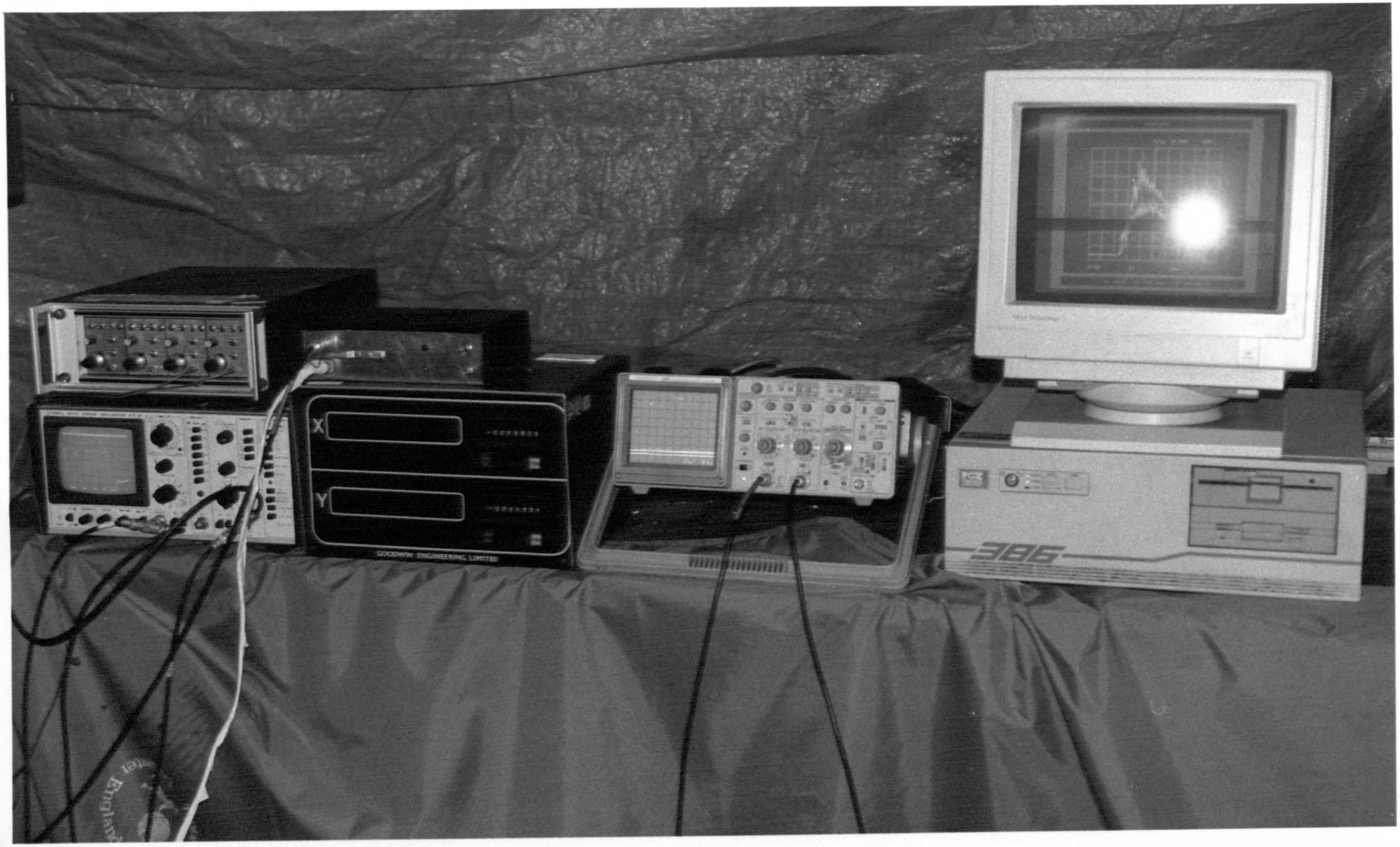
X
Y
GOODWIN ENGINEERING LIMITED
386

Plate 4 Micro-hardness tester

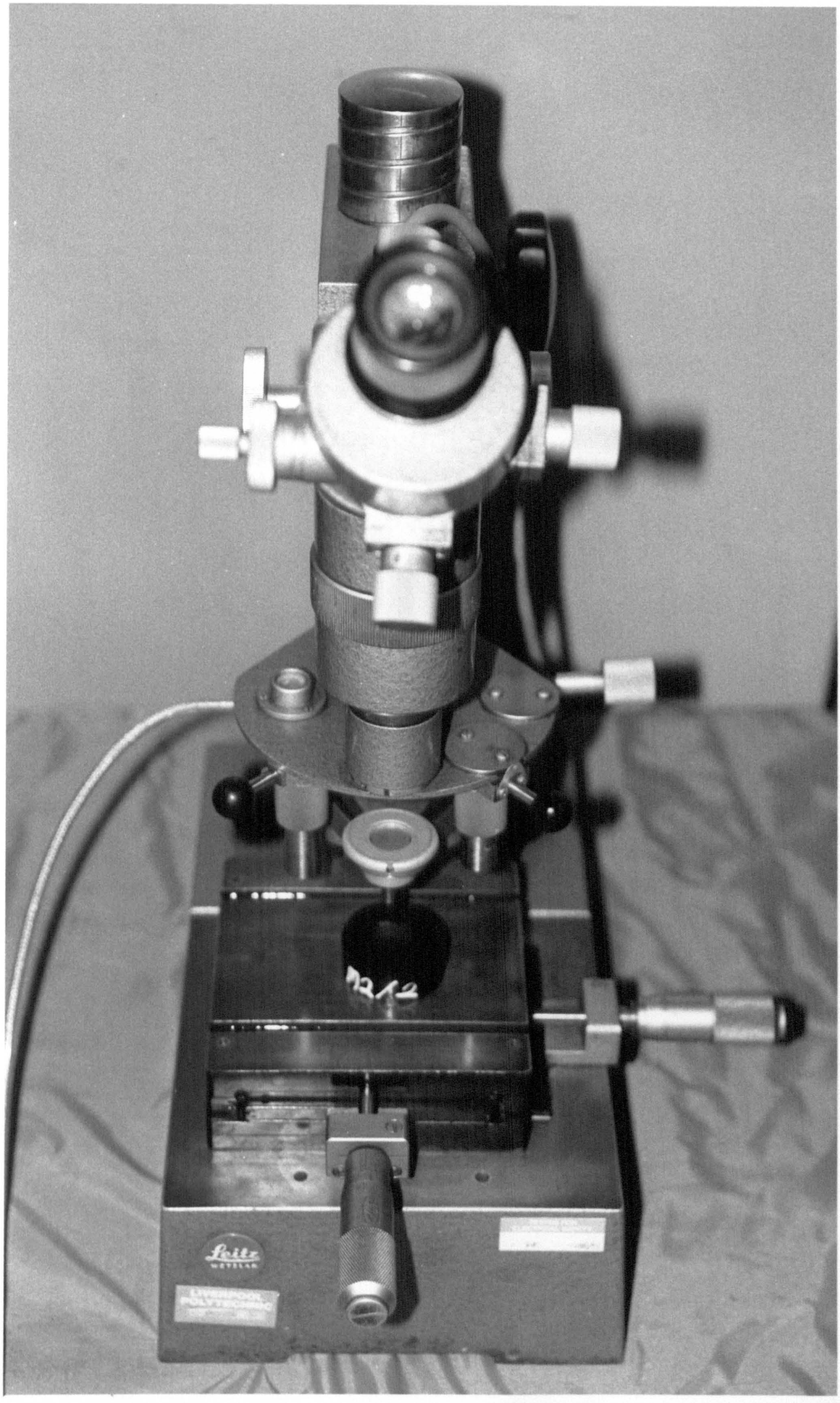
Leitz
WETZLAR

Plate 5 Microscope mounted over the grinding wheel

SC35
TYPE 12
SELF TIMER
OLYMPUS
OM SYSTEM
OLYMPUS

Plate 6 Brake dressing of the CBN wheel